Department of Energy Enegineering
School of Engineering - ETSI
University of Seville

Innovative Energy Storage Concepts Based on Power-to-Power Solutions Using Micro Gas Turbines

Antonio Escamilla Perejón

Seville, July 2023

Research work submitted in partial fulfillment of
the requirements for the degree of Doctor of Philosophy

PhD programme in Energy, Chemical and Environmental Engineering
Department of Energy Engineering
School of Engineering - ETSI
University of Seville

Innovative Energy Storage Concepts Based on Power-to-Power Solutions Using Micro Gas Turbines

Author: Antonio Escamilla Perejón
Supervisor: Prof. David Sánchez Martínez, University of Seville
Co-Supervisor: Prof. Lourdes García Rodríguez, University of Seville

Seville, July 2023

Research work submitted to the Department of Energy Engineering, School of Engineering, of the University of Seville in partial fulfilment of the requirements for the degree of Doctor of Philosophy

To my family and close friends...
...for motivating me during tough times, for having fun with me during good times.

For knowing that no matter what happens, ...
... they will always be there for me whenever I need them.

There is no greater certainty in life than knowing that ...
... there are people who love you unconditionally.

Acknowledgements

I wish to acknowledge the main supervisor of this thesis, Prof. David Sánchez, for the long-time motivation, guidance and help throughout the course of my doctoral studies. I am also grateful to Dr. Lourdes García-Rodríguez, the second supervisor of this thesis, for her strong support from the very beginning of my research.

I would also like to express my gratitude for the academic support received at the University of Seville and sincerely thank my colleagues (and friends) at the Thermal Power Group (GMTS).

I would like to express my gratitude to everyone I have had the opportunity to collaborate with. I am especially thankful to Eugenio Trillo for his invaluable assistance and guidance during the early stages of my PhD. I would also like to extend my appreciation to Dr. Mario Ferrari and Dr. Loredana Magistri at the University of Genoa for welcoming me to Savona Campus for a duration of three months. Additionally, I am grateful to the ETN Global Team, and in particular to Christer Bjorkqvist, for hosting me at the ETN office in Brussels for three months. Their belief in my abilities, encouragement, and support in advancing my professional career has been truly invaluable.

Above all, I am grateful to my family for their continuous support and confidence. Last but not least, I sincerely thank my friends. This would have not been possible without their help, support and understanding.

Seville, 19th July 2023 Antonio Escamilla Perejón

Summary

The NextMGT project aims to advance micro gas turbine technology as a decentralised energy system and promote its integration into renewable energy sources. The current thesis on power-to-power energy storage systems based on micro gas turbines to produce backup power by burning hydrogen aligns closely with the objectives and focus of the NextMGT project. Indeed, the thesis contributes to this mission by exploring the utilisation of hydrogen as a fuel for micro gas turbines, which not only offers a clean and reliable energy option in off-grid applications but also addresses the challenges of energy storage and grid stability in applications connected to the grid. By investigating the technical aspects, performance optimisation, interaction with the end-user requirements, and grid integration potential of power-to-power energy systems with micro gas turbines running on hydrogen, this research brings valuable insights to the NextMGT project. The findings from this thesis can help guide the development and implementation of micro gas turbine technologies that efficiently generate power from renewable hydrogen sources, paving the way for a more sustainable and reliable energy future.

Micro gas turbines play a crucial role as decentralised energy systems with the potential to enable significant shares of renewable energy. These compact and efficient devices offer a versatile solution to generate electricity and heat in a wide range of applications, from residential buildings to small industrial facilities. Their ability to run on various fuels, including natural gas, biogas, and even hydrogen, allows for greater flexibility and integration with existing energy infrastructure. Moreover, micro gas turbines can complement intermittent renewable sources by providing reliable and on-demand power, thereby addressing the issue of grid instability. Despite their immense potential, the market has been slow to accept micro gas turbines as a viable option. This hesitance can be attributed to factors such as limited awareness, high upfront costs, and the dominance of established energy technologies. However, as the need for decentralised energy systems and the demand for renewable integration continue to grow, it is crucial to recognise and explore the untapped potential of micro gas turbines for a more sustainable and resilient energy future.

Therefore, the document explores the use of micro-gas turbines integrated into power-to-power systems, as the option to produce backup power to the grid, with a focus on off-grid applications. The interest in power-to-power energy storage systems has been increasing steadily in recent times, in parallel with the also increasingly larger shares of variable renewable energy (VRE) in the power generation mix worldwide. Owing to the characteristics of VRE, adapting the energy market to a high penetration of VRE will be of utmost importance in the coming years. Variable renewable energies like wind or solar are characterised as being an intermittent source of energy whose availability for power generation depends mainly on local weather conditions, which can be predicted accurately within 24–36 h in advance only.

This, along with the very limited options for large-scale energy storage available today and the increasingly larger share of VREs in the energy mix, implies that the grid must still rely on conventional power generation technologies to generate electricity when VREs are not available. These conventional power generation technologies are very reliable but they also feature high emissions of greenhouse gases (GHG) and, in some cases, other hazardous emissions like nuclear waste. Large-scale energy storage is thus one of the most pressing technical challenges to achieve carbon neutrality by 2050. Additionally, and parallel to this, smart energy systems for managing the production, distribution and consumption of electricity, heat, and gas are very much needed to enable a 100% renewable energy scenario.

The first chapter introduces the efforts to fight against climate change, the global energy landscape, and the problem in certain regions where access to electricity is not universal, presenting the pillars that motivate the research on power-to-power energy storage systems and the use of micro-gas turbines. The chapter concludes by highlighting the original contribution to knowledge and the different publications and activities in which the author has taken part.

The second chapter introduces a comprehensive assessment of the current advancements in water electrolysis. The chapter begins with a discussion of the various methods used to produce hydrogen and delves into the intricate thermodynamic principles underlying the electrochemical process that facilitates water splitting through electrolysis. The subsequent section focuses on different electrolyser technologies, with special emphasis on Alkaline, Proton-Exchange Membrane, and Solid Oxide electrolysers. Their performance, manufacturing considerations, and economic parameters are closely examined. Concluding the chapter, an outlook is provided for the future of these technologies, including the identification of barriers that need to be addressed to enable large-scale hydrogen production.

The third chapter delves into the concept of power-to-power, indicating the processes involved and reviewing the technologies that can be applied for each of them along with their Technology Readiness Level. The chapter also introduces technology and thermodynamic market research to shed light on the options commercially available. The figure of merit round-trip efficiency is presented and used to evaluate the different layouts that could be adopted, highlighting those that stand out and making a critical review of which systems have the highest potential to increase their performance, yielding higher round-trip efficiency for this energy storage option.

After a thermodynamic analysis of the processes that enable setting up the energy requirements for the different types of electrolysers, storage systems and micro gas turbines available in the market, the fourth chapter investigates the design modelling of each of the systems involved in detail, with the aim to build a software tool that allows running techno-economic simulations of power-to-power energy storage systems, evaluating accurately the performance of each system and integrating them all to carry out hourly energy balances while yielding important economic parameters, such as the Levelised Cost of Hydrogen (LCOH) and Energy (LCOE). The fifth chapter introduces a detailed review of the economics of each system by carrying out an extensive literature review and extracting the information for each of the systems, paying special attention to the capital and operational expenditure of the renewable energy sources, electrolysers, compression system, storage media, and micro-gas turbine.

Furthermore, there are metrics that are reported to evaluate the impact of economics, such as the LCOH and LCOE, as well as the payback period and internal rate of return.

The sixth chapter puts into practice the modelling built to carry out techno-economic studies of power-to-power with mGTs. The application considered involves an off-grid system that requires a continuous power supply of 30 kWe. The chapter presents a conceptual plan for an off-grid system that can be implemented across various locations in Europe with two distinct layouts. The study presents valuable insights into how the power-to-power system needs to be redesigned in different locations across Europe. It also provides knowledge of the footprint of each system along with key economic parameters. The second part of the study successfully demonstrates that hybridising the reference system with battery energy storage enables a reduction of the footprint of the PV solar field and the amount of seasonal storage, yielding much lower LCOE.

Chapter 6 investigates the further improvement of the power-to-power system based on micro gas turbines through hybridisation with other storage technologies, and Chapter 7 looks at the potential to improve the electric efficiency of the micro gas turbine with the final objective of improving the round-trip efficiency of the complete storage system, reducing the overall footprint and final LCOE. This chapter investigates the incorporation of an ORC system as a waste-heat recovery system making use of the waste heat from the micro gas turbine. The research successfully demonstrates that the solution from Chapter 6 can be further improved when upgrading the efficiency of a 30 kWe micro gas turbine from 27% to 42%.

Chapter 8 presents the main remarks from this research and exposes the pathways toward the further advancement of power-to-power energy storage systems as well as micro gas turbines to make this technology competitive.

The primary finding of the thesis is that power-to-power systems offer an excellent solution for storing energy over extended periods of time, weeks or even months, and can be deployed in almost any location with intermittent renewable energy resources and access to water. When implementing these systems for off-grid applications, maximising round-trip efficiency becomes crucial. This optimisation results in a reduced footprint for the PV solar field, electrolyser, and seasonal storage, which typically accounts for approximately 50% of the overall cost (levelised cost of hydrogen). To enhance round-trip efficiency, a key requirement is for the micro-gas turbine to achieve an electric efficiency exceeding 40%, particularly challenging at low power levels (< 100 kW) where efficiency typically falls below 30%. The research has successfully explored two approaches to enhance the competitiveness of power-to-power systems utilising micro gas turbines: a) integrating with battery energy storage systems, and b) utilising an organic Rankine cycle system to recover waste heat from the exhaust gases of the micro gas turbine. Both methods significantly reduce the overall system footprint and the levelised cost of electricity. Consequently, future research should focus on improving the efficiency of the electrolyser and micro-gas turbine systems.

Keywords: *Power-to-Power, Micro-gas turbines, Renewable hydrogen, Energy storage systems*

Resumen

El proyecto NextMGT tiene como objetivo avanzar en el campo de las microturbina de gas como sistema de energía descentralizada y promover su integración con fuentes de energía renovables. La tesis actual sobre sistemas de energía *power-to-power* que utilizan microturbina de gas para proporcionar energía eléctrica (y térmica) mediante la combustión de hidrógeno se alinéa estrechamente con los objetivos y enfoque del proyecto NextMGT. La tesis contribuye a esta misión explorando la utilización de hidrógeno como combustible para microturbinas de gas, lo cual no solo ofrece una opción de energía limpia en aplicaciones no conectadas a red sino que, también, aborda los desafíos del almacenamiento de energía y la estabilidad de la red en aplicaciones conectadas. Al investigar los aspectos técnicos, la optimización del rendimiento y el potencial de integración en la red de los sistemas de energía *power-to-power* con microturbina de gas que funciona con hidrógeno, esta investigación aporta ideas valiosas al proyecto NextMGT. Los hallazgos de esta tesis pueden ayudar a guiar el desarrollo e implementación de tecnologías de microturbina de gas que generen energía de manera eficiente a partir de hidrógeno renovable , allanando el camino hacia un futuro energético más sostenible y seguro.

Las microturbina de gas desempeñan un papel crucial como sistema de energía descentralizada que tiene el potencial de permitir una mayor presencia de energías renovables en la red. Estos dispositivos compactos y eficientes ofrecen una solución versátil para generar electricidad y energía térmica en una amplia gama de aplicaciones, desde edificios residenciales hasta pequeñas instalaciones industriales. Su capacidad para funcionar con diversos combustibles, incluyendo gas natural, biogás e incluso hidrógeno, permite una mayor flexibilidad e integración con la infraestructura energética existente. Además, las microturbina de gas pueden complementar fuentes renovables intermitentes al proporcionar energía fiable y bajo demanda, abordando así el problema de la inestabilidad de la red. A pesar de su inmenso potencial, el mercado ha sido lento en aceptar las microturbinas de gas como una opción viable. Esto puede atribuirse a factores como la falta de conocimiento, los altos costos iniciales y el dominio de tecnologías consolidadas. Sin embargo, a medida que la necesidad de sistemas de energía descentralizados y la demanda de integración renovable continúan creciendo, es crucial reconocer y explorar el potencial sin explotar de las microturbina de gas para un futuro energético más sostenible y resiliente.

Por lo tanto, el documento explora el uso de microturbina de gas integradas en sistemas de almacenamiento energético *power-to-power*, como opción para proporcionar seguridad energética al usuario, con especial atención a aplicaciones no conectadas a red. El interés en los sistemas de almacenamiento de energía *power-to-power* ha aumentado constantemente en los últimos tiempos, en paralelo con la creciente participación de las fuentes de energía

renovable variable en el mix de generación de energía a nivel mundial. Debido a las características de las fuentes de energía renovable variable, adaptar el mercado de energía a una alta penetración de estas fuentes será de suma importancia en los próximos años. Las energías renovables variables como la eólica o solar se caracterizan por ser una fuente intermitente de energía cuya disponibilidad para la generación eléctrica depende principalmente de las condiciones climáticas locales, que solo pueden predecirse con precisión con 24-36 horas de anticipación. Esto, junto con las opciones muy limitadas de almacenamiento de energía a gran escala disponibles en la actualidad y la participación cada vez mayor de las fuentes de energía renovable variable en el mix energético, implica que la red aún debe depender de tecnologías convencionales de generación de energía para generar electricidad cuando las fuentes renovables no están disponibles. Estas tecnologías convencionales de generación de energía son altamente fiables, pero también generan altas emisiones de gases de efecto invernadero y, en algunos casos, otros contaminantes peligrosos como residuos nucleares. Por lo tanto, el almacenamiento de energía a gran escala es uno de los desafíos técnicos más urgentes para lograr la neutralidad en la huella de carbono para 2050. Además, en paralelo a esto, los sistemas *smart-grid* para gestionar la producción, distribución y consumo de electricidad, calor y gas son de suma importancia para permitir un escenario de energía 100% renovable.

El primer capítulo introduce los esfuerzos para combatir el cambio climático, el panorama energético mundial y el problema de acceso a la red eléctrica en ciertas regiones, introduciendo el fundamento que motiva esta investigación de los sistemas de almacenamiento de energía *power-to-power* y el uso de microturbina de gas. El capítulo finaliza destacando la contribución original al conocimiento y las diferentes publicaciones y actividades en las que el autor ha participado.

El segundo capítulo presenta una evaluación exhaustiva de los avances actuales en la electrólisis del agua. El capítulo comienza discutiendo los diversos métodos utilizados para producir hidrógeno y profundiza en los principios termodinámicos que subyacen al proceso electroquímico que facilita la división del agua mediante la electrólisis. La sección siguiente se centra en las diferentes tecnologías de electrolizadores, con especial énfasis en los electrolizadores alcalinos, de membrana de intercambio de protones y de óxido sólido. Se examina de cerca su rendimiento, consideraciones de fabricación y parámetros económicos. Concluyendo el capítulo, se ofrece una perspectiva del futuro de estas tecnologías, incluida la identificación de barreras que deben superarse para permitir la producción de hidrógeno a gran escala.

El tercer capítulo profundiza en el concepto de *power-to-power*, indicando los procesos involucrados y revisando las tecnologías que se pueden aplicar para cada uno de ellos junto con su escala de madurez tecnológica. El capítulo también presenta una investigación de mercado para arrojar luz sobre las opciones disponibles comercialmente. Se establece la figura de mérito de eficiencia del almacenamiento y se utiliza para evaluar los diferentes diseños que podrían adoptarse, destacando aquellos con mejores resultados y haciendo una revisión crítica de los sistemas que tienen el mayor potencial para aumentar su rendimiento, lo que produce una mayor eficiencia de almacenamiento de las soluciones *power-to-power*.

Después de un análisis termodinámico de los procesos que permitieron establecer los requi-

sitos energéticos para los diferentes tipos de electrolizadores, sistemas de almacenamiento y microturbina de gas disponibles en el mercado, el cuarto capítulo investiga en detalle el modelado del diseño de cada uno de los sistemas involucrados con el objetivo de construir una herramienta de software que permita realizar simulaciones tecnoeconómicas de sistemas de almacenamiento de energía *power-to-power*, evaluando con precisión el rendimiento de cada sistema e integrándolos todos para realizar balances energéticos en base horaria y obtener importantes parámetros económicos, como el Coste Nivelado del Hidrógeno (LCOH) y la Energía (LCOE).

El quinto capítulo presenta una revisión detallada de las características económicas de cada sistema mediante una extensa revisión bibliográfica y extrayendo la información de cada uno de los sistemas, prestando especial atención a la inversión de capital y los gastos operativos de las fuentes de energía renovable, electrolizadores, sistemas de compresión, medios de almacenamiento y microturbina de gas. Además, se proporciona información para evaluar el impacto económico, como LCOH y LCOE, así como el período de retorno de la inversión y la tasa interna de retorno.

El sexto capítulo pone en práctica el modelado construido para realizar estudios tecnoeconómicos de sistemas *power-to-power* basados en microturbina de gas. La aplicación considerada se basa en un usuaroio independiente de la red y que requiere un suministro continuo de energía de 30 kWe. El capítulo presenta un plan conceptual para un sistema autónomo que se puede implementar en varios lugares de Europa con dos diseños distintos. El estudio proporciona información valiosa sobre cómo se debe rediseñar el sistema *power-to-power* en diferentes localizaciones. También proporciona conocimientos sobre la superficie requerida por cada sistema junto con los principales parámetros económicos. La segunda parte del estudio demuestra con éxito cómo la hibridación del sistema *power-to-power* con un sistema de almacenamiento basado en baterías logra reducir el tamaño del campo solar fotovoltaico y la cantidad de almacenamiento estacional, lo que resulta en un LCOE mucho menor.

Tras investigar en el Capítulo 6 cómo se puede mejorar el sistema *power-to-power* basado en microturbina de gas mGT mediante la hibridación con otras tecnologías de almacenamiento, el séptimo capítulo analiza el potencial para mejorar la eficiencia eléctrica de la microturbina de gas con el objetivo final de mejorar la eficiencia de almacenamiento del sistema *power-to-power* y así reducir el tamaño de los sistemas involucrados y el LCOE final. Este capítulo investiga la incorporación de un sistema ORC como sistema de recuperación del calor residual en los gases de escape de la microturbina de gas. La investigación concluye con éxito que aumentar la eficiencia eléctrica del sistema de producción de potencia puede mejorar significativamente la solución del Capítulo 6, en particular al mostrar soluciones viables para aumentar la eficiencia de una microturbina de gas de 30 kWe del 27% al 42%.

El octavo capítulo resume las principales conclusiones de esta investigación y expone las diferentes vías para seguir desarrollando tanto los sistemas de almacenamiento de energía *power-to-power* como las propias microturbinas de gas, para hacerlas competitivas desde el punto de vista tecnológico.

El hallazgo principal de la tesis es que los sistemas de almacenamiento *power-to-power* ofre-

cen la única solución viable para almacenar energía durante períodos prolongados de tiempo, semanas e incluso meses, y se pueden implementar en casi cualquier lugar con recursos de energía renovable y acceso a agua. Cuando se implementan estos sistemas para aplicaciones autónomas, maximizar la eficiencia de almacenamiento se vuelve crucial. Esta optimización resulta en una reducción del tamaño del campo solar fotovoltaico, electrolizador y almacenamiento estacional, que representa aproximadamente el 50% del coste nivelado del hidrógeno. Para mejorar la eficiencia de almacenamiento, se requiere que la microturbina de gas logre una eficiencia eléctrica superior al 40%, lo cual es particularmente desafiante en sistemas de baja potencia (<100 kW) donde la eficiencia típicamente cae por debajo del 30%. La investigación ha explorado con éxito dos enfoques para mejorar la competitividad de los sistemas *power-to-power* que utilizan microturbinas de gas: a) integración con baterías eléctricas, y b) utilización de un sistema de ciclo Rankine orgánico para recuperar el calor residual de los gases de escape de la microturbina de gas. Ambos métodos reducen significativamente el tamaño del sistema y el coste nivelado de la electricidad. En consecuencia, la investigación futura debería centrarse en mejorar la eficiencia de los sistemas de electrolizador y microturbina de gas.

Palabras Claves: *Power-to-Power, microturbina de gas, hidrógeno renovable, sistemas de almacenamiento de energía*

Abstract

Power-to-Power is a process whereby the surplus of renewable power is stored as chemical energy in the form of hydrogen. Hydrogen can be used in situ or transported to the consumption node. When power is needed again, hydrogen can be consumed for power generation. Each of these processes incurs energy losses, leading to a certain round-trip efficiency (Energy Out/Energy In). Round-trip efficiency is calculated considering the following processes: water electrolysis for hydrogen production, compression, liquefaction or use of metal-hydride for hydrogen storage, fuel-cell-electric-truck for hydrogen distribution and micro-gas turbine for hydrogen power generation.

From a first analysis of the commercial technologies available in the market, the achievable round-trip efficiency of the power-to-power energy storage system proposed is 29% when considering solid oxide electrolysis and metal hydride storage. This number decreases sharply when using alkaline or proton exchange membrane electrolysers, 22.2% and 21.8% respectively. Round-trip efficiency is further reduced if considering other storage media, such as compressed- or liquefied-H_2. Even if this is not positive, this thesis shows that there is a large margin to increase round-trip efficiency again, mostly through improvements in the hydrogen production process and the thermo-mechanical energy conversion step, which could lead to round-trip efficiencies of around 40%–42% in the next decade, for power-to-power energy storage systems based on micro gas turbines.

By prioritising the development of a rapid techno-economic assessment tool, accurate models for the various components of the system have been successfully created and incorporated into a Python-based tool. The models encompass renewable energy sources such as PV Solar and Wind Turbines, electrolyser technologies including proton-exchange membrane and solid oxide, a high-pressure storage system comprising volumetric compressors and high-pressure vessels, and the power block featuring a micro gas turbine. After completing the design modelling, a thorough examination of the economic aspects of each system is conducted. This involves conducting an extensive literature review and extracting relevant information regarding the capital and operational expenditures associated with renewable energy sources, electrolysers, compression systems, storage media, and micro-gas turbines. Additionally, various metrics are reported to assess the economic impact, including the levelised cost of hydrogen and energy, as well as the payback period and internal rate of return.

The techno-economic assessment tool is put into practice for analysing an off-grid application with a continuous demand of 30 kWe for three European cities: Palermo, Frankfurt, and Newcastle. In the first part of the analysis, the results show that the latitude of the location is a very strong driver in determining the size of the system (footprint) and the amount of seasonal

storage. The rated capacity of the PV plant and electrolyser is 37%/41% and 58%/64% higher in Frankfurt and Newcastle, respectively, as compared to the original design for Palermo. And not only this, but seasonal storage also increases largely from 3125 kg H_2 to 5023 and 5920 kg H_2. As a consequence of this, LCOE takes values of 0.86 €/kWh, 1.26 €/kWh, and 1.5 €/kWh for the three cities, respectively, whilst round-trip efficiency is approximately 15.7% for the three designs at the said cities.

With the aim to reduce the footprint and rating of the different systems, two strategies are followed: hybridisation with other storage technologies and improvement of the electric efficiency of the power conversion unit. For the former, the system is hybridised with a battery energy storage system, leading to 20% LCOE reduction and 10% higher round-trip efficiency. For the latter, the incorporation of an ORC system as a waste-heat recovery system using the exhaust gases of the micro gas turbine is investigated. It is shown that a 30 kWe micro gas turbine can see efficiency rising from 27% to 42%. Analysing again the system with the incorporation of the battery storage system and the upgraded micro gas turbine yields 50% reduction of the PV solar system footprint, 60% reduction in the rated capacity of the electrolyser, and 40% reduction in the levelised cost of electricity.

The present thesis effectively makes strides towards implementing power-to-power energy storage systems utilising micro gas turbines for off-grid applications. Moreover, by developing design models for each system component and integrating them with an economic assessment, the thesis successfully identifies crucial parameters to be considered during the design process. Importantly, it highlights weak areas that require further research and development to facilitate the successful deployment of the technology. This progress aims to achieve a minimal footprint and low LCOE while contributing to the wider adoption of renewable energy sources and the global fight against climate change.

Keywords: *Power-to-Power, Micro-gas turbines, Renewable hydrogen, Energy storage systems*

Breve Resumen

Power-to-Power es la denominación habitual para sistemas en los que el excedente de energía renovable se almacena como energía química en forma de hidrógeno. El hidrógeno se puede utilizar in situ o transportarse al punto de consumo. Cuando se necesita energía nuevamente, se puede consumir hidrógeno para generar energía eléctrica y térmica. Cada uno de estos procesos incurre en pérdidas de energía, lo que lleva a una cierta eficiencia de almacenamiento (Energía Eléctrica Salida / Energía Eléctrica Entrada). La eficiencia de almacenamiento se calcula teniendo en cuenta los siguientes procesos: electrólisis del agua para la producción de hidrógeno, almacenamiento de hidrógeno comprimido, licuado o en forma de hidruros metálicos, distribución de hidrógeno mediante camiones eléctricos con pila de combustible y generación de energía mediante microturbina de gas operando con hidrógeno.

En un primer análisis de las tecnologías comerciales disponibles en el mercado, la eficiencia de almacenamiento alcanzable es del 29%, al considerar la electrólisis de óxido sólido y el almacenamiento en hidruros metálicos. Este número disminuye drásticamente al utilizar electrolizadores alcalinos o de membrana de intercambio de protones, 22.2% y 21.8% respectivamente. La eficiencia de almacenamiento se reduce aún más si se consideran otros medios de almacenamiento, como H_2 comprimido o licuado. Sin embargo, el objetivo de la tesis es resaltar que todavía hay un margen amplio para aumentar la eficiencia de almacenamiento del sistema *power-to-power*, principalmente en los bloques de producción de hidrógeno y generación de energía, lo que podría llevar a eficiencias de almacenamiento de alrededor del 40% -42% en la próxima década, para sistemas de almacenamiento de energía *power-to-power* basados en microturbinas de gas.

Al priorizar el desarrollo de una herramienta de evaluación tecnoeconómica rápida, se han creado con éxito modelos robustos para los diversos componentes del sistema y se han incorporado en una herramienta basada en Python. Los modelos abarcan fuentes de energía renovable como paneles solares fotovoltaicos y turbinas eólicas, tecnologías de electrolizadores que incluyen membrana de intercambio de protones y óxido sólido, un sistema de almacenamiento a alta presión que comprende compresores volumétricos y depósitos de alta presión, y el bloque de potencia basado en microturbina de gas. Después de completar el modelado del diseño, se realiza un examen exhaustivo de los aspectos económicos de cada sistema. Esto implica llevar a cabo una extensa revisión bibliográfica y extraer información relevante sobre los costes de capital y operativos asociados con fuentes de energía renovable, electrolizadores, sistemas de compresión, medios de almacenamiento y microturbina de gas. Además, se proporcionan diversos indicadores para evaluar el impacto económico, incluido el coste nivelado del hidrógeno y la energía, así como el período de retorno de la inversión y la tasa interna de retorno.

La herramienta de evaluación tecnoeconómica se pone en práctica para analizar una aplicación autónoma para un usuario con una demanda continua de 30 kWe, considerando tres localizaciones en Europa: Palermo, Frankfurt y Newcastle. En la primera parte del análisis, los resultados muestran que la latitud de la localización es un factor determinante en el tamaño del sistema y en la capacidad de almacenamiento estacional. La capacidad nominal de la planta fotovoltaica y el electrolizador es un 37%/41% y un 58%/64% más alta en Frankfurt y Newcastle, respectivamente, en comparación con el diseño original para Palermo. Y no solo eso, sino que el almacenamiento estacional también aumenta considerablemente, de 3125 kg de H_2 a 5023 kg y 5920 kg de H_2 respectivamente. Como consecuencia de esto, el coste nivelado de electricidad toma valores de 0.86 €/kWh, 1.26 €/kWh y 1.5 €/kWh para las tres ciudades, respectivamente, mientras que la eficiencia de almacenamiento es aproximadamente del 15.7% para los tres diseños, independientemente de la ciudad.

Con el objetivo de reducir el tamaño y la potencia de los diferentes sistemas, se siguen dos estrategias: la hibridación con otras tecnologías de almacenamiento y la mejora de la eficiencia eléctrica del bloque de potencia. Para lo primero, el sistema se hibrida con un sistema de baterías eléctricas, lo que conduce a una reducción del 20% en el coste nivelado de la electricidad y una eficiencia de almancemiento un 10% más alta. Para lo segundo, se investiga la incorporación de un sistema ORC como un sistema de recuperación del calor residual en los gases de escape de la microturbina de gas. Se muestra que es factible aumentar el rendimiento eléctrico de una microturbina de gas de 30 kWe del 26.9% al 42.1%. Al analizar nuevamente el sistema con la incorporación de las baterías y la microturbina de gas de alto rendimiento, se logra una reducción del 50% en el tamaño del sistema solar fotovoltaico, una reducción del 60% en la potencia nominal del electrolizador y una reducción del 40% en el coste nivelado de la electricidad.

La tesis presenta avances en la implementación de sistemas de almacenamiento de energía *power-to-power* utilizando microturbina de gas para aplicaciones autónomas. Además, al desarrollar modelos de diseño para cada componente del sistema e integrarlos con una evaluación económica, la tesis identifica con éxito parámetros críticos que deben tenerse en cuenta durante el proceso de diseño. Es importante destacar que se señalan áreas de debilidad que requieren más investigación y desarrollo para facilitar la implementación exitosa de la tecnología. Este progreso tiene como objetivo lograr minimizar el tamaño y coste de estos sistemas, al tiempo que contribuir a la mayor presencia de fuentes de energía renovable y, de manera general, a la lucha global contra el cambio climático.

Palabras Claves: *Power-to-Power, microturbina de gas, hidrógeno renovable, almacenamiento de energía*

Contents

Acknowledgements i

Summary iii

Resumen vii

Abstract xi

Breve Resumen xiii

List of figures xix

List of tables xxiii

1 Introduction 1
- 1.1 Next Generation of Micro Gas Turbines for High Efficiency, Low Emissions and Fuel Flexibility . . . 1
- 1.2 Background . . . 3
- 1.3 Motivation for this research . . . 10
- 1.4 Original contribution to knowledge . . . 12
- 1.5 Organisation of the report . . . 13
- 1.6 List of publications and activities . . . 14

2 Water Electrolysis - A review 19
- 2.1 History of hydrogen and its properties . . . 19
- 2.2 Overview of hydrogen production processes . . . 21
  - 2.2.1 Hydrocarbon reforming . . . 21
  - 2.2.2 Hydrogen pyrolysis . . . 22
  - 2.2.3 Biomass processing . . . 22
  - 2.2.4 Water splitting . . . 23
  - 2.2.5 Comparison of hydrogen production processes . . . 24
- 2.3 Water Electrolysis . . . 28
  - 2.3.1 Water Electrolysis fundamentals . . . 28
  - 2.3.2 Electrolyser technologies – AE, PEM & SOEC . . . 35
  - 2.3.3 Performance comparison . . . 37
  - 2.3.4 Outlook of water electrolysis . . . 40
- 2.4 Hydrogen roadmap. Main projects . . . 43
- 2.5 Barriers for scaling-up hydrogen production . . . 45

2.6 Conclusions . . . 45

3 Power-to-Power **47**
3.1 Introduction . . . 47
3.2 Review of Power-to-Hydrogen-to-Power systems . . . 50
3.2.1 Hydrogen production . . . 50
3.2.2 Hydrogen storage . . . 52
3.2.3 Hydrogen transportation . . . 60
3.2.4 Hydrogen consumption . . . 63
3.3 Round-trip efficiency (RTE) analysis . . . 68
3.3.1 Potential to increase round-trip efficiency . . . 73
3.4 Conclusions . . . 73

4 Power-to-Power System Modelling **77**
4.1 Introduction . . . 77
4.2 Renewable Energy Sources Modelling . . . 79
4.3 Water Electrolysis Modelling . . . 80
4.3.1 Modelling overpotentials in Proton-Exchange Membrane electrolysers . 81
4.3.2 Modelling overpotentials in Solid-Oxide electrolysers . . . 84
4.3.3 Estimating the properties of the electrolyser . . . 89
4.4 High-Pressure Hydrogen Storage . . . 90
4.4.1 Tank refilling . . . 90
4.4.2 Tank geometry . . . 91
4.5 Compression system . . . 93
4.5.1 Thermodynamic analysis of reciprocating compressors: Theoretical Compression Cycle . . . 95
4.5.2 Thermodynamic analysis of reciprocating compressors: real compression cycle . . . 99
4.5.3 Multistage reciprocating compressor . . . 102
4.6 Micro Gas Turbine . . . 104
4.6.1 Air filtration . . . 104
4.6.2 Combustor . . . 105
4.6.3 Compressor and turbine . . . 107
4.6.4 Recuperator . . . 108
4.6.5 Off-design operation of the micro gas turbine . . . 111
4.7 Conclusions . . . 114

5 Power-to-Power Economics **119**
5.1 Capital and Operating Expenditures for each subsystem . . . 119
5.1.1 Renewable energy: solar PV and wind turbine . . . 119
5.1.2 Electrolyser . . . 121
5.1.3 Reciprocating compressor . . . 125
5.1.4 High-Pressure storage vessels . . . 127
5.1.5 Micro gas turbine . . . 128
5.2 Future cost projection . . . 129
5.3 Economic Indexes . . . 130
5.3.1 calculation of LCOE and LCOH . . . 130

5.3.2 Payback Period . . . 131
5.3.3 Internal Rate of Return . . . 132
5.4 Conclusions . . . 133

6 Power-to-Power Practical Case **135**
6.1 Introduction to the problem . . . 136
6.2 System description and design parameters . . . 138
6.2.1 Solar photovoltaic plant . . . 139
6.2.2 Battery energy storage system . . . 139
6.2.3 Proton-exchange membrane electrolyser . . . 140
6.2.4 High-pressure hydrogen storage . . . 141
6.2.5 Micro gas turbine . . . 142
6.3 Economic analysis of the storage systems . . . 143
6.4 Base-case scenario: power-to-power P2P with mGT . . . 143
6.4.1 Performance enhancement gained from tailored P2P-ESS designs . . . 149
6.5 Performance enhancement through hybridisation with battery storage . . . 152
6.6 Conclusions . . . 156

7 High-efficiency micro gas turbines **157**
7.1 Introduction to the problem . . . 157
7.2 Introduction to the integration of the Brayton cycle with a bottoming organic Rankine cycle . . . 159
7.3 Simulation of base case scenario . . . 161
7.3.1 Selection of thermodynamic cycle parameters and simulation . . . 161
7.3.2 Selection of organic working fluid and parameters of the ORC system . . . 163
7.4 Integration of mGT and ORC systems . . . 165
7.5 Turbomachinery efficiency using specific speed *vs.* specific diameter diagrams 167
7.5.1 Applying intercooling and internal heat recovery in a 30 kWe mGT . . . 171
7.6 Incorporation of the upgraded combined mGT-ORC system into the power-to-power energy storage system . . . 174
7.7 Conclusions . . . 177

8 Conclusions **179**

Annexes **183**
Annexe I: Tank Refilling . . . 183

List of Figures

1.1 NextMGT work-package structure and individual topics of each of ESR 2
1.2 Energy-related CO_2 emissions, expressed as gigaton CO_2 per annum [6]. The chart excludes emissions from cement, flaring, or other emissions beyond oil-, coal-, and gas-related combustion emissions. 5
1.3 Net-zero commitments by region, as of July 2022 (does not reflect commitments made during COP27) [5]. [2] Net-zero target either achieved or enforced in law. . 6
1.4 Final energy consumption by fuel, million terajoule. [5]. [1] Includes heat and synthetic fuels. 7
1.5 Global net-energy related CO_2 emissions, CO_2 per annum [6, 5]. Process emissions from cement production, chemical production and refining, and negative emissions from applying CCUS are included. 8
1.6 Share of global population with access to electricity in 2021 [8] 10

2.1 General pathways for the production of hydrogen [11]. 22
2.2 Hydrogen production processes from biomass [14] 23
2.3 Global Warming Potential (GWP) and Acidification Potential (AP) for hydrogen production processes [21]. 26
2.4 Eco-Indicator 95 for hydrogen production processes [21]. 26
2.5 $\Delta G(T)$, $\Delta H(T)$ and $T{\cdot}\Delta S(T)$ of the water splitting reaction at P = 1 bar. (-) data for pressurised liquid water up to 250°C. [12] 29
2.6 Effect of operating temperature of free energy electrolysis voltage $E(T)$ and enthalpy electrolysis voltage $V(T)$ of water (P=1 bar). [12] 33
2.7 Plots of free energy voltage $E(P)$ (left) and enthalpy voltage $V(P)$ (right) of water electrolysis as a function of pressure for three different operating temperatures. [12] 33
2.8 Two-dimensional schematic diagrams of (a) gap cell, (b) zero-gap, and (c) an SPE (solid polymer electrolyte) cell. [12] 34
2.9 Schematic diagram of an Alkaline Electrolysis Cell (AEC). [30] 36
2.10 Schematic diagram of a Proton Exchange Membrane Electrolyser (PEMEC). [30] 36
2.11 Schematic representation of a single repeat unit (SRU) including the three-layer cell (cathode/electrolyte/anode) and the two half-interconnects; a highlight of the anodic and cathodic half-reactions occurring in the cell [12]. 38
2.12 Comparison of representative experimental $V-i$ curves of AEC, PEM and SOEC water electrolysis cells. [36]. 40

3.1 Competitiveness of hydrogen applications versus low-carbon and conventional alternatives. *Courtesy of the Hydrogen Council [57].* 49

3.2 Power-to-X solutions [64]. 50
3.3 Technology readiness level of technologies along the hydrogen value chain [65]. 51
3.4 Volume energy density of different fuels [50]. 54
3.5 Hydrogen compression work for several compression layouts and initial pressures. 55
3.6 Assumptions to calculate the flow rate of cooling water in a H_2/H_2O intercooler 56
3.7 Generic process flow diagram of hydrogen liquefaction [77]. (*Copyright © IIF/IIR. Published with the authorization of the International Institute of Refrigeration (IIR): www.iifiir.org*) 58
3.8 PCT Curve for a metal hydride storage. *Courtesy of h2planet [91]* 59
3.9 Operating principle of (a) ion-conducting and (b) proton-conducting electrolytes. 64
3.10 Power-to-Power Energy Storage System options considered. 69
3.11 Energy balance for the P2P solutions considered. EC: Electrolyser, ESS: Energy Storage System. 71
3.12 Power-to-Power energy storage system based on mGT technology. Proposed layout. 72
3.13 Round-trip efficiency for the P2P solutions presented in Figure 3.11 72
3.14 Storage technologies compared for their storage capacity and discharge duration [118] 74

4.1 Contributions of each overpotential to polarization curve of the PEMECs with TT-LGDLs [131]. 85
4.2 Schematic of refilling process. 90
4.3 a) Ellipsoidal head, b) Torispherical head, c) Hemispherical head. 93
4.4 Reduced flow rate capacity of a reciprocating compressor undergoing polytropic compression and with a certain dead volume. 94
4.5 Types of compressor based on final pressure and volume flow rate [145]. 95
4.6 Layouts of reciprocating compressors, a) single acting, b) double acting. 96
4.7 Compression cycles, a) ideal, b) theoretical. 97
4.8 Compression cycles, a) ideal, b) theoretical. 100
4.9 Real compression cycle (indicative). 101
4.10 Real compression cycle: calculation of polytropic work. 101
4.11 Intercooled multistage compression. 102
4.12 *p-V* diagram of a 2-stage intercooled compression. 103
4.13 Systems comprising a mGT. 104
4.14 Corrected compressor map for a 30 kW mGT. [156] 112
4.15 Corrected turbine map for a 30 kW mGT. [156] 113
4.16 Off-design performance of an exemplary 30 kW_e mGT engine. [156] 115

5.1 Cost breakdown for a 1 MW PEM electrolyser, moving from full system, to stack, to CCM. Courtesy of IRENA [116]. 121
5.2 Alkaline Electrolyser. 122
5.3 Proton-Exchange Membrane Electrolyser. 122
5.4 Solid Oxide Electrolyser. 122
5.5 CapEx vs Index Year for different electrolyser types. In the legend, '*y*' is CapEx and '*x*' is Index Year. R^2 stands for R-squared. The dotted line corresponds to the regression function (quadratic). 122

6.1 Layout of the reference Power-to-Power energy storage system. P_{el} stands for exchange of electric power and $\dot{m}_{H_2}$ and $\dot{m}_{EG}$ stand for streams of hydrogen, and exhaust gases, respectively. 137
6.2 Layout of the upgraded Power-to-Power energy storage system incorporating electric batteries. P_{el} stands for exchange of electric power and $\dot{m}_{H_2}$, and $\dot{m}_{EG}$ stand for streams of hydrogen, and exhaust gases, respectively. 137
6.3 BESS Layout (Behind-the-meter and DC-connected). 140
6.4 PEMEC polarisation curve. Validated against experimental data in [231]. 141
6.5 Off-design curve of the 30 kW_e mGT used in this work. 143
6.6 Energy Balance of a P2P-ESS system designed and operated in Palermo over a complete year (8760 hours). Close-ups in periods of interest are shown in Figs. 6.7 and 6.8. 145
6.7 Close-up of the Power-to-H_2 energy balance for selected days in Fig. 6.6. 146
6.8 Close-up of the H_2-to-Power energy balance for selected days in Fig. 6.6. 146
6.9 Net hourly hydrogen balance of the P2P-ESS for the reference locations. Design parameters are listed in Table 6.7. 147
6.10 Breakdown of the Levelised Cost of Hydrogen LCOH of a P2P-ESS installed in Palermo, Frankfurt, and Newcastle upon Tyne. Design parameters and detailed energy balance are listed in Tables 6.7 and 6.8. 148
6.11 Breakdown of the Levelised Cost of Energy of the micro gas turbine $LCOE_{mGT}$ of a P2P-ESS installed in Palermo, Frankfurt, and Newcastle upon Tyne. Design parameters and detailed energy balance are listed in Tables 6.7 and 6.8. 149
6.12 LCOH breakdown for a P2P-ESS in Palermo, Frankfurt, and Newcastle upon Tyne. Design parameters for each location can be found in Table 6.9. 151
6.13 Pareto front of the global optimisation problem. Settings displayed on Table 6.11. 153
6.14 Input parameters for the Pareto front displayed on Fig. 6.13, and associated linear trends. 153
6.15 LCOH for the base-case (Tables 6.7 and 6.8) and the optimised scenario (Tables 6.12 and 6.13). Results correspond to the city of Palermo. 155

7.1 Combined mGT-ORC system layout and T-s diagram of the bottoming cycle. . . 160
7.2 Heat and mass balance of R-MGT-1. 161
7.3 Heat and mass balance of R-MGT-2. 161
7.4 Heat and mass balance of ICR-MGT. 162
7.5 Layout of the ORC (3-4-5-6-7-3) coupled with the exhaust gas stream of the mGT (1 – 2). 165
7.6 Total electric efficiency as a function of pressure ratio of the ORC system, for the three mGT configurations and three organic fluids considered. 167
7.7 Specific speed (n_s) vs. specific diameter (d_s) diagram for single stage turbines [246]. 168
7.8 Specific speed (n_s) vs. specific diameter (d_s) diagram for single stage compressors [246]. 169
7.9 Heat and mass balance of the upgraded 30 kWe mGT incorporating intercooling and internal heat recovery. 172
7.10 Heat and mass balance of an ORC system running on R1234ze. Exhaust gas corresponds to mGT exhaust. 173

7.11 Scaling of the off-design performance curve of the upgraded 30 kWe mGT used in Chapter 6 to a rated efficiency of 42.1%. 175

List of Tables

2.1 Chemical properties of hydrogen 20
2.2 Overview of major hydrogen production processes [11, 19] 25
2.3 Summary of hydrogen production processes [11, 27] 28
2.4 Water electrolysis reactions. 30
2.5 Relationships among the free energy electrolysis voltage (E), enthalpy voltage (V), and fuel cell voltage (U). 31
2.6 Characteristics of different electrolyser technologies. 39
2.7 Outlook of alkaline electrolysis cells. Updated from [12, 39, 40, 41]. 41
2.8 Outlook of PEM electrolysis cells. Updated from [12, 39, 40, 41]. 42
2.9 Outlook of solid oxide electrolysis cells. Updated from [12, 50]. 43

3.1 Commercial availability of electrolysers. 53
3.2 Compressed-H_2 scenarios. 56
3.3 Types of high-pressure vessels [50, 75]. 57
3.4 Liquefied H_2 scenarios. 59
3.5 Market availability of storage systems based on metal hydrides 60
3.6 Transportation capacity of a truck for hydrogen in different states. 61
3.7 Admissible hydrogen content H_2 %vol in different systems. 63
3.8 Comparison of fuel cell technologies [100] 65
3.9 Areas of research for the different micro-gas turbine systems. 69
3.10 Maximum H_2 %vol admitted in different systems. 70
3.11 Round-trip efficiency of various energy storage systems [41, 115]. 70
3.12 Assessment of the potential to decrease/increase energy consumption/production of the different systems involved in a P2P-ESS. 74

4.1 SAM photovoltaic solar sections and parameters 80
4.2 SAM wind turbine sections and parameters 81
4.3 Exchange current density for several different PEM electrolyser cell models. . . 83
4.4 Models used to estimate the proton conductivity of the membrane Springer's equation is experimentally obtained from a Nafion®117 membrane, and its range of validity is 30-80°C). 84
4.5 Resistivity of anode (ρ), cathode and electrolyte. T in K 86
4.6 Characteristic lengths. 88
4.7 Collision integral constants. 88
4.8 Service pressure and volume flow rate limits for some non-lubricated compressors. [72] 94
4.9 Characteristics of non-lubricated compressors. [72] 95

4.10 Summary of equations for the semi-empirical modeling of electrolysers 116
4.11 Summary of equations for the storage system modeling 117

5.1 Reference CapEx and OpEx of selected renewable energy technologies. 120
5.2 Reference electrolyser CapEx from Glenk *et al.*. [159]. 123
5.3 Cost correlations for hydrogen compression systems, as reported in reference [203]. 2019 US$. kW represents compressor power 126
5.4 Coefficients to be used in Eq. 5.4 126
5.5 Large bundle and tube-trailer storage cost projection [198]. Values reported as in the source. 127
5.6 CapEx and OpEx of micro gas turbines [211] 128
5.7 mGT CapEx and OpEx for different case scenarios [213] 129
5.8 Summary of equations for the LCOH 132

6.1 Comparison between the features considered in this work (PhD) and other works available in the literature. "X" indicates that a reference incorporates/covers the feature in the corresponding row of the first column. 138
6.2 Specifications of the solar PV module. 139
6.3 BESS design specifications. 140
6.4 PEMEC design specifications. 141
6.5 Design specifications of the hydrogen storage system. 142
6.6 Input economic data of the components of the plant. These data are used to calculate the LCOH and LCOE of the P2P-ESS. €refers to 2021. 144
6.7 Design specifications for Palermo. 145
6.8 Energy balance at different locations when using the system sized for Palermo. 148
6.9 Tailored design parameters for the locations considered 150
6.10 Techno-economic data for the cities of Palermo, Frankfurt, and Newcastle upon Tyne, when tailored designs are considered. 151
6.11 Settings of the optimisation problem. P2P-ESS with BESS in Palermo. 152
6.12 Design parameters of the optimised design in the city of Palermo 154
6.13 Techno-economic figures of merit for the optimised design in the city of Palermo.154

7.1 Input data for the simulation of the Brayton cycle for different layouts. 162
7.2 Main output parameters of the simulated micro gas turbines. Input data are displayed in Table 7.1. 163
7.3 Thermodynamic properties of fluids (Coolprop [76]). 164
7.4 Input parameters for the ORC layouts considered. 164
7.5 Results of the combined (Brayton + ORC) system considering a maximum pressure of 20 bar. Input parameters are found in Table 7.4. 166
7.6 Inlet and outlet conditions of turbomachines in the ICR-MGT + ORC system using R1234ze, as reported in Table 7.5. 169
7.7 Rotational speed for the low and high-pressure compressors and turbines of the ICR-MGT layout and turbine of the ORC system. Obtained from the specific speed and diameter diagrams. 170
7.8 Rotational speed for the low and high-pressure compressors and turbines of the ICR-MGT layout and for the turbine of the ORC system, as obtained from the n_s *vs.* d_s charts. 170

7.9 Diameter for the low and high-pressure compressors and turbines of the ICR-MGT layout and for the turbine of the ORC system, as obtained from the n_s *vs.* d_s charts. 170
7.10 Input data for the simulation of the upgraded 30 kWe micro gas turbine. 171
7.11 Main performance parameters of the upgraded micro gas turbine. Input data are displayed on Table 7.10 172
7.12 Results of the combined Brayton + ORC system. The ORC system has a peak pressure of 20 bar and runs on R1234ze. Input data shown in Table 7.4. 173
7.13 Shaft speed of the low and high-pressure compressors and turbines of the intercooled, recuperated 30 kWe engine and of the turbine in the bottoming ORC system, as obtained from the n_s *vs.* d_s charts. 173
7.14 Diameter of the low and high-pressure compressors and turbines of the intercooled, recuperated 30 kWe engine and of the turbine in the bottoming ORC system, as obtained from the n_s *vs.* d_s charts. 174
7.15 Comparison of the rated specifications of the P2P-ESS designed for the city of Palermo, based on an upgraded intercooled, recuperated mGT (rated efficiency of 42.1%). 176
7.16 Techno-economic performance of a P2P-ESS designed for the city of Palermo, based on an upgraded intercooled, recuperated mGT (rated efficiency of 42.1%). 176

Nomenclature

Introduction - symbols

AEC Alkaline electrolyser

AP Acidification Potential

$ASME$ The American Society of Mechanical Engineers

ATR Auto-thermal Reaction

BDC Bottom Dead Center

$BESS$ Battery Energy Storage System

$CAES$ Compressed Air Energy Storage

$CapEx$ Capital Expenditure

CCS Carbon Capture and Storage

$CCUS$ Carbon Capture Utilisation and Sequestration

CHP Combined Heat & Power

CRF Capital Recovery Factor

DES Decentralised Energy System

EPA Efficiency Particulate Air Filter

ESS Energy Storage System

FAR Fuel-Air Ratio

FC Fuel Cell

$FCET$ Fuel Cell Electric Truck

FCR Fixed Charge Rate

FOC Fixed annual Operating Cost

GHG Green Gas House

GHI Global Horizontal Irradiance

GWP Global Warming Potential

$HEPA$ High-Efficiency Particulate Air Filter

HHV High Heating Value

$HICP$ Harmonised Index of Consumer Prices

HRR Heat Release Rate

ICE Internal Combustion Engine

IRR Internal Rate of Return

$LCOE$ Levelised Cost of Energy

$LCOH$ Levelised Cost of Hydrogen

LHV Low Heating Value

LNG Liquefied Natural Gas

mGT micro Gas Turbine

$NextMGT$ Next Generation of Micro Gas Turbines for High Efficiency, Low Emissions and Fuel Flexibility

NPV Net Present Value

$NREL$ National Renewable Energy Laboratory

NTP Normal Temperature and Pressure

$O\&M$ Operation and Maintenance

$OECD$ The Organization for Economic Cooperation and Development

OEM Original Equipment Manufacturer

$OpEx$ Operational Expenditure

ORC Organic Rankine Cycle

$P2P$ Power-to-Power

$P2X$ Power-to-X

PEM Proton Exchange Membrane

$PEMEC$ Proton Exchange Membrane electrolyser

PHS Pumped Hydroelectric Storage

POX Partial Oxidation

PPA Power Purchase Agreement

PtG	Power-to-Gas
PV	Photovoltaic
$R\&D$	Research & Development
RES	Renewable Energy Systems
RFQ	Request for Quotation
RTE	Round-Trip Efficiency
SAM	System Advisory Model
SMR	Steam Methane Reforming
SO	Solid Oxide
SoC	State-of-Charge
$SOEC$	Solid Oxide Electrolyser
SRC	Steam Rankine Cycle
TCC	Capital Cost
TDC	Top Dead Center
TIT	Turbine Inlet Temperature
TMY	Typical Meteorological Year
TRL	Technology Readiness Level
UHC	Unburned Hydrocarbons
$ULPA$	Ultra Low Particulate Air Filter
VOC	Variable Operating Cost
VRE	Variable Renewable Energy
WHP	Waste Heat to Power

1 Introduction

In the initial chapter, the overall framework of the thesis within the NextMGT project is presented, which serves as the foundation for the research conducted in this work. This is followed by a ***general background*** *of the thesis -in terms of sustainable development and energy utilisation- and a justification of its research topic, along with a discussion of the specific objectives and associated general methodology. Also in this chapter, a brief description of the structure of the document and of the original contributions to knowledge provided by the thesis are presented.*

1.1 Next Generation of Micro Gas Turbines for High Efficiency, Low Emissions and Fuel Flexibility

Next Generation of Micro Gas Turbines for High Efficiency, Low Emissions and Fuel Flexibility (NextMGT) has received funding from the European Union's Horizon 2020 research and innovation programme under Marie Sklodowska-Curie grant agreement No 861079. It aims to enhance technical expertise and scientific knowledge to gain deeper understanding of the essential design and operational aspects of micro gas turbine technology. The aim is to facilitate the successful commercialisation of mGT technology by developing and validating analytical and numerical models that encompass the various physical aspects of these machines. The program is also focused on addressing component-level technology and optimising its integration. Additionally, it provides valuable insights into the emerging mGT community, collaborative research structures between academia and industry, and pertinent energy policies and regulatory frameworks. The ultimate objective is to establish a thriving European industry that leads in distributed power generation and renewable energy utilisation. This program's scientific outcomes will significantly contribute to the economy and help reduce emissions during the transition period, ultimately leading to the long-term goal of zero-emission power generation.

More specifically, the topics to be addressed in the corresponding work packages are:

- To examine cycle innovations required to achieve high overall mGT efficiency to match other prime movers of similar power range and to develop advanced methods to optimise micro gas turbine systems for several applications based on a standard core technology as well as smart integration with energy systems (WP1).
- To investigate advanced combustion technologies for achieving low emissions and fuel flexibility including biofuels in solid, liquid and gaseous forms and combustible industrial waste (WP2).

- To develop innovative methods to enhance aerodynamic, mechanical and electrical aspects of mGTs and utilisation of new materials and to develop suitable storage systems to enable effective operation (WP3).
- To investigate the measures enabling commercialisation of the technology, focusing on dependence of innovation and industry growth on intellectual/industrial property management, energy policy and regulatory framework and standardisation requirements (WP4).
- To train ESRs using a structured programme which covers: individual personalised research projects that lead to their PhDs; specialised training courses offered by the participating institutions; network-wide training activities in the format of seminars, workshops, conferences and summer schools, and knowledge exchange with the members of the network through activities such as secondments and events (WP5).
- To create a wider impact in the relevant scientific arena and applications fields that come together in energy systems through wide communications dissemination of results including the general public (WP6).
- To manage the proposed programme according to the guidelines of the Marie-Skłodowska Curie Action and to disseminate the knowledge acquired through international publications (WP7).

The programme integrates 14 Early Stage Researchers that are investigating the topics presented in Figure 1.1, organised in four work packages. The research presented in this PhD thesis is developed within Work Package 1, which is focused on Cycle Innovations and Optimisation. In particular, as described before, this thesis is ESR2, investigating Power-to-gas-to-Power systems.

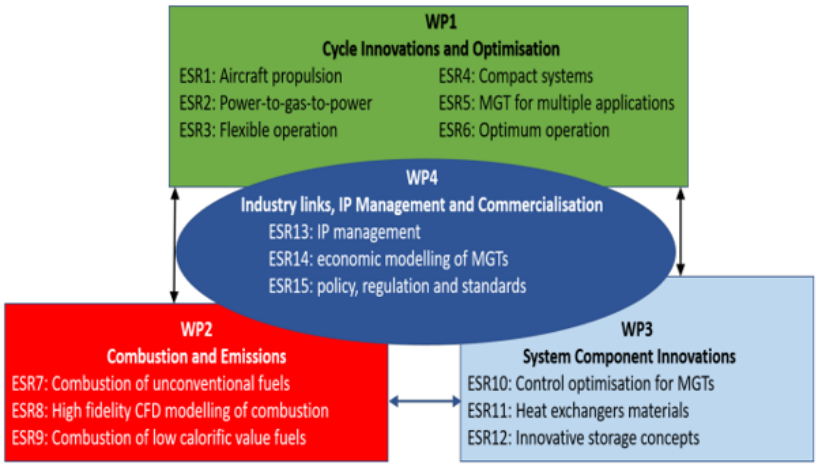

Figure 1.1: NextMGT work-package structure and individual topics of each of ESR

.

Speaking about the author of this thesis, in particular, the programme also allowed the researcher to spend nine months seconded tp external organisations that have allowed the author to increase the quality of the work while working closely with experts related to the subject under investigation. This information is treated in more detail in Section 1.6.

1.2 Background

Energy is the lifeblood of modern society, powering our homes, businesses, and industries. It is the driving force behind technological advancements and economic growth. However, as global energy demand continues to rise and concerns about climate change intensify, the need for sustainable and efficient energy sources becomes increasingly urgent. In this introduction, a comprehensive overview of the general background in energy and energy storage worldwide is provided, while also exploring the geopolitical tensions that arise from energy dependence and competition.

Fight against climate change

The current international debate on global warming has been a culmination of efforts spanning two generations by the United Nations and the international community. Initially, environmental issues, including climate change, were not major concerns for the UN. The first notable UN engagement with environmental matters occurred in 1949, with the UN *Scientific Conference on resource conservation and Utilisation*. However, the focus at that time was on managing resources for economic and social development, rather than on conservation.

It was not until 1968 that environmental issues gained serious attention within major UN organs. The first United Nations *Conference on the Human Environment*, held in Stockholm in 1972, marked a significant milestone. This conference, also known as the *First Earth Summit*, addressed the preservation and enhancement of the human environment. It was during this summit that climate change was acknowledged for the first time, cautioning governments to evaluate activities that could lead to climate change.

Over the next two decades, efforts to implement the 1972 decisions led to an increasing concern for the atmosphere and global climate. The United Nations Environment Programme (UNEP) and the World Meteorological Organisation (WMO) played important roles in monitoring air pollution and addressing climate change-related issues. The depletion of the ozone layer and the emergence of acid rain further highlighted the need for global action.

In 1988, global warming and the ozone layer depletion gained prominent attention, leading to the establishment of the Intergovernmental Panel on Climate Change (IPCC). The UN General Assembly identified climate change as a specific and urgent issue and initiated comprehensive reviews and recommendations through the WMO and UNEP. The year 1989 marked significant global efforts, including preparations for negotiations on a framework convention on climate change.

In 1992, the United Nations *Conference on Environment and Development*, known as the *Earth Summit*, took place in Rio de Janeiro. The conference resulted in the signing of the United Nations Framework Convention on Climate Change (UNFCCC), aimed at stabilising greenhouse gas concentrations. The UNFCCC provides a framework for international cooperation and sets the stage for subsequent agreements and protocols.

The Kyoto Protocol [1], adopted in 1997, is an important addition to the UNFCCC. It established binding emission reduction targets for industrialised countries for the period 2008-2012.

The Protocol introduced mechanisms such as emissions trading and the Clean Development Mechanism (CDM) to help countries achieve their targets. While the Kyoto Protocol had limitations, it played a crucial role in initiating international action on climate change.

The Paris Agreement [2], adopted in 2015 and ratified by nearly all countries, is a landmark international accord to combat climate change. It builds upon the UNFCCC and aims to limit global warming to well below 2 degrees Celsius above pre-industrial levels, while pursuing efforts to limit the temperature increase to 1.5 degrees Celsius. The agreement emphasises nationally determined contributions (NDCs), requiring countries to regularly submit their emission reduction targets and take actions to achieve them. It also promotes climate finance, technology transfer, and capacity-building support for developing nations.

The Katowice Rulebook [3] agreed upon during the 2018 United Nations Climate Change Conference (COP24) in Katowice, Poland, provides detailed guidelines for implementing the Paris Agreement. It outlines common reporting standards, transparency mechanisms, and the global stocktake process to assess collective progress in achieving the agreement's goals. The Rulebook enhances the transparency and accountability of countries' climate actions, ensuring a level playing field for all parties.

The Marrakech Partnership for Global Climate Action [4], launched during the 2016 United Nations *Climate Change Conference* (COP22) in Marrakech, is a collaborative initiative involving governments, cities, businesses, and civil society organisations. It aims to mobilise and accelerate climate action across various sectors and stakeholders, complementing the efforts of national governments. The partnership fosters cooperation, knowledge sharing, and the implementation of transformative projects to drive the transition to a low-carbon and resilient future.

In addition to global agreements, various regional and bilateral agreements have been established to address climate change. For example, the European Union has its own emission reduction targets and policies, such as the European Green Deal. The Asia-Pacific region has the Asia-Pacific Partnership on Clean Development and Climate to promote cooperation on clean technologies and sustainable development. Numerous countries have also formed bilateral agreements to collaborate on climate action, including technology transfer, capacity building, and financial support.

Global Energy Landscape

After a decline in 2020, global emissions experienced a significant recovery and are estimated to reach 2019 levels this year. The ongoing energy crisis in Europe will likely result in temporary increases in emissions, as certain applications and countries switch from gas to oil or coal. However, many countries have revised their decarbonisation plans in the last two years to include more ambitious targets for reducing emissions.

According to Mckinsey's Global Energy Perspective 2022 [5], which considers four different scenarios, global energy-related CO_2 emissions are projected to reach their peak before 2030. By 2050, it is expected that emissions will be 30 to 70% lower than the levels recorded in 2019. For instance, in the Achieved Commitments scenario, global energy-related CO_2 emissions

are predicted to reach their highest point around 2023 and then decline by 69%, reaching 11 gigaton of CO_2 (Gt CO_2) by 2050.

However, even with these projected reductions, there are uncertainties regarding the relationship between emission concentrations and the impact of global warming. The scenarios in the cited report indicate that there is a one-in-six probability that global warming could exceed 2.1°C to 2.9°C by 2100. It is important to note that the global mean surface air temperature (GSAT) is expected to increase by 1.7°C to 2.4°C by 2100 across all scenarios. Accordingly, although there has been accelerated progress in projected emission reductions compared to previous outlooks, thanks in part to more ambitious efforts and commitments from stakeholders, it is clear that the world is still far from achieving the 1.5° Pathway.

The COVID-19 pandemic led to the most significant reduction in various factors driving the growth of greenhouse gas (GHG) emissions in the past two decades. These factors include economic development, energy demand, and the resulting emissions. As economies began to recover, there was a 4% increase in CO_2 emissions in 2021, following a 5% decline in 2020, Fig. 1.2. In comparison to 2019 levels, both coal and gas emissions were higher, while oil emissions only partially recovered in 2021, primarily due to the slow revival of the aviation sector. Consequently, although many anticipated that COVID-19 would bring about lasting changes that could contribute to lower emissions levels, global CO_2 emissions have now returned to the levels observed prior to the pandemic.

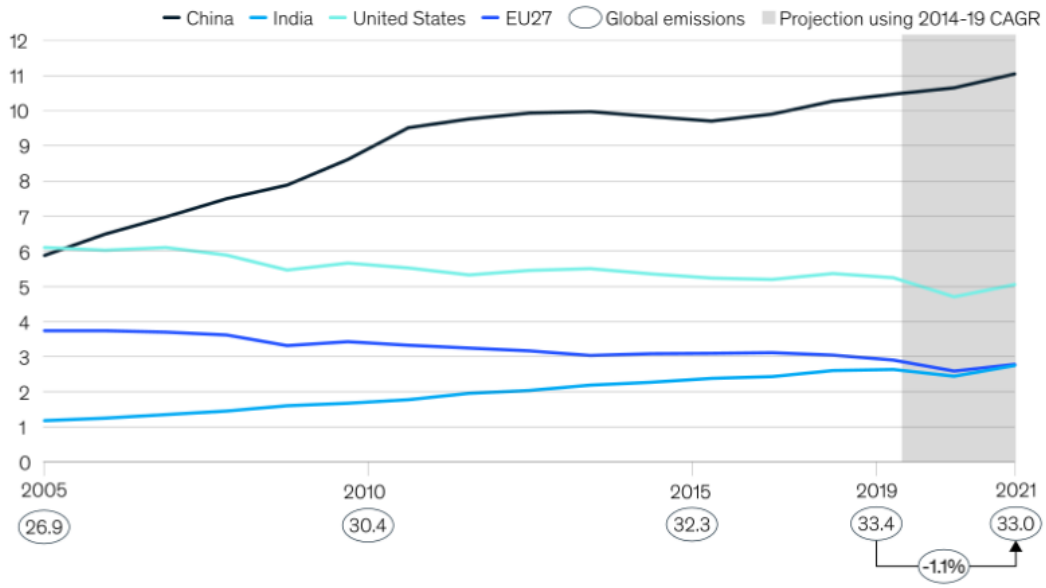

Figure 1.2: Energy-related CO_2 emissions, expressed as gigaton CO_2 per annum [6]. The chart excludes emissions from cement, flaring, or other emissions beyond oil-, coal-, and gas-related combustion emissions.

In the meantime, there is a growing emphasis on achieving net-zero objectives. Countries that have made announcements, commitments, or adopted climate plans to reduce emissions in

the coming decades represent more than 91% of global GDP and approximately 88% of global CO_2 emissions. Moreover, numerous regions and cities have embraced or pledged to pursue more ambitious targets, demonstrating a readiness to surpass national efforts, Fig. 1.3.

Corporations are aligning with or even surpassing governmental commitments by setting goals to reduce their carbon footprints. Around 2,000 multinational and national companies have established science-based targets. The drive to mitigate emissions has permeated various regions of the world and the global economy, underscoring substantial public support for addressing the challenges posed by climate change.

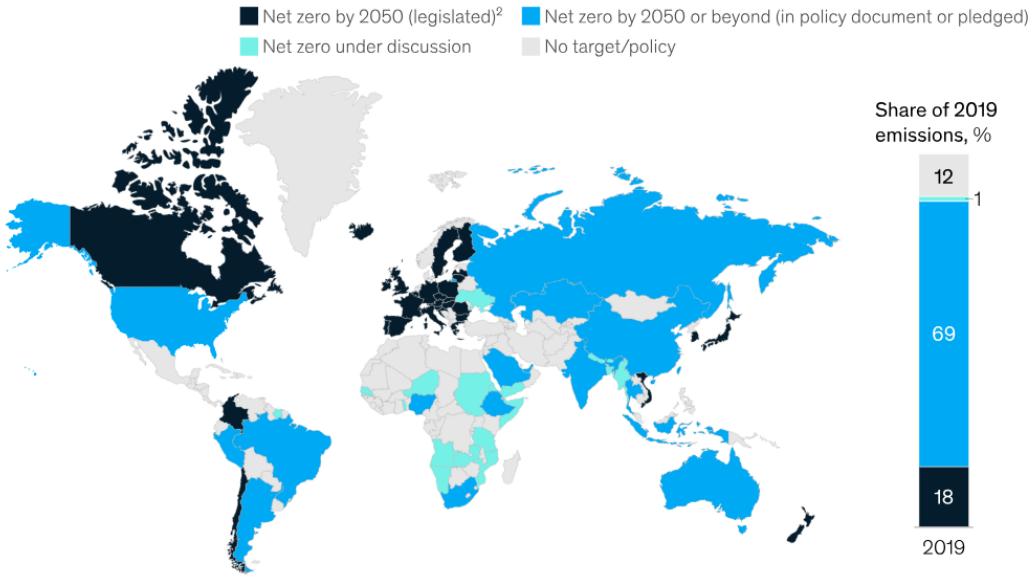

Figure 1.3: Net-zero commitments by region, as of July 2022 (does not reflect commitments made during COP27) [5]. [2] Net-zero target either achieved or enforced in law.

Fossil fuels are expected to be replaced by electricity, hydrogen, and biofuels in the future, Fig. 1.4. Projections indicate that global energy consumption will reach a plateau in the coming decades. Despite the rapid growth of the global economy and an increase of two billion people in the population, energy consumption is estimated to grow by only 14% by 2050 compared to 2019 levels.

This trend is driven by continuous improvements in the energy efficiency of GDP. Greater efficiency in end-use sectors such as buildings, transportation, and industry is contributing to the reduction of energy intensity. Electrification also plays a significant role in lowering energy intensity, as the shift to electrical solutions often brings about a significant increase in efficiency in various segments, like space heating and passenger cars. Consequently, as fossil-fuel consumption declines, energy-related CO_2 emissions are projected to decrease at similar rates. Emissions from coal and oil are expected to decline first, followed by a decline in emissions from natural gas toward 2050.

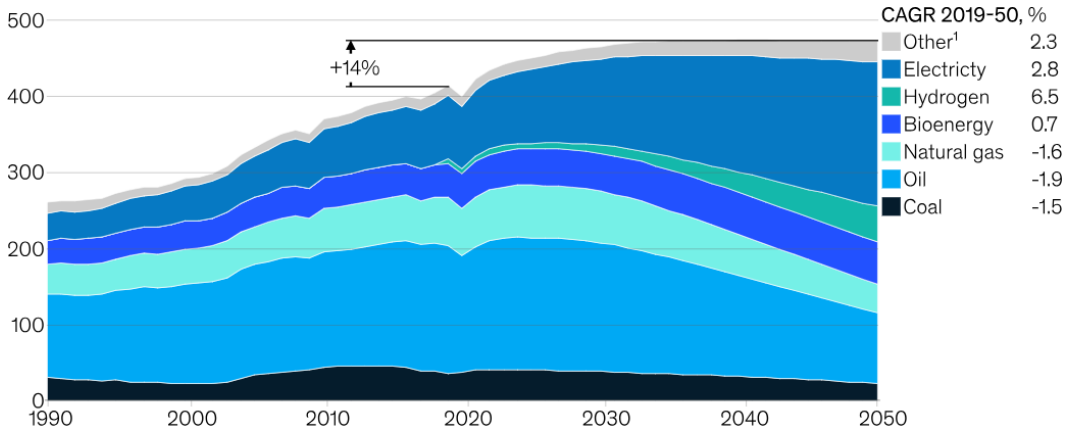

Figure 1.4: Final energy consumption by fuel, million terajoule. [5]. [1] Includes heat and synthetic fuels.

While reducing energy-related CO_2 emissions is crucial for decarbonisation, it is also necessary to address the reduction of other greenhouse gases. Methane emissions make up the largest portion of non-CO_2 emissions. During 2021, more than 100 countries with significant emission levels pledged to the Global Methane Pledge, which aims to decrease methane emissions by 30% by 2030. The successful attainment of this goal necessitates the utilisation of innovative technologies such as high-resolution satellite imagery, which can aid in identifying the most environmentally detrimental sources.

CO_2 emissions are projected to reach their highest point in the mid-2020s across various scenarios, Fig. 1.5. In the Achieved Commitments scenario, it is anticipated that emissions will decrease by approximately 69% by 2050, whereas the Further Acceleration scenario predicts a reduction of 55%, and the Current Trajectory scenario suggests a decrease of 35%. Depending on the specific scenario, there is a 50% probability that the global mean surface air temperature will rise by over 1.7°C to 2.4°C. This increase in global mean temperature implies that certain regions may experience even more substantial temperature rises. Due to significant uncertainties surrounding temperature increases, the average global increase could surpass 2.1°C to 2.9°C with a one-in-six probability. Even if countries succeed in achieving their net-zero commitments, the likelihood of exceeding 2°C of global warming is higher than rolling a six on a die. In the light of this information, to limit global warming to below 1.5°C, it is crucial for the global energy system to undergo a significant acceleration in its transformation. This entails a rapid transition away from fossil fuels toward greater efficiency, electrification, and the adoption of new fuels—faster than the pace set by the announced net-zero commitments.

To restrict global warming, a collective endeavour involving private companies, public institutions, and citizens is imperative. Given the intricacies involved, a crucial step at this point is to gain a deeper understanding of the essential prerequisites for resolving the net-zero equation. There are nine requirements that can be categorised into three groups:

- Physical building blocks: these encompass technological advancements, establishing large-scale supply chains and supporting infrastructure, and ensuring the availability of

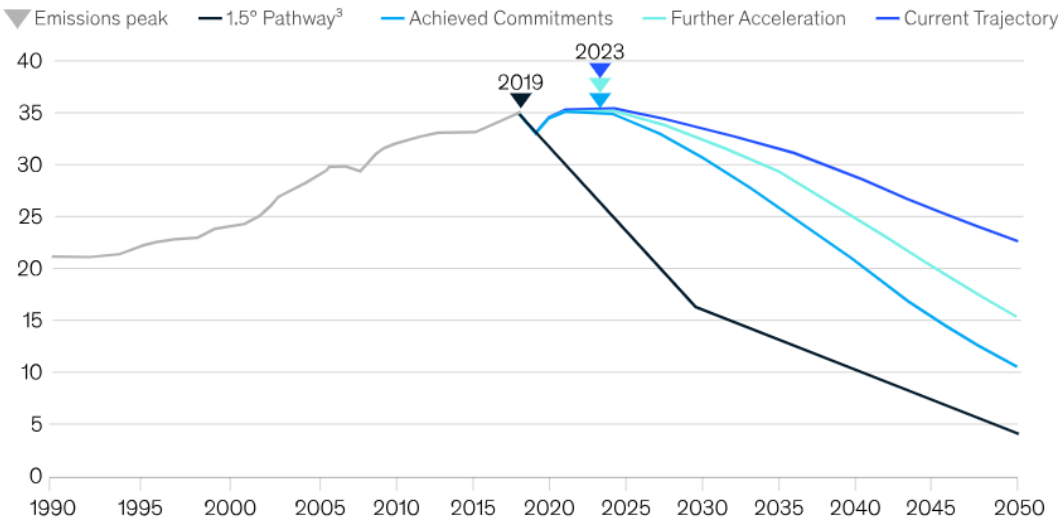

Figure 1.5: Global net-energy related CO_2 emissions, CO_2 per annum [6, 5]. Process emissions from cement production, chemical production and refining, and negative emissions from applying CCUS are included.

.

necessary natural resources.

- Commitments and enabling mechanisms: this category includes the establishment of governing standards, implementing tracking and market mechanisms, and fostering effective institutions. It also entails the commitment and collaboration of leaders from the public, private, and social sectors on a global scale, along with support from citizens and consumers.
- Economic and societal adjustments: this comprises the effective reallocation of capital and the establishment of financing structures that facilitate the transition. It also involves managing shifts in demand and addressing potential near-term increases in unit costs, as well as implementing compensatory mechanisms to mitigate socioeconomic impacts.

By addressing these requirements comprehensively, society should work towards limiting global warming and achieving the goal of net-zero emissions.

Access to electricity

The Energy Trilemma, consisting of energy security, energy sustainability, and energy affordability, is approached differently based on the energy circumstances of each region. When starting from scratch, the primary focus is on ensuring energy security as the most pertinent factor. Once energy security is adequately addressed, the attention shifts towards addressing affordability. Finally, once energy security and affordability are achieved, the focus turns to addressing energy sustainability as a pressing concern.

Developed nations, including Europe and North America, are now shifting their attention towards energy sustainability. However, it is important to acknowledge that there are millions

of individuals residing in remote areas where the main power grid does not extend, resulting in a lack of access to electricity. Additionally, numerous regions face challenges related to poor quality of energy supply, characterised by frequent and prolonged power outages until the grid is restored.

The recent advancements are not sufficient to achieve universal access by 2030. Over the period from 2010 to 2021, global access to electricity experienced an average annual growth of 0.7 percentage points, resulting in an increase from 84% to 91% of the world's population having access. The number of individuals without electricity nearly halved during this timeframe, declining from 1.1 billion in 2010 to 675 million in 2021. However, the pace of annual growth slowed down to 0.6 percentage points between 2019 and 2021.

To bridge the existing gap, particularly for those residing in impoverished and remote areas, the annual growth rate for access needs to be 1 percentage point per year starting from 2021, which is almost twice the current rate. Without implementing additional efforts and measures, approximately 660 million people, primarily concentrated in Sub-Saharan Africa, will remain without access in 2030 [7]. Policies concerning energy access should exhibit political dedication and maximise the socioeconomic benefits associated with access, with a focus on prioritising the most vulnerable populations in order to address the access disparity effectively.

From 2010 to 2021, there was a consistent decline in the global number of individuals without access to electricity. However, the progress varied across different regions, Fig. 1.6. In the developing world, 51 countries have achieved universal access, with 17 of them located in Latin America and the Caribbean. On the other hand, in 2021, 95 countries, primarily in Sub-Saharan Africa, still fell short of the target, despite some progress being made in approximately one-quarter of them. This progress included half of the 20 countries with the largest deficits in access (defined as the population lacking electricity). Interestingly, in Sub-Saharan Africa, the number of people without access remained nearly unchanged from 2010 to 2021.

The majority of the reduction in the unserved population occurred in Asia. Central and Southern Asia experienced a drastic decrease, with the number of people without access dropping from 414 million in 2010 to 24 million in 2021. This improvement was largely observed in Bangladesh, India, and other densely populated countries. In Eastern and South-eastern Asia, the number of individuals without access to electricity declined from 90 million to 35 million during the same period. In Northern Africa and Western Asia, the decrease in the unserved population was less significant, declining from 37 million in 2010 to 30 million in 2021.

In 2021, the 20 countries with the largest deficit in access accounted for 75% of the global population lacking electricity access. The countries with the highest number of people without access were Nigeria (86 million), the Democratic Republic of Congo (76 million), and Ethiopia (55 million). India and South Sudan dropped out of the top 20, while Zambia and Mali joined the list. Between 2019 and 2021, electrification efforts did not keep pace with population growth in the Democratic Republic of Congo, resulting in an increase of approximately 2 million people in the access deficit. In contrast, both Nigeria and Ethiopia saw a decrease of 2 million people each year in their unserved populations, although they still remain within the top 3 countries in terms of unserved population. During the same period, Kenya increased its

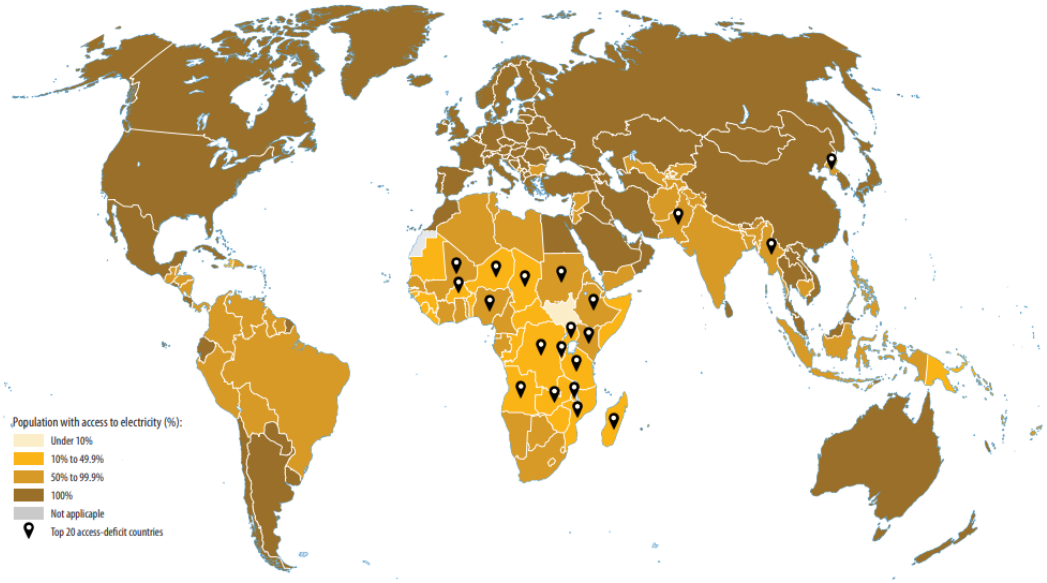

Figure 1.6: Share of global population with access to electricity in 2021 [8]

.

access rate by more than 3 percentage points, leading to a decline of approximately 2 million unserved individuals per year, similar to the progress observed in Ethiopia.

1.3 Motivation for this research

The global energy landscape is undergoing a significant transformation as the need for sustainable and resilient energy systems becomes increasingly imperative. The traditional centralised energy infrastructure, characterised by large-scale power plants and extensive transmission networks, is no longer sufficient to address the complex challenges faced by society today. In order to achieve sustainability, it is crucial to shift towards decentralised energy systems that prioritise efficiency, resource utilisation, and decarbonisation.

One of the primary motivations for transitioning towards decentralised energy systems is the urgent need to ensure environmental sustainability. The traditional energy model heavily relies on fossil fuels, which contribute to greenhouse gas emissions and exacerbate climate change. By embracing decentralised energy systems, we can significantly reduce our carbon footprint by leveraging renewable energy sources such as solar, wind, and hydropower. Decentralisation empowers communities and individuals to generate clean energy locally, minimising transmission losses and dependency on non-renewable resources. This shift is crucial in mitigating the environmental impact of energy production and consumption, and ensuring a sustainable future for generations to come.

Furthermore, increasing energy efficiency is a key driver behind the adoption of decentralised energy systems. The centralised model suffers from inherent inefficiencies, including transmission losses over long distances and limited control over energy generation and distribution. Decentralisation allows for localised energy generation, enabling communities to tailor their

energy production to their specific needs. By optimising the utilisation of energy resources at a local level, we can reduce waste, improve overall efficiency, and enhance energy security. This not only leads to cost savings but also promotes a more sustainable use of limited resources.

Additionally, decentralised energy systems play a crucial role in addressing the energy poverty prevalent in many parts of the world. Numerous regions, particularly in developing countries, still lack reliable access to electricity, hindering socio-economic development and quality of life. By implementing decentralised energy solutions, such as mini-grids and off-grid systems, these marginalised communities can gain access to clean and affordable energy. Decentralisation enables the deployment of scalable and modular energy solutions, tailored to local needs and resources. This empowerment enhances energy access, stimulates economic growth, and improves the overall well-being of individuals and communities.

In the light of these pressing challenges, this thesis aims to explore the potential of decentralised energy systems as a catalyst for sustainability, energy efficiency, and increased access to electricity. By investigating various technological, policy, and socioeconomic aspects, this research aims to shed light on the opportunities and barriers associated with the adoption and integration of decentralised energy solutions. Ultimately, the findings of this study seek to contribute to the development of effective strategies and frameworks that promote the widespread adoption of decentralised energy systems, enabling a more sustainable and inclusive energy future.

One promising solution that aligns with the objectives of decentralised energy systems is the utilisation of power-to-power energy storage systems. Power-to-power technology, often achieved through electrochemical or chemical storage, has the potential to address several key challenges associated with the integration of renewable energy sources into both centralised and decentralised energy systems.

One significant challenge of renewable energy sources, such as solar and wind power, is their intermittency. The availability of these energy sources fluctuates with weather conditions and time of day, posing a reliability challenge for any energy system. Power-to-power energy storage systems offer a viable solution by storing excess energy during periods of high generation and releasing it during periods of low generation. This mechanism not only smooths out the intermittency of renewable sources but also enables the utilisation of a higher share of renewable energy while ensuring a consistent and reliable power supply.

Moreover, power-to-power energy storage systems play a crucial role in achieving the net-zero emissions goal. By storing excess renewable energy during times of high generation, the reliance on fossil fuel-based power plants during peak demand periods can be reduced or even eliminated. This shift towards renewable energy storage not only reduces greenhouse gas emissions but also contributes to the overall decarbonisation of the energy sector, supporting global climate change mitigation efforts.

Furthermore, power-to-power energy storage systems offer a unique advantage in regions where access to power grids is limited or nonexistent. In such areas, decentralised energy systems combined with energy storage technologies can provide a reliable and accessible

power supply, promoting economic development and improving the quality of life for local communities. Additionally, the versatility of power-to-power systems allows for the integration of various energy sources, including renewable sources and locally available resources, such as biomass or waste heat. This integration enhances the accessibility of power and heat in regions that would otherwise struggle to establish a conventional power grid infrastructure.

By incorporating power-to-power energy storage systems into decentralised energy systems, multiple challenges can be addressed simultaneously. These systems not only increase the share of renewable energy and ensure energy security of supply but also facilitate the achievement of net-zero goals while enhancing accessibility to power and heat in regions lacking a power grid. Exploring the potential, limitations, and optimal integration strategies of power-to-power energy storage systems within decentralised energy systems forms an integral part of this thesis. Through in-depth analysis and evaluation, this research aims to contribute to the development of effective and sustainable energy storage solutions that support the wider adoption of decentralised energy systems, thereby accelerating the transition towards a more sustainable and inclusive energy future.

1.4 Original contribution to knowledge

The core work of the present doctoral research is almost entirely original. The author has developed a software tool from scratch to allow for fast techno-economic analyses of the technology considered in the thesis. The main contribution to the current state-of-art for power-to-power energy storage systems is, first, the development of specific models for the systems involved and, secondly, the integration of all models into a unique software tool developed from scratch, where different operation strategies have been made available to simulate a scenarios featuring requirements and boundary conditions that are representative of a large number of applications and end-user profiles.

The software tool has been widely tested against different cases and the associated results have already been disseminated, either through publication in high-quality and recognised journals or presented at high-level conferences or forums, as described at the beginning of each chapter as well as in the next section. Furthermore, the software tool has been used by the author of this thesis to predict and run a techno-economic analysis on the first green hydrogen generation plant that will be developed and constructed in the city of Seville, strategically located at the industrial port of the city. This work has been carried out while on a secondment at Alener Solar, an industrial partner of the NextMGT consortium.

The author of this thesis has also widely disseminated the use of a micro-gas turbine as the main driver to produce power again in the power-to-power energy storage system. Before the contribution in this research, micro gas turbines were rarely conceived as competitors of fuel cells or reciprocating internal combustion engines. Furthermore, the author not only increased the accuracy of the modelling and integration of the micro gas turbine into the power-to-power energy storage systems, but he also made a significant contribution to what the next steps should be in order to increase the competitiveness of micro gas turbines to be a real alternative to fuel cells and internal combustion engines; this contributes to road-mapping the next steps towards more competitive micro gas turbine technology, pin-pointing

where research should focus in the next years.

Lastly, it is important to recognise the proactive approach taken by the author in reaching out to and collaborating with experts from both the private sector and academia. This collaboration increases the credibility to the review of the current state-of-the-art technologies, the analysis of the implemented models and their adaptations, as well as the large number of system integration aspects involved. Furthermore, the author's engagement with experts allowed for meaningful discussions on the obtained results, which in turn guided the development of future research. The collaborations with Eugenio Trillo, CEO of Lean Hydrogen, Francisco Caballero and Pablo Gutierrez, CEO and Lead Project Engineer at Alener Solar, Dr Mario Ferrari, full-time Professor at the University of Genoa, Christer Björkqvist and Rene Vijgen, Managing Director and Senior Project Engineer at ETN Global are worth noting in this regard.

1.5 Organisation of the report

The report is structured as follows. Chapter 1 provides an introduction to the global energy landscape, framing the current research and highlighting the original contributions to knowledge by the author. The dissemination and communication activities undertaken are also presented. Chapter 2 provides a comprehensive overview of water electrolysis, exploring its thermodynamic, technological, and economic performance indicators aim a comprehensive manner. Chapter 3 delves deep into the concept of power-to-power, of which water electrolysis is a constituent element, and reviews the other systems involved thoroughly. The chapter concludes by conducting an overall thermodynamic analysis of the power-to-power energy storage system, considering the various commercial technologies available for each system and providing key recommendations for the further improvement of the technology.

In Chapter 4 and Chapter 5, the mathematical modelling and economic parameters of each system are examined in greater detail. The information produced with the models and the models themselves are then utilised to develop a Python-based software tool that enables accurate and efficient techno-economic assessments of power-to-power energy storage systems.

Chapter 6 applies the aforedescribed models to carry out a case study to evaluate the feasibility of implementing a power-to-power energy storage system with a micro gas turbine for an electricity-only application with continuous demand. The chapter also explores the hybridisation of the system through incorporation of electric battery energy storage, aiming to further enhance the global performance of the system.

In alignment with the objectives of the previous chapter, Chapter 7 introduces the integration of a micro gas turbine with an organic Rankine cycle system to render a more efficient power conversion unit, thereby increasing the heat-to-power ratio of the micro gas turbine. The integrated system is then incorporated into the case study presented in Chapter 6 in order to assess the benefits of the concept with respect to the standard case.

Finally, Chapter 8 provides specific and general conclusions drawn from the research. It also outlines the next steps necessary to foster the applicability of power-to-power energy storage solutions based on micro gas turbines.

1.6 List of publications and activities

This section provides a detailed list of publications and activities carried out by the author of this research in the context of the NextMGT project and beyond.

Publications

All publications are to some extent contained in the development of the different chapters.

Journal publications:

- A. Escamilla, D. Sánchez, L. García-Rodríguez, 2022, *Assessment of power-to-power renewable energy storage based on the smart integration of hydrogen and micro gas turbine technologies*, International Journal of Hydrogen Energy, Vol. 47, Issue 40, pp. 17505-17525.
- A. Escamilla, D. Sánchez, L. García-Rodríguez, 2023, *Techno-economic study of Power-to-Power renewable energy storage based on the smart integration of battery, hydrogen, and micro gas turbine technologies*, Energy Conversion and Management: X, Vol. 18, pp. 100368.

Conference publications:

- A. Escamilla, D. Sánchez, L. García-Rodríguez, 2022, *Exergy Analysis of Green Power-to-Hydrogen Chemical Energy Storage*, Proceedings of the ASME Turbo Expo: Turbomachinery Technical Conference and Exposition. Volume 4: Cycle Innovations; Cycle Innovations: Energy Storage. Rotterdam, The Netherlands. June 13–17. V004T07A004. ASME.
- G. Tilocca, D. Sánchez, M. Torres García, A. Escamilla Perejón, S. Minet, *A methodology to quantify product competitiveness and innovation requirements for micro gas turbine systems in hydrogen backup applications*,Proceedings of the ASME Turbo Expo: Turbomachinery Technical Conference and Exposition. Volume 4: Cycle Innovations; Cycle Innovations: Energy Storage. Boston (MS). June 26-30. ASME.
- A. Escamilla, D. Sánchez, L. García-Rodríguez, 2023, *Achieving 45% micro gas turbine efficiency through hybridisation with organic Rankine cycles*, in: 7^{th} International Seminar on O.R.C. Power Systems. Seville, Spain. September 4-6, 2023. 86. Accepted for presentation at the conference.
- L. Pilotti, J. Runyon, S. Mori, A. Escamilla, *Prerequisites for the use of low-carbon alternative fuels in gas turbine power generation*, 2023, in: 11^{th} International Gas Turbine Conference (IGTC). Brussels, Belgium. October 10-11, 2023. Accepted for presentation at the conference.

Conference activities:

- Poster: A. Escamilla, D. Sánchez, L. García-Rodríguez, 2022, *Micro-Gas Turbines for Chemical Energy Storage Poster*, in: ASME Turbo Expo: Turbomachinery Technical Conference and Exposition. Rotterdam, The Netherlands. June 13–17. ASME
- Tutorial of Basics (ToBs): T. Allison, N. Smith, A. Rimpel, A. Escamilla, D. Sánchez, 2021, *Grid-Scale Energy Storage Systems and Technologies*, in: ASME Turbo Expo: Turbomachinery Technical Conference and Exposition. Virtual. June, 7-11.

- Tutorial of Basics (ToBs): S. D. Cich, J. Neveu, B. Connolly, F. Hickey, T. Allison, A. Escamilla, D. Sánchez. *Hydrogen for Power and Energy Storage*, in: ASME Turbo Expo 2021: Turbomachinery Technical Conference and Exposition. Virtual.
- Poster: A. Escamilla, D. Sánchez, L. García-Rodríguez, *Footprint Analysis of a P2P-ESS with mGTs*, in: ASME Turbo Expo 2022: Turbomachinery Technical Conference and Exposition. Rotterdam, The Netherlands. June 13–17.
- Tutorial of Basics (ToBs): T. Allison, N. Smith, A. Rimpel, A. Escamilla, D. Sánchez. *Grid-Scale Energy Storage Systems and Technologies*, in: ASME Turbo Expo 2022: Turbomachinery Technical Conference and Exposition. Rotterdam, The Netherlands. June 13–17.
- Tutorial of Basics (ToBs): A. Escamilla, G. Tilocca, J. Al-Zaili, T. Seljak, D. Sánchez. *Micro-Gas Turbine: Technological Advancements and Market Research*, in: ASME Turbo Expo 2022: Turbomachinery Technical Conference and Exposition. Rotterdam, The Netherlands. June 13–17.

Collaborations

The author has carried out collaborations with different organisations and partners, as detailed below:

- Collaboration with Eugenio Trillo, CEO of Lean Hydrogen. Lean Hydrogen is an engineering and consultancy company specialising in green hydrogen projects. During this collaboration, the author has gained knowledge in the field of hydrogen production, and more specifically, on the development of the electro-chemical modelling of the different types of electrolysers.
- Collaboration with Energy and Turbomachinery Network, ETN Global. ETN Global is a non-profit membership association bringing together the entire value chain of gas turbine technology. During this collaboration, the author has been able to carry out discussions with different key players in the field of gas turbines, focusing on micro-gas turbines and decentralised energy systems. The author has taken an active role in the Decentralised Energy Systems Working Group and the Young Engineers Committee (YEC). The author has actually served as vice-chair and chair of the YEC from June-2023 to October-2023.
- Collaboration with Alener. A Sevillian company promoting the construction of green hydrogen projects in west Andalucía. The author has carried out techno-economic studies for the development of a 1 MW green hydrogen plant at the port of Seville. The author has also carried out an analysis of the filling and emptying of low and high-pressure H_2 storage vessels to accurately know how often they could provide hydrogen to potential off-takers.
- Collaboration with Giuseppe Tilocca, ESR-13 within NextMGT project. The author has carried out collaborations with Giuseppe Tilocca in order to support the assessment of micro gas turbine competitiveness against internal combustion engines and fuel cells, as well as the overall competitiveness of these three technologies when integrated into a Power-to-Power energy storage system. Out of this collaboration, a conference paper has been written.

Participation in conferences and technical meetings

- NextMGT Workshop 1 - Online. September, 16^{th} - 17^{th}, 2020.

- NextMGT Combustion Winter School - Online. January, 21st - 22nd, 2021.
- NextMGT Mid-Term Check - Online. March, 09th, 2021.
- NextMGT Workshop 2 - Online. June, 16th - 17th, 2021.
- ASME Turbo Expo 2021, Turbomachinery Technical Conference & Exposition - Online. June, 7th-11th, 2021.
- NextMGT Workshop 3 - Stavanger, Norway. November, 08th - 10th, 2021.
- ETN Global Annual General Meeting - Brussels, Belgium. March, 29th - 30th, 2022.
- ETN Global GE-LM2500 User Group Meeting - Aberdeen, United Kingdom. June, 07th - 09th, 2022.
- ASME Turbo Expo 2022, Turbomachinery Technical Conference & Exposition - Rotterdam, The Netherlands. June, 13th-17th, 2022.
- NextMGT Summer School - Savona Campus, Italy. June, 21st - 23rd, 2022.
- NextMGT Workshop 4 - Thessaloniki, Greece. September, 07th - 09th, 2022.
- October Workshop by ETN Global - Berlin, Germany. October, 12th - 13th, 2022.
- NextMGT Winter School - London, United Kingdom. January, 17th - 18th, 2023.
- Marie Curie Alumni Association Annual Conference - Córdoba, Spain. February, 24th - 25th, 2023.
- ETN Global Annual General Meeting - London, United Kingdom. March, 28th - 29th, 2023.
- ETN Global SGT-A35 User Group Meeting - Aberdeen, United Kingdom. May, 10th - 11th, 2023.
- ETN Global GE-LM2500 User Group Meeting - London, United Kingdom. June, 06th - 08th, 2023.
- Just Green AFRH2ICA Spanish Stakeholders' Event - Madrid, Spain. June, 27th, 2023.
- International Seminar on ORC Power Systems - Sevilla, Spain. September, 04th - 06th, 2023.
- ETN Global High-Level User Meeting - Brussels, Belgium. October, 09th, 2023.
- ETN Global International Gas Turbine Conference (ETN's IGTC) - Brussels, Belgium. October, 10th - 12th, 2023.
- 4^{th} European Micro Gas Turbine Forum (EMGTF) - Brussels, Belgium. October, 12th - 13th, 2023.

Communication activities

- Article in *The Conversation*, published on December 8th 2020, "*La hoja de ruta del hidrógeno en España: ¿podemos cumplir los objetivos?*" ("*The green hydrogen roadmap in Spin: can the objectives be met?*").
- Article in *The Conversation* published on the February 3rd 2021, "*¿Por qué cambia tanto el precio de la electricidad en España?*" ("*Why is the price of electricity changing so much in Spain?*").
- Interview in *Radio Clásica (Radio Nacional España, RNE)*, about fluctuations of the electricity price in Spain. Broadcasted by the radio program *Longitud de Onda* on February 3th 2021.

Secondments

- University of Genoa (September 01st 2021 to November 30th 2021). The candidate spent three months at the Savona Campus (Italy), working on the following topics:

  - solar power production,
  - hydrogen production with proton-exchange membrane electrolysers,
  - storage of hydrogen at high pressure,
  - production of power with a micro gas turbine (experimental data of a T100 micro gas turbine) have been provided by the University of Genoa).
- ETN Global (May 09th 2022 to August 10th 2022). The author spent three months at the ETN office in Brussels (Belgium), working on the following topics:
  - active engagement in ETN's Young Engineers Committee, leading a team of young engineers who assisted in drafting ETN's response to the European Commission's REPowerEU Plan & Winter Preparedness Package through an analysis of additional measures that the European commission and the Member States could implement to attain more energy and economic savings for the upcoming winter.
  - coordinating the work of ETN's Decentralised Energy Systems (DES) Working Group (WG) by:
    * assisting the Chairs of the WG on technical matters.
    * providing support to the Chairs by drafting a techno-economic report structure and identifying the most promising DES applications amongst combined heat and power fleet databases in the US.
  - coordinating and planning ETN's LM2500 User Group Meeting on 07-09 June 2022 at Total Energies E&P facility in Aberdeen, Scotland, and following up on the outcomes and agreements made by the members.
  - supporting the ETN Office with coordination and logistics of ETN's participation at ASME Turbo Expo 2022.
  - learning from ETN about best practices as well as challenges when coordinating/-managing EU-funded R&D projects within a large consortium.
- Alener Solar (November 10th 2022 to February 10th 2023). The candidate spent three months at Alener, Seville (Spain), working on the following topics:
  - techno-economic analysis of the 1 MW hydrogen production plant to be constructed at the Port of Seville.
  - performance and economic evaluation of alkaline and proton-exchange membrane electrolyser quotations.
  - performance evaluation of high-pressure H_2 storage.
  - interaction with suppliers and vendors to characterise each of the principal and auxiliary systems of the H_2 production plant.
  - elaborated the request for quotation (RFQ) document of the PV solar system, electrolyser, civil work, and hydrogen plant for the aforecited green hydrogen production facility.

Other achievements

- Representative of the board of Early Stage Researchers in NextMGT.
- Participation in the Vodafone Campus Lab as a representative of University of Seville, obtaining the second-best place out of more than 90 teams.
- Participation in ***Babson Build***, *The Entrepreneurship Program for University Students*. The candidate received a scholarship from University of Seville to attend this event,

thanks to the second place achieved at the Vodafone Campus Lab programme.
- Recipient of the Student Advisory Committee Travel Award to attend Turbo Expo 2022 in Rotterdam, The Netherlands.
- Participation in the development and writing of Horizon-2020 proposals.
- Vice-Chair and Chair of the ETN's Young Engineers Committee (YEC).

2 Water Electrolysis - A review

*This chapter presents a review of the **state of the art** of water electrolysis. Firstly, it introduces the pathways to produce hydrogen, followed by a deep thermodynamic understanding of the electrochemical reaction that allows the splitting of water through electrolysis. The second part focused on the different electrolyser technologies, paying close attention to the Alkaline, Proton-Exchange Membrane and Solid Oxide electrolyser technologies with regard to performance, manufacturing and economic parameters. The chapter finalises by introducing the way forward for the different technologies and highlighting the barriers to scaling up hydrogen production.*

Some contents of this chapter are available in:

A. Escamilla, D. Sánchez, L. García-Rodríguez, 2022, Exergy Analysis of Green Power-to-Hydrogen Chemical Energy Storage, Proceedings of the ASME Turbo Expo 2022: Turbomachinery Technical Conference and Exposition. Volume 4: Cycle Innovations; Cycle Innovations: Energy Storage. Rotterdam, Netherlands. June 13–17, 2022. V004T07A004. ASME.

Tutorial of Basics (ToBs): T. Allison, N. Smith, A. Rimpel, A. Escamilla, D. Sánchez. Grid-Scale Energy Storage Systems and Technologies, in: ASME Turbo Expo 2021: Turbomachinery Technical Conference and Exposition.

Tutorial of Basics (ToBs): S. D. Cich, J. Neveu, B. Connolly, F. Hickey, T. Allison, A. Escamilla, D. Sánchez. Hydrogen for Power and Energy Storage, in: ASME Turbo Expo 2021: Turbomachinery Technical Conference and Exposition.

Tutorial of Basics (ToBs): T. Allison, N. Smith, A. Rimpel, A. Escamilla, D. Sánchez. Grid-Scale Energy Storage Systems and Technologies, in: ASME Turbo Expo 2022: Turbomachinery Technical Conference and Exposition.

2.1 History of hydrogen and its properties

Hydrogen is the simplest chemical element on Earth. It is a colourless, odourless, tasteless, and flammable gaseous substance whose atom has a nucleus comprised of a proton and a neutron, bearing one unit of positive charge, whilst the electron around it has one negative electrical charge. Under atmospheric conditions, hydrogen gas is a loose aggregation of diatomic hydrogen molecules, each consisting of a pair of atoms, H_2. A well-known chemical property of hydrogen is that it burns with oxygen in a wide range of concentrations, forming

water.

Hydrogen is the most abundant element in the universe. However, it accounts for only about 0.14% of the Earth´s crust by weight. In this, hydrogen can be found in vast quantities as part of water in oceans, ice packs, rivers, lakes, and the atmosphere. Furthermore, as part of numerous carbon compounds, hydrogen is also present in all animal and vegetable tissues and in petroleum.

Hydrogen is widely used in the chemical industry for the manufacturing of ammonia and in the hydrogenation of carbon monoxide and organic compounds. In the last decade, hydrogen has also been seen as a carbon-free fuel for the future thanks to its very favourable chemical properties which make it an excellent energy carrier.

In the early 1500s, the alchemist Paracelsus noted that the bubbles released when iron filings were added to sulfuric acid were flammable. Robert Boyle, in 1671, made the same observation. However, neither of them followed up on their discovery of hydrogen and so Henry Cavendish gets the credit for it. In 1766, he collected the bubbles and showed that they were different from other gases. Furthermore, he showed that, when hydrogen burns, water is formed, thereby ending the belief that water was an element. Following the discovery of hydrogen, the French scientist Antoine-Laurent Lavoisier repeated Cavendish's experiment in 1766 and baptised the gas with its current name, hydro-gen, meaning water-former. In addition, Lavoisier was the first to apply a method to isolate hydrogen (a rudimentary form of electrolysis) in the early nineteenth century.

Table 2.1 shows the basic physical and chemical properties of the hydrogen molecule.

Parameter	Value	Unit
Molecular weight	2.016	mol
Melting point	13.96	K
Boiling point (at 1 atm)	14.0	K
Density solid (at 4.2 K)	0.089	$g \cdot cm^{-3}$
Density liquid (at 20.4 K)	0.071	$g \cdot cm^{-3}$
Gas density (at 0°C and 1 atm)	0.0899	$g \cdot l^{-1}$
Gas Thermal Conductivity (at 25°C)	0.00044	$cal \cdot cm \cdot s^{-1}$
Gas viscosity (at 25°C and 1 atm)	0.0089	cP
Autoignition temperature	858	K
Flammability limit in oxygen	4 – 94	%
Flammability limit in air	4 – 74	%

Table 2.1: Chemical properties of hydrogen

The energy content of 1 kg of hydrogen (when reacting with oxygen to form water) is 33.3 kWh, corresponding to 120 MJ (Low Heating Value, LHV), if water vapour is formed, and 39.4 kWh, corresponding to 142 MJ (High Heating Value, HHV), if water is in the liquid state. The difference between these two values is known as the molar enthalpy of vaporisation of water,

which is 44.01 kJ·mol^{-1}.

Hydrogen has been used in numerous applications for the last 100 years because it has the highest energy-to-weight ratio amongst the different fuels (about three times more than natural gas, butane, or kerosene [9]), though it can also be hazardous to handle. Furthermore, hydrogen ignites very easily and burns in a wide range of concentrations in oxygen or air, compared to any other fuels, see Table 2.1. This flammability range is very high but does not pose a threat if the gas stays under well-ventilated conditions since the ignition temperature, 858 K, is relatively high compared to other fuels. It is also to note that the flammability limits increase with temperature, the lower limit decreasing from 4 vol% at Normal Temperature and Pressure (NTP) (293 K and 1 atm) to 3 vol% at 373 K and the same pressure. Because of its low density, hydrogen dissipates in the air and cannot be collected near the ground as is the case for other fuels, such as gasoline or diesel.

2.2 Overview of hydrogen production processes

Molecular hydrogen cannot be found on Earth but, rather, the hydrogen molecule, H_2, must be obtained by processing a wide range of primary energy resources, either renewable or non-renewable. Based on this, hydrogen production processes can be classified according to the origin of the primary energy resource used. Three different categories (types) are commonly identified: grey, blue, and green hydrogen. “Grey” hydrogen is produced from fossil fuels via carbon intensives processes, such as Steam Methane Reforming (SMR) and coal gasification. “Blue” hydrogen is grey hydrogen whose CO_2 emitted during production is sequestered via Carbon Capture and Storage (CCS). “Green” hydrogen is a low or zero-emission hydrogen produced with clean energy sources whose main production route is water electrolysis supported by renewable energy sources. In 2020, 96% of the hydrogen produced worldwide classified was “grey” [10].

Figure 2.1 presents the general pathways for hydrogen production. It is observed that the primary energy sources and processes (mainly reforming, electrolysis, gasification, biomass and biomass-derived fuels conversion, and water splitting) involved can be different.

2.2.1 Hydrocarbon reforming

In chemistry, reforming is a processing technique whereby the molecular structure of a hydrocarbon is rearranged to modify its properties; for hydrogen production, this means a hydrocarbon fuel being converted into hydrogen. Natural gas is the dominant fossil fuel used but liquid hydrocarbons such as gasoline can also be used, and the hydrogen resulting from this method is catalogued as “grey” hydrogen. Several reforming processes exist depending on the reactant that is used (in addition to the hydrocarbon): if it is steam, the endothermic reaction is known as steam reforming whereas, if this is oxygen, the exothermic reaction is known as partial oxidation (POX). When these two reactions are combined, another reforming process arises, called auto thermal reaction (ATR). A typical reforming plant is comprised of a desulphurization unit, reforming and clean-up sections, and auxiliary equipment such as heat exchangers, coolers, combustors, compressors, pumps, etc. [11]. More information about the different hydrocarbon reforming methods can be found in the bibliography [11, 12, 13, 14].

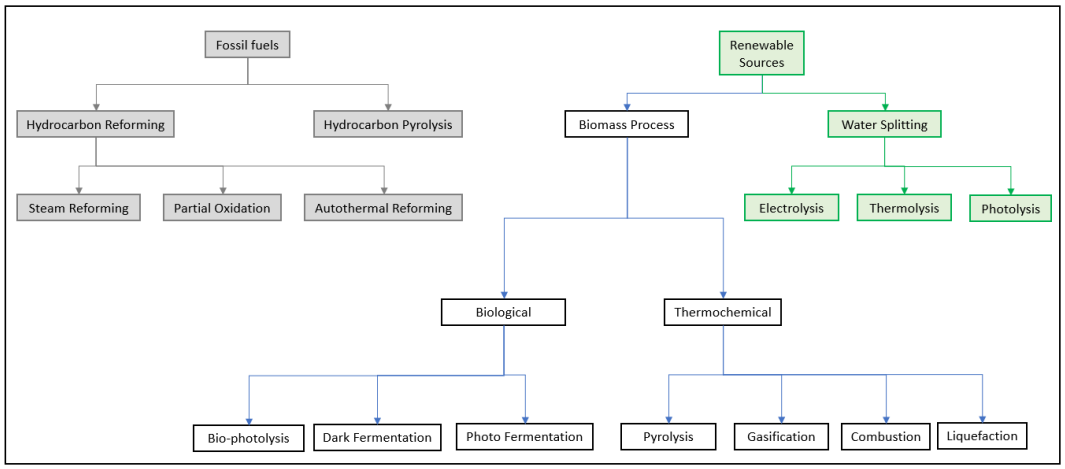

Figure 2.1: General pathways for the production of hydrogen [11].

2.2.2 Hydrogen pyrolysis

Pyrolysis is a processing technique whereby the molecular structure of a hydrocarbon is rearranged to modify its properties with the main characteristic that the only reactant is the hydrocarbon itself, which is decomposed by heating without any addition of steam or oxygen. Biomass, methane, and hydrogen sulphide are the main reactants in the production of hydrogen by pyrolysis. In this case, the hydrogen produced can be catalogued as “blue”, when biomass is the raw hydrocarbon used, or “grey” when fossil fuels are used as reactants. More information about hydrocarbon pyrolysis can be found in the bibliography [11, 12, 13, 14, 15].

2.2.3 Biomass processing

Biomass is a renewable source of primary energy derived from plant and animal materials. Biomass classifies as net-zero emission because it is organic matter in which the energy of sunlight is stored in chemical bonds via photosynthesis. Although CO_2 is released when biomass is utilised for the production of energy, these emissions equal the CO_2 that was absorbed by the living organisms earlier (CO_2 cycle).

The conversion of biomass can be classified into two main categories: thermochemical and biological processes. Thermochemical processes, in chemistry, are those using heat to promote chemical transformations of biomass into energy and chemical products. In the case of hydrogen production, the processes that are more widely used to produce a hydrogen-rich stream of gases known as “syngas” -a blend of hydrogen, carbon monoxide and other non-combustible gases- are gasification and pyrolysis. Biological processes are those that are vital for an organism to live, thus shaping its capacities to interact with the environment. Biological processes are made of many chemical reactions or other events that are involved in the persistence and transformation of life forms; when it comes to hydrogen production, those biological processes are adapted for the generation of hydrogen instead of carbon-containing biomass. The main biological processes used nowadays are bio-photolysis, dark fermentation, and photo fermentation. More information about these processes can be found in the bibliography [11, 12, 13, 14, 16, 17]. Figure 2.2 shows an overview of hydrogen production from biomass, identifying the different processes and their feedstocks.

Although biological processes are less energy-intensive, since they operate at moderate pressure and temperature, they feature low production rates of hydrogen (mol H_2/mol feedstock), even if this also depends on the raw material used [17]. Thermochemical processes are, on the other hand, much faster and offer higher stoichiometric yield (production rate) of hydrogen, with gasification being a promising option from economic and environmental standpoints [18].

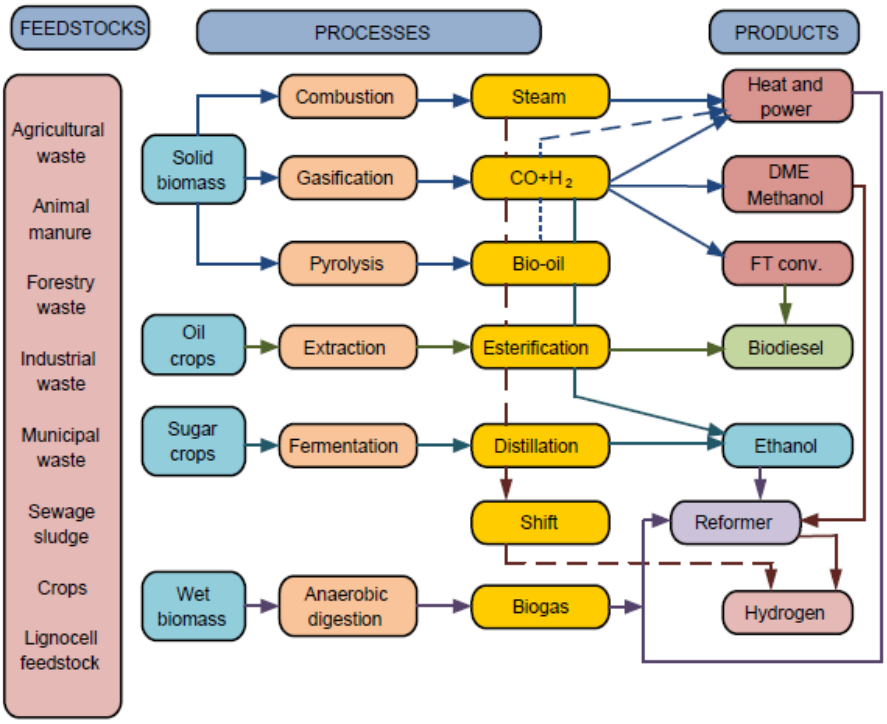

Figure 2.2: Hydrogen production processes from biomass [14]

2.2.4 Water splitting

Water splitting is the chemical reaction in which water is broken down into oxygen and hydrogen.

$$2H_2O + \text{energy} \rightarrow 2H_2 + O \tag{2.1}$$

Water is one of the most abundant compounds on Earth and it can be used to produce H_2 through water-splitting processes such as electrolysis, thermolysis and photolysis. This chemical reaction does not take place spontaneously and it is endothermic, which means that an energy input is needed to drive the formation of hydrogen and oxygen from water: electrolysis when the energy input is electricity, thermolysis when it is thermal energy, and photolysis when it is visible light. Water splitting and, especially, electrolysis are treated in more detail in the next section.

2.2.5 Comparison of hydrogen production processes

A brief overview of the different hydrogen production processes has been provided in earlier sections of this chapter. This is now complemented by a comparison of the environmental, economic and technical features of each of them.

Table 2.2 lists the efficiency and the advantages and disadvantages of the different methods used to produce hydrogen. The range of efficiencies in the table is very wide. For instance, reforming-based processes have been used widely in the last decades thanks to their very high efficiency; hence, they are very mature and the infrastructures for production and distribution are already in place. On the negative side, these processes are highly energy-intensive and run on fossil fuels, therefore producing CO_2 as a byproduct. 96% of the hydrogen produced in 2020 comes from these methods.

Hydrogen production from renewable energy sources sorts out the environmental issue associated with hydrocarbon reforming, though it features much lower efficiency. Additionally, the fact that it has not been commercialised at larger scale implies that capital costs are still high. On the other hand, these processes contribute to the integration of variable renewable energies through energy storage, thus holding a large potential to contribute to carbon neutrality by 2050.

Other parameters such as availability of the feedstock and technology, production capacity, O&M cost, and contribution to global warming, amongst many others must also be considered. In this regard, Figure 2.3 considers the environmental impact of these technologies based on the Global Warming Potential (GWP) measured in grams of CO_2 equivalent ($g_{CO_{2,eq}}$) and the Acidification Potential (AP) measured in grams of SO_2 equivalent ($g_{SO_{2,eq}}$) for each kilogram of hydrogen produced. To obtain a measure of the overall environmental impact of these technologies, the Eco-Indicator 95 is used; this method takes the GWP and AP into account by multiplying the Acidification Potential by 10 and the Global Warming Potential by 2.5 [20] (Figure 2.4).

Natural gas steam reforming has the highest overall environmental impact, a result that was expected due to it being highly energy-intensive and to the nature of the fuel used. Nuclear based thermochemical processes and renewable energy-based electrolysis have much lower environmental impact compared to thermochemical processes based on fossil fuels. As said already, cataloguing hydrogen production as “green”, “grey” or “black” is related to its environmental impact as a contribution to increasing greenhouse effects. This is monitored globally by the overall indicators shown in Figures 2.3 and 2.4 which have been produced from the information in [21]; it is to note that, even if today’s latest technology may deviate from the absolute values in these charts, the relative difference amongst the hydrogen production methods compared regarding their overall environmental impact still hold.

Another important environmental aspect is the water consumption of water electrolysis. This consumption of water can be as high as 17-20 kg_{H_2O}/kg_{H_2} [22, 23] when proton exchange membrane (PEM) electrolysers are used. A study conducted by Marcus Newborough and Graham Cooley ([22]) aimed to determine the proportion of water usage required to substitute all fossil fuels with green H2. The findings indicate that this replacement would account for

Process	Efficiency [%]	Major Advantages	Major Disadvantages
SR	74-85	Most developed technology, existing infrastructure.	CO_2 byproduct, dependence on fossil fuels.
POX	60-75	Proven technology, existing infrastructure.	
ATR	60-75	Proven technology, existing infrastructure.	
Biomass pyrolysis	35-50	CO_2-neutral, abundant, and cheap feedstock	Tar formation, variable H_2 content due to seasonal availability and feedstock impurities.
Bio-photolysis	1 – 14	CO_2-consumed, O_2 is the only byproduct, operation at moderate p/T.	Requires sunlight, low H_2 production rates, the requirement of large reactor volume, O_2 sensitivity, and high raw material cost.
Dark fermentation	60-80	CO_2-neutral, simple, can produce H_2 without light, contributes to waste recycling, no O_2 limitation.	Fatty acids removal, low H_2 production rates, low conversion efficiency, the requirement of large reactor volume.
Photo-fermentation	0.1	CO_2-neutral, contributes to waste recycling and can use different organic wastes and wastewater.	Requires sunlight, low H_2 production rates, low conversion efficiency, the requirement of large reactor volume, O_2 sensitivity.
Electrolysis	AE: 62 – 82 PEME: 67-84 SOE: 75-80	No pollution with RES, proven technology, existing infrastructure, O_2 only byproduct, contribute to RES integration as ESS.	Low overall efficiency, high capital costs.
Thermolysis	20 – 50	Clean and sustainable, abundant feedstock, O_2 is the only byproduct.	Toxicity, corrosion problems, high capital costs.
Photo-electrolysis	0.06	Emission-free, abundant feed-stock, O_2 only byproduct.	Requires sunlight, low conversation efficiency, non-effective photocatalytic material.

Table 2.2: Overview of major hydrogen production processes [11, 19]

a mere 1.8% of the overall water consumption. However, water supply is already a problem in many regions of the world where competition between different end-uses is taking place: agriculture, industry, and cities. Thus, the analysis of water scarcity will play a key role to

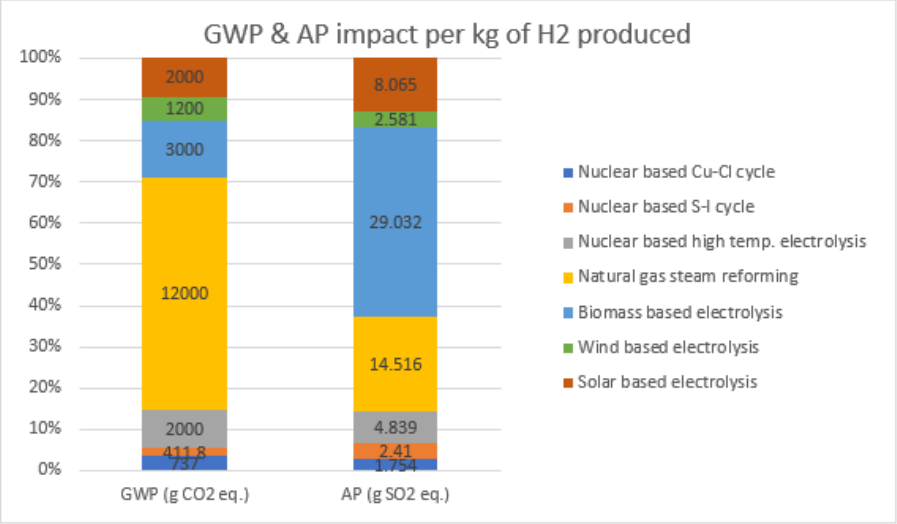

Figure 2.3: Global Warming Potential (GWP) and Acidification Potential (AP) for hydrogen production processes [21].

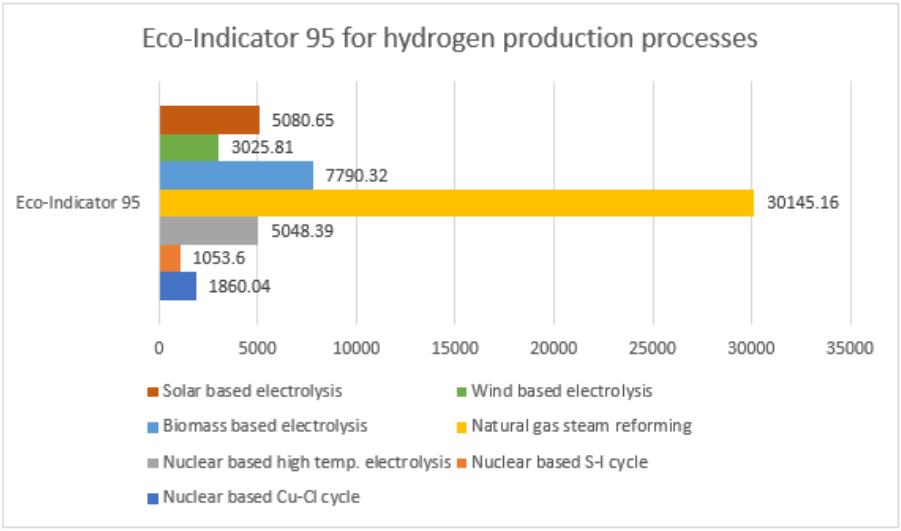

Figure 2.4: Eco-Indicator 95 for hydrogen production processes [21].

produce hydrogen at a greater scale when water electrolysis is used. Hydrogen production methods do not only need to perform efficiently and have low environmental impact but they also need to be economically competitive. In the following, an overview of the capital and operating cost of the different hydrogen production methods is introduced. The cost analysis is highly affected by the maturity of the production technology considered, economy of scale, availability and price of feedstock, etc. The intention is not to give a very detailed study but an overview of what is found in the literature. Data is variable from one source to another and not up to date due to the many uncertainties and the lack of operating plants of certain technologies, many of them being still under development or only demonstrated at the lab scale.

Table 2.3 shows the capital costs of some hydrogen production methods in the last decades along with the associated cost of hydrogen produced. In some cases, the production of certain by-products in the same process may affect the cost of hydrogen produced, either positively or negatively; this is considered in the analysis shown in Table 2.3. In the case of using feedstock based on fossil fuels, this applies to CO_2, which affects the cost of hydrogen as a consequence of the need to incorporate CO_2 sequestration; cost variations of up to about 8% can be experienced accordingly [11]. However, the processing of fossil fuels is already a mature technology and the added cost of carbon sequestration has a weak impact on the cost-effectiveness against other technologies; this is confirmed by the very low cost of hydrogen produced: 2.27 \$/kg H_2. Moreover, when in combination with the most efficient reforming technology, ATR, the cost of hydrogen can be reduced to 1.48 \$/kg H_2, the lowest value reported in Table 2.3. Additionally, based on a 600 MW_{H_2} power plant, the same table reports capital costs for this technology of ~300 \$/kW_{H_2}, which is highly competitive considering the low production cost of hydrogen.

When water-splitting processes where renewable energy is the primary energy source are considered, there are no environmentally harmful by-products. Moreover, in some cases, the by-product is steam at high temperatures and this allows hybrid systems able to provide hydrogen, heat, electricity, and cooling. Unfortunately, even with these incentives, these technologies are not cost-effective yet.

The lowest cost of hydrogen based on water electrolysis is yielded by nuclear electrolysis, 4.15 \$/kg H_2, closely followed by solar photovoltaic and wind electrolysis. This is about three times higher than the production cost enabled by ATR. In the case of thermolysis, thermal energy is the primary energy source and nuclear technology is a great source of high-quality steam; the combination of these two processes yields hydrogen production costs of 2.17 \$/kg H_2, which is highly competitive against the most mature technologies. Akin to the development and implementation of solar PV and wind turbines a decade ago, water electrolysis needs to be incentivised (or either grey-blue hydrogen production penalised somehow) in order to grow the necessary economies of scale that will reduce both capital and operating costs.

As deduced from the foregoing discussion, the choice of feedstock and technology drives the final cost of hydrogen production. Amongst the two, capital cost is the main barrier to the wide market deployment, even if the production cost, in the long run, could eventually be competitive against traditional technologies. For instance, the capital cost of a hydrogen plant with a rated capacity of 583 ton_{H_2}/day based on methane steam reforming is around 371 M\$, whereas a similar plant based on nuclear thermolysis has a capital cost of around 2108 M\$. More literature about CapEx and OpEx for hydrogen production plants can be found at [11, 23, 24, 25, 26].

Process	Feed-stock	Capital cost [M$]	Hydrogen cost [$/kg H_2]
CG w/o CCS	Coal	435.9	1.34
ATR w/ CCS	Natural gas	183.8[1]	1.48
CG w/ CCS	Coal	545.6	1.63
Biomass gasification	Woody biomass	149.3-6.4[2]	1.77-2.05
SMR w/o CCS	Natural gas	180.7	2.08
Nuclear thermolysis	Water	39.6 – 2107.6[3]	2.17 – 2.63
SMR w/ CCS	Natural gas	226.4	2.27
Direct bio-photolysis	Water + algae	50 $/$m^2$	2.13
Indirect bio-photolysis	Water + algae	135 $/$m^2$	1.42
Dark fermentation	Organic biomass	-	2.57
Nuclear electrolysis	Water	-	4.15 – 7.00
Solar thermal electrolysis	Water	421-22.1[4]	5.10 – 10.49
Solar PV electrolysis	Water 12-54.5	5.78 – 12.6	
Wind electrolysis	Water	504.8-499.6[5]	5.89 – 6.03
Solar thermolysis	Water	5.7-16[6]	7.98 – 8.4
Photo-electrolysis	Water	-	10.36

[1] Based on a600 MW_{H_2} power plant with a capital cost of 306.35 $/$kW_{H_2}$.
[2] The capital cost of 149.3 M$ corresponds to a plant capacity of 139.7 tn/day. 6.4 M$ is referred to a 2 tn/day plant output.
[3] The capital cost of 39.6 M$ corresponds to a Cu-Cl plant capacity of 7 tn/day, 2107.6 M$ is referred to a 583 tn/day S-I plant output.
[4] The capital cost of 421 M$ is referred to as a power-tower electrolysis plant and 38.4 tn_{H_2}/day, 22.1 M$ corresponds to Stirling-dish technology and 1.4 tn_{H_2}/day.
[5] The cost of 504.8 M$ assumes the coproduction of electricity along with hydrogen whereas, 499.6 M$ represents the cost of hydrogen production only.
[6] The capital cost of 5.7 M$ corresponds to a plant capacity of 1.2 tn_{H_2}/day. 16 M$ refers to a 6 tn_{H_2}/day plant output.

Table 2.3: Summary of hydrogen production processes [11, 27]

2.3 Water Electrolysis

2.3.1 Water Electrolysis fundamentals

Thermodynamic principles of water splitting

Liquid water can be dissociated into molecules of hydrogen and oxygen according to the following reaction:

$$H_2O(l) \rightarrow H_2(g) + 1/2O_2(g) \tag{2.2}$$

In standard conditions of temperature and pressure (298 K and 1 bar), water is liquid, and hydrogen and oxygen are gaseous. The changes of enthalpy, entropy, and Gibbs free energy in the previous reaction are, respectively [12]:

$\Delta H_d^0(H_2O(l)) = +285.84$ kJ mol^{-1}

$\Delta S_d^0(H_2O(l)) = +163.15$ kJ mol^{-1} K^{-1}

$$\Delta G_d^0(\mathrm{H_2O}(l)) = \Delta H_d^0(\mathrm{H_2O}(l)) - T \cdot \Delta S_d^0(\mathrm{H_2O}(l)) = +237.22 \ \ \mathrm{kJ\ mol^{-1}}$$

In spite of a favourable contribution of the entropy term, as a consequence of the formation of 1.5 moles of gaseous species, enthalpy and Gibbs free energy changes are positive. This means that the reaction is endothermic and not spontaneous.

Water steam can be also dissociated into its constituents. The corresponding changes of enthalpy, entropy and Gibbs free energy are [28]:

$$\Delta H_d^0(H_2O(vapour)) = +241.80 \ \ \mathrm{kJ\ mol^{-1}}$$

$$\Delta S_d^0(H_2O(vapour)) = +44.10 \ \ \mathrm{kJ\ mol^{-1}\ K^{-1}}$$

$$\Delta G_d^0(H_2O(l)) = \Delta H_d^0(H_2O(l)) - T \cdot \Delta S_d^0(H_2O(l)) = +228.66 \ \ \mathrm{kJ\ mol^{-1}}$$

The differences between the enthalpy/entropy of liquid and vapour water are due to the enthalpy/entropy of water vaporization: +44.04 kJ mol^{-1} and +119.05 kJ mol^{-1} K^{-1} respectively.

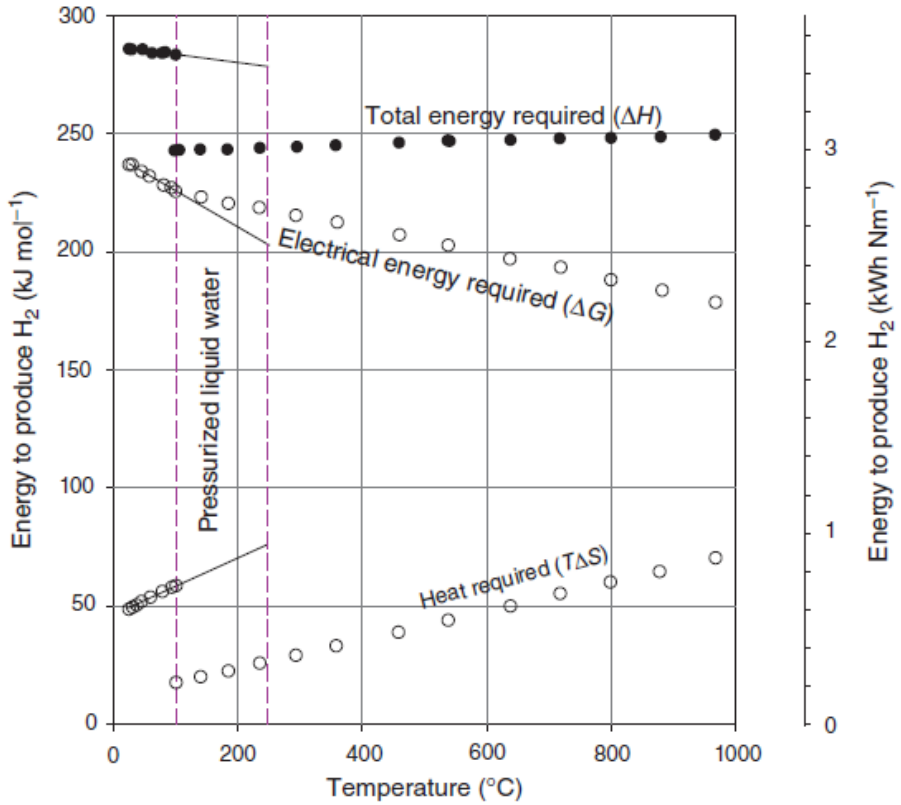

Figure 2.5: ΔG(T), ΔH(T) and T·ΔS(T) of the water splitting reaction at P = 1 bar. (-) data for pressurised liquid water up to 250°C. [12]

Figure 2.5 illustrates the molar changes of enthalpy, entropy and Gibbs free energy as a function of temperature. The enthalpy change (ΔH) does not depend on temperature from a

practical standpoint; on the contrary, both the electric work (ΔG) and heat (TΔS) required (by the electrolyser) change linearly with temperature, these functions exhibiting similar slopes with opposite signs. Gibbs free energy change is positive, becoming negative at very high temperatures (>2500 K). Hardly any material known today can withstand such hard conditions and, therefore, direct thermo-dissociation is unattainable in practice.

It is observed in the plot that higher operation temperatures decrease the electric energy needed to initiate the dissociation of water. About 1/3 of the total energy required by the process is in the form of thermal energy when temperatures are ~ 1000°C, significantly reducing the electric energy needed and, therefore, the operating cost due to a higher cost of electricity than heat. The latter statement drives the question of what the temperature that maximises the system's cost-effectiveness is. At any operating temperature T, ΔH(T) is the total amount of energy required to split 1 mole of water into its constituents (hydrogen and oxygen), ΔG(T) is the electrical work and T·ΔS(T) is the heat demand. Hence, the following relationship is satisfied:

$$\Delta H(T,1) = \Delta G(T,1) + T \cdot \Delta S(T,1) \tag{2.3}$$

Looking at Figure 2.5, the higher the temperature, the lower the electric input and the higher the thermal energy that can be used. One criterion to optimise the operating conditions is to minimise OpEx. Based on the price of industrial heat and electricity, OpEx can be minimised and the operating temperature obtained based on the cost ratio from kilowatt hours of electricity to kilowatt-hours of thermal energy, which is usually in the range 3–5. Additionally, the use of a high-temperature system enables reusing the waste heat downstream of the process in a cogeneration system (a minimum exhaust temperature of 200-300°C is needed). A second criterion that can be used relies on the maturity of the technology, which is normally less favourable to high-temperature systems due to problems related to material science, differential strains, and higher degradation rates, all of which reduce the lifetime of the system.

Electrochemical water splitting

The water-splitting reaction is a non-spontaneous transformation, requiring that energy be provided to the process. This is a so-called endergonic transformation and the device that makes this happen is called an "electrolyser". An electrolysis cell (elementary electrolyser) contains two electrodes (electronic conductors) placed face to face and separated by a thin layer of an ionic conductor (electrolyte). The electrodes are supplied with electricity in water electrolysis cells, driving so-called half-cell reactions that depend on the electrolyte's pH. Table 2.4 shows these half-reactions at the anode and cathode of electrolysis cells in media with different pH.

	Acidic media	Alkaline media
Anode (+)	$H_2O(l) \rightarrow 1/2O_2(g) + 2H^+$	$2OH^- \rightarrow H_2O + 1/2O_2 + 2e^-$
Cathode (-)	$2H^+ + 2e^- \rightarrow H_2$	$2H_2O + 2e^- \rightarrow H_2 + 2OH^-$
Full reaction	$H_2O \rightarrow H_2 + 1/2O_2$	

Table 2.4: Water electrolysis reactions.

Applying the first law of Thermodynamics, the electricity ($n \cdot F \cdot E$) required to split 1 mole of water in equilibrium conditions, according to the full reaction presented in Table 2.4, equal the Gibbs free energy change (ΔG) of the water dissociation reaction:

$$\Delta G_d - nFE = 0 \qquad \text{where} \qquad \Delta G_d > 0 \tag{2.4}$$

In this equation, $n = 2$ is the number of electrons exchanged during the reaction; $F \approx 96485$ C·mol^{-1} is the electric charge of 1 mole of electrons (Faraday's constant); and E (in Volts) is the free energy electrolysis voltage associated with the reaction (full-reaction at Table 2.4). ΔG_d [J·mol^{-1})] is the Gibbs free energy change.

Two different thermodynamic voltages are used to characterise water electrolysis.

- The free energy electrolysis voltage E is defined as:

$$E(T,P) = \frac{\Delta G_d(T,P)}{n \cdot F} \tag{2.5}$$

- The enthalpy or thermo-neutral voltage V is defined as:

$$V(T,P) = \frac{\Delta H(T,P)}{n \cdot F} \tag{2.6}$$

Different situations might be found depending on the cell voltage applied to the electrolysis cell, $U(T,P)$ (Table 2.5).

Situation	Consequence
$U(T,P) = E(T,P)$	Electrolysis does not start.
$E(T,P) < U(T,P) < V(T,P)$	Enough electricity to start the process but not enough to sustain constant T
$U(T,P) > V(T,P)$	Increase in current density and the amount of heat produced. Electrolysis is sustained

Table 2.5: Relationships among the free energy electrolysis voltage (E), enthalpy voltage (V), and fuel cell voltage (U).

At standard conditions of temperature (T=298 K) and pressure (P=1 bar), water is liquid and hydrogen and oxygen are gaseous. For these conditions, E(298 K, 1 bar) $\approx$ 1.23 V and V(298 K, 1 bar) $\approx$ 1.48 V. It should be noted that the energy required for the electrolysis of water vapour is lower than that for liquid water, E(298 K, 1 bar) $\approx$ 1.18 V, although the enthalpy voltage needed in practice is in either case higher than these values given the need to overcome a number of energy losses, such that, in practice, a voltage higher than 1.8 V is needed [29].

Effects of pH, temperature and pressure on voltage

The cell voltage required to break a molecule of water in an acidic medium does not depend on pH, and the same applies to an alkaline medium. However, the selection of pH is important

for the stability of the electrode material. In acidic media, most metals are corroded and, hence, metals of the Platinum group are needed, which increases the capital cost of the electrolysis cell. In alkaline media, Nickel and Cobalt are passivized and oxides/hydroxides are electrochemically active.

As already explained, enthalpy, entropy and Gibbs free energy change depending on temperature and pressure and, therefore, so do the free energy and enthalpy voltages. Figure 2.6 reveals the dependence of free energy electrolysis voltage, $E(\mathrm{T})$, and enthalpy electrolysis voltage, $V(\mathrm{T})$, on the temperature at 1 bar. $E(\mathrm{T})$=1.23 V at 25°C and drops to 1.18 V at 100°C. Above 100°C, $E(\mathrm{T})$ continues to decrease down to 0.9 V at around 1000°C. However, from a practical point of view, temperatures higher than ~ 130°C are not attainable for low-temperature systems: evaporation of water at this high temperatures is not a problem since it can be counteracted by through pressurization, but materials may suffer from mechanical instability above certain temperatures, such as some hydrated polymers used in PEM technology above 100°C.

Nowadays, hydrogen storage at high pressure is feasible from a technical standpoint since vessels can sustain pressures as high as 700 bar. Currently, there are two ways to fill these high-pressure hydrogen storage tanks. One of them is performing water electrolysis at atmospheric pressure and then mechanically compressing the hydrogen produced. Another option is to pressurise the electrolyser such that high-pressure hydrogen is obtained directly. The first option increases OpEx due to the high cost of mechanical compression in terms of energy consumption. The second option increases CapEx dramatically due to the high cost of having the entire electrolyser system under very high pressures. Therefore, trade-offs between the Key Performance Indicators (CapEx, OpEx, efficiency) must be assessed to identify the best option. Usually, the best solution is a hybrid system where the electrolyser is pressurized (15 – 50 bar) and then the final storage pressure is achieved through mechanical compression. Figure 2.7 shows why the hybrid solution is usually selected. The effect of pressure on free energy voltage E is very strong (approximately +200 mV at 298 K, when changing pressure from 1 to 700 bar) but it is still more efficient than mechanical compression to increase pressure from 1 to 50 bar. From this pressure, mechanical compression is used to increase pressure until the storage value, since the capital cost increase of a highly pressurised system becomes unaffordable.

General characteristics of water splitting cells

As already stated, an electrolyser is a device consuming electricity to split the water molecule electrochemically. Electrolysers are comprised of several (even hundreds) elementary electrolysis cells connected in series. There are three main constituents of an electrolysis cell: an electrolyte and two electrodes (anode and cathode). During operation, continuous current flows across the cell: electrons in the electrodes and ions in the electrolyte.

There are three main electrolyser configurations, depending on the arrangement of these constituent parts. The simplest and most conventional arrangement is the so-called “gap cell”, Figure 2.8a. Two planar electrodes are placed face-to-face, with a liquid electrolyte in between and separated by a separator to prevent the reaction products from reacting spontaneously. The distance between electrodes and the diaphragm must be long enough to let the gases flow freely but not too long to increase ohmic (conduction-related) losses unnecessarily. This

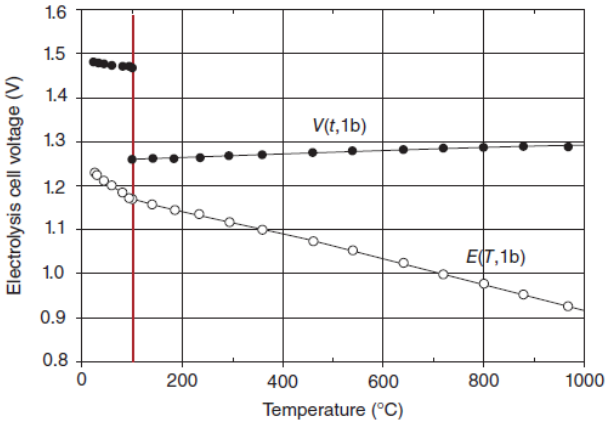

Figure 2.6: Effect of operating temperature of free energy electrolysis voltage $E(T)$ and enthalpy electrolysis voltage $V(T)$ of water (P=1 bar). [12]

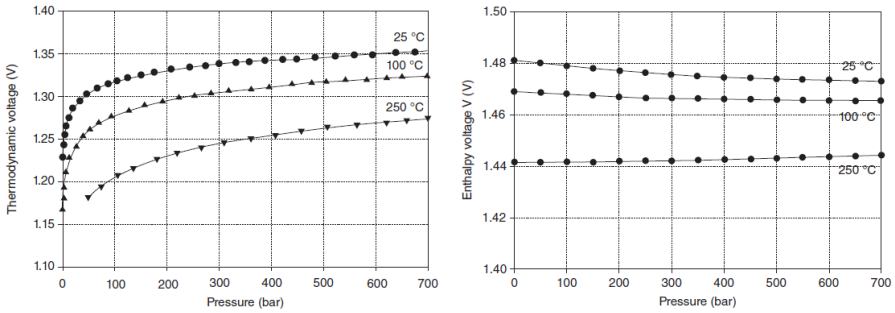

Figure 2.7: Plots of free energy voltage $E(P)$ (left) and enthalpy voltage $V(P)$ (right) of water electrolysis as a function of pressure for three different operating temperatures. [12]

configuration is, in practice, limited by the formation of bubbles at the electrodes, which limits the maximum operating current density attainable. To solve this problem, other arrangements are available, such as the so-called “zero gap” cell, Figure 2.8b. In this configuration, there is no gap and the porous electrodes are in contact with the separator itself. This reduces ohmic losses considerably, enabling higher maximum current density without incurring higher ohmic losses. This concept is applied in advanced, modern alkaline electrolysers. However, it still needs a liquid electrolyte and is not appropriate for acidic media. The third concept is called “Proton Exchange Membrane (PEM) cell”, Figure 2.8c. The cell separator is a thin ion-conducting polymeric film used for the twofold purpose of conveying electric charges from the anode to the cathode and separating gas products. In this case, the porous catalytic layers are coated on each side of the membrane surface and electric contact is obtained by simply pressing the porous current collectors on each side. No liquid electrolyte is needed, only de-ionized water is circulated on the anode side to feed the electrochemical half-reaction. This same concept is also applied to high-temperature cells, the separator and electrolyte being a thin oxide-ion-conducting ceramic membrane.

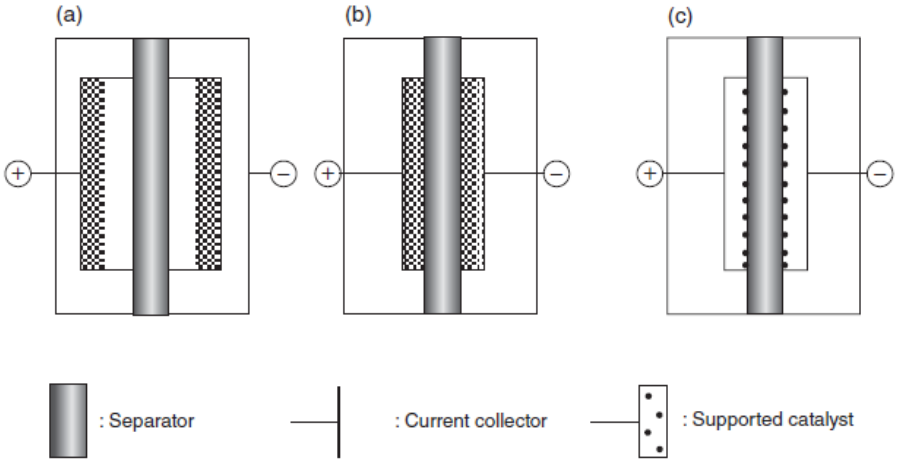

Figure 2.8: Two-dimensional schematic diagrams of (a) gap cell, (b) zero-gap, and (c) an SPE (solid polymer electrolyte) cell. [12]

Energy efficiency of water electrolysis

The concepts of reversible and thermo-neutral voltage were introduced in the previous section. However, consideration has to be given to the fact that the water electrolysis is not a reversible voltage and, therefore, the voltage for the reaction to happen will be higher to account for any irreversibility. Thus, a higher voltage (V_{cell}) is needed and a voltage efficiency can be defined as follows:

$$\eta_{rev} = \frac{V_{rev}}{V_{cell}} \tag{2.7}$$

$$\eta_{tn} = \frac{V_{tn}}{V_{cell}} \tag{2.8}$$

Knowing the cell voltage, the electrical work consumed by a cell can hence be expressed in terms of voltage (V_{cell}) and current (I_{cell}), Eq.(2.9).

$$W_{el} = V_{cell} \cdot I_{cell} = V_{cell} \cdot i \cdot A_{cell} \tag{2.9}$$

In Eq.(2.9), i and A_{cell} are the current density and active area of the electrolyser cell. Based on this energy balance, the energy efficiency of an electrolyser can be defined in terms of the produced chemical energy referred to as either the high or low heating values of hydrogen, η_{HHV} and η_{LHV} respectively, though the former case is used more often (η_{HHV}):

$$\eta_{LHV} = \frac{\dot{m}_{H_2} \cdot LHV}{\dot{W}_{el} + \dot{Q}} \tag{2.10}$$

$$\eta_{HHV} = \frac{\dot{m}_{H_2} \cdot HHV}{\dot{W}_{el} + \dot{Q}} \tag{2.11}$$

The performance of an electrolyser can be illustrated using a polarisation curve, which can be broken into three sections: activation losses (V_{act}), ohmic losses (V_{ohm}), and concentration (related to mass-diffusion) losses (V_{diff}). All these voltage losses need to be added to

the reversible voltage (V_{ocv}), or the theoretical minimum voltage when neglecting all other overpotentials. This is shown in Eq.(2.12).

$$V_{cell} = V_{ocv} + V_{act} + V_{diff} + V_{ohm} \tag{2.12}$$

The discussion on each of the terms in Eq. 2.12 will be discussed in detail in Chapter 4. More information about the energy efficiency of water electrolysis processes and systems can be found in the bibliography [12, 30, 31].

2.3.2 Electrolyser technologies – AE, PEM & SOEC

Three main types of electrolysers are currently keeping most of the application interests:

- Alkaline.
- Proton Exchange Membrane (PEM).
- Solid Oxide (SO).

Alkaline electrolyser (AEC)

The alkaline electrolyser is the most mature electrolyser technology, with the first prototype being manufactured and commercialized in 1902 [32]. The main advantage of this technology compared to others is the availability of construction materials at an inexpensive price. The electrochemical reactions that take place in an alkaline electrolyser, at the anode and cathode, are as follows:

- Anode: $4OH^- \rightarrow O_2 + 2H_2O + 4e^-$
- Cathode: $4H_2O + 4e^- \rightarrow 2H_2 + 4OH^-$

These reactions produce gas at the electrodes, at a rate proportional to current flowing through the electric circuit. A schematic diagram of the operation of an alkaline electrolyser cell is illustrated in Figure 2.9.

The electrodes are immersed in the liquid electrolyte, a highly-concentrated alkaline aqueous solution made of concentrated potassium hydroxide. The anode is usually made of nickel or nickel-based catalyst, with two or three non-noble elements (Co, Mn, NiMoFe, etc.) or even noble metal elements (Pt, Pd, IrO_2 and RuO_2), while the cathode is made of nickel or nickel-based catalyst. A porous solid material (diaphragm) allows the transport of hydroxyl ions (OH^-) between the electrodes whilst it features low permeability to oxygen and hydrogen. Historically, the separator was made of asbestos but it is currently made of Zirfon PERL. The motive force of the reaction is the voltage difference applied between electrodes; in practice, this potential is in the range of 1.3 – 2.0 V.

Proton Exchange Membrane electrolyser (PEMEC)

Proton exchange membrane (PEM) systems are based on the solid polymer electrolyte (SPE) concept for water electrolysis, introduced in the 1960s. Commercially-available PEM electrolysers today are more flexible and tend to have a smaller footprint than alkaline electrolysers. The general features of PEM electrolysers are shown schematically in Figure 2.10.

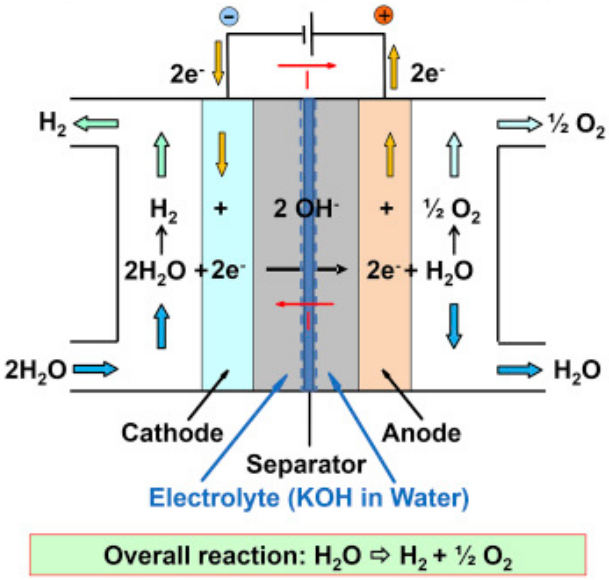

Figure 2.9: Schematic diagram of an Alkaline Electrolysis Cell (AEC). [30]

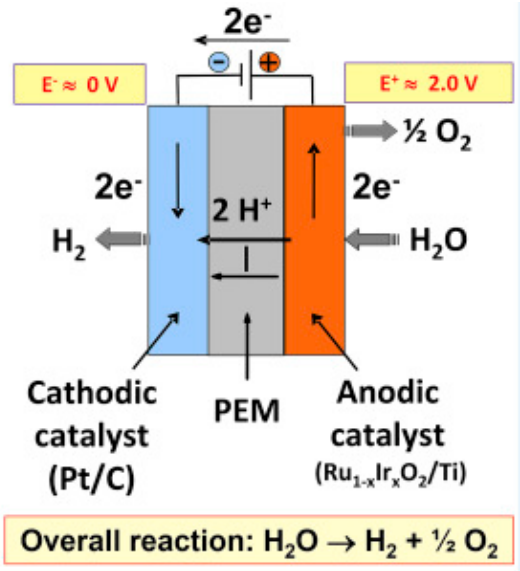

Figure 2.10: Schematic diagram of a Proton Exchange Membrane Electrolyser (PEMEC). [30]

In PEM cells, there is no liquid electrolyte as such; only deionized water circulates through the anodic compartment of the cell. The core component of the cell is a thin (≈ 0.2 mm thick) membrane of a proton-conduction polymer electrolyte. The membrane is used for the twofold purpose of carrying ionic charges and separating the products from the electrolysis half-reactions. The most popular membrane material is a perfluorosulfonic acid (PFSA) ionomer (for instance, *Nafion*®products). On both sides of the membrane, two porous catalytic layers are coated. These catalytic layers are connected to an external DC power source that provides electrical energy for the reaction. The electrochemical half-cell reactions that happen in a proton exchange membrane cell, at anode and cathode, are as follows:

- Anode: $H_2O(l) \rightarrow 1/2O_2(g) + 2H^+ + 2e^-$
- Cathode: $2H^+ + 2e^- \rightarrow H_2(g)$

Water molecules are oxidised at the catalytic anode (usually made of unsupported Ir-based oxide particles), leading to the production of molecular oxygen and protons. This molecular oxygen is then found in the exhaust duct from the anode. Electrons released in this process circulate along the external circuit while protons migrate, across the polymer membrane, towards the cathode (usually made of unsupported Pt particles or of carbon-supported Pt nanoparticles) where they are reduced by the electrons injected by the external DC power supply. As a result, molecular hydrogen is produced at the anode.

Solid Oxide Electrolyser (SOEC)
Solid oxide electrolysers belong to the group of so-called High-Temperature Steam Electrolysis (HTSE). As discussed already, water electrolysis can be performed at either low or high temperatures, using liquid water or steam. However, as shown in Figure 2.5, the main advantage of this technology is that the dissociation of steam requires less energy, and this decreases even further as temperature increases. The operating temperature of a SOEC is within the range of 700-900°C. The technology is immature and has only been tested at a laboratory scale; however, the working principle is the reverse functioning of a Solid Oxide Fuel Cell (SOFC), from which a significant amount of knowledge about materials and operation has already been accumulated. The half-cell reactions are as follows:

Solid Oxide Fuel Cell (SOFC)

- Anode: $O^{2-} \rightarrow 1/2O_2(g) + 2e^-$
- Cathode: $H_2O + 2e^- \rightarrow H_2 + O^{2-}$

The electrochemical cell, the so-called solid oxide electrolysis cell, one of the electrolyser's components, is made of three ceramic layers: a dense electrolyte (usually made of Yttria-stabilized zirconia) and two porous electrodes placed on both sides of the electrolyte. Given the high operating temperature, the electrochemical cell is made of ceramic material. The electrolyser also uses interconnects, which enable the flow of electric current and act as separators between the anode and cathode of adjacent stacks (Figure 2.11). The gaseous atmospheres consist of a mixture of water-hydrogen on the cathode side and oxygen on the anode side. A very attractive feature is the high-grade heat available in the stream of exhaust gases, which can be coupled to produce cogeneration. More information about the different electrolyser technologies can be found in the bibliography [12, 30, 33].

2.3.3 Performance comparison

A summary of the main characteristics and performances of the three electrolyser technologies presented previously is reported in Table 2.6. Electrical energy consumption is highly reduced in solid oxide electrolysers owing to the high operating temperature, which translates into lower electrical energy demand (2.5 – 3.5 kWh/Nm^3 H_2), as compared to alkaline electrolysers (4.3 – 4.9 kWh/Nm^3 H_2). Hence, the highest efficiencies (η_{HHV}) are achieved by SOECs ($\approx$ 100%) and the lowest by AECs ($\approx$ 60 – 80%). In terms of durability, AECs are the most

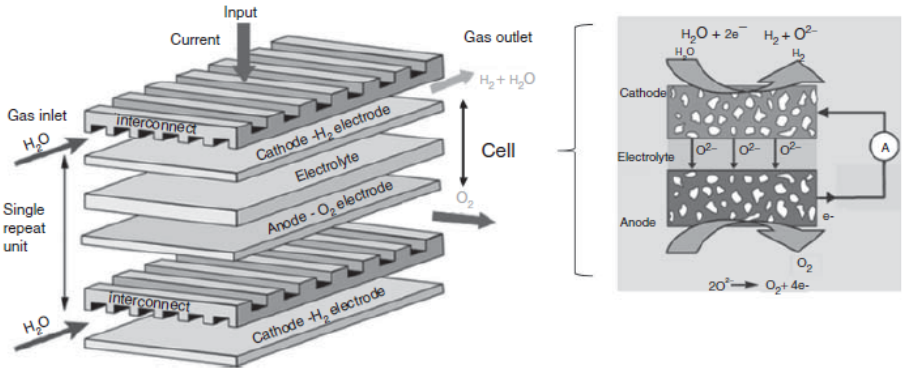

Figure 2.11: Schematic representation of a single repeat unit (SRU) including the three-layer cell (cathode/electrolyte/anode) and the two half-interconnects; a highlight of the anodic and cathodic half-reactions occurring in the cell [12].

robust (up to 100,000 h), mostly due to the utilisation of materials that are stable and highly resistant under mild operating conditions. The sustained R&D experienced by this technology over several decades has increased its maturity to higher levels than the other technologies. PEM technology also exhibits long useful lives (up to 60,000 h to 80,000 h) and, despite being commercialised for a shorter time than AECs, it is considered proven technology with numerous advantages over the former electrolysers. In contrast to these, SOEC technology is still under development and thus it does have much lower durability, having been tested up to around 2000 h to date [33]. Operation at such a high temperature increases the degradation of the electrolyser cell, this being one of the main challenges faced by R&D to make this technology commercially viable.

Very importantly, electrolysers must be designed to allow discontinuous operation due to the energy source used in the most common applications (RES, mobility, etc.); in particular, stop/start cycling is a major source of degradation of system performance, like in most electrochemical systems. The best performer in this situation is the PEM electrolyser, which seems to be very resistant to changes in the operating conditions, therefore suitable for applications driven by variable RES. In the case of SOEC electrolysers, shutdown or start-up manoeuvres may take up to 8 – 12 hours due to the high-temperature change needed from room temperature to the operating temperature. AECs need some 1-2 hours to stabilise under large changes of operating conditions, in particular, start-up or shutdown [12].

Measured current–voltage curves of different electrolysis cells show the different performances between electrolyser technologies. Figure 2.12 shows typical ranges of cell voltage and current density for different electrolysers currently available from the industry. Both alkaline and PEM electrolysers work at high pressure, 6 and 30 bar respectively, whereas the solid oxide electrolyser works at 1 bar. Additionally, the operating temperature is fairly similar for AEC and PEMEC, 82°C and 65°C respectively, and this explains the fact that they have very similar free energy voltage ~1.23V. As opposed to this, the SOEC electrolyser exhibits a low voltage of 0.85V, due to the high operating temperatures which reduce the demand for electric energy to initiate the reaction. The plots in Figure 2.12 reports the operating temperature, $V - i$ relationship and specific electric consumption (kWh/kg$_H$2) for the three electrolyser technologies considered.

Technology	AEC	PEMEC	SOEC
Development stage	Commercial large-scale plant	Prototypes and commercial units	Laboratory stage units
Conventional temperature range [°C]	70 – 90	80 – 150	700 – 1000
Conventional pressure range [bar]	1 – 200	Up to 400	1 – 8 [34]
Electrolyte	25 – 35% KOH	Nafion Membrane	Y_2O_3+ZrO_2
Conventional current density [A/cm^2]	0.2 – 0.5	0.8 – 2.5	1.0 – 2.0
Energy consumption, [kWh/Nm^3 H_2]	4.3 ÷ 4.9	3.6 ÷ 4.0	2.5 ÷ 3.5
Efficiency [%]	60 – 80	80	100
Capacity [Nm^3/h]	1 – 500	1 – 250	1
Durability [h]	100,000	10,000 – 50,000	500 - 2000
Load cycling	Medium	Good	No data available
Stop/go cycling	Weak	Good	Weak
Cost [€/kW]	800 to 1300 [35]	1200 to 2000 [35]	Not commercialized

Table 2.6: Characteristics of different electrolyser technologies.

Conventional alkaline cells can operate at almost 100°C because the high concentration of KOH increases the boiling point of the electrolyte. However, the kinetics of the reaction are not always optimised, and the cell resistance is large. As a result, the cell voltage and the specific energy consumption tend to increase rapidly, and the maximum operating current density is limited to a few hundred mA/cm^2. This technology is therefore most suitable for applications where compactness and high power density are not required. As exposed earlier, the CapEx of this technology is the lowest among the different electrolyser technologies.

PEM electrolysers were made to overcome the different problems found with AEC technology. Even though the free energy voltage, 1.23V, is similar for both technologies, the thin and highly conducting protonic membrane brings about much more favourable reaction kinetics. As a consequence of this, the current density can be increased to higher values whilst still attaining high efficiency. One of the main barriers to this technology though is the higher CapEx, which is still expensive to make it profitable (1200-2000 €/kW [35]). However, PEM technology renders excellent behaviour under pressurised conditions (up to 350 bar) and this yields a very good opportunity to reduce the cost of hydrogen compression while simplifying the release of oxygen to the atmosphere (should operation at such high pressures in the electrolyser be achieved).

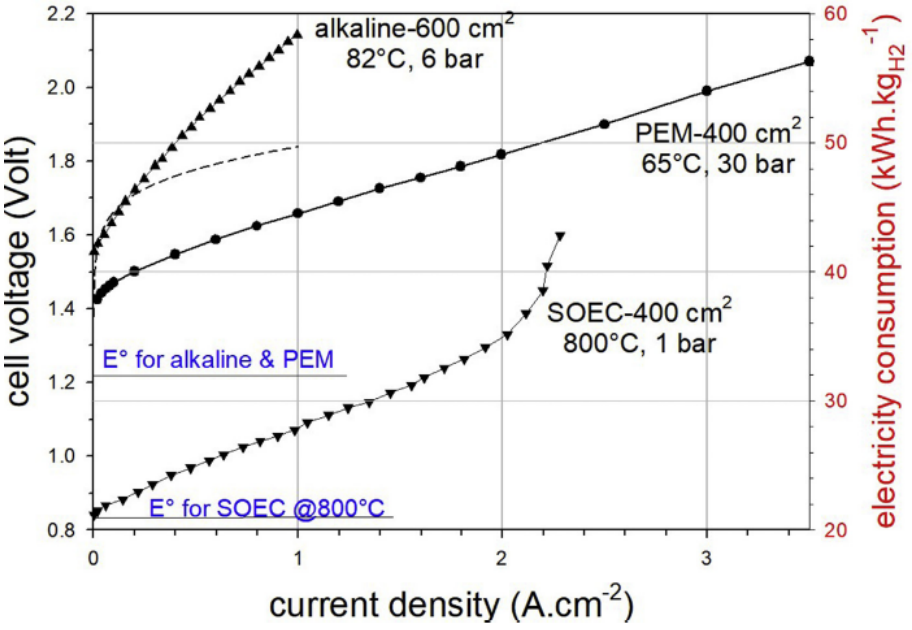

Figure 2.12: Comparison of representative experimental $V-i$ curves of AEC, PEM and SOEC water electrolysis cells. [36].

Regarding SOECs, the free energy voltage E° is much lower, for thermodynamic reasons, yielding much higher efficiency. The slope of $V-i$ curves is caused mostly by the conductivity of ceramic materials until concentration overpotential kicks in at high current density. Nevertheless, even though this technology seems promising from a thermodynamic standpoint, highly efficient and suitable for cogeneration applications, the extreme operating conditions still pose a challenge for materials both in terms of durability and costs. In this latter regard, efforts are being made to reduce the CapEx of SOECs (>2000€/kW today).

2.3.4 Outlook of water electrolysis

In this section, the limitations and challenges of the different water electrolyser technologies are discussed. In general, it can be stated that the R&D-related drivers of the technology are, in one way or another, aimed at reducing CapEx (for instance, increasing current density, finding cheaper materials with wider availability, etc.) and OpEx (for instance, increasing efficiency, enabling operation at high pressure, etc.).

For Alkaline electrolysers, the main research pathways are [37]:

- Development of zero-gap technology, increasing compactness, reducing ohmic losses and increasing current density.
- New advanced diaphragm materials that allow higher operational flexibility [38] while keeping hydrogen purity high.
- Development of high-temperature alkaline water electrolysers. Working temperatures

up to 150°C increase the electrolyte conductivity and promote the kinetics of the electrochemical reactions on the surface of the electrode.

- Development of advanced electrocatalytic materials to reduce electrode overvoltages. The anode is especially challenging because the oxidation half-cell reaction is the most demanding one; cobalt oxides are being considered for the anode.

Table 2.7 summarises the current state-of-art (based on 2014 data), the target imposed for this decade (2020-2030) and the goals that need to be achieved for the implementation of the technology at a large scale.

	Property	Unit	2020	Target 2020-30
Stack	Operating current density	[A cm^{-2}]	0.6 – 0.8	>0.8
	Operating temperature	[°C]	40 – 90	Ambient to 150
	Operating pressure	[bar]	1 – 30	1 – 100
	Cobalt contained in catalyst	[mg/W]	3.4	0.7
System	Durability	[h]	100,000	>100,000
	Degradation rate	[%/1000h]	0.12	0.10
	Cyclability	[-]	Poor	Improved
	Energy consumption	[kWh/$Nm^3 H_2$]	4.5	4.3
	Equipment cost	[€/kW][1]	600	400

[1] 100 MW production volume for a single system supplier is considered, and the system is assumed to operate stably for 10 years. The system is installed at a site with properly constructed foundations. This equipment cost includes transformers and rectifiers, but it does not include the cost of replacing the stacks.

Table 2.7: Outlook of alkaline electrolysis cells. Updated from [12, 39, 40, 41].

PEM water electrolysis technology has already achieved (enthalpy based) efficiencies of up to 80 – 85% (referred to the high heating values of hydrogen) and it has not been only proved at lab scales (with up to 1 A/cm^2) but also in industrial projects. However, the main challenge that this technology is still facing nowadays is the upscaling to the industrial size of a single stack (minimum of 10 kg H_2/h), for which higher current densities and durability are needed. In addition, the replacement of catalysts based on Platinum and expensive SPE [42, 43] remains a challenge that is making it difficult to reduce the capital cost of the technology to the levels arguably accepted by the market for large-scale deployment (US$ 500/kW). In addition to cost, the high sensitivity of Platinum to being poisoned by trace amounts of mineral and organic impurities found in the feed water [44] is also calling for solutions/alternatives. The performance of state-of-art and future PEM electrolysers is summarised in Table 2.8.

R&D activities in the area of PEM electrolysers are focused on:

- Reduction of the Iridium loading at the anode by developing stable catalyst carriers or allowing Ruthenium with Iridium and an inert oxide [12].

- Reduction of the Platinum loading at the cathode using carbon carriers and/or specifying printing methods such as screen printing [12, 45].

	Property	Unit	2020	Target 2020-30
Stack	Operating current density	[A/cm^2]	2.2 – 3.0	> 3
	Operating temperature	[°C]	50 – 75	80 – 120
	Operating pressure	[bar]	1 – 80	1 – 350
	Enthalpy efficiency with PGM catalyst	[-]	80% at 1A/cm^2	80% at 2 A/cm^2
	Enthalpy efficiency with non-PGM catalyst	[-]	30-40% at 1 A/cm^2	60% at 1 A/cm^2
	SPE voltage drop	[mV at 1 A/cm^2]	150	100
	SPE ionic conductivity	[S/cm^{-1} at 80° C]	0.17	0.20
	SPE gas permeability to H_2	[cm^{-2} s^{-1} Pa^{-1}] (80°C, full humidity)	10^{-11}	10^{-9}
	Cathodic PGM (Pt) content	[mg/cm^2]	1.0 – 0.5	0.5 – 0.05
	Anodic PGM (Ir, Ru) contents	[mg/cm^2]	1.0 – 2.0	0.5 – 0.1
	Degradation rate	[%/1000h]	0.19	0.12
System	Durability	[h]	30,000-90,000	> 100,000
	Energy consumption	[kWh/Nm^3 H_2]	4.9	4.5
	Equipment cost	[€/kW]	1000	500 – 700
Others	Hot[1]/ Cold[2]start	[sec]	2/30 1/10	
	Footprint	[m^2/MW]	60-100	45

[1] The time needed to achieve full load operation from standby, reported for an outside temperature of 15°C.
[2] The time needed to achieve full load operation from standby, reported for an outside temperature of –20°C.

Table 2.8: Outlook of PEM electrolysis cells. Updated from [12, 39, 40, 41].

- Development of alternative Solid Polymer Electrolyte (SPE) (research is carried out mostly for PEM fuel cells but it can then be applied to [46]).

As said, SOEC is a promising high-temperature steam electrolysis process for the production of hydrogen. However, it is the least developed technology and extensive R&D is still needed to take it to the market at a relevant scale. Key issues of this technology relate to the demanding operating conditions, with materials exposed to large thermal stresses and potential degradation rates. Hence, the development of electrochemically efficient and chemically stable SOECs with minimal thermal stresses (differential strains) is very important in the path to commercialisation. Research is hence mostly focused on:

- Improvement of the protonic conductivity of electrolytes as they feature higher production rates of pure hydrogen, minimal oxidation of Nickel, and lower operating temperature than conventional oxygen-ion-conducting SOECs [47].

- Development of recuperative FC/electrolysers systems with the same working principle and similar designs to existing SOECs/SOFCs [48, 49].

	Property	Unit	2020	Target 2020-30
Stack	Operating temperature	[° C]	800 – 900	600 – 700
	Operating pressure	[bar]	1	1 – 30
	Operating current density	[A/cm^2]	2	> 2
	Area specific resistance	[Ω cm^2]	0.3 – 0.6	0.2 – 0.2
	Degradation rate	[%/1000h]	2.8 – 1.9	0.5
System	Energy consumption	[kWh/kg H_2]	41 – 40	37
	Durability	[h]	10,000 – 25,000	> 50,000
	Load cycles	[-]	Unknown behaviour	10,000
	Start-up times	[h]	12	1 – 6
	Shutdown time	[-]	Few hours	Few minutes
	Start-up/shutdown cycles	[-]	< 10	100

Table 2.9: Outlook of solid oxide electrolysis cells. Updated from [12, 50].

The performances of state-of-the-art and future SOECs are reported in Table 2.9. The following research areas are identified for the future development of the technology:

- Achieve higher current densities whilst maintaining or increasing enthalpy-based efficiency to enable smaller footprints and higher hydrogen production rates.

- Replace expensive or unavailable materials with the aim to reduce CapEx (market requirements is ~US$500/kW) and facilitate the wide deployment of water electrolysers to produce hydrogen while also increasing durability.

- Find stable materials experiencing low degradation to allow highly flexible systems with cycling capabilities (start-up/shutdown), hence integration with RES.

2.4 Hydrogen roadmap. Main projects

In July 2020, the European Commission unveiled its plans to promote green hydrogen. However, low-carbon hydrogen derived from fossil fuels, such as that produced through SMR with CCS - so-called blue hydrogen-, will be also supported by the "Hydrogen Roadmap Europe" plan [51]. In addition to this, some member states in Europe have also developed their own hydrogen roadmap in order to set specific, concerted actions aimed at accelerating the deployment of hydrogen technologies towards the decarbonisation goal to be achieved by 2050.

"Hydrogen Roadmap Europe" is the driving plan for all EU member states. This plan has set the following main targets for the next 30 years:

- From 2020 to 2024, the Commission's objective is to support the installation of renewable hydrogen electrolysers with a total installed capacity of 6 GWe in the EU, in order to produce up to 1 million tonnes of green hydrogen.

- From 2025 to 2030, hydrogen needs to become an intrinsic part of Europe's integrated energy system with at least 40 GWe capacity of renewable hydrogen electrolysers, producing of up to 10 million tonnes of green hydrogen in the EU.
- From 2030 to 2050, the aim is for green hydrogen technologies to reach maturity and be deployed at large scale across all hard-to-decarbonise sectors, such as the chemical and steel-making industries.

Achieving these targets will also bring collateral results:

- Unlock a market of EUR ~150 Bn and ~1 M jobs with up to EUR 55 Bn annual sales by 2030.
- Construction of ~3740 refuelling stations by 2030.
- ~8M hydrogen vehicles sold per year by 2050.
- Hydrogen could provide up to 24% of the total energy demand by 2050 (~2,250 TWh).
- A 10-18% share of building heat and power in Europe could be provided by hydrogen by 2050.
- Potential to generate a share of up to 23% of high-grade heat for the industry by 2050.

Along with these measures, the Spanish government also approved a national hydrogen roadmap in October 2020, setting major goals for 2030, with a mid-step in 2024 [52]. This document plans four areas of action (regulation, implementation of proposals, public awareness, and R&D) with a total of 60 measures. The most tangible measures are:

- 4 GWe of green hydrogen electrolysers by 2030 (300 to 600 MWe in 2024), a share of 10% of the capacity targeted by Europe.
- 25% of the hydrogen consumed by the industry should be green by 2030.
- Regarding hydrogen transportation, implementation of 150 buses, 5,000 small-medium vehicles, and at least 2 commercial train lines by 2030. Achieving this will also require the construction of, at least, 100 hydrogen refuelling stations (as of 2023, 20 stations are already in service, with another 12 in construction [53]).

The commitment and engagement of public and private stakeholders is needed to achieve all the goals set by the European Union and the member states, through participation in research actions funded by both public institutions and the industry. Some of the projects and research activities in this area are listed below:

- **NextMGT**. The EU-funded NEXTMGT project aims at the development of technical expertise and scientific knowledge of the fundamental design and operational aspects of micro-gas turbines (MGT) technology, including the development of components and systems for decentralised energy systems running on hydrogen.
- **HYFLEXPOWER**. The EU-funded HYFLEXPOWER project will develop and operate the first fully integrated power-to-hydrogen-to-power power plant at an industrial scale, including an advanced dry-low emissions hydrogen gas turbine.

- **HYSTOCK**. The project developed by EnergyStock, a subsidiary of the Dutch gas transmission system operator Gasunie, is the first power-to-gas facility in the Netherlands. The project consists of a 1 MWe PEMEC together with a 1 MWe solar photovoltaic farm that will supply part of the electricity required to generate hydrogen from water [54].

Apart from these projects, there are many more involving all the areas that are needed to build a hydrogen economy able to decarbonise the current energy system. More information about these projects can be found on the website of the International Energy Agency [55], including a dataset with all the projects to produce hydrogen for energy or climate-change-mitigation purposes commissioned worldwide since 2000.

2.5 Barriers for scaling-up hydrogen production

Urgent actions are needed to achieve net-zero targets, and hydrogen can be part of the solution. Indeed, hydrogen has a very large potential to become the most cost-efficient, low-carbon solution for several applications in the short term, later expanding into other end uses. Nevertheless, at the same time, the cost-effectiveness of hydrogen technologies can only be achieved with initial political and financial support from public and provate stakeholders. Governments are already increasingly including hydrogen in their energy mix strategies and investment plans have been announced. However, there are three major areas for which coordinated and well-funded actions are needed: investment, policy alignment and market creation.

Substantial investment is needed due to the higher cost of hydrogen than, for instance, fossil fuels. Reaching the market volume required to significantly reduced costs calls for large-scale funding to accelerate the maturity of the technology. This is a known path since similar strategies to what is needed nowadays for hydrogen were already adopted for solar PV and wind power until these technologies were cost-competitive against conventional fossil-fuel technologies. Areas in need of investment have already been identified in the “Hydrogen Roadmap Europe” document [51].

In addition to investments and policy support, there is a need for the creation of a hydrogen market, built upon 5 levers: reducing demand uncertainty, scaling applications with the largest cost improvement per dollar invested, deploying complementary solutions to spark virtuous cycles, designing distribution networks to maximise utilisation and scaling up production to drive down supply costs.

The benefits of scaling up the hydrogen economy extend beyond its head-to-head cost competitiveness. Hydrogen can play a crucial role in securing governments’ energy security goals, and its relative abundance creates opportunities for new players to emerge in the energy supply and for new job creation to simulate the global economy.

2.6 Conclusions

In this chapter, the author provides a comprehensive overview of the current state of water electrolysis. The review covers various methods of hydrogen production and emphasises the theoretical concepts and modelling of water electrolysis. Furthermore, a thorough examination of existing technologies for water electrolysis is conducted, including Alkaline, Proton-Exchange Membrane, and Solid Oxide electrolysers (as shown in Table 2.6).

From a global perspective, there is no doubt that PEMEC offers certain advantages that make it well-suited for hybridisation with intermittent renewable energies. However, it is crucial to deeply consider whether the electrolyser should be directly connected to a renewable source or connected to the grid where fluctuations may be minimal. In the latter case, AEC might be a preferable option due to its robustness and cost-effectiveness. Additionally, SOEC is still in the developmental stage, with only initial industrial pilot projects underway. If waste heat is available and this technology reaches commercial maturity, SOEC has the potential to be a game changer due to its high efficiency in large-scale hydrogen production.

The integration of water electrolysis with the concept of hydrogen storage is a crucial process considering the substantial energy demand for hydrogen production. In the subsequent steps, the concept of water electrolysis will be incorporated into a chemical energy storage process, and its suitability for various applications will be evaluated in different scenarios.

3 Power-to-Power

Hydrogen is proposed as the future energy carrier that will help decarbonise highly energy-intensive applications, not only because it can be used as a fuel (energy carrier) in applications where electrification is difficult, but also because it can store large amounts of renewable energy for long periods of time. Power-to-H_2-to-X is a process whereby surplus renewable power is converted into chemical energy in the form of hydrogen through electrolysis of water, then stored in either solid, liquid or gas state, and eventually consumed for mobility, power or heat generation through fuel cells, gas turbines, or boilers. Interestingly, P2P energy storage systems are applicable where renewable power and water are available, independently from specific geographic features, unlike other high-capacity energy storage systems such as pumped hydro-electric or compressed air. A review of this technology as well as a preliminary thermodynamic study of this solution is provided in this chapter.

The contents of this chapter are partially available in:

A. Escamilla, D. Sánchez, L. García-Rodríguez, 2022, *Assessment of power-to-power renewable energy storage based on the smart integration of hydrogen and micro gas turbine technologies*, International Journal of Hydrogen Energy, Vol. 47, Issue 40, pp. 17505-17525.

Poster: A. Escamilla, D. Sánchez, L. García-Rodríguez, Micro-Gas Turbines for Chemical Energy Storage Poster, in: ASME Turbo Expo 2021: Turbomachinery Technical Conference and Exposition.

Tutorial of Basics (ToBs): T. Allison, N. Smith, A. Rimpel, A. Escamilla, D. Sánchez. Grid-Scale Energy Storage Systems and Technologies, in: ASME Turbo Expo 2022: Turbomachinery Technical Conference and Exposition.

3.1 Introduction

The Hydrogen (H_2) economy is flourishing as a consequence of the high penetration of Renewable Energy Sources (RES) into the energy mix of different regions. The installed renewable energy capacity worldwide doubled in the last decade (2010-19) [56], led by wind and solar (photovoltaic), which represented 75% of the new installed capacity respectively. Both wind and solar energies are characterised by being Variable Renewable Energy (VRE). VRE, in contrast with continuous/dispatchable renewable energy, is characterised by being an

intermittent source of energy whose availability (therefore power generation) depends mainly on the weather conditions at the plant's site. Hence, with very limited options for large-scale energy storage and with the growing penetration of VRE into the energy mix, energy systems still need to rely on conventional non-renewable energy sources to generate power. In other words, large-scale energy storage stems as one if not the most pressing technical challenges towards achieving carbon neutrality by 2050.

Nowadays, only two large-scale energy storage systems have achieved high maturity. These are Pumped Hydroelectric Storage (PHS) and Compressed Air Energy Storage (CAES). However, both of them are restricted to places where specific geographic features are found, such as available basins at different altitudes for PHS and salt caverns for CAES. Hence, their wide deployment is just not possible.

Chemical energy storage, a system that converts primary or secondary energy into energy carriers with high energy density, has gained interest in recent years. This is a consequence of the increasing development of water electrolysis technology and the penetration of RES in the energy mix. It is now possible, from technical and economic standpoints, to produce hydrogen through water electrolysis activated by renewable energy [57]; this is termed Power-to-Hydrogen. The main advantage of this energy storage technology is that hydrogen is a convenient energy carrier, such that it can be stored, transported, and converted into other forms of energy, such as mechanical or electric power or heat (Power-to-Hydrogen-to-X). Unlike PHS and CAES, hydrogen can be produced *in-situ* as long as electric power and water can be supplied. This is very interesting for sectors where decarbonisation through electrification is challenging as they can benefit from P2X energy storage: long-distance transportation, power generation, highly energy-intensive industries, etc.

In recent years, many studies on this topic have been conducted, aiming to prove the concept experimentally at a moderate scale. About 143 power-to-gas projects producing either hydrogen or methane have been in operation since 1988, 64 of them in Germany, most of which were pilots or demonstration projects under 1 MWe [58, 59]. The number of active Power-to-Hydrogen projects was 56 in 2019, with a total installed capacity of 24.1 MWe [58]. The political commitment to the energy transition based on Hydrogen is reflected in the adoption of hydrogen technology road-maps for the next 30 years [51, 60, 61, 62].

At the end of 2018, the production of hydrogen worldwide amounted to 74 Mt only, over 97% of it grey hydrogen, used for refineries and for ammonia production [40, 63]. By 2050, the expected hydrogen production worldwide will be 240 Mt (29 EJ) [63], and this will imply that hydrogen plays a key role in the future mobility, power and heat industries; this will require substantial efforts, for instance, an annual installation rate of around 50 to 60 GWe electrolyser capacity. Nonetheless, even if this were possible, it would still cover 7.5% of the global energy demand worldwide only.

The scaling up of hydrogen technologies opens up many opportunities for industrial sectors immersed in the energy transition as shown in Figure 3.2. In this figure, a total of 22 applications where hydrogen can become a cost-effective low-carbon solution before 2030 are identified [57]. For this to become a reality though, large investments of around USD 70 Bn

are required, and this must be accompanied by complementary actions for policy alignment whereby governments can level out the playing field: National strategies, Coordination, Regulation, Standardisation, Infrastructure and Incentives. In addition, all this needs to come in parallel with both creating the hydrogen demand and establishing a hydrogen market. Further to this, the cost-effectiveness of hydrogen technologies can be enabled from the following specific areas of work: market uncertainty reduction, boosting of technologies with the largest "improvement-for-investments", development of hybrid solutions, increasing utilisation rates in distribution networks and blue/green hydrogen investment.

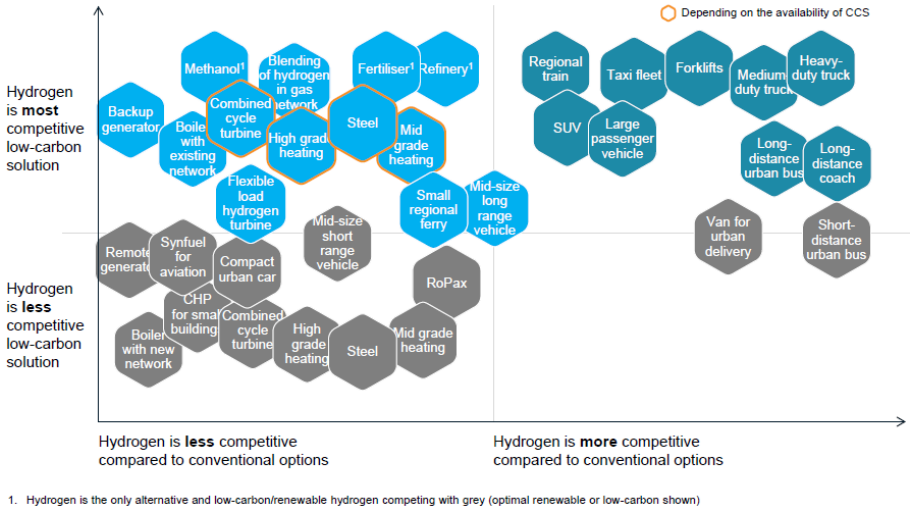

Figure 3.1: Competitiveness of hydrogen applications versus low-carbon and conventional alternatives. *Courtesy of the Hydrogen Council [57].*

The main research topics for P2P solutions can be divided into hydrogen production, storage and consumption. On the production side: direct coupling of variable renewable energy sources and electrolysers, high-temperature electrolysis, footprint reduction and more resistant materials with lower costs. For hydrogen storage: higher storage capacity at high pressure (>60kg H_2 at >700 bar), solid storage in the form of metal hydrides, utilisation of NG-H_2 blends in the gas distribution grid. For power generation: hydrogen combustion, high-temperature fuel cells, hybrid systems (control, power electronics, and other auxiliary systems).

In this chapter, different hydrogen production technologies are presented first, focusing on water electrolysis. Then, different strategies to store hydrogen, and transport it in case production and consumption do not take place in the same location, are introduced. This is followed by an assessment of the different end-uses of hydrogen and the technologies associated with each of them. This is used in the final section of this chapter, where an exhaustive thermodynamic analysis is presented to assess the potential to increase the round-trip efficiency of power-to-power systems based on micro-gas turbines.

3.2 Review of Power-to-Hydrogen-to-Power systems

Power-to-Power (P2P) is a process whereby (surplus) renewable energy is stored as chemical energy in the form of hydrogen, which can then be used *in-situ* or transported to the consumption node. When energy is needed again, hydrogen can be used as a fuel for power generation in either thermo-mechanical (i.e., heat engines) or electrochemical (i.e., fuel cells) devices. Four separate processes can hence be identified to assess energy losses of the entire setup: production, storage, transportation and power generation (Figure 3.2). When hydrogen is used for power production, the term P2P is used.

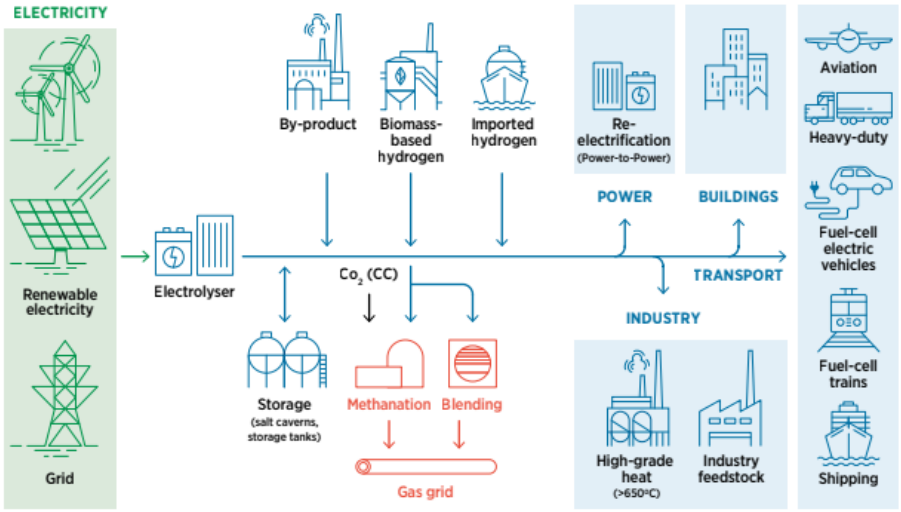

Figure 3.2: Power-to-X solutions [64].

Figure 3.3 shows the Technology Readiness Level (TRL) of the different processes involved in the energy conversion steps in a power-to-hydrogen-to-x solution. It is worth highlighting that, even if some of these processes are already mature because hydrogen has been used as feedstock for a long time in very specific applications, most of the processes are still in a demonstration phase. The next subsections will discuss this further, considering four different areas: hydrogen production, storage, transportation and consumption.

3.2.1 Hydrogen production

Hydrogen cannot be found as a free molecule on Earth but, rather, as forming part of other compounds. Many different processes have been researched to produce hydrogen molecules, H_2, but only a few of them have achieved been taken to high technology readiness level. All hydrogen productions share the need to have an energy supply (electrical, thermal or both) so it is common to classify hydrogen according to the origin of this energy. In practice, this translates into a colour scale [40]:

- ***Brown hydrogen***: coal is used as primary energy source (19 tCO_2/tH_2).
- ***Grey hydrogen***: natural gas is used as primary energy (11 tCO_2/tH_2).

Figure 3.3: Technology readiness level of technologies along the hydrogen value chain [65].

- ***Blue hydrogen***: same as grey hydrogen but incorporating Carbon Capture and Sequestration (CCS) (0.2 tCO_2/tH_2).
- ***Green hydrogen***: renewable energy sources are used as primary energy sources, mostly to drive electrolysis (potentially zero GHG emissions).

The worldwide demand for pure hydrogen was around 70 Mt in 2020, mostly for the oil refining and chemical industries [40]. Virtually all of this hydrogen was produced from natural gas and coal, thus the associated CO_2 emissions were significant. Actually, grey hydrogen based on methane reforming has historically been the least expensive and most mature technology

to produce hydrogen, featuring 5 to 8 times lower production costs than green hydrogen [40, 63, 57]. With many more applications set to use hydrogen in the future, the demand for pure hydrogen is foreseen to rise steadily over the next decades, with blue and green hydrogen setting to lead hydrogen production to ensure carbon neutrality in 2050. Nevertheless, considering the sustainable goals for 2050 set forth in the *Paris Agreement* [2], only green hydrogen will be further considered in the next sections.

The selection of an optimum electrolyser technology depends on the working conditions of the electrolyser, mostly temperature and pressure, and the nature of the application, such as continuous or intermittent power supply. As already discussed in Chapter 2, three main electrolyser technologies are considered today: AEC, PEMEC and SOEC. Table 3.1 presents technical specifications taken from Original Equipment Manufacturers (OEMs) of different types of electrolysers, in order to provide accurate information about the current state of the art of the technology. Not only the power consumption and energy losses of the stack are considered, but also the power consumption of the auxiliary systems, such as pumps, and energy losses of other components, such as the converter. Labels are assigned to each electrolyser model as this will be used in later sections in this chapter.

3.2.2 Hydrogen storage

Hydrogen, as an energy carrier, can be stored in different ways and for as long as needed. Nonetheless, the storage period for which hydrogen is most attractive as energy storage media is in the order of days to months. There are many options for shorter storage times but not as many for longer periods.

Hydrogen is the fuel with the highest density but it features one of the lowest mass volumes at ambient conditions among conventional fuels. This latter characteristic is typically overcome through the utilisation of different storage strategies, either in the form of gas, liquid or solid. Unfortunately, most of these storage processes are highly energy intensive, therefore reducing the final round-trip efficiency of the energy storage system.

Figure 3.4 shows the different energy densities of hydrogen at different conditions and also other fuels with similar applicability. The energy density of hydrogen at ambient conditions, as compared to others such as methane, ethanol or ammonia, reveals the challenges presented to storing hydrogen energy efficiently. From this information, it is concluded that hydrogen storage remains one of the most, if not the most, critical processes for the deployment of an energy market based on hydrogen.

Compressed-gas H_2

Compressed H_2 is the most usual method to store and distribute hydrogen in relatively small quantities, 5 to 10 kg/H_2 per vessel. The pressure to which hydrogen is compressed depends on whether or not it is transported and on the final application where it will be used. Keeping in mind that the higher the target pressure, the higher the capital and operational expenditures, a balance between the storage volume needed (footprint) and costs must be found. Hence, in mobility applications such as cars or forklifts, the availability of storage volume is limited and

Type	Label	OEM	Model	P_{output} [bar]	H_2 Prod. [Nm^3/h]	System Consump. [kWh/kg H_2]
AEC	A1	SunFire[66]	HYLINK	30	1090	52.3
	A2	Enapter[67]	EL 2.1	35	0.5	53.4
	A3	Green Hydrogen[68]	A30	35	30	52.2
	A4		A60		60	52.2
	A5		A90		90	53.6
	A6	McPhy[69]	Baby	1	0.4	83.5
	A7		P	1 - 2.5	0.5 - 0.8	66.8 - 62.6
	A8		M	1 - 2.5	2.4 - 4.4	64.9 - 65.7
	A9		H	4 - 8	3 - 10	66.7
	A10		McLyzer 10-30	30	10	55.6
	A11		McLyzer 20-30		20	
	A12		McLyzer 100-30		100	
	A13		McLyzer 200-30		200	
	A14		McLyzer 400-30		400	
	A15		McLyzer 800-30		800	
	A16	Nel Hydrogen[70]	A150	1 - 200	50-150	42.3[a]- 49.0[a]
	A17		A300		150-300	
	A18		A485		300-485	
	A19		A1000		600-970	
	A20		A3880		2400-3880	
PEMEC	A21	Nel Hydrogen[70]	S10	13.8	0.27	67.9
	A22		S20		0.53	
	A23		S40		1.05	
	A24		H2	15 - 30	2	81.2
	A25		H4		4	77.9
	A26		H6		6	75.7
	A27		C10		10	69.0
	A28		C20		20	66.8
	A29		C30		30	64.5
	A30		M100	30	103	50.4[1]
	A31		M200		207	
	A32		M400		413	
	A33		M4000		4000	
	A35	ITM Power[71]	HGAS1SP	20	0.99	63.6
	A35		HGAS2SP		1.98	63.2
	A36		HGAS3SP		3.24	65.3
	A37		HGASXMW		15.17	59.7
	A38	Hydrogenics[2][71]	HyLYZER 300	30	300	53.4
	A39		HyLYZER 1000		1000	
	A40		HyLYZER 5000		5000	
SOEC	A41	SunFire[66]	HYLINK	1 - 40[3]	750	40.0

[1] Power consumption provided by the manufacturer accounts for the stack only.
[2] Hydrogenics has been acquired by Cummins.
[3] After compression.

Table 3.1: Commercial availability of electrolysers.

therefore very high pressure is needed to increase the density of hydrogen (≈ 700 bar). On the opposite, in stationary applications such as small auxiliary power systems, the availability of storage volume is usually not as critical and lower hydrogen volume densities are acceptable (150 bar to 500 bar).

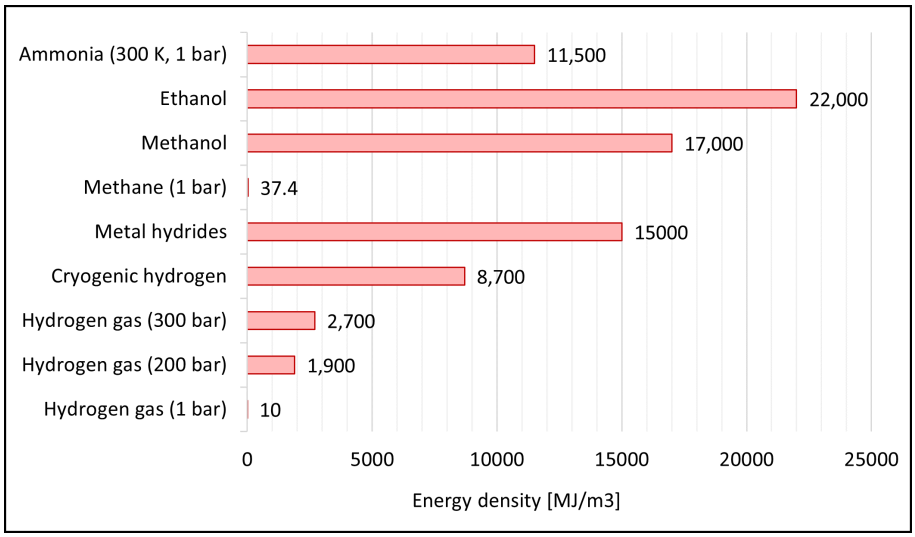

Figure 3.4: Volume energy density of different fuels [50].

Given the usual pressure of hydrogen at the exit of the electrolyser (Table 2.6), compressors are required to take this gas to the final storage pressure. These compressors deal with high-pressure ratios, often higher than 30, which limits the availability of equipment suitable for the application. Diaphragm compressors efficiently compress small to medium flow rates of hydrogen to high and, if required, even extremely high pressures of more than 5000 bar [72]. The diaphragm principle ensures oil- and leakage-free compression with excellent product purity. However, the lifetime of the diaphragm is potentially reduced when the operation is intermittent, which increases maintenance costs. Thus, when subject to variable operating conditions, hydraulically-driven, dry piston compressors can be a better alternative. These also enable very high pressures of up to 3000 bar [72] with also oil, leakage and technically abrasion-free compression.

The operating pressure and temperature of the electrolyser are key parameters for determining compressor power during the downstream compression of H_2 for storage since these are the inlet pressure and temperature of the storage compressor. Figure 3.5 shows the adiabatic power consumption of compression stations with different layouts and considering that hydrogen is available at 30 bar and 40°C at the outlet from the electrolyser (Table 3.1). Due to the high pressure ratios that the compressor is to deliver, the compressor is arranged in several stages with intercooling in between them in order to keep the overall process as isothermal as possible. This helps reduce compression work and reduces thermal stress on the components. The pressure ratio per compression stage in a typical hydrogen compression station can be estimated according to the following guidelines [73]:

- Maximum pressure ratio per stage is 4:1.
- Maximum outlet temperature per stage is 420 K. Compliance with this constraint can be ensured by decreasing inlet gas temperature or by increasing stage count.

The number of stages and specific compressor work can be estimated from Eqs. (3.1-3.2) [74]),

$$n_{stages} = \frac{\log \frac{P_2}{P_1}}{\log PR_{stage}} \tag{3.1}$$

$$W_{compressor} = n_{stages} \cdot \frac{\frac{n}{n-1} \cdot R \cdot T_1 \cdot Z_{avg} \cdot PR^{\frac{n-1}{n}} - 1}{\eta_{compressor}} \qquad [\text{kWh / kg } H_2] \tag{3.2}$$

where:

- P_1 and P_2 are the inlet and outlet pressures of the compressor.
- PR is the stage pressure ratio.
- n is the polytropic coefficient, 1.41 for hydrogen.
- R is the universal gas constant, 8.314 [J/mol/K].
- Z_{avg} is the average compressibility factor across the compressor.
- n_{stages} is the number of stages.
- $\eta_{\text{compressor}}$ is the efficiency of the compressor.

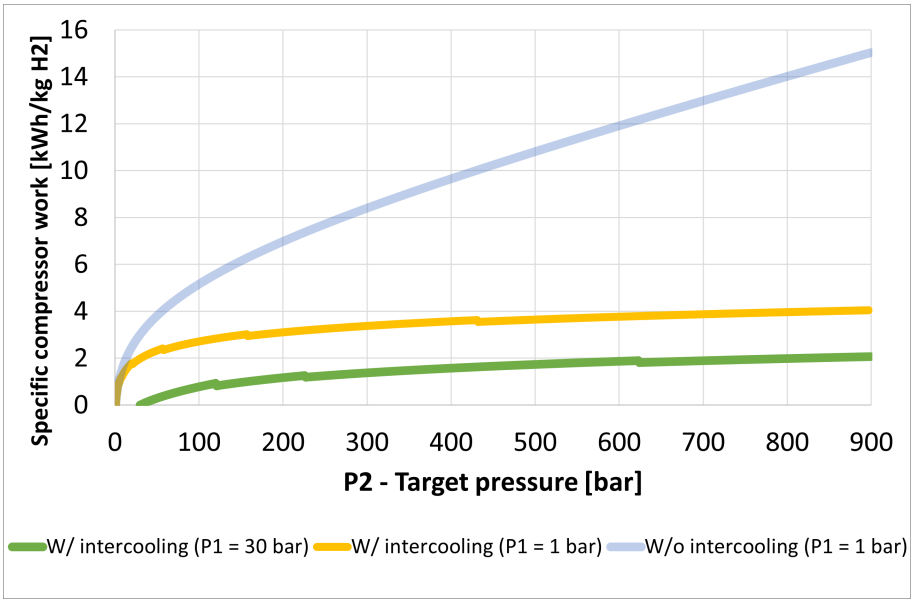

Figure 3.5: Hydrogen compression work for several compression layouts and initial pressures.

In addition to the specific work of the compressor, the work needed to drive the cooling water pump must also be calculated in order to obtain the total power consumption of the hydrogen compression station [74]. Figure 3.6 shows the assumptions made to obtain these estimates.

$$\frac{\dot{m}_{H_2O}}{\dot{m}_{H_2}} = \frac{h_{1_{H_2}} - h_{2_{H_2}}}{h_{2_{H_2O}} - h_{1_{H_2O}}} \qquad [\text{kg/s } H_2O \text{ / kg/s } H_2] \tag{3.3}$$

$$W_{\text{pump}} = n_{\text{stages}} \cdot \frac{g \cdot H \cdot \frac{\dot{m}_{H_2O}}{\dot{m}_{H_2}}}{\eta_{\text{pump}}} \qquad [\text{kWh / kg } H_2] \tag{3.4}$$

where:

- h refers to the mass enthalpy of H_2O and H_2 at the inlet (1) and outlet (2) to/from the intercooler [J/kg/K].
- $\dot{m}_{H_2}$ and $\dot{m}_{H_2O}$ are the corresponding mass flow rates [kg/s].
- g is the gravitational acceleration, estimated at 9.81 [m/s^2].
- H is the head of the pump [m].
- η_{pump} is the efficiency of the pump [%].
- The pressure ratio between the hot (hydrogen) and cold (water) sides of the heat exchangers is set to 10. Therefore, pressure on the hydrogen side is ten times higher than on the waterside. This assumption is considered when calculating the pump head for each intercooling system.

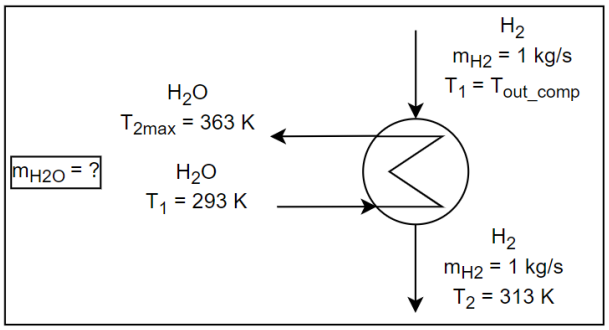

Figure 3.6: Assumptions to calculate the flow rate of cooling water in a H_2/H_2O intercooler

Table 3.2 shows the power requirement of the compression station for different cases, based on the calculations in Eqs. (3.2 and 3.4).

After compression, hydrogen is commonly stored in high-pressure vessels. Depending on the pressure at which hydrogen is stored, different types of vessels are used. The vessels are differentiated mainly by the materials and thickness of the walls. Table 3.3 presents the four types of pressure vessels considered in this research, along with their main characteristics.

Liquid Hydrogen

At ambient pressure, hydrogen is in the liquid state if the temperature is below 20.37 K [76]. Given that hydrogen production takes place at 1-30 bar and 303-343 K typically, Table 2.6,

Label	T_1 [K]	P_1 [bar]	$\eta_{compressor}/\eta_{pump}$ [%]	n_{stages} [-]	P_{target} [bar]	$w_{Compression\ System}$ [kWh/kg H_2]
B1	313	30	70/90	3	50	0.29
B2					350	1.48
B3					500	1.73
B4				4	700	1.89
B5					900	2.07

[1] Hydrogen temperature at the outlet from the intercooler is set to T_1 for all stages.

Table 3.2: Compressed-H_2 scenarios.

Type	Material	Pressure [kg/L]	Weight [bar]	Relative Cost[1]
I	All-metal construction, generally steel.	150 - 300	≈ 1.4	1.0
II	Mostly steel or aluminium with a glass-fibre composite overwrap in the hoop direction.	450 - 800	≈ 1.0	1.5
III	Metal liner with a full composite overwrap, generally aluminium, with a carbon fibre composite.	350 - 700	≈ 0.3 to 0.45	3.5
IV	An all-composite construction featuring a polymer liner with carbon fibre or hybrid carbon/-glass fibre composite.	350 - 700	≈ 0.3 to 0.45	3.5

[1] Cost relative to Type I.

Table 3.3: Types of high-pressure vessels [50, 75].

cryogenic processes are needed in order to liquefy hydrogen. Figure 3.7 shows a general layout of the different processes involved in a cryogenic plant:

- Precompression (at ambient conditions).
- Precooling (ambient to about 80 K).
- Cryo-cooling (80 K to 30 K).
- Liquefaction (30 K to LH_2 at 1 atm).

Losses along the LH_2 pathway are intrinsic to the utilisation of a cryogenic fluid. They occur when the molecule is transferred between two vessels (liquefaction plant to the trailer, trailer to storage station, storage station to pump or compressor, then fuel cell electric vehicles, ...) and when the fluid is warmed up due to heat transfer with the environment [78]. Nevertheless, in spite of the highly energy-intensive processes to liquefy hydrogen and of the auxiliary equipment to keep it at those conditions, the direct benefit of increasing hydrogen density, going from 0.083 kg/m^3 (at 1.013 bar and 295 K) to 76.2 kg/m^3 (at 1.013 bar and 15K), more than compensates for this [76].

Much optimisation has been done in the last decades with the aim of reducing the power consumption of the H_2 liquefaction plant. In literature, around 12 concepts tackling this have been published over the last decades, Table 3.4, some of which were built whilst others have only been studied with simulations. One of the most recent projects on this topic is the H2020 project IDEALHY [79], completed in 2013. The main outcome of this project was an innovative cryogenic hydrogen plant with a power consumption of around 6.7 kWh/kg H_2, which is almost half of the power consumption from already existing liquefaction plants [80]. Furthermore, recent investigations have already shown that lower power requirements of around 5.9 kWh/kg H_2 can be achieved with further optimisation [81, 82].

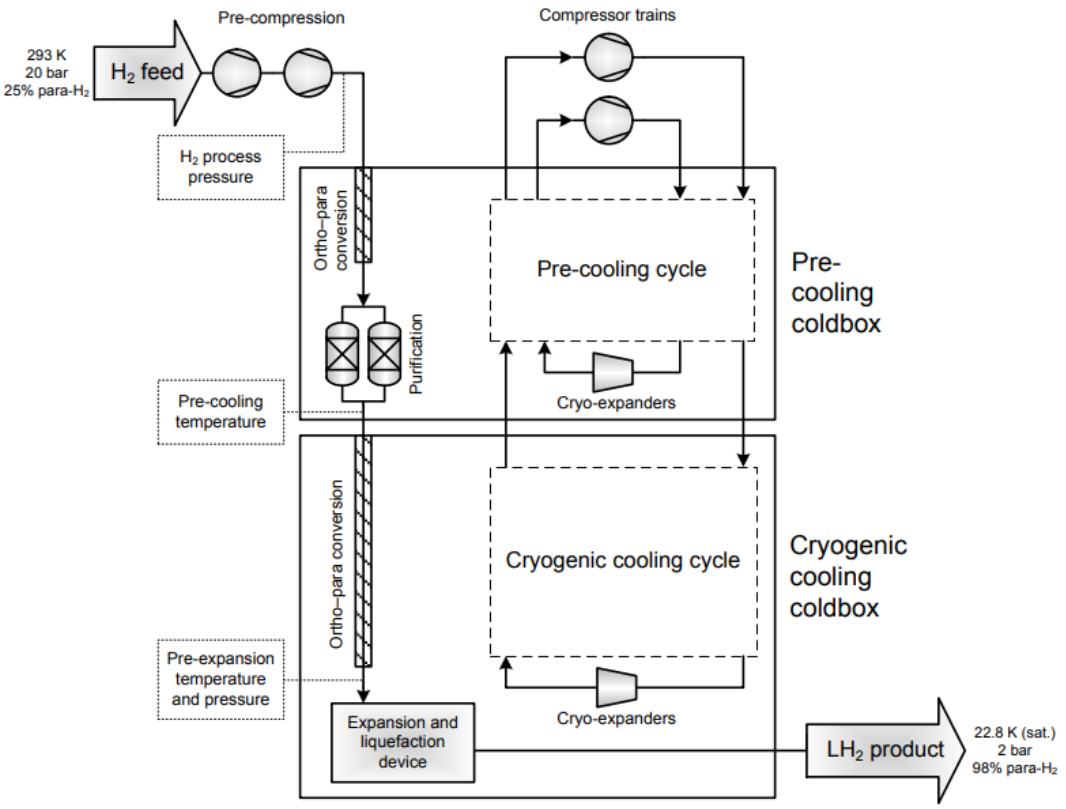

Figure 3.7: Generic process flow diagram of hydrogen liquefaction [77]. (*Copyright © IIF/IIR. Published with the authorization of the International Institute of Refrigeration (IIR): www.iifiir.org*)

Metal hydrides

The combination of metals or alloys with hydrogen leads to the formation of a new compound, named *Metal Hydride*. The new compound is characterised by its high mass volume, as shown in Figure 3.4, reaching values above 115 kg/m^3. The loading and unloading of hydrogen relies on chemical reactions and it is therefore influenced by thermodynamics and kinetics processes.

Metal hydrides can reversibly store (absorb) and discharge (desorb) large amounts of hydrogen, absorbing and releasing heat respectively during these processes. This process can be described by the following equation:

$$M_e + \frac{x}{2}H_2 \longleftrightarrow M_eH_x \qquad \text{, where M refers to a specific metal} \tag{3.5}$$

Many of the challenges posed by the utilisation of metal hydrides relate to the thermodynamics and kinetics of dehydrogenation, which determine the hydrogen discharge rate and associated heat release rate needed to desorb hydrogen efficiently from the metal hydride. These two parameters depend on the composition metal hydride of choice. It is very common to summarise all this information into a PCT diagram (pressure, composition, temperature).

Ref.	P_1 [bar]	T_{target} [K]	P_{target} [bar]	Power requirement [kWh/kg H_2]	Year	Built/Study
[83]	1.01	20.57	9.29	10.85	1978	Study
[84]	1.06	20.45	1.06	8.53	1997	
[84]	1.06	20.45	1.06	8.69	1997	
[84]	1.06	20.45	1.06	8.58	1997	
[85]	1.00	20.20	1.00	6.93	2001	
[86]	1.01	20.40	1.06	8.72	2004	
[87]	1.00	20.00	1.00	8.73	2008	
[88]	60.00	20.00	1.50	5.29	2008	
[89]	21.00	20.20	1.00	6.35	2010	
[82, 81]	25.00	22.80	2.00	6.00	2017	
[82, 81]	25.00	22.80	2.00	6.30	2017	
[90]	21.00	21.00	1.30	13.60	1992	Built
[80]	24.00	21.00	1.30	11.90	2007	

Table 3.4: Liquefied H_2 scenarios.

PCT diagrams summarise the concentration of hydrogen (C) in an MH at a certain pressure (P) and temperature (T), considering the system is at equilibrium. This shows the fundamental character of the hydrogen absorption ability of the MH alloy. Figure 3.8 shows an exemplary PCT diagram for a of given MH. The formation of an MH is characterised by three phases:

- α phase: at low hydrogen concentration, pressure needs to be increased significantly to enable higher absorption of hydrogen by the MH.
- $(\alpha + \beta)$ phase: remarkable increase in the hydrogen content at almost constant temperature and pressure is possible.
- β phase: all metal has been transformed into metal hydride. A further increase of the hydrogen content in the MH is only possible with high pressure increase.

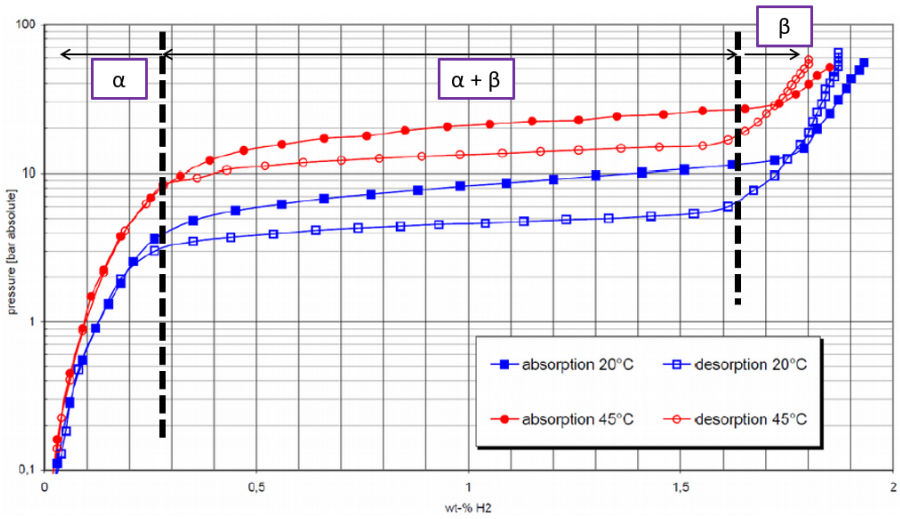

Figure 3.8: PCT Curve for a metal hydride storage. *Courtesy of h2planet [91]*

From the PCT diagram, it is deduced that it is possible to absorb and desorb hydrogen into/out of the MH through modification of temperature and pressure. Hence, if absorption is carried out at a low temperature, such as 20°C, and desorption at a higher temperature, such as 45°C, it is possible to increase the storage pressure in the MH, Figure 3.8. Therefore, in addition to storing hydrogen, MHs can also be used as hydrogen compressors. More information about metal hydrides can be found in the reference list [92].

Research has been conducted to find the different MHs available for H_2 storage. These options are typically characterised by low release rates but this can be solved by arranging several systems together. As far as this research is concerned, Table 3.5 shows the largest capacity MH systems available in the market.

Label	Manufacturer	Model	Capacity [Nm_3]	P_{charge} [bar]	$P_{discharge}$ [bar]	H_2 discharge rate [Nm_3/h]
B19	HBank [93]	HB-SS-3300	3.3	4-5	$> 0.1 \leq 2.0$	≤ 10 (25°C)
B20		HB-SS-16500	16.5	(25°C)	(25°C)	≤ 50 (25°C)
B21	Pragma Industries [94]	MH 7000he[a]	7.0	-	10 to 1	6.6
B22		MH 10000he[1]	10.0			9
B23	h2planet[2][91]	MyH2 7000	7.0	≤ 30	≤ 30	2 (25°C)

[1] Cooling water is needed. No more data is provided by the manufacturer.
[2] Personal communication with *h2planet*.

Table 3.5: Market availability of storage systems based on metal hydrides

3.2.3 Hydrogen transportation

Hydrogen can be produced locally or in centralised production facilities that can feed several consumption nodes. Having on-site hydrogen production has a positive impact on the round-trip efficiency of power-to-power systems since the (nonexistent) transportation process does not incur further energy losses. Additionally, if storage space is not constrained on-site, compressed-H_2 storage is the most common choice and it does not have to make use of very high storage pressures, therefore reducing energy losses too. However, the advantages of having a centralised hydrogen production that can serve several consumption nodes could potentially and largely improve the economics thanks to the exploitation of economies of scale, in particular when making use of renewable energy sources.

It is nevertheless found that hydrogen offers the possibility to create a more decentralised market concept where the production and consumption nodes are at the same location or nearby, hence avoiding the transportation of an energy carrier with such a low mass volume. Based on these trade-offs, it is not foreseen that hydrogen will be transported very long distances (>1000 km) but it will rather be consumed within a short distance from the production centres (<300 km). To this aim, the most common means of transportation are high-pressure tank trucks and gas pipelines; these solutions have proved to be efficient in the range of 300 km or lower. For larger distances, liquefied-H_2 is preferred due to the increase in mass volume, mostly to be transported by ships like liquefied natural gas (LNG).

Since H_2 transportation is foreseen mostly for short distances, both truck and gas pipelines

will be the two solutions analysed in the next sections.

Tube-trailers / Multi-Element Gas Container
Distribution of gases within short distances (< 300 km) is done mostly by truck. This has been common practice for gases such as hydrogen, oxygen, nitrogen, etc.; until today, using this to distribute hydrogen or other gases has worked well to cover low and moderate demands. However, if hydrogen is to take a much higher share of the energy transportation industry, distribution and transportation based on trucks is highly inefficient from energy and economic standpoints. This is due to the low mass volume of hydrogen which is around 20 times lower than other hydrocarbon fuels like petrol or diesel currently using trucks for this aim. An option would be to incorporate cryogenic systems in the trucks, in order to increase the mass volume of hydrogen, but this would have an additional economic and energy cost.

Two variables are used to pick the best way to transport hydrogen by truck, from the production to the consumption nodes: amount of hydrogen and distance. Table 3.6 shows the different volume capacities that can be transported per truck and per trip for different states of hydrogen. Interestingly, the table also shows the amount of hydrogen consumed during transportation, both to fuel the truck and the cryogenic process (if any) (H_2 consumption per kg of H_2 transported when travelling 200 km per trip).

H_2 State				**Capacity**	**Spec. fuel consump.[1] [200 km]**
[0.5ex] State	P [bar]	T [K]	ρ [kg/m^3]	[kg H_2/truck]	[kg H_2 consumed/kg H_2 transported]
Gas	200	288	15.0	605[2]	-
Gas	300	288	21.2	605[3]	0.0279
Gas	500	288	31.7	1135[4]	0.0141
Liquid	2	15	76.3	3815[5]	0.0042
Solid	-	-	$\approx$ 115.0	900[95]	0.0178

[1] Specific power consumption is calculated using the specific fuel consumption of different H_2 production scenarios reported in Table 3.1, the compression power in Table 3.2 (30 to 900 bar) and considering H_2 is transported by a Fuel Cell Electric Truck (FCET) which consumes 8 kg H_2/100 km.
[2] Considered an available volume of 26 m^3 with a tube-trailer configuration with Type I cylinder.
[3] Considered a volume available of 27 m^3 with a MEGC (Multiple Elements Gas Container) configuration incorporating a Type II cylinder.
[4] Considered an available volume of 35 m^3 with a tube-trailer configuration incorporating a Type IV cylinder.
[5] Considered an available volume of 50 m^3.

Table 3.6: Transportation capacity of a truck for hydrogen in different states.

Hydrogen pipelines
Hydrogen distribution through a pipeline that connects the production node with several consumption nodes seems to be the most secure supply in the long term. Nevertheless, pipeline transportation requires very high capital investments which, most likely, exhibit long payback times unless there is a continuous and large hydrogen flow through it.

The infrastructure of natural gas pipelines in Europe and North America is almost completely developed, with millions of km covering most metropolitan areas and small towns. Hence, the option to use the natural gas grid to distribute hydrogen seems a very attractive option.

However, due to the clear differences between hydrogen and natural gas, not only in density but also in thermal conductivity, viscosity, auto-ignition temperature, calorific value, embrittlement of metals and others, the introduction of a large share of hydrogen directly into the gas network is not possible and only small quantities of hydrogen are currently allowed. This is known as *hydrogen-blending* and it is limited to ~5%. Indeed, the limit of hydrogen content is not set by the gas infrastructure only but also by the end-users, in particular, the equipment making use of this blended natural gas. The criterion is not unified within regions, such as Europe, but each country does have different limits within their gas network and appliances. For instance, Germany allows a maximum hydrogen injection of 2%vol (increased to 10% under certain conditions) whereas this drops to 6%vol in France [96, 97]. *HyLAW* [96] is a project funded by the Europen Union whose main target is to boost the market uptake of hydrogen and fuel cell technologies providing market developers with a clear view of the applicable regulations, whilst calling attention to policymakers to the legal barriers to be removed. Through their website, they offer a database to show the different regulations for most European countries under several different subjects within the hydrogen chain.

Marcogaz, the technical association of the European natural gas industry, through a study carried out in 2019, revealed the maximum hydrogen content that can currently be used for systems that use primarily natural gas [98]. The study clarified this information for systems within these five gas-grid segments: transmission, gas storage, grid/pressure regulation and metering, distribution, and end use.

Table 3.7 shows that the maximum hydrogen content that the grid can take is, at most, 20%vol. Hence, adapting the natural gas grid infrastructure to increase the content of hydrogen would incur high costs associated with R&D as well as their subsequent implementation. The alternative solution is to include a "methanation" plant after the production of hydrogen, a process that combines carbon dioxide and hydrogen to form synthetic methane. The process is considered carbon-neutral since carbon dioxide is used for the methanation process and is later released when methane is burnt by the end-user. Hence, the overall process would be comprised of electrolysis, Eq.(2.2), and methanation, (Eq.3.6).

$$4H_2 + CO_2 \rightarrow CH_4 + 2H_2O \tag{3.6}$$

As stated at the beginning of the section, building an entire hydrogen gas network for transportation would incur an extremely high capital investment. Nevertheless, at a smaller scale, building a small hydrogen gas pipeline connecting the production centre with several consumption nodes that need a continuous supply of hydrogen might be a cost-effective alternative to hydrogen blending and methanation. Nowadays, there is more than 5,000 km of pure hydrogen pipelines installed in industrial hubs worldwide, 2600 of which are in the United States [99].

A study carried out by Naturgy [50] shows the emission of GHG for the distribution of hydrogen in the form of gas, by truck and pipelines, or liquid, by truck, as a function of distance. The emissions of greenhouse gases from hydrogen liquefaction are revealed as high pollutants, 60 $g_{CO_2,eq}/MJ_{H_2}$, whereas pipelines and compressed-H_2 have a much lower carbon footprint, 3 and 8 $g_{CO_2,eq}/MJ_{H_2}$ respectively. Over distance, both pipelines and LH_2 behave very steadily with an increase of 7 and 2 $g_{CO_2,eq}/MJ_{H_2}$ when hydrogen is distributed at 500 km; in contrast,

	w/o modifications	w/ modifications	R&D
gas transmission and distribution	10	20	>20
residential systems	10-20	20	>20
industrial systems	5	15	>15

Table 3.7: Admissible hydrogen content H_2 %vol in different systems.

compressed-H_2 has a very steep increase over distance. For distances longer than 450 km, compressed-H_2 becomes more polluting than LH_2.

3.2.4 Hydrogen consumption

Hydrogen can be used in many applications: mobility, heat and power for buildings, heat and power for industry, and industrial feedstock. This typically requires an energy conversion process (except when used as a reactant in the industry) which can be either combustion or electrochemical oxidation:

- **Electrochemical process**: fuel cells.
- **Combustion process**: gas turbines, either large or small, reciprocating internal combustion engines, and boilers.

In order to evaluate the viability of hydrogen applications, it is important to determine hydrogen competitiveness versus low-carbon and conventional alternatives, as shown in Figure 3.1.

Following a study by the Hydrogen Council, twenty two applications where hydrogen can become a cost-competitive low-carbon solution before 2030 have been identified so far [57]. All these applications amount to 15% of the total energy used worldwide and, while hydrogen is not meant to cover all this demand, it will play a key role in the next decades for the decarbonisation of the energy sector. Moreover, in some of these applications, hydrogen is virtually the only low-carbon solution; for instance, in the chemical industry such as ammonia production and hydrocracking (refining).

Out of these twenty two applications, there are only nine where hydrogen is also competitive in comparison with the standard processes used today. Examples of these include long-distance transport applications, regional trains, and medium- and heavy-duty trucks, although this statement refers to a scaled-up market context and not to the current market with limited penetration. Conversely, for other applications, including combustion in turbines, industry feedstock, or synthetic fuel for aviation, a carbon tax of at least EUR 90 per ton of carbon dioxide equivalent (CO_{2e}) would be required to make hydrogen competitive with conventional fuels (given the current market conditions, in particular, energy prices).

The present research study is focused on micro-gas turbines to produce power through hydrogen combustion. However, due to the importance of fuel cell technology, a short introduction to the technology is provided below.

Fuel cell

Fuel cells are power generation systems producing electrical work from the electrochemical oxidation of hydrogen, without combustion, with the main advantage of achieving higher

conversion efficiency. This is because the efficiency of the energy conversion process is not limited by Carnot efficiency.

In a fuel cell, hydrogen reacts with oxygen to form water according to the following half-reactions:

- Anode: $H_2 \rightarrow 2H^+ + 2e^-$
- Cathode: $1/2O_2 + 2e^- \rightarrow O^{2-}$

Each unit cell in a fuel cell is comprised of two electrodes -anode and cathode- separated by an electrolyte that can be either solid or aqueous, see Table 3.9. The fuel, typically hydrogen, is supplied to the anode, where the oxidation half-reaction takes place, whereas oxygen is supplied to the cathode (usually in the form of an air stream) where the reduction half-reaction occurs. As a consequence of the oxidation of hydrogen, electrons are released at the anode and collected at the cathode, producing an electrical current. The electrolyte on the other hand is an electrical insulator that allows the transportation of oxide ions or protons between electrodes. This is presented in Figure 3.9.

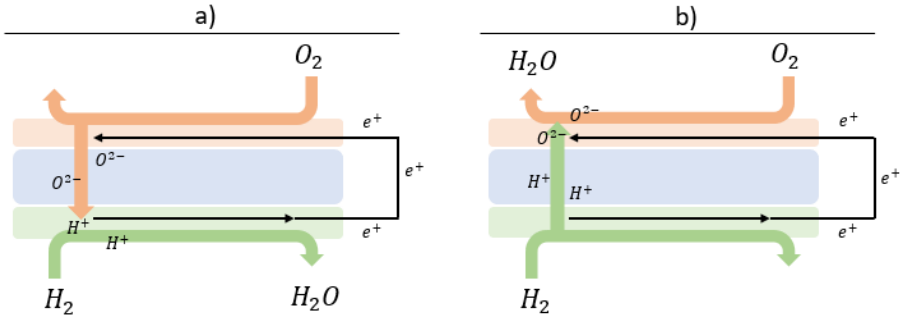

Figure 3.9: Operating principle of (a) ion-conducting and (b) proton-conducting electrolytes.

With the aim to increase the power output of fuel cells, the unit cells described above are stacked together in series in a so-called *fuel cell stack*. This enables higher operating voltage and current, hence power. The main advantages of fuel cells are:

- No (harmful) gaseous emissions are produced (NO_x, SO_x or particles).
- Chemical energy is converted into electric power directly at a much higher efficiency than thermo-mechanical conversion systems relying on thermodynamic cycles.
- Quiet and safe operation, thanks to the lack of moving parts.
- Versatility due to the capability to easily stack electrochemical cells to increase fuel cell voltage and, therefore, power.

There are five main types of fuel cells, which can be classified according to their operating temperature, Table 3.8.

Fuel Cell Type	Common Electrolyte	Operating Temperature	Typical Stack Size	Electrical Eff. (LHV)	Applications	Advantages	Challenges
Polymer Electrolyte Membrane (PEM)	Perfluoro sulfonic acid	<120°C	<1kW-100kW	60% direct H_2; 40% reformed fuel	Backup power, portable power, distributed generation, transportation, speciality vehicles	Solid electrolyte reduces corrosion & electrolyte management problems; Low temperature; Quick start-up and load following	Expensive catalysts; Sensitive to fuel impurities
Alkaline (AFC)	Aqueous potassium hydroxide soaked in a porous matrix, or alkaline polymer membrane	<100°C	1kW-100kW	60%	Military, space, backup power, transportation	Wider range of stable materials allows lower cost components; Low temperature; Quick start-up	Sensitive to CO_2 in fuel and air; Electrolyte management (aqueous); Electrolyte conductivity (polymer)
Phosphoric Acid (PAFC)	Phosphoric acid soaked in a porous matrix or imbibed in a polymer membrane	150-200 °C	5-400kW, 100kW module (liquid PAFC); <10kW (polymer membrane)	40%	Distributed generation	Suitable for CHP; Increased tolerance to fuel impurities	Expensive catalysts; Long start-up time; Sulfur sensitivity
Molten Carbonate (MCFC)	Molten lithium, sodium, and/ or potassium carbonates, soaked in a porous matrix	600-700 °C	300kW-3MW, 300kW module	50%	Electric utility, distributed generation	High efficiency; Fuel flexibility; Suitable for CHP; Hybrid/gas turbine cycle	High temperature corrosion and breakdown of cell components; Long start-up time; Low power density
Solid Oxide (SOFC)	Yttria stabilized zirconia	500-1000 °C	1kW-2MW	60%	Auxiliary power, electric utility, distributed generation	High efficiency; Fuel flexibility; Solid electrolyte; Suitable for CHP; Hybrid/gas turbine cycle	High temperature corrosion and breakdown of cell components; Long start-up time; Limited numbers of shutdowns

Table 3.8: Comparison of fuel cell technologies [100]

(Micro) Gas Turbines

Gas turbines are heat engines that convert thermal energy into mechanical work following the operating principle of a Brayton cycle. Most gas turbines are internal combustion engines (i.e., internally fired) which means that thermal energy is supplied to the engine by means of a combustion process taking place inside the engine itself (i.e., fuel is added to the working fluid of the engine). In a gas turbine, a compressor increases the pressure of an air stream dragged from the surroundings of the engine. This air at high pressure is then mixed with a certain fuel and the resulting mixture is burnt in a combustion chamber at constant pressure. The hot combustion gases flowing out from the combustor are then expanded across a turbine, down to atmospheric pressure again. The work produced by the turbine is higher than that consumed by the compressor, which means that, in addition to driving the compressor, the turbine can also drive an electric generator. Therefore, the elements common to all gas turbine engines are: an upstream air compressor, a combustor, and a downstream turbine, usually on the same shaft as the compressor. The electric generator is typically assembled on this shaft as well, though individual turbines in series are sometimes used to drive the compressor and generator independently.

Gas turbines in the power industry are mostly powered by natural gas, a fossil fuel with a strong negative effect on climate change. In 2019, 23% of the electricity produced came from natural gas-fired power plants, 3% more than the previous year due to the 8% higher consumption of natural gas in the United States, and also some regions in Europe [101]. This is also caused by the phasing out of coal power stations, replaced by natural gas power plants not incorporating carbon capture and sequestration yet. An alternative to natural gas-fired power plants (with carbon capture) is to use hydrogen in gas turbines. This technology is still in the demonstration phase (Figure 3.3) but there are several research programs studying the combustion of hydrogen and natural gas mixtures in gas turbines with the objective to achieve operation on hydrogen only in the near future [102, 103, 104].

Gas turbines with a power rated below 500 kW (or even 1 MW) are termed micro-gas turbines. Their main application is in packaged, small-scale CHP which can be installed in single or multiple units, achieving an overall fuel utilisation higher than 80%. Micro-gas turbines can be also used for emergency or standby power generation as well as mechanical drives of pumps and compressors. Several major differences can be found between micro-gas turbines and large gas turbines:

- **Low pressure ratio**: micro gas turbines have very low volumetric flow rates and, therefore, they mostly make use of radial turbomachinery (low specific speed). Radial compressor stages typically achieve pressure ratios not higher than 4-4.5:1 and this limits the engine's pressure ratio. The utilisation of multistage compressors to achieve higher pressure ratios is not considered in micro gas turbines, due to i) the large pressure losses incurred by the return channel between stages, and ii) the negative impact of small-scale effects (low Reynolds number and large tip gaps) on stage efficiency. The fact that the pressure ratio cannot be increased beyond 4-5 in these engines has a negative impact on the thermal efficiency of the working cycle.

- **Blade cooling is not possible**. Due to the reduced power rating, generally <500 kW, radial turbomachinery is used in a micro gas turbine. Therefore, radial expanders

cannot incorporate internal/blade cooling, as is customary in axial turbines. This has an impact on the Turbine Inlet Temperature attainable which is, indeed, the main driver for high efficiency in gas turbines (and virtually any heat engine). State-of-art in micro-gas turbines feature TITs in the order of 950°C (limited by material melting temperature) whereas this increases to 1700-1800°C in larger gas turbines, yielding efficiencies higher than 40% in the latter case. Of course, this calls for the application of advanced blade cooling techniques. However, the addition of regenerative heat exchangers tends to increase thermodynamic efficiency by 10% approximately as exposed above.

- **Addition of a recuperative heat exchanger**. This is introduced to make use of the hot exhaust gases from the turbine to pre-heat the air coming from the compressor, before entering the combustor. The addition of this component offsets the negative impact of low-pressure ratios on engine efficiency, enhancing the thesis parameter from 22-23% to 32-33% without any other major modification. Recuperative heat exchangers are compact heat exchangers which feature very high costs.

- **Combustion**. Turbine inlet temperatures in micro gas turbines are much lower than in heavy-duty gas turbines and, therefore, the formation of NOx in diffusion flames is not an issue. Accordingly. micro gas turbines do not need to incorporate low-NOx combustion systems, making use of conventional diffusion flame combustors.

The comparison of micro-gas turbines with gas turbines is necessary to visualise the differences between both technologies and to evaluate system improvements that could be transferred between applications thanks to the same (or similar) working principle. However, in terms of commercialisation, micro-gas turbines target a different market, since they compete directly against internal combustion engines (ICE) and, in the next decades, with fuel cells (FC) too. Moreover, it can also compete with batteries. Even though hydrogen micro-gas turbines should be seen as a complement to those applications where direct electrification is not possible since the energy conversion of electricity – hydrogen – electricity would incur lower efficiency to the final end-user application.

Micro-gas turbines gather characteristics that make this technology the best suit for applications where other options would not be appropriate:

- High energy density.
- Increased redundancy and reliability.
- Increased operational flexibility.
- Well-understood technology and high maturity.

Energy infrastructures in the EU member states are transitioning towards decentralised heat and power generation, promoting high efficiency systems that can be integrated with RES. The interest in using mGT in this context comes about because of the challenges posed by VRE when it comes to delivering power and heat on demand, as discussed previously, given that mGT can provide fast and reliable power ensuring customer satisfaction and grid stability. Indeed, hybrid systems where mGT are integrated with wind and solar farms, biomass processing, fuel cells and energy storage would provide secure, stable, efficient, economical,

and environmentally friendly on-site energy production systems, close to the consumers without major transportation and conversion losses. Some solutions for hybrid systems with mGT are:

- CHP systems where mGTs operate on biomass syngas [105].
- CHP systems where mGTs operate on hydrogen produced by solar PV/PEMEC arrays [106].
- CHP systems relying on solar mGTs [107].
- CHP systems relying on integrated mGT/SOFC units [105, 108].

This flexibility and relevance of mGT technology for CHP have been acknowledged by the European Parliament in their resolution on an EU Strategy on Heating and Cooling (2016/2058(INI)). Unfortunately, in spite of the proven operation of mGTs in the first two decades of the XXI century, market penetration has been not as significant as expected initially [109]. In order to foster commercial deployment, technology drivers for the continuous development of mGT systems are presented in Table 3.9.

Table 3.10 presents the most representative micro gas turbine engines in the market (in terms of sales volume). Even if none of these engines can presently work on pure hydrogen, the equivalent consumption of hydrogen if this were possible (i.e., assuming the same energy supply as for the engine running conventional fuels) is reported in the table.

3.3 Round-trip efficiency (RTE) analysis

The processes involved in power-to-power energy storage solutions have been discussed in Section 3.2: production, storage, transportation and consumption. Storing energy to deliver it at a later time does not come without energy losses. This is due to several reasons. Certain energy conversion processes are constrained by the principles of Thermodynamics (such as the Second Law of Thermodynamics, which imposes limitations on the efficiency of thermo-mechanical conversion in a power cycle). Additionally, these processes encounter supplementary losses attributable to irreversibility. In addition, there is always the need to incorporate auxiliary equipment that consumes part of the energy being managed. The ratio from the energy delivered back to the user (or the grid) to that taken from the primary source of electricity (in the context of this work) is termed round-trip efficiency (RTE) and is typically expressed as a percentage (%):

$$RTE = \frac{E_{in}}{E_{out}} \cdot 100 \qquad [\%] \tag{3.7}$$

Table 3.11 presents the RTE of different technologies used for short and long-term energy storage. In this section, the RTE of micro power-to-power energy storage solutions using micro gas turbines is studied. The different cases considered are shown schematically in Figure 3.10.

For the micro power-to-power energy storage considered in this work, power is converted to hydrogen through water electrolysis (Table 3.1), meaning that this concept classifies as

System	Areas of Research
Recuperator	• Increased effectiveness. • Increased performance at a lower temperature. • Corrosion resistance. • Footprint and weight (cost). • Clogging/fouling resistance. • Lower backpressure at higher mass flow. • Lifetime. • Cycles resistance lifetime.
Turbomachinery	• Increased TIT. • Increased efficiency. • Increased efficiency at a lower speed. • Increased performance at a lower temperature. • Increased efficiency at part load. • Extended operating range. • Corrosion resistance. • Wear resistance. • Lifetime.
Combustion system	• Higher TIT. • Corrosion resistance. • Lower pressure loss. • Lower emissions. • Wear resistance. • Lifetime. • Higher temperature resistance. • Cycling resistance.
Power electronics	• Increased efficiency. • Higher grid-micro-interruption resistance. • Power factor correction. • Grid code compliance. • Connection with energy storage. • Off-grid capability.

Table 3.9: Areas of research for the different micro-gas turbine systems.

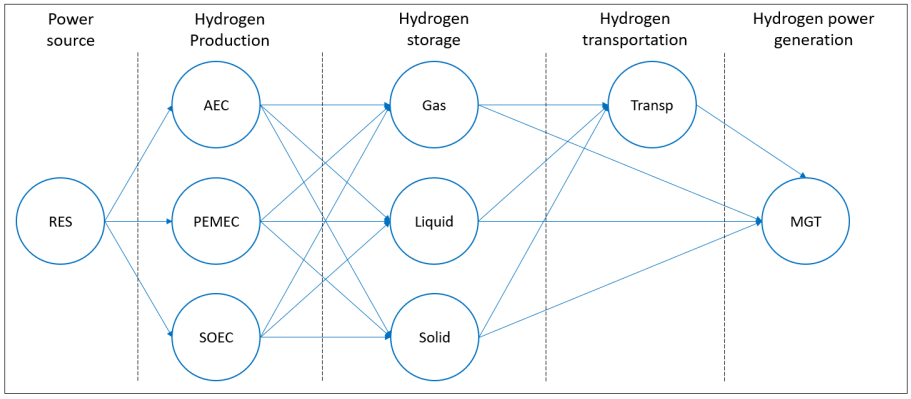

Figure 3.10: Power-to-Power Energy Storage System options considered.

chemical energy storage. Power is consumed to operate the electrolyser and to further process the hydrogen produced, be it for high-pressure gaseous storage (Table 3.2), liquefied

Label	Manufacturer	Model	Fuel Consump. [kg H_2/h][2]	Rated **Power** [kWe]	Spec. Rated **Power** [kWe/kg H_2][2]	η_e [%]
D1	Capstone[110]	C30	3.22	30	9.32	28.0
D2		C65	6.25	65	10.39	31.2
D3		C200s[1]	16.90	200	11.83	35.5
D4	Flex Energy[111]	GT333s	30.77	333	10.82	32.5
D5		GT1300s	119.57	1300	10.87	32.6
D6	Ansaldo Energia[112]	AE-T100	9.99	100	10.01	30.0
D7	Aurelia[113]	A400	29.85	400	13.40	40.2
D8	MTT[114]	EnerTwin	0.60	3.2	5.33	16.0

[1] Capstone C600s, C800s and C1000s packages are comprised of 3, 4 and 5 C200s modules respectively.
[2] Assuming the micro gas turbine could run on hydrogen with the same efficiency as the factory engine.

Table 3.10: Maximum H_2 %vol admitted in different systems.

ESS	$\eta_{\text{round-trip}}$
Hydro	from 65% (in older installations) to 75-85% (in modern facilities).
Flywheels	80% to 90%.
Batteries	75% to 85%.
Electro-thermal	65% to 75%.
Compressed air	45% to 70%.

Table 3.11: Round-trip efficiency of various energy storage systems [41, 115].

H_2 storage (Table 3.4) or to load/unload metal hydrides (Table 3.5). Finally, the amount of H_2 consumed by FCETs for transportation can also be expressed in terms of auxiliary power consumption (Table 3.6). Eventually, the stored energy is discharged to the grid through hydrogen combustion in an mGT (Table 3.10).

In order to avoid dealing with a large number of theoretically-feasible solutions, the analysis is limited to possible combinations between the three electrolyser technologies, one option for each H_2 storage state and one mGT option. This yields a total of nine micro power-to-power energy storage solutions to be studied (codes correspond to the numbering used in the tables cited in the previous paragraph):

- Production: A1 (AEC), A39 (PEMEC) and A41 (SOEC).
- Storage and transportation: B3-C2 (compressed gas at 500 bar), B15-C3 (liquefied-H_2), B20-C4 (metal hydride).
- Power generation: D3 (mGT).

Figure 3.11 shows the energy balance of the power-to-power solutions listed above. As expected, the electrolyser holds the largest share of energy consumption, ranging from 86 to 98% of the total flow of energy into the system, with storage and transportation well behind. For the compressed-H_2 case, the energy consumed to drive the compressors more than doubles that needed for transportation, 3.5% and 1.5% respectively. For liquefied-H_2 storage, liquefaction stems as a highly energy intensive process but, on the other hand, it provides a much higher

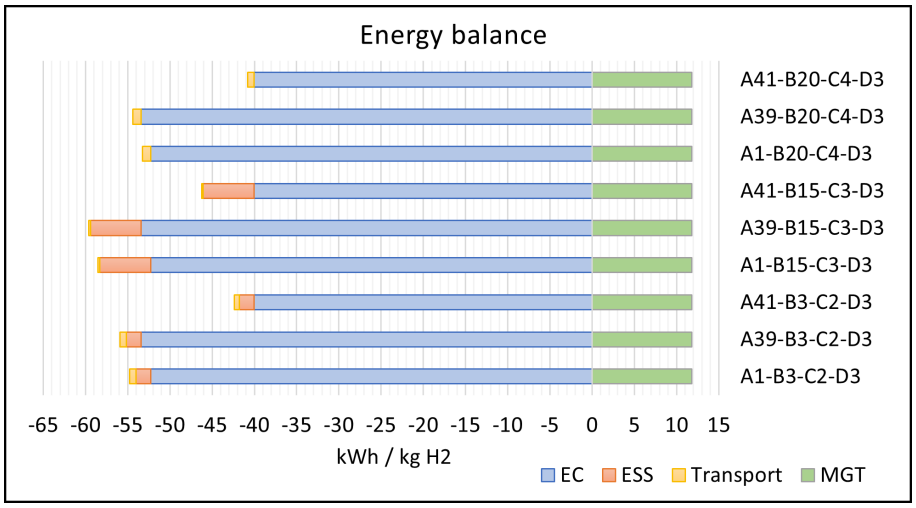

Figure 3.11: Energy balance for the P2P solutions considered. EC: Electrolyser, ESS: Energy Storage System.

energy density; i.e., much more energy is transported on each trip (see Table 3.6). As a result, storage accounts for 10% to 13% of the total energy consumption whereas transportation takes 0.4% of it only. The case of metal hydrides is different to the other two storage options since storage is almost for free (energy-wise) if and when there is a heat source available at a suitable temperature or the metal hydride is suitable to work at ambient conditions (see Section 3.2.2). Therefore, storage is considered energy-neutral and transportation takes 2% of the total energy in.

A closer look into the energy consumed by the electrolyser in each case, Table 3.1 and Figure 3.11 reveals that this energy consumption is largely reduced when SOECs are used, in lieu of either AEC or PEMEC: 40 kWh/kg$_{H_2}$ against 52 kWh/kg$_{H_2}$ and 53 kWh/kg$_{H_2}$ respectively; this is due to the working temperature as explained in Section 3.2.1. Nevertheless, it is to note that, in order to operate the SOEC, a higher-grade heat source able to sustain the high operating temperature is needed. Otherwise, a boiler burning H_2 could be used but this would be at the cost of reducing electrolyser efficiency and adding more capital cost to the system; therefore, using SOECs seems an interesting option only if there is a high-grade heat source available. This is despite the fact that solid oxide electrolysers can potentially be operated reversibly as solid oxide fuel cells, thus reuniting hydrogen and power generation into one single device. Such an option is out of the scope of this work due to a lower technology readiness level and it would therefore not be considered further.

A conceptual scheme of the power-to-power system proposed in this work is presented in Figure 3.12. Based on this and on the energy balance shown in Figure 3.11, the RTE of the systems shown in Figure 3.13 can be calculated with Eq. (3.7), yielding values ranging from 20% to 29%, depending on the chosen configuration. According to the foregoing discussion in this section, the primary drivers of RTE are the power consumption of the electrolyser and the thermo-mechanical energy conversion of the micro gas turbine; yet, given that the mGT specifications are the same for all cases, the variations of RTE from one case to another in

Figure 3.13 are brought about solely by the electrolyser technology used (AEC or PEMEC or SOEC). For cases based on SOEC, the highest efficiency is obtained when hydrogen is stored in the form of metal hydrides, ~29%, followed closely by compressed H_2, ~27.9%, and liquid H_2 at a further distance, ~25.6%. This latter value is obtained when one of the lowest specific power requirements of the liquid H_2 plant is chosen from the options in Table 3.4, but it does not correspond to the minimum value (B18). Actually, if the value of one of the already built LH_2 plants were selected (11.9 kWh/kg$_{H_2}$ corresponding to case B19), RTE would decrease to 22.7% and the energy consumption of the liquid H_2 facility would take 20% of the total energy demand of the power-to-power storage system.

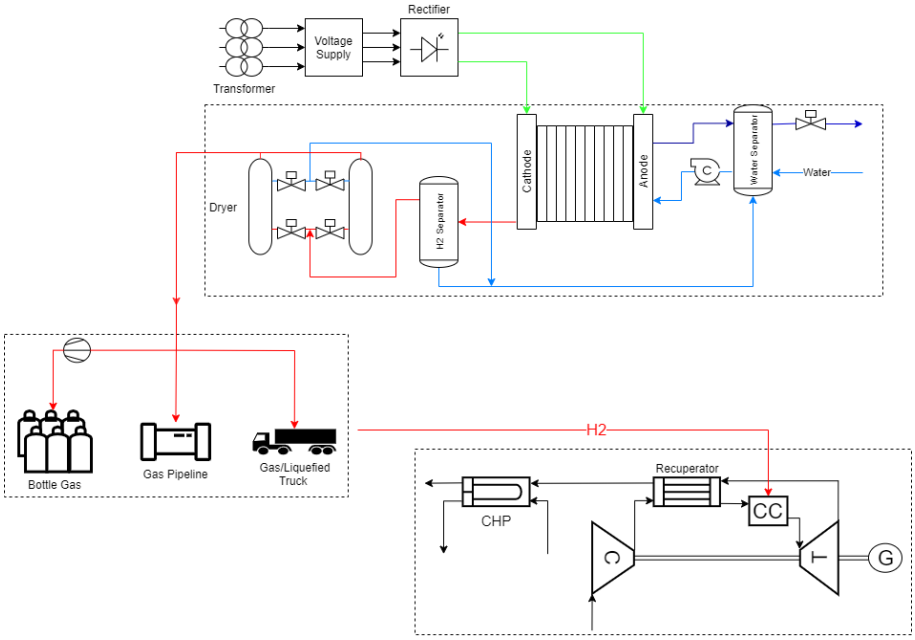

Figure 3.12: Power-to-Power energy storage system based on mGT technology. Proposed layout.

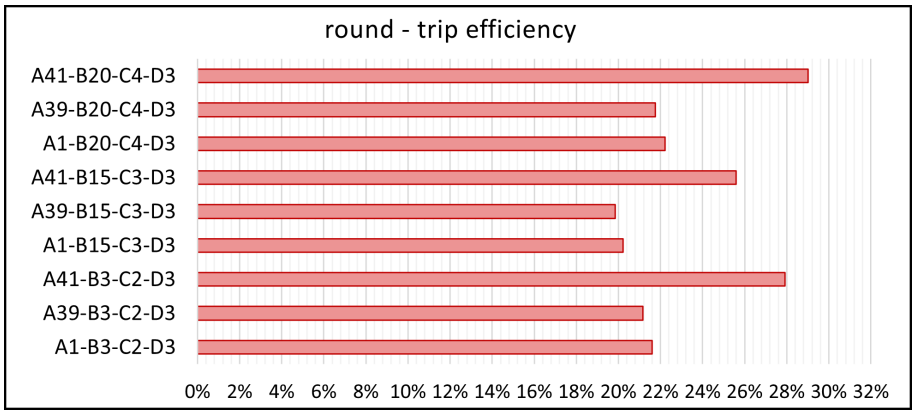

Figure 3.13: Round-trip efficiency for the P2P solutions presented in Figure 3.11

It becomes clear that the second most influential driver energy-wise is storage and, in this regard, hydrogen liquefaction brings about a substantial RTE reduction. Thus, for both on-site and small-distance transportation of liquid H_2, this storage option is not of interest given that the increase in H_2 density does not offset the much higher energy consumption of the hydrogen-conditioning process. In addition, even though economic aspects are not considered in this study, the implementation of a hydrogen liquefaction plant would expectedly have a negative impact on the total capital cost of the storage facility.

As far as the other electrolyser technologies are concerned, AEC and PEMEC, their round trip efficiencies are very similar due to their very similar specific energy consumption. Nonetheless, this is not always the case, as shown in Table 3.1, given that these electrolyser types experience the same RTE fluctuations when liquid H_2 storage is considered: efficiency lower than 20% for liquid H_2 storage and around 21-22% if compressed H_2 or metal hydrides are considered.

3.3.1 Potential to increase round-trip efficiency

In spite of the maximum RTE of ~30% reported in this work for P2P systems based on mGT technology, there is still a large margin for improvement. Two routes are devised in order to assess this potential: 1) considering the thermodynamic limits or 2) considering the technological limits of each of the systems involved. From Figure 3.11, the largest sources of performance enhancement seem to be water electrolysis and power generation.

On the one hand, the operation of an ideal electrolyser without energy losses would require 33.33 kWh/kg_{H_2} which translates into a potential 13-15% RTE gain. Even if this is a theoretical limit that cannot be achieved in practice, predictions from different energy organisations worldwide [50, 40, 116] estimate that the energy consumption of electrolysers is expected to decrease by a few kWh/kg_{H_2} in the next decade (Tables 2.7, 2.8 and 2.9), leading to a RTE improvement of around 3-5% (one-third of the theoretical efficiency gain). On the other hand, an even larger performance enhancement could come from improvements in micro gas turbine technology. Indeed, the efficiency of these engines could increase to ~40% [113, 117] in the next decade and the combination of SOEC/SOFC and mGT in so-called hybrid systems would boost power generation efficiencies to values as high as 55%-60% [108]. The cumulative effect of this foreseen progress on the performance of mGT-P2P technology would translate into RTE higher than 40-42% in the next decade which would take this technology closer to and beyond cost-effectiveness, putting it on the map of essential technologies to enable carbon neutrality by 2050.

3.4 Conclusions

The current chapter has introduced the concept of Power-to-H_2-to-Power energy storage, which belongs to the wider category of chemical energy storage systems. Prior to the storage of energy, electricity is converted into hydrogen through water electrolysis. This hydrogen produced can be stored in several forms: compressed H_2, liquefied H_2, and solid H_2 (metal hydride). The stored hydrogen can later be used for the different applications listed in Figure 3.2.

Power-to-Power energy storage systems do have advantages over other energy storage systems,

Process	E (Thermo. limits) [kWh/kg$_{H_2}$]	E (Tech. limits) [kWh/kg$_{H_2}$]
Electrolysis	-33.33	-47.8 / -50.1 / -37.0 [1]
Compression	-0.089[2]	-1.21[3]
Transportation	-	-
Combustion	28.2[4]	15.0[5]/ 20.0[6]
Round-Trip Eff. [%]	99.7%	30.6% / 29.2% / 39.2% 40.8% / 39.0% / 52.3%

[1] 2030 targets of alkaline, PEM and solid-oxide electrolysers respectively.
[2] Isothermal compression at 330K from 30 bar to 500 bar.
[3] Two stages inter-cooling compression at 330K and from 30 bar to 500 bar with 100% compressor efficiency.
[4] Carnot efficiency considering high/low temperatures of 1600°C and 15°C.
[5] Considering 45% (instead of 35.5%) for the Capstone C200s turbine.
[6] Considered hybrid power system (MGT + SOFC) with a total power block efficiency of 60%.

Table 3.12: Assessment of the potential to decrease/increase energy consumption/production of the different systems involved in a P2P-ESS.

even with relatively low RTE values. Technologically, they enable large energy storage capacity, satisfying the requirements for monthly or even seasonal energy storage, and exhibit long discharge times in comparison with energy storage capacity, Figure 3.14. Environmentally, power-to-gas-to-power brings large advantages in regard to climate change actions inasmuch as it enables direct storage of variable renewable energy through green hydrogen (also blue).

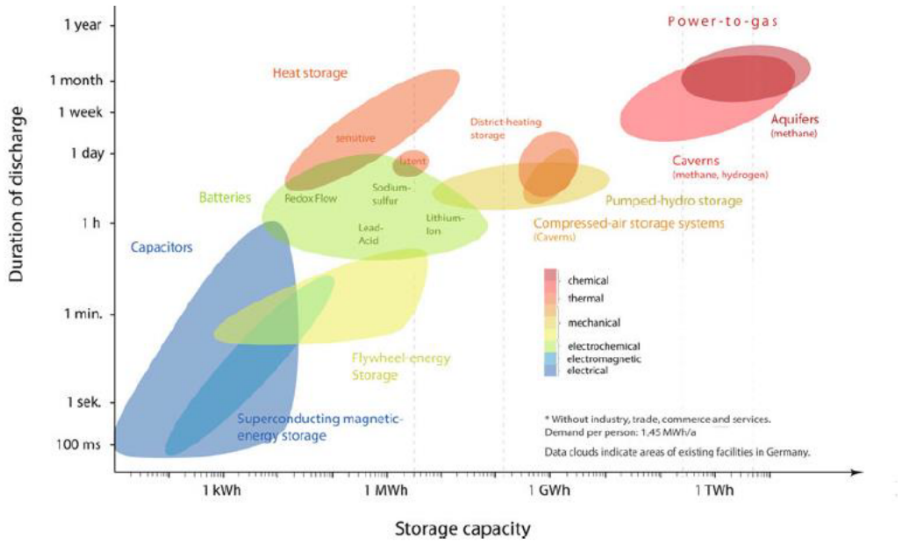

Figure 3.14: Storage technologies compared for their storage capacity and discharge duration [118]

This chapter has presented an assessment of the current state of the art processes involved in Power-to-Power energy storage systems, along with a thermodynamic study to establish the RTE achievable when using a H_2-fired microturbine to deliver energy (power) back to the grid.

Different options for each process have been investigated with the aim to evaluate alternative technologies for the production, storage and utilisation of hydrogen (Tables 3.1, 3.2, 3.4, 3.5, 3.6, 3.10). For the current technology readiness level, the highest RTE is ~29%, achieved when incorporating solid oxide electrolysers with still low technology readiness level (Figure 3.3). Solutions that can be commercialised today rely on either alkaline or proton-exchange membrane electrolysers and compressed gas H_2 storage. With the latter configurations, the maximum efficiency does not exceed 22%, 7 percentage points lower than the former option mostly due to the change from high-temperature to low-temperature electrolysis. These results are obtained considering a 200 kW_e micro turbine with an LHV efficiency of around 30.5%. However, if smaller microturbines are considered, RTE decreases to not more than 14%.

Overall, the chapter has achieved three complementary objectives. First, it has presented a detailed review of the state of the art of the technologies needed in each step throughout the power-to-power energy storage system. Second, it has provided an estimate of the RTE that can be achieved by these systems if state-of-the-art technology is used. Third, the low RTE estimated in this second step, ~ 22% calls for the development of solutions that can help develop more effective small-scale storage solutions for decentralised combined heat and power systems. A simple evaluation of the potential for performance enhancement shows that a maximum RTE of ~53% could be expected in the next decade. More details about this latter aspect are discussed in the next chapters.

4 Power-to-Power System Modelling

Power-to-Power energy storage systems were introduced in chapter 3, providing a detailed analysis of each process involved in this scheme and a review of the state-of-art associated. Then, a thermodynamic analysis of these processes enabled setting up the energy requirements for the different types of electrolysers, storage systems and micro gas turbines available in the market. Based on this, an optimisation of the power-to-power energy storage concept is possible, in order to achieve the efficient storage of renewable energy. With round-trip efficiencies between 22% to 29%, estimated in the previous chapter, not only is optimisation needed to increase competitiveness against other large-capacity energy storage options but, more importantly, to also reduce the gap between green and grey hydrogen production, allowing for more cost-effective power production of H_2-fired microturbines. This task is more easily achieved with a tool allowing fast and accurate prediction of the performance of power-to-power energy storage systems. The current chapter introduces the modelling of each component of these systems, integrated into a software tool for the techno-economical analysis of power-to-power energy storage systems based on micro gas turbines.

The contents of this chapter are partially available in:

A. Escamilla, D. Sánchez, L. García-Rodríguez, 2022, *Exergy Analysis of Green Power-to-Hydrogen Chemical Energy Storage*, Proceedings of the ASME Turbo Expo 2022: Turbomachinery Technical Conference and Exposition. Volume 4: Cycle Innovations; Cycle Innovations: Energy Storage. Rotterdam, Netherlands. June 13–17, 2022. V004T07A004. ASME.

A. Escamilla, D. Sánchez, L. García-Rodríguez, 2023, *Techno-economic study of Power-to-Power renewable energy storage based on the smart integration of battery, hydrogen, and micro gas turbine technologies*, Energy Conversion and Management: X, Vol. 18, pp. 100368.

G. Tilocca, D. Sánchez, M. Torres García, A. Escamilla Perejón, S. Minet, A methodology to quantify product competitiveness and innovation requirements for micro gas turbine systems in hydrogen backup applications, in: Turbo Expo: Power for Land, Sea, and Air, Vol. 102606, American Society of Mechanical Engineers, 2023. 46.

4.1 Introduction

Integration of all systems within a power-to-power concept is a complex process due to the large number of largely different processes involved. It is necessary to develop models of

individual components and to integrate these and other models available in literature into a single platform where they can all exchange information and interact with one another. The first link is between a power generation technology exploiting renewable energy sources, either wind or solar power, and an electrolyser producing hydrogen. The profiles of wind and solar power production are substantially different, bringing about also different profiles of hydrogen production in the electrolyser. Furthermore, choosing between low-temperature or high-temperature electrolysis and a particular form of hydrogen storage is another important decision to make, even if the more appropriate hydrogen storage technology for small power-to-power systems seems to be compressed-H_2 due to its lower system complexity and the good trade-off between power requirements and storage density.

Hydrogen storage enables the decoupling of renewable energy surplus and deficit periods in the power grid thanks to the independent operation of electrolyser and microturbine. Nevertheless, the requirements of the end user (not only the grid) also determine the working mode of the microturbine, influencing all systems upstream. In order to determine possible consumer patterns for either power generation or combined heat and power systems where microturbines can be used, the author has worked closely with the Decentralised Energy Systems Working Group of the European Turbine Network (ETN Global).

Based on the foregoing considerations, the author has developed a software tool to automate the calculations and integration of the different systems involved, with the aim of using the tool to carry out techno-economic analyses of any P2P-ESS. This tool has been tested during a three-month secondment period at Alener Solar (Seville), a company currently designing and constructing a green hydrogen production facility at the industrial port of Seville. A summary of the main capabilities of the mathematical models and software tool follows:

Renewable Energy Sources

- Design of renewable energy sources plants based on wind, solar photovoltaic or both. The design is performed with the System Advisory Model (SAM) [119] and integrated with the main platform using PySAM [120].
- Prediction of the hourly yield of electricity over a year.
- Calculation of the Levelised Cost of Energy (LCOE).

Water Electrolysis

- Semiempirical model to determine the operating characteristics of either Proton-Exchange Membrane or Solid Oxide electrolysis cells: polarisation curve, hydrogen production, power consumption and rated power.
- Integration of renewable energy technologies with electrolyser, determining the hourly operating conditions of the electrolyser, hence hydrogen production.

Hydrogen Storage

- Sizing of the high-pressure tank, according to the Boiler and Pressure Vessel Code of ASME [121]. This depends on user inputs: tank volume and maximum tank pressure.

- Design and sizing of the compression system, including interstage cooling system, based on upstream and designer's data.
- Integration of hydrogen production and storage, hence predicting the filling time, pressure, temperature, and compressor work on a minute basis over a day.

H_2-fired Micro Gas Turbine

- Integration of hydrogen production and storage with the consumption of hydrogen in a micro gas turbine.
- Detail heat and power production of the micro gas turbine, both at nominal and off-design operating conditions.

Economics

- Estimation of the Levelised Cost of Energy (LCOE) of each subsystem(renewable energy technology, battery, micro gas turbine) as well as the plant globally.
- Estimation of the Levelised Cost of Hydrogen (LCOH), considering the cumulative capital and operating costs of renewable energy technologies, water electrolyser, and storage system.

4.2 Renewable Energy Sources Modelling

The modelling of renewable energy technologies is done directly by SAM [119], an open-source software developed by NREL (National Renewable Energy Laboratory) enabling performance and financial simulations. SAM provides performance predictions and cost of energy estimates for grid-connected power projects based on installation and operating costs and system design parameters that the user specifies as inputs to the model. Projects can be either on the customer's side of the utility meter, buying and selling electricity at retail rates, or on the utility's side of the meter, selling electricity at a price negotiated through a power purchase agreement (PPA). SAM represents the cost and performance of renewable energy projects using computer models, each of which represents a part of the system, and a financial model representing a specific financial structure of the project. The models require input data to describe the performance characteristics of physical equipment in the system and project costs. SAM includes several databases of solar and wind resource data, as well as performance data and coefficients for system components such as photovoltaic modules and inverters, and wind turbines. Moreover, the option to introduce customised weather or performance data and coefficients is also available.

Tables 4.1 and 4.2 summarise the main input parameters for the performance modelling of solar photovoltaic and wind turbine systems. It is worth highlighting that SAM is only used for the performance predictions of renewable energy sources whilst the financial model, LCOE, is directly implemented in the software developed. After performing the calculations, SAM provides a wide selection of result parameters which can be visualised either hourly, monthly or yearly. More information about SAM can be found in the bibliography [119].

SAM has a Python package available, PySAM [120], which can be used to call the SAM simulation Core (SSC) from Python to compute modules or to access SAM's default values and input variables. PySAM is a wrapper around the SAM library that groups together the C API functions by technology or financial model into modules. There are two ways to insert input data into PySAM, either setting up each input parameter in each section (see Tables 4.1 and 4.2), or delivering a JSON file with all the input data that can be obtained from SAM software. The latter option is used in the software developed in this thesis since the former alternative would have meant developing an interface very similar to the already existing interface of SAM, which is open-source and available for download.

Section	Description
Location and Resource	This information is given by a file with all the information about the location and solar resources of a particular place over a year.
Module	Several models to represent the photovoltaic module's performance. For each time step of the simulation, the module model calculates the DC electric output of a single module based on the design parameters and the incident solar irradiance calculated from data in the weather file.
Inverter	Several models to represent the inverter's performance model and either choose an inverter from a list or enter inverter parameters from a manufacturer's data sheet using either a weighted efficiency or a table of part-load efficiency values.
System Design	Use the System Design variables to size the photovoltaic system and choose tracking options. The number of inverters, DC to AC ratio, and Subarray 1 Configuration are some of the parameters which need to be set in this section.
Shading and Layout	Shading and snow losses are reductions in the incident irradiance caused by shadows or snow on the photovoltaic modules in the array.
Losses	These inputs account for soiling and electrical losses that the module and inverter models do not account for. These are: Irradiance loss, DC losses, AC Losses, Transformer Losses, Transmission Losses, and System Availability.

Table 4.1: SAM photovoltaic solar sections and parameters

4.3 Water Electrolysis Modelling

Chapter 2 gives an overview of water electrolysis, describing the fundamentals of water electrolysis and its main drivers as well as the different types of electrolysers in detail. This section aims at describing the semi-empirical modelling of different types of water electrolysers, such as Proton-Exchange Membrane and Solid-Oxide, low and high-temperature electrolysis respectively. The models presented are a result of combining existing models obtained from a thorough literature review, aiming to improve the accuracy of the polarisation curve produced. Polarisation curves are the standard indicator of electrolyser performance, either analytically or experimentally, as they allow for easy comparison of different systems or tests. The polarisation curve displays the operating voltage of the electrolysis cell for a given current density. This information can be obtained experimentally with a potentiostat/galvanostat,

Section	Description
Wind Resource	Provides all the information about the location and wind resources of a particular place over a year. There are several options for defining the wind resource: wind resource file, wind speed Weibull distribution, and wind resource probability table.
Wind Turbine	The wind turbine parameters specify the turbine power curve and a hub height of a single turbine. There are two options available to specify this: wind turbine from the data library, or defining the turbine design parameters.
Wind Farm	Deciding the number of turbines, wake effects (losses that account for the reduction in output of turbines positioned in the wake of other turbines in the wind farm), and turbine layout.
Losses	Accounts for system performance losses that are not included in the wind turbine power curve from the Wind Turbine page and other assumptions, such as Wake Losses, Availability Losses, Electrical Losses, Turbine Performance Losses, Environmental Losses, Curtailment/Operation strategies Losses.
Uncertainties	Allows to specify uncertainty as a percentage of either mean wind speed or mean energy production for a range of different factors that contribute to uncertainty in the wind resource or power output of a wind farm.

Table 4.2: SAM wind turbine sections and parameters

which supplies a fixed current to the electrolysis cell and measures the associated voltage. By slowly "stepping up" the load on the potentiostat, the voltage response of the electrolysis cell can be determined. Hence, the polarisation curve provides the voltage required depending on operating conditions such as temperature, pressure and required hydrogen production rate.

In practice, the voltage actually required by the cell to produce hydrogen at a certain rate (i.e., associated current density) is higher than the theoretical value due to a number of energy losses: (1) activation losses, (2) ohmic losses, and (3) mass transport losses. All these voltage losses must be added to the reversible voltage, or the theoretical minimum voltage when neglecting losses (losses are termed overpotentials). Refer to Eq. 2.12.

The terms in Eq. 2.12 are the following: V_{ocv} (also E in chapter 2) is the open circuit which is the minimum theoretical voltage of the electrolyser when losses are neglected, V_{act} is the overpotential due to the kinetics of the electrochemical reaction, V_{diff} is the diffusion overpotential caused by the limited diffusion rate of reactants and products at the electrodes of the electrolyser, and V_{ohm} is the ohmic overpotential associated to the transport of ions and electrons. The following sections will deal with each of the terms expressed in Eq. (2.12).

4.3.1 Modelling overpotentials in Proton-Exchange Membrane electrolysers

The performance of PEM electrolyser cells can be expressed through voltage-current density relationships. To produce these, the following assumptions are made [122]:

1. Liquid water exerts its saturated vapour pressure on both the cathode and anode, at the

prevailing conditions.

2. The gaseous products present at the anode are oxygen and water vapour only and the gaseous products present at the cathode are hydrogen and water vapour only.
3. All gases have ideal behaviour.
4. The solubility of oxygen and hydrogen in water is negligible.
5. Diffusion of hydrogen and oxygen through the membrane is negligible.
6. Pressure at the anode is atmospheric.
7. There are no temperature gradients within the stack.

Open circuit voltage
When the electrochemical cell operates in reversible conditions, that is, in open-circuit conditions, its voltage can be expressed as:

$$V_{ocv} = -\frac{\Delta G}{2F} \qquad [\text{V}] \tag{4.1}$$

where V_{ocv} is the open circuit voltage, ΔG is the Gibbs function change of the electrolysis reaction and F is Faraday's constant (= 96485 C/mol). Since the reaction taking place is:

$H_2O \rightarrow H_2 + 1/2O_2$

its Gibbs function change in standard conditions can be evaluated as:

$$\Delta G^0 = G^0_{f,products} - G^0_{f,reactants} = G^0_{f,H_2} + \frac{1}{2} \cdot G^0_{f,O_2} - G^0_{f,H_2O} \qquad [\text{J/mol}]$$

Since non-standard pressure and temperature conditions are possible, the following relation is used to apply pressure corrections:

$$\Delta G = \Delta G^* + R \cdot T_{cell} \cdot ln \frac{a_{H_2} \cdot a^{0.5}_{O_2}}{a_{H_2O}} \qquad [\text{J/mol}] \tag{4.2}$$

where ΔG^* is the Gibbs function change at any temperature but standard pressure, R is the universal gas constant (= 8.315 J/mol K), T_{cell} is the electrolysis cell working temperature, and a is the activity of species H_2, O_2 and H_2O respectively (which can be approximated by the respective partial pressures). ΔG^* can be calculated as follows:

$$\Delta G^* = \Delta H^* - T_{cell} \cdot \Delta S^* \qquad [\text{J/mol}] \tag{4.3}$$

where ΔH^* (J mol^{-1}) and ΔS^* (J mol^{-1} K^{-1}) are the enthalpy and entropy changes at temperature T_{cell} and standard pressure p_0.

The thermodynamic functions in these equations are evaluated with either empirical correlations or the dedicated software *CoolProp* [123].

Activation overpotential

The activation overpotential is a voltage loss brought about by the need to overcome the activation energy of the reaction in order to trigger the conversion of the water molecule into hydrogen and oxygen. This activation energy, and hence the associated overpotential, is significantly affected by physical and chemical parameters such as operating temperature, loading and composition of the catalyst on the electrodes, the morphology of the active reaction sites and the electrode... Since some effects are very difficult to model, the activation overpotential is typically derived from the Butler-Volmer equation, which is the fundamental electrochemical relationship describing how current depends on voltage in the electrode.

$$V_{act} = V_{act,ano} + V_{act,cat} \qquad [\mathrm{V}] \tag{4.4}$$

$$V_{act,ano} = \frac{R \cdot T_{ano}}{\alpha_{ano} \cdot F} \sinh^{-1}\left(\frac{j}{2 \cdot j_{0,ano}}\right) \qquad [\mathrm{V}] \tag{4.5}$$

$$V_{act,cat} = \frac{R \cdot T_{cat}}{\alpha_{cat} \cdot F} \sinh^{-1}\left(\frac{j}{2 \cdot j_{0,cat}}\right) \qquad [\mathrm{V}] \tag{4.6}$$

where $V_{act,ano}$ and $V_{act,cat}$ are the anode and cathode overpotentials, T_{ano} and T_{cat} indicate the operating temperatures of anode and cathode, and α_{ano} and α_{cat} are the charge transfer coefficient at the anode and cathode. $\alpha_{ano} = 2$ and $\alpha_{cat} = 0.5$ are typical values for PEM electrolyser [124, 122]. $j_{0,ano}$ and $j_{0,cat}$ are the exchange current densities on the anode and cathode and they are largely variable according to different sources, depending on material composition and shape of electrodes and interconnections. Values of these parameters for different PEM electrolysers are shown in Table 4.3.

$j_{0,ano}$ [A/cm^2]	$j_{0,cat}$ [A/cm^2]	Anode and cathode catalyst	Reference
$1.0 \cdot 10^{-12}$	$1.0 \cdot 10^{-3}$	Pt-Ir anode Pt cathode	[125]
$1.65 \cdot 10^{-8}$	$9.0 \cdot 10^{-2}$	Pt-Ir anode Pt cathode	[126]
$1.0 \cdot 10^{-7}$	$1.0 \cdot 10^{-3}$	Pt-Ir anode Pt cathode	[122]

Table 4.3: Exchange current density for several different PEM electrolyser cell models.

Ohmic overpotential

The ohmic overpotential is associated with the internal resistance to the transport of ions and electrons across the elements of the electrolyser. This resistance remains constant (in specific values) irrespective of the operating current density and obeys Ohm's law, hence the name ohmic. The magnitude of the ohmic loss depends on the electrolyte material, electrode material, bipolar plate material, and the interface between the electrode and the electrolyte, as well as on the operating temperature of these elements. Manufacturing techniques and processes are also an important factor in keeping this overpotential to a minimum.

$$\Delta V_{Ohm} = (R_{electrodes} + R_{mem}) \cdot j_{useful} \cdot A \qquad [V] \tag{4.7}$$

Ideal electrodes offer low resistance to the conduction of electrons and protons (H^+ ions), while the membrane facilitates the flow of protons whilst avoiding (as much as possible) permeation of other species. Analytically:

$$R_{electrodes} = R_{ano} + R_{cat} = \frac{t_{ano} \cdot \rho_{ano}}{A} + \frac{t_{cat} \cdot \rho_{cat}}{A} \qquad \text{[Ohm]}$$

$$R_{mem} = \frac{t_{mem} \cdot \rho_{mem}}{A} = \frac{t_{mem}}{\sigma_{mem} \cdot A} \qquad \text{[Ohm]}$$

where t is thickness, ρ_x is the electrical resistivity of each electrode and σ_{mem} is the proton conductivity of the membrane, for which models are presented in Table 4.4. In this project, σ_{mem} is calculated with the Springer model. A is the area of the cell and j_{useful} is the useful current density taking into account Faraday's efficiency ($j_{\text{useful}} = j \cdot \eta_{Faradays}$), which can be estimated at 0.98 - 0.99.

Model	Formula
Kopitzke [127]	$\sigma_{mem} = 2.29 \cdot \exp(-\frac{7829}{R \cdot T})$
Springer [128]	$\sigma_{mem} = (0.005139 \cdot \lambda - 0.00326) \exp\left(1268 \cdot (\frac{1}{303} - \frac{1}{T})\right)$
Benardi [129]	$\sigma_{mem} = \frac{F^2 \cdot C^{H^+} \cdot D^{H^+}_{mem}}{R \cdot T}$

Table 4.4: Models used to estimate the proton conductivity of the membrane Springer's equation is experimentally obtained from a Nafion®117 membrane, and its range of validity is 30-80°C).

Diffusion overpotential

Diffusion losses are due to the limited rate of mass transport to and from the reaction sites at the interface between electrodes and membrane, which reduces the reaction rate (i.e., current density) accordingly, such transport rate depends on mass diffusivity and concentration gradients between bulk flow and reaction sites. In practice, diffusion losses are driven by current, the reactant activity and the electrode's structure. Nevertheless, experimental evidence has shown that the influence of this contribution to the total voltage loss is much smaller than the two previous contributions (activation and ohmic) except for very high current densities that are rarely considered [130, 131]. Figure 4.1 shows the results from Zhenye Kang *et al.* [131], clearly showing that V_{diff} is negligible with respect to the other overpotentials in the range from 0-2 A/cm^2. Since, as described in Chapter 2, the range at which PEMECs work does not exceed 2 A/cm^2, the diffusion overpotential is neglected in the current work.

4.3.2 Modelling overpotentials in Solid-Oxide electrolysers

Solid Oxide electrolyser cells operate at higher temperatures than PEMECs and this implies that the steam electrolysis reaction becomes increasingly endothermic. A portion of this thermal energy demand needed to sustain electrolysis can be obtained from the irreversible heat generation within the cell, which depends on the operating conditions. Thus, depending on operating voltage, the heat generated due to the ohmic resistance and other loss mechanisms might be lower, equal, or higher than the amount of heat required for the endothermic

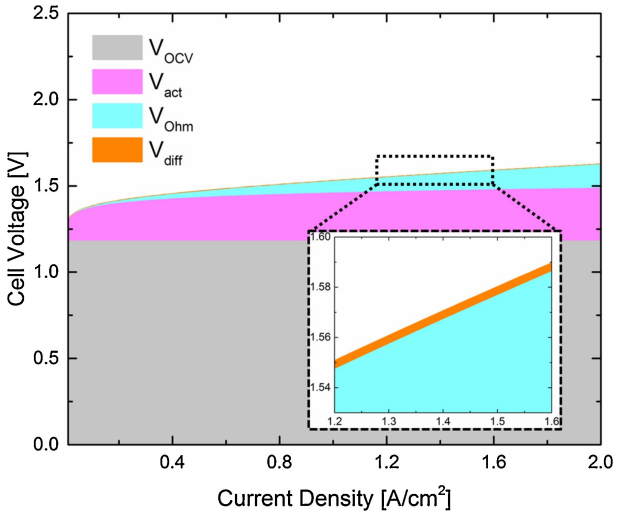

Figure 4.1: Contributions of each overpotential to polarization curve of the PEMECs with TT-LGDLs [131].

reduction of steam. At the thermoneutral voltage condition, the thermal energy required for steam electrolysis is equivalent to the heat of reaction within the cell, meaning that the net heat flux to/from the cell is zero in this condition. Operation near or at the thermoneutral voltage tends to simplify the thermal management of the stack since both the external heat input and associated thermal stress are minimised at this voltage [132].

For steam electrolysis, the thermoneutral voltage can be estimated based on the overall cell energy balance:

$$V_{tn} = \frac{\Delta H_R}{2F} \approx 1.287V \qquad \text{at } 800\ ^\circ\text{C}$$

where ΔH_R is the enthalpy of the steam reduction reaction. The thermoneutral voltage, V_{tn}, is weakly dependent on temperature (e.g., changing only by +5 mV for an increase of 200 °C in cell temperature).

Open circuit voltage
Open circuit voltage is calculated for a proton-exchange membrane electrolyser.

Activation Overpotential
Activation overpotential is provided by Eq. (4.4). However, there is one significant change in the calculation of the exchange current densities on anode and cathode since $j_{0,ano}$ and $j_{0,cat}$ vary greatly with reaction kinetics, temperature and pressure. These are, in practice, calculated following the following Arrhenius equation:

$$j_{0,i} = \gamma_i \cdot \exp\left(-\frac{E_{act,i}}{R \cdot T}\right) \tag{4.8}$$

where:

- γ_i is the pre-exponential coefficient for electrode exchange current density at the anode and cathode, A/m^2.
- E_{act} is the activation energy at the anode and cathode, J mol^{-1} K^{-1}.

Ohmic overpotential
Ohmic overpotential is determined similarly to the previous case, just substituting the contribution of the electrolyte for that of the membrane in Eq. (4.7):

$$\Delta V_{Ohm} = (R_{electrodes} + R_{electrolyte}) \cdot j_{useful} \cdot A = R_{eq,Ohm} \cdot j_{useful} \cdot A \qquad [V] \tag{4.9}$$

$$R_{eq,ohm} = \frac{\rho_{cat} \cdot t_{cat} + \rho_{el} \cdot t_{el} + \rho_{an} \cdot t_{an}}{A} \qquad \text{[Ohm]} \tag{4.10}$$

where:

- ρ_i is the resistivity of element i, Ohm · m.
- t_i is the thickness of element i, m.

Table 4.5 provides the information needed to estimate the resistivity of anode, cathode and electrolyte depending on temperature.

	Specific resistivity [Ohm· cm]
Anode	$1.053\text{E-}6 \cdot T \cdot \exp\left(\frac{1150}{T}\right)$
Cathode	$2.381\text{E-}6 \cdot T \cdot \exp\left(\frac{1200}{T}\right)$
Electrolyte	$2.994\text{E-}3 \cdot \exp\left(\frac{10300}{T}\right)$

Table 4.5: Resistivity of anode (ρ), cathode and electrolyte. T in K

Diffusion overpotential
Diffusion losses are due to mass transport limitations, determined by the concentration gradient between the bulk flow and the reaction sites at the interface between electrodes and electrolytes. They depend on current, reactant diffusivity and electrode structure. The associated loss due to mass diffusion is termed diffusion or concentration overpotential:

$$\Delta V_{con} = V_{con_{H_2}} + V_{con_{O_2}} \qquad [V]$$

The concentration overpotential contributed by the cathode is estimated as [133]:

$$V_{con_{H_2}} = \frac{R \cdot T}{2 \cdot F} \ln\left(\frac{1 + \frac{j \cdot R \cdot T \cdot d_{H_2}}{2 \cdot F \cdot D^{eff}_{H_2O} \cdot P^0_{H_2}}}{1 - \frac{j \cdot R \cdot T \cdot d_{H_2}}{2 \cdot F \cdot D^{eff}_{H_2O} \cdot P^0_{H_2O}}}\right) \qquad [V] \tag{4.11}$$

Diffusion in the porous SOEC electrodes is mainly based on two mechanisms, namely, molecular diffusion and Knudsen diffusion. Molecular diffusion is the dominant mechanism if the

pore size is much larger than the mean free path of the molecular species. In this case, the molecule-molecule interaction governs the diffusion process. On the other hand, if the pore size is much smaller than the mean free path of the species, the molecule-pore wall interaction dominates over the molecule-molecule interaction. Thus, Knudsen diffusion becomes an important mechanism. In most porous structures, both mechanisms are significant. The effective diffusion coefficient of steam can be expressed by combining these two diffusion mechanisms using Bosanquet's formula [134, 135, 136],

$$\frac{1}{D_{H_2O}^{eff}} = \frac{\xi}{\epsilon}\left(\frac{1}{D_{H_2O-H_2}} + \frac{1}{D_{H_2O,k}}\right)$$

where:

- ξ/ϵ is the ratio of cathode tortuosity to porosity,
- $\xi/(\epsilon \cdot D_{H_2O-H_2})$ is the reciprocal of the effective molecular diffusion coefficient of an H_2O-H_2 binary system, and
- $\xi/(\epsilon \cdot D_{H_2O,k})$ is the reciprocal of an effective Knudsen diffusion coefficient for steam.

For Knudsen diffusion, since gas molecules collide with the walls of the pores frequently, the transport of molecules can be modelled using the kinetic theory [134, 135, 136],

$$D_{H_2O,k} = \frac{4}{3} r \sqrt{\frac{8 \cdot R \cdot T}{\pi \cdot M_{H_2O}}}$$

where:

- r is the mean pore radius, and
- M_{H_2O} is the molar weight of H_2O (18 g·mol^{-1}).

The binary molecular diffusion coefficient $D_{H_2O-H_2}$ can be obtained from the Chapman-Enskog theory for ideal gases [136],

$$D_{H_2O-H_2} = 0.00133\left(\frac{1}{M_{H_2}} + \frac{1}{M_{H_2O}}\right)^{1/2} \frac{T^{3/2}}{p \cdot \sigma_{H_2O,H_2}^2 \cdot \Omega_D}$$

where:

- M_{H_2} is the molar weight of H_2 (2 g·mol^{-1}),
- σ_{H_2O,H_2} is the mean characteristic length of species H_2O and H_2, and
- Ω_D is the dimensionless diffusion collision integral.

The analytical values of σ_{H_2O,H_2} and Ω_D can be obtained as follows [137]:

$$\sigma_{H_2O,H_2} = \frac{\sigma_{H_2} + \sigma_{H_2O}}{2} \qquad [\text{Å}]$$

$$\Omega_D = \frac{A}{\tau^B} + \frac{C}{\exp(D \cdot \tau)} + \frac{E}{\exp(F \cdot \tau)} + \frac{G}{H \cdot \tau}$$

$$\tau = \frac{k \cdot T}{\epsilon_{i,j}}$$

$$\epsilon_{i,j} = \sqrt{\epsilon_i \cdot \epsilon_j}$$

where:

- k is Boltzmann's constant ($1.38066 \cdot 10^{-23}$ J·K^{-1}),
- $\epsilon_{i,j}$ is the characteristic Lennard-Jones length [K], and
- *A, B, C, D, E, F, G* and *H* are the Lennard-Jones 12-6 potentials.

Values of the characteristic lengths are reported in Table 4.6 and the constants appearing in the collision integral are reported in Table 4.7 [136].

	N_2	O_2	CH_4	H_2O	CO	H_2	CO_2
σ_i	3.798	3.467	3.758	2.641	3.690	2.827	3.941
ϵ_i/k	71.4	106.7	148.6	809.1	91.7	59.7	195.2

Table 4.6: Characteristic lengths.

A	B	C	D	E	F	G	H
1.06036	0.15610	0.19300	0.47635	1.03587	1.52996	1.76474	3.89411

Table 4.7: Collision integral constants.

The anode concentration overpotential can be expressed as

$$V_{con_{O_2}} = \frac{R \cdot T}{4 \cdot F} ln \left(\frac{\sqrt{(p^0_{O_2})^2 + \frac{j \cdot R \cdot T \cdot \mu \cdot t_{ano}}{2 \cdot F \cdot B_g}}}{p^0_{O_2}} \right) \qquad [\text{V}] \tag{4.12}$$

where:

- μ is the dynamic viscosity of O_2,
- B_g is the flow permeability, and
- t_{ano} is the thickness of the anode.

The viscosity of oxygen μ can be determined by the sixth-order polynomial function developed by Todd and Young [138]:

$$\mu = -1.692 + 889.75 \cdot t - 892.79 \cdot t^2 + 905.98 \cdot t^3 - 598.36 \cdot t^4 + 221.64 \cdot t^5 - 34.75 \cdot t^6$$

where $t = T/1000$.

Flow permeability B_g can be determined by the Kozeny-Carman relationship [139, 140]:

$$B_g = \frac{\epsilon^3}{72 \cdot \xi \cdot (1-\epsilon)^2} (2 \cdot r)^2$$

4.3.3 Estimating the properties of the electrolyser

The mathematical model described in the previous section is used to calculate the voltage of a single electrolyser cell at a specific current density. When several cells are connected in series (stack), the voltage is calculated as follows:

$$V_{stack} = V_{cell} \cdot N_{cells} \qquad [\mathrm{V}] \tag{4.13}$$

The power consumption of the electrolyser stack can be calculated as:

$$\dot{W}_{stack} = V_{stack} \cdot I \qquad [\mathrm{W}] \tag{4.14}$$

The hydrogen production rate at the cathode depends on the electrochemical behaviour of the cells. The associated consumption of water and production of oxygen is determined accordingly, through stoichiometry:

$$\dot{m}_{H_2} = 80.676 \cdot \frac{N_{cells} I \cdot \eta_F}{2 \cdot F} \qquad [\mathrm{Nm^3/h}] \tag{4.15}$$

where η_F is Faraday's efficiency and F Faraday's constant (= 96500 C/mol).

The Second Law efficiency of the electrolyser is expressed as the ratio from the Gibbs function change of the electrochemical reaction at standard conditions, ΔG^*, to the electrical work consumed by the cells, W:

$$\epsilon_{\Delta G} = \frac{\Delta G^*}{W} \qquad [-] \tag{4.16}$$

The Gibbs function at standard conditions, ΔG^*, is calculated as specified in Eq. (4.3) whilst the electrical work is a function of cell voltage, V_{cell} and Faraday's efficiency:

$$W = 2F \frac{V_{cell}}{\eta_F} \qquad [\mathrm{J/mol}]$$

Faraday's efficiency is the ratio of the number of electrons theoretically required to produce a given amount of hydrogen to the actual number of electrons supplied by the electrical current to produce the same amount of hydrogen. Even though, in this work, water electrolysis is based on a PEMEC technology using Nafion membranes, an empirical expression of Faraday's efficiency for AEC-based water electrolysis can also be used; according to Ullberg [141]:

$$\eta_F = 0.995 \exp\left[\frac{-9.5788 - 0.0555 \cdot T}{i} + \frac{1502.708 - 70.8005 \cdot T}{i^2}\right] \qquad [-]$$

4.4 High-Pressure Hydrogen Storage

This section describes a thermodynamic analysis of the refilling process of a gaseous hydrogen tank, the ASME Section VIII for the design of high-pressure vessels as well as the compression system put in place for refilling the tank. The refilling of the tank can be assumed to be either an ideal adiabatic process or an ideal diathermal process. In both cases, the treatment of the gas will be ideal; this allows using the ideal gas law which simplifies the calculus of the final equations to determine the status of the tank at any time as well as the progress during the refilling of a tank. For the design of high-pressure vessels, the ASME section VIII includes calculations to determine the thickness of the different bodies of the tanks based on internal pressure, material properties and tank geometry.

In the case of the compression process, volumetric compressors are considered and treated in detail. Both the compression and expansion processes, when using a piston compressor, are considered polytropic. Furthermore, an intercooling process is considered when more than one compression stage is needed, resulting in a more isothermal process.

4.4.1 Tank refilling

Figure 4.2 shows a simplified schematic of an idealised refuelling process. The following assumptions are applied [142]:

- The inlet or feed conditions do not vary with time and remain constant during refilling.
- The gas flow rate into the tank is considered to be constant over a period of time, t.
- The system under consideration is the hydrogen gas in the fuel tank.

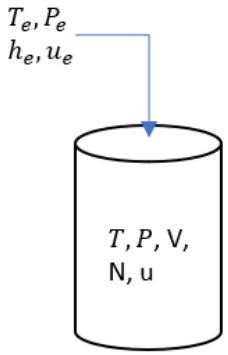

Figure 4.2: Schematic of refilling process.

The following numerical treatment is based on that in [142]. Starting from the First law of thermodynamics for a simple open system, Eq. 4.17 can be derived.

$$(N_i + K \cdot t)\frac{du}{dt} + u \cdot K = \dot{Q} + h_e \cdot K \tag{4.17}$$

where N_i is the initial (total) number of moles in the tank at time $t = 0$ (before refilling), K is the constant molar flow rate into the tank, u is the molar internal energy, h_e is the molar enthalpy at the inlet (assumed to be constant), and $\dot{Q} = \delta Q / dt$ is the heat transfer rate to the system

from the surroundings. Knowing the Equation of State, characteristics of the input stream and the initial conditions of the tank, and the thermodynamic process describing refilling, Eq. 4.17 can be used to predict the final conditions (T, P, and N) of the tank at any given time, where T and P are temperature and pressure of the tank respectively.

Annex 8 describes the refilling process of the tank when considering an adiabatic process and a diathermal process for an ideal gas.

4.4.2 Tank geometry

High-pressure vessels can be built according to ASME Section VIII, Divison 1, 2 or 3 [143]. Division 1 was the first one released, and it is often chosen to design high pressure vessels. However, Divisions 2 and 3 offer a more optimised design, leading to significant material savings in some cases, for the construction of high-pressure vessels. Hence, high-pressure vessels should be designed following the minimum wall thickness criteria detailed in either Division 2 or Division 3, Section VIII of the ASME Code.

The design of such vessels can be divided into shells and heads. Each of these can be of different types, such as cylindrical or spherical shells, and ellipsoidal or torispherical heads. Moreover, the dimensions and design of each of these parts is different depending on whether they are subject to internal or external pressure. In this case, all the equations and criteria exposed below belong to "under internal pressure".

Cylindrical shells

The standard equation yielding the minimum thickness of a cylindrical shell under internal pressure is detailed in Eq. 4.18.

$$t = \frac{P \cdot R}{2 \cdot S \cdot E - 0.2 \cdot P} \qquad [UG-27] \tag{4.18}$$

Where t is the minimum wall thickness, P is the internal design pressure, R is the internal radius, S is the allowable stress, and E is the efficiency of the joint.

This equation is applied to meet either of the following criteria:

1. $P < 0.385 \cdot S \cdot E$
2. $t < 0.5 \cdot R$

For thick walls, when the previous criteria are not met, the equations presented in Appendix 1-2 of ASME Section VIII [143] are used. These equations are detailed below:

- Division 1

$$t = R_i \left[\left(\frac{S+P}{S-P} \right)^{1/2} - 1 \right] \tag{4.19}$$

- Division 2

$$t = R_i \left(e^{P/S} - 1 \right) \tag{4.20}$$

- Division 3
  Division 3 does not have an equation to calculate wall thickness directly. Instead, it yields the maximum allowable pressure given an assumed wall thickness. Hence, an iterative process is carried out to get the optimum wall thickness that yields the maximum allowable pressure.

$$P_m = 0.667 \cdot F_y \cdot \ln(R_o/R_i) \tag{4.21}$$

  where F_y is the minimum specified yield strength. If $S = 0.667F_y$, Eq. 4.21 can be transformed into Eq. 4.20.

Spherical Shells
The standard equation for the minimum thickness of a spherical shell under internal pressure is detailed in Eq. 4.22.

$$t = \frac{P \cdot R}{2 \cdot S \cdot E - 0.2 \cdot P} \qquad \text{[UG-27]} \tag{4.22}$$

This equation is used as meeting either of the following criteria;

1. $t < 0.356 \cdot R$, or
2. $P < 0.665 \cdot S \cdot E$

For thick walls, when the previous criteria are not met, the equations presented in Appendix 1-3 of ASME Section VIII [143] are used.

Ellipsoidal heads
The standard equation for the minimum thickness of ellipsoidal heads under internal pressure is detailed in Eq. 4.23.

$$t = \frac{P \cdot D}{2 \cdot S \cdot E - 0.2 \cdot P} \qquad \text{[UG-32(d)]} \tag{4.23}$$

Where D is the inside diameter of the head skirt. This equation is used as meeting the following criteria: $D/h = 2{:}1$.

Torispherical heads
The standard equation for the minimum thickness of torispherical heads under internal pressure is detailed in Eq. 4.24.

$$t = \frac{0.885 \cdot P \cdot L}{S \cdot E - 0.1 \cdot P} \qquad [UG-32(e)] \tag{4.24}$$

where L equals the inside radius of the crown.

Hemispherical heads
The standard equation for the minimum thickness of hemispherical heads under internal pressure is detailed in Eq. 4.25.

$$t = \frac{P \cdot L}{2 \cdot S \cdot E - 0.2 \cdot P} \qquad [UG-32(f)] \tag{4.25}$$

This equation is used as meeting the following criteria:

1. $t < 0.356 \cdot L$, or
2. $P < 0.655 \cdot S \cdot E$

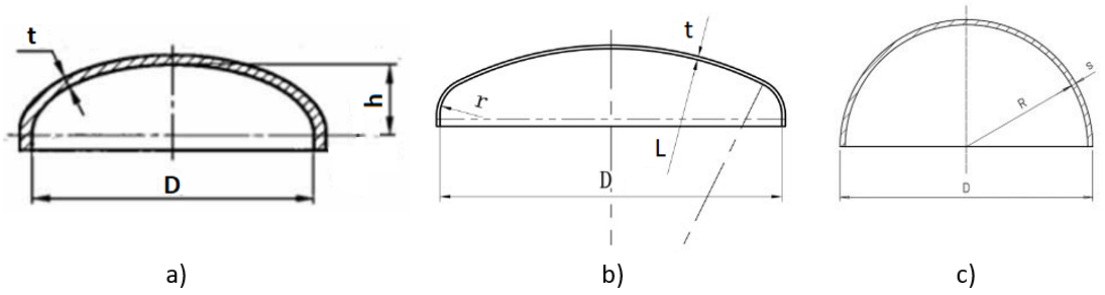

Figure 4.3: a) Ellipsoidal head, b) Torispherical head, c) Hemispherical head.

4.5 Compression system

A first and general approach to model the compression process was used in Section 3.2.2. In this case, the compression process was treated as a polytropic process, applying a polytropic efficiency to obtain the compression work required for different mass flow rates and pressure ratios, disregarding the technology used for compressing. This approach is conservative in calculating the compression work with existing technology due to the fact that it does not consider the pecularities of a specific type of compressor; for instance, the effect of dead volume in reciprocating compressors. This is better represented by Fig. 4.4 where the area enclosed by the working diagram of the compression process represents compression work. The negative impact of dead volume on flow rate capacity becomes evident, even though this is disregarded in this preliminary calculations.

From this, the aim of this section is to characterise the technologies available to compress hydrogen, as well as the most suitable type of compressor for different operating conditions, final service pressure and volume flow rate. The different technologies available to compress hydrogen are described in [144] from a technical standpoint, disregarding the thermodynamics of each compressor type; this section aims at filling the thermodynamic knowledge gap for the different hydrogen gas compression systems.

Section 3.2.2 gave an introduction to isothermal, polytropic, and adiabatic compression processes. Further to this and from a technological point of view, compressors can be divided into two main categories; positive-displacement and dynamic compressors. The former category is divided into two main groups: reciprocating and rotary compressors. The latter is also

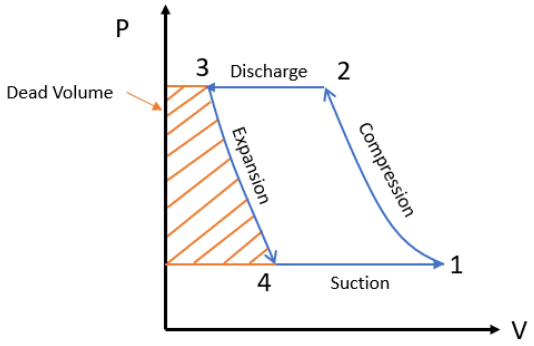

Figure 4.4: Reduced flow rate capacity of a reciprocating compressor undergoing polytropic compression and with a certain dead volume.

divided into two groups: centrifugal and axial. The type of compressor used is determined by the final service pressure and volume flow rate but there are other relevant aspects such as maintenance intervals and costs and the use of oil for lubrication purposes.

Figure 4.5 shows the range of compressor types depending on delivery pressure and volume flow rate. Due to the very light weight of hydrogen, internal leakages are a main problem for compression, in particular at very high pressure. Thus, turbo compressors are found to be very low efficient compared to other technologies whilst screw compressors are usually limited to 40 bar when considering non-lubricated machines. All other compressor options fall in the category of reciprocating compressors, which are characterised for delivering a very high final pressure for reduced flow rates. Lubricated piston compressors can reach more than 1000 bar but with the disadvantage of hydrogen contamination due to oil leakage. Therefore, only three types are left for compressing hydrogen with relatively high efficiency and without hydrogen contamination. Non-lubricated mechanically driven piston compressors can handle up to 250 bar nowadays but with this is likely to increase to 400 bar in the next years.Non-lubricated hydraulically driven piston compressors and diaphragm compressors could achieve more than 1000 bar, making them suitable for H_2 filling stations. The main characteristics of these two latter compressors are presented in Table 4.8 and Table 4.9.

Compressor Type	Final Pressure [bar]	Volume Flow Rate [Nm^3/h]
Mechanically driven piston compressor	≈ 250	≈ 5000
Hydraulically driven piston compressor	≈ 3000	≈ 15
Diaphragm compressor		≈ 200

Table 4.8: Service pressure and volume flow rate limits for some non-lubricated compressors. [72]

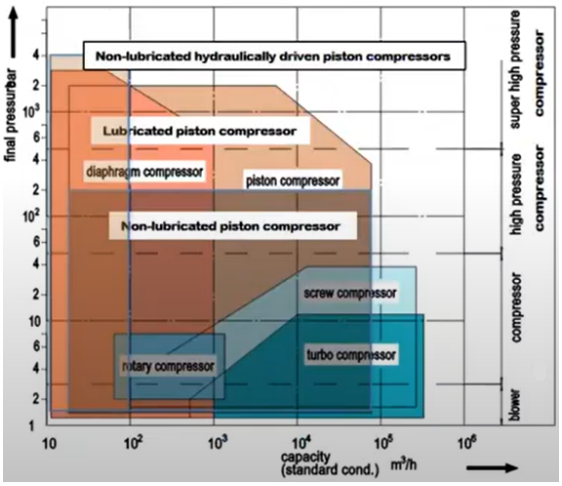

Figure 4.5: Types of compressor based on final pressure and volume flow rate [145].

Positive Feature	Mechanically Driven	Hydraulically driven	Diaphragm
High pressure	-	X	X
High flow rate	-	-	X
Oil-free	X	X	X
Abrasion free	-	X	X
Leakage free	-	-	X
Frequent Start/Stop	X	X	-
Reliability	X	X	-
Flow Control	X	X	-
Scalable	X	X	-
Footprint	X	X	-

Table 4.9: Characteristics of non-lubricated compressors. [72]

4.5.1 Thermodynamic analysis of reciprocating compressors: Theoretical Compression Cycle

A piston compressor is comprised of cylinder, cylinder head and piston with piston rings, inlet and outlet spring-loaded valves, connecting rod, crankshaft, and bearings. The crankshaft is typically driven by an electric motor and, thanks to the connecting rod, the piston moves linearly in an alternate motion between the Top Dead Center (TDC) and the Bottom Dead Center (BDC).

When the piston moves from TDC to BDC, the pressure in the cylinder falls below atmospheric pressure, and due to the pressure difference across the inlet valve, the inlet valve overcomes the spring force and opens to allow gas into the cylinder. Then, the piston moves from BDC towards TDC, increasing the confined gas pressure, and causing the inlet valve to close. When the piston approaches the TDC, there is a sufficient pressure difference across the discharge valve to overcome the spring force, hence allowing gas to be released. Then, once the cylinder is empty (assuming no dead volume), the discharge valve closes and the piston moves again

towards BDC. The discharge pipe can be connected to either a storage tank or to a process making use of the compressed gas directly.

The aforedescribed operation corresponds to a single acting reciprocating compressor. An alternative design would be the so-called double acting configuration. In this case, compression is carried out in both directions, from BDC towards TDC and from TDC towards BDC, increasing the volume flow rate for the same footprint. Both layouts are shown in Fig. 4.6. For the double-acting type, the discplacement of the piston is also alternative but always axial. Additionally, there are also other configurations that allow multistage compression, useful to further increase the pressure of the fluid through several compression stages in series.

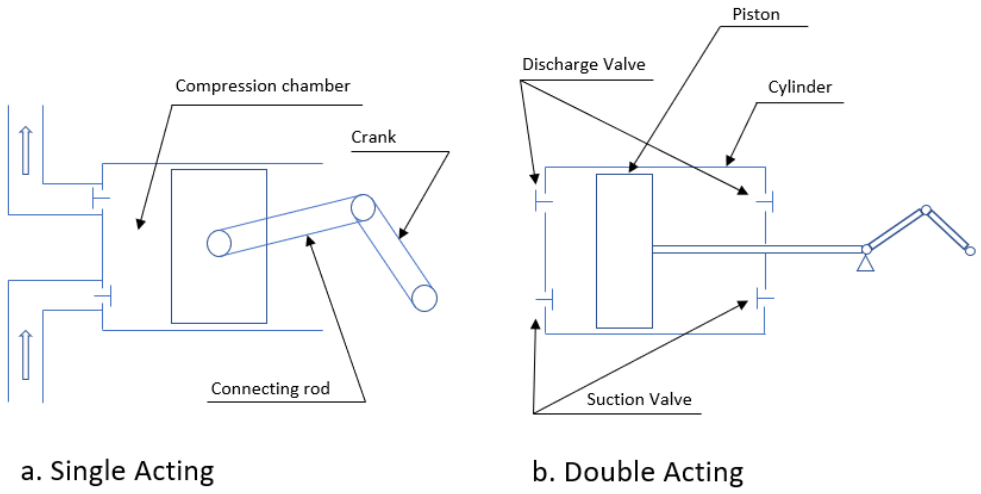

Figure 4.6: Layouts of reciprocating compressors, a) single acting, b) double acting.

Starting from the simplest compression cycle, Fig. 4.7a shows the ideal compression cycle with no dead volume. It is assumed that the opening and closing of the valves do not require a physical volume to allow for valve lift or for the gas to flow into the cylinder. With no dead volume, the pressure drop inside the cylinder is instantaneous (3-4) when the piston moves towards the BDC. Nevertheless, this is not possible in practice and a dead volume is always needed (Fig. 4.7b).

Modelling compression and expansion (1-2 and 3-4, Fig.4.7) is not straightforward but it is common to assume that the following polytropic behaviour applies:

$$p \cdot v^n = \text{constant} \tag{4.26}$$

where p refers to pressure, v to specific volume, and n to polytropic coefficient. Since compression and expansion are carried out at a constant volume, the specific volume can be replaced by the volume occupied, V. For air cylinders with external cooling fins, n is usually between 1.25 and 1.38, whereas for cylinders with cooled jackets, n is usually between 1.2 and 1.35. It is common to consider that n is equal for both expansion and compression. However, due to different conditions of thermal exchange and the lack of air tightness during the different cycle processes, the value of n might be different in practice.

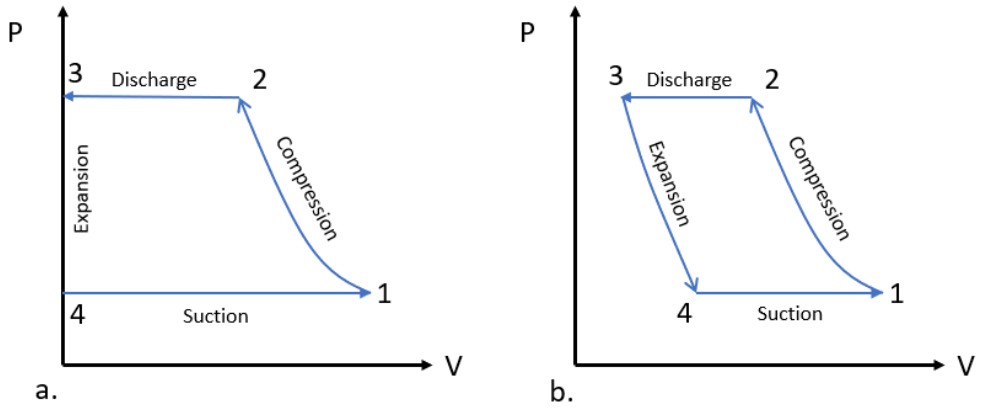

Figure 4.7: Compression cycles, a) ideal, b) theoretical.

Effects of decreased volume flow rate

• Dead Volume

The swept volume of the piston for a single turn is:

$$V_D = V_1 - V_3$$

The dead volume, V_3, is a topological characteristic of the cylinder, usually expressed as a fraction of displacement, $V_3 = C \cdot V_D$. C usually takes values between 0.02 and 0.10. Hence, a volumetric efficiency, or filling capacity, can be defined as:

$$e_{v0} = \frac{V_1 - V_4}{V_1 - V_3}$$

It is important to highlight that compression work increases due to part of the fluid being compressed but not leaving the cylinder but the impact on total work over a complete cycle is partially compensated for by the work produced by the same fluid in the expansion stroke.

The volumetric efficiency can be also expressed as a function of pressure ratio, PR, and C:

$$e_{v0} = 1 - C(PR^{1/n} - 1)$$

where e_{v0} decreases when PR increases. Hence, the maximum pressure ratio achievable corresponds to $e_{v0} = 0$:

$$PR = (1 + 1/C)^n$$

• Heating at the entrance

The gas entering the cylinder heats up due to the thermal transfer between the fluid and the duct walls which are at a higher temperature. Moreover, the walls of the cylinder are at an even higher temperature, increasing the temperature of the fluid during the intake (filling) phase, and reducing gas density. Hence, the volume for each filling is actually lower than $V_1 - V_4$. Referring to the inlet conditions at compressor intake, the actual volume is reduced by a factor $e_{v1} < 1$. If the temperature at the inlet to the cylinder can be measured,

$$e_{v1} = T_1 / T_i$$

This factor usually takes values between 0.97 and 0.99.

• Pressure losses at the inlet
From the inlet to the compressor to the cylinder inlet valve, there is a pressure loss due to filters, collectors and valves. Hence, both the pressure and density of the fluid are lower than at the inlet to the compressor. Referring to the inlet section to the compression system, the actual volume is reduced by a factor $e_{v2} < 1$. If the pressure at the inlet to the cylinder can be measured,

$$e_{v2} = P_i / P_1$$

This factor usually takes values between 0.97 and 0.99.

The factors e_{v0}, e_{v1} and e_{v2} refer to a reduced flow capacity, but they do not have a direct relation with the consumption of energy.

• Leakages
The flow at the compressor outlet is not the same as at the inlet section, mainly due to:

- Lack of tightness of the valves.
- Lack of tightness of the piston rings.
- Lack of tightness between the piston rod and the head, in case of a double-acting compressor.

If $\dot{V}$ is the useful volume flow rate (downstream of the discharge valve), f is defined as the fraction of $\dot{V}$ that is lost due to the aforelisted causes. Hence, a volumetric efficiency can be defined as:

$$\eta_v = \frac{\dot{V}}{\dot{V} + f\dot{V}} = \frac{1}{1+f}$$

f is strongly dependent on PR but it can be considered constant initially, with values between 0.01 and 0.06. As opposed to the previous factors, leakage directly affects compression work since it takes place once the fluid has been compressed.

Volume flow rate calculation
Defining D and L as piston diameter and stroke, displacement is calculated as:

$$V_D = V_1 - V_3 = \frac{\pi D^2}{4} L$$

If N is shaft speed and the number of cylinders operating in parallel is Z, the volume flow rate delivered is:

$$\dot{V} = V_D \cdot N \cdot Z \cdot j \cdot e_{v0} \cdot e_{v1} \cdot e_{v2} \cdot \eta_v$$

where j is 1 for single-acting or 2 for double-acting pistons. In the latter case, for higher accuracy, the volume of the connecting rod volume should also be considered, even though it is low compared to the entire volume.

Work for the theoretical compression cycle
The work needed to carry out a complete compression cycle like that presented in Fig. 4.7b is deduced in this section.

Equation 4.26 represents the polytropic compression and expansion processes. Compression work can be expressed as:

$$W = -\int_1^2 p \cdot dV + P_2 \cdot (V_2 - V_3) - \int_3^4 p \cdot dV + P_1 \cdot (V_1 - V_4) \tag{4.27}$$

Considering Eqs. 4.26 and 4.27, the following expression is achieved when considering a polytropic process with exponent n:

$$W = \frac{n}{n-1} \cdot P_1 \cdot (V_1 - V_4) \cdot \left(PR^{\frac{n-1}{n}} - 1 \right) \tag{4.28}$$

4.5.2 Thermodynamic analysis of reciprocating compressors: real compression cycle

This section deals with the influence that some phenomena that are not present in the theoretical cycle have on the real compression cycle (Fig. 4.7b), such as:

- Pressure loss due to valves.
- Delay in valve opening.
- Compression and expansion are not exactly polytropic.

The motion of suction and discharge valves is, in practice, driven by a pressure difference. If F is the force that the spring exerts on the valve plate, S is the surface exposed to the gas, and p_T is the target pressure, the discharge valve actually opens when:

$$p_T < F/S$$

Once the valve is open and the fluid starts flowing, there is a pressure loss Δp_f through the valve, as F also increases. Accordingly, the following condition ensures that the valve remains open and thew working fluid flows out from the cylinder:

$$p_T \leq F/S - \Delta p_f$$

The operation of the suction valve is similar. Once the working fluid trapped in the dead volume is expanded, the external pressure lifts the inlet valve. In particular, if the external pressure is p_e, F' is the force exerted on the inner side of the valve plate, and S' is the inner area of the valve, the suction valve opens when:

$$p_e > F'/S'$$

Once the valve opens and fluid starts to flow into the cylinder, there is a pressure loss Δp_f through the valve, and the cylinder pressure decreases further:

$$p_e - \Delta p_f \geq F'/S'$$

These processes are represented in the P-V diagram in Fig. 4.8, 2-2'-3 and 4-1'-1 for the discharge and suction valves, respectively. The curly waves from 2'-3 and 4-1' are due to the

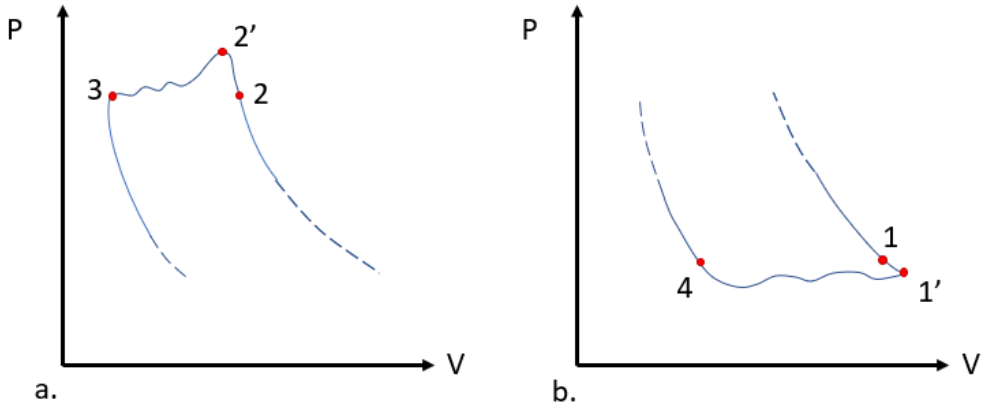

Figure 4.8: Compression cycles, a) ideal, b) theoretical.

vibrations of the valves.

Regarding processes 1-2 and 3-4 (Fig. 4.7b), Section 4.5.1 deals with them as polytropic processes where the polytropic exponent, n, is set to a constant value. However, this is not what actually happens due to the fluctuating temperatures of the fluid when entering/exiting the cylinder. When the fluid enters the cylinder, heat is transferred from the cylinder walls to the fluid, $\Delta Q > 0$, increasing its temperature. Hence, during compression, the polytropic coefficient is $n > k = C_p/C_v$.

In addition to the foregoing, and still during compression, the temperature of the fluid increases with pressure (Eq. 4.26). However, the cylinder wall temperature does not change significantly due to its higher mass and to the action of the cooling system. At some point, heat transfer changes direction and heat is transferred from the fluid to the cylinder walls. The opposite behaviour is observed during expansion. When the fluid is at station 3, the gas is hotter than the cylinder wall, but while expanding, the heat transfer is in the opposite direction.

For these reasons, the real compression cycle differs from the theoretical one, having the approximate shape of Fig. 4.9. Having the right instrumentation, it is possible to obtain the information to represent this cycle.

Polytropic work of real compression cycle

The suction and discharge pressures of the theoretical compression cycle are set to ambient (P_{ext}) and storage tank (P_{tank}) pressure respectively (Section 4.5.1). However, a better approximation would be to take into account the decrease in pressure due to pressure losses across the valves. This is shown in Fig. 4.10 where P_1 and P_2 are the inlet and outlet pressures of the theoretical compression cycle and $P_{1'} = P_1 - \Delta P_i$ and $P_{2'} = P_2 + \Delta P_s$ are the actual extreme pressures. Hence, adapting Eq. 4.28:

$$W = \frac{n}{n-1} \cdot P_{1'} \cdot (V_{1'} - V_{4'}) \cdot \left(PR^{\frac{n-1}{n}} - 1 \right)$$

since $P_{1'}/P_1 = e_{v2}$,

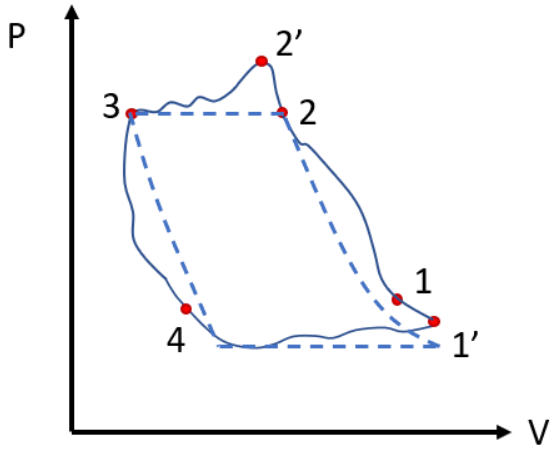

Figure 4.9: Real compression cycle (indicative).

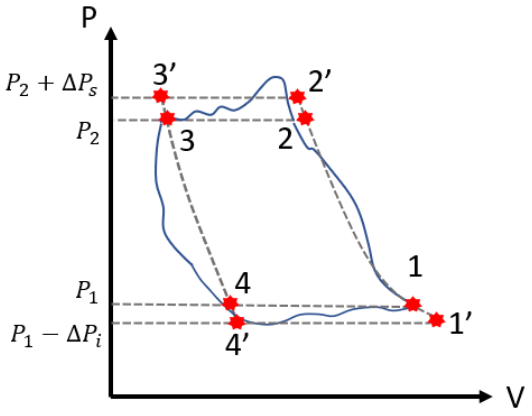

Figure 4.10: Real compression cycle: calculation of polytropic work.

$$W = \frac{n}{n-1} \cdot P_1 \cdot e_{v2} \cdot \frac{V_{1'} - V_{4'}}{V_1 - V_4} \cdot (V_1 - V_4) \cdot \frac{\left(PR^{\frac{n-1}{n}} - 1\right)}{\left(PR^{\frac{n-1}{n}} - 1\right)} \cdot \left(PR^{\frac{n-1}{n}} - 1\right)$$

It can be assumed that $(V_{1'} - V_{4'}) \approx (V_1 - V_4)$. In addition,

$$\frac{\left(PR^{\frac{n-1}{n}} - 1\right)}{\left(PR^{\frac{n-1}{n}} - 1\right)} \approx \frac{T_{2'}/T_{1'} - 1}{T_2/T_1 - 1} = \frac{T_1}{T_{1'}} \frac{T_{2'} - T_{1'}}{T_2 - T_1} \approx \frac{T_1}{T_{1'}} = e_{v1}$$

Hence,

$$W_p = \frac{n}{n-1} \cdot P_1 \cdot e_{v1} \cdot e_{v2} \cdot (V_1 - V_4) \cdot \left(PR^{\frac{n-1}{n}} - 1\right)$$

The power needed to operate the compressor according to the polytropic cycle is $\dot{W}_p = W_p \cdot N$. If

$$\dot{V} = V_D \cdot Ne_{v0} \cdot e_{v1} \cdot e_{v2} \cdot \eta_v = (V_1 - V_4) \cdot Ne_{v1} \cdot e_{v2} \eta_v$$

Then,

$$\dot{W}_p = \frac{n}{n-1} \cdot \frac{P_1 \cdot \dot{V}}{\eta_V} \cdot \left(PR^{\frac{n-1}{n}} - 1 \right) \tag{4.29}$$

4.5.3 Multistage reciprocating compressor

The compression ratio of a single cylinder (or stage) is limited by the temperature of the fluid inside the cylinder. Hence, when pressure ratio is very high, compression is split between several stages with an intercooling process to allow for the cooling of the main fluid prior to entering the next compression stage (Fig. 4.11). Additionally, very high pressure gradients might cause premature failure in bolts, connecting rods, bearings, etc.

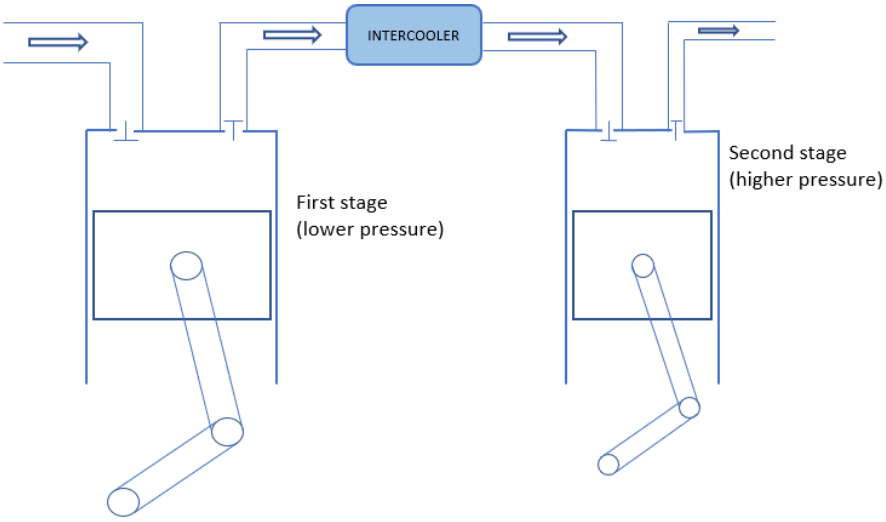

Figure 4.11: Intercooled multistage compression.

If the previous concept is represented in a p-V diagram (Fig. 4.12), the fluid is compressed until station 2' in the first cylinder. Then, the fluid is cooled in an intercooler (2'-1'), at essentially constant pressure (except for a minimum pressure loss) and compressed again in a second cylinder ownstream of the intercooler, now until station 2". This yields a total compression work per cycle (1-2'-3'-4" + 1'-2"-3-4') that is lower than in the reference case without intercooling and the same inlet conditions and service pressure (dashed line: 1-2-3-4).

Optimal compression ratio

An optimisation process needs to be carried out to find the optimal intermediate pressures in the case of multistage compression, with the objective to minimise specific compression work. The following hypotheses are made to find the optimal intermediate pressure:

1. The polytropic efficiency (η_P) is kept constant among stages.

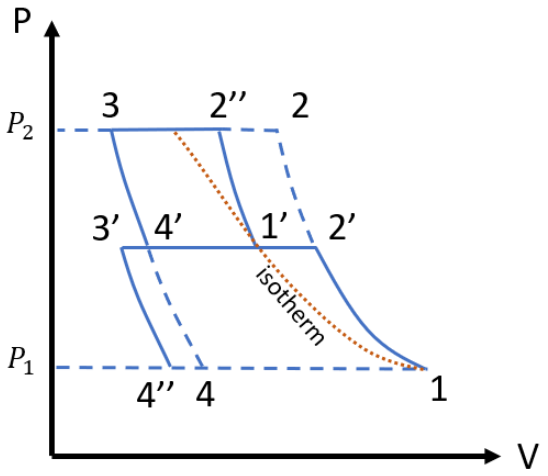

Figure 4.12: p-V diagram of a 2-stage intercooled compression.

2. There is no pressure loss through the intercooler.
3. Points 1 and 1' are on the same isotherm. That means that the fluid is cooled down to the same temperature as at the inlet of the first stage; even if this would be very costly, it can still be taken as a first approximation for the purpose of this section.

Taking into account hypotheses 1 and 2 in conjunction with Eq. 4.29,

$$\dot{W} = \dot{W}_A + \dot{W}_B = \frac{n}{n-1} \cdot \frac{1}{\eta_P} \cdot \left(P_1 \cdot \dot{V}_1 \cdot \left(PR_A^{\frac{n-1}{n}} - 1 \right) + P_{1'} \cdot \dot{V}_{1'} \cdot \left(PR_B^{\frac{n-1}{n}} - 1 \right) \right)$$

For hypothesis 3,

$$P_1 \cdot \dot{V}_1 = \eta_{V_A} \cdot P_{1'} \cdot \dot{V}_{1'}$$

Additionally, considering $\dot{V} = \frac{V_1}{\eta_{V_A} \cdot \eta_{V_B}}$, where $\dot{V}$ is the outlet volume flow rate (see Section 4.5.1),

$$P_1 \cdot \dot{V}_1 = \frac{P_1 \cdot \dot{V}}{\eta_{V_A} \cdot \eta_{V_B}}$$

Hence,

$$\dot{W} = \frac{n}{n-1} \cdot \frac{P_1 \cdot \dot{V}}{\eta_P} \left(\frac{1}{\eta_{V_A} \cdot \eta_{V_B}} \cdot \left(PR_A^{\frac{n-1}{n}} - 1 \right) + \frac{1}{\eta_{V_B}} \cdot \left(PR_B^{\frac{n-1}{n}} - 1 \right) \right)$$

In order to minimise specific power, $\dot{W}/\dot{V}$, PR_A and $PR_B = PR/PR_A$ must be chosen such that the following term is minimised,

$$\frac{PR_A^{\frac{n-1}{n}}}{\eta_{V_A}} + \left(\frac{PR}{PR_A} \right)^{\frac{n-1}{n}}$$

Cancelling the derivative regarding PR_A,

$$PR_A = \eta_{V_A}^{n/2(n-1)} \sqrt{PR}$$

Considering that η_{V_A} is 1 (Section 4.5.1),

$$PR_A = PR_B = \sqrt{PR} = \sqrt{\frac{P_2}{P_1}}$$

The prior analysis can be extended to more than 2 stages, in which case it results in:

$$PR_{stage} = PR^{1/No.stages}$$

4.6 Micro Gas Turbine

Section 3.2.4 introduced the general concept micro gas turbine (mGT), discussing the main differences between large GTs and mGTs, the main applications, and the main areas in need of research, respectively. The aim of this section is to describe the methodology followed to design and assess the performance of the different components in a mGT, as well as the engine as a whole. Figure 4.13 helps visualise the different subsystems and effects to be taken into account:

- Systems: Air filter, compressor, combustor, turbine, heat exchanger, and generator.
- Effects: Pressure loss in the air filter, combustor, heat exchanger, and pipes. Mechanical power loss due to shaft friction.

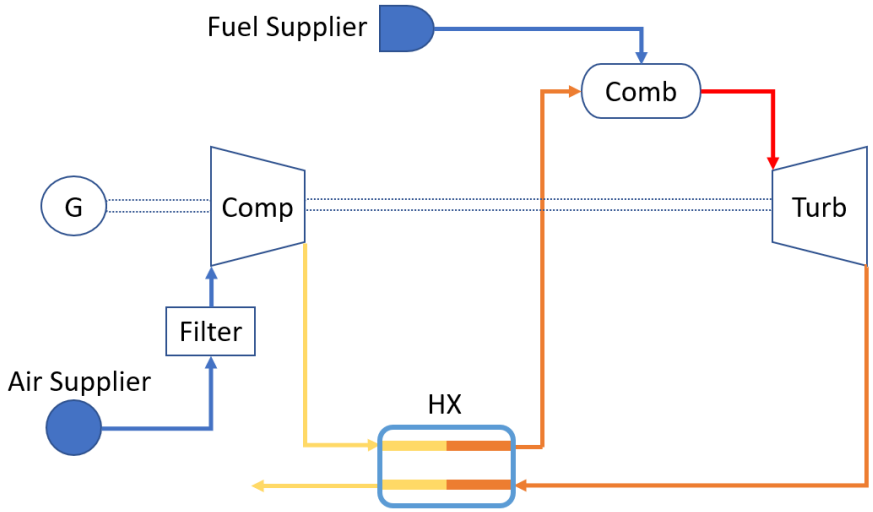

Figure 4.13: Systems comprising a mGT.

4.6.1 Air filtration

The quality of air entering the gas turbine is of utmost importance to ensure good performance and the long life of components. Hence, filtering ambient air upstream of the compressor significantly reduces erosion, fouling, and corrosion problems. Furthermore, air filtering allows for the reduction of gas turbine degradation and compressor washing, increasing the time between maintenance services. This is translated to higher profits from the operation of

the gas turbine.

Depending on the site where the mGT is located as well as the target filtration efficiency, the filtration system will rely on different filtration mechanisms (inertial impaction, interception, diffusion, and electrostatic), often using a comnination of them to ensure particles of different size and nature are trapped before entering the engine [146]. Filters are rated according to two main standards: ASHRAE standard 52.2:2007 (United States of America), which outlines the requirements for performance tests and the methodology to calculate the efficiencies, and EN 779:2002 / EN 1822:2009 (Europe). EN 779:2002 is used to rate coarse and fine efficiency filters. EN 1822:2009 presents a methodology for determining the performance of high-efficiency filters: Efficiency Particulate Air Filters (EPA), High-Efficiency Particulate Air Filters (HEPA), and Ultra Low Particulate Air Filters (ULPA) [147].

There are many considerations to be considered when it comes to selecting a filtration system:

- Filtration efficiency for a given particle size. The higher the target efficiency and the lower the particle size, the higher the pressure loss across the air filtration system.
- Degradation rate that is acceptable for the gas turbine.
- Maintenance labour that will be needed to maintain performance the filtration system.
- Type of washing scheme (online, offline or a combination of both).
- Cost of the filtration system.

The thermal performance is influenced by the pressure loss across the air filter, lowering the inlet pressure of the compressor and harming both specific output and cycle efficiency. To compensate for this, either engine pressure ratio or air flow rate needs to be increased if power output is to be kept constant, and in any case fuel consumption increases. The foregoing advantages of air filtration (longer life of components and lower performance degradation rate of the engine) more than offset the pressure loss across the the air filter. For the sake of modelling in this work, air filters are treated as a mere pressure loss upstream of the compressor.

4.6.2 Combustor

The power output of an mGT is controlled by heat input, generated by burning fuel in the combustor. In this regard, controlling combustor outlet temperature is crucial to avoid reducing the creep life of the turbine or, simply, overheating (melting) of it. This even more important in micro gas turbines due to the lack of turbine cooling.

This section aims to characterise the combustion process such that the following is known: stoichiometric fuel-air ratio, combustion heat release rate, combustion pressure loss and efficiency, calculation of NO_x and Unburned Hydrocarbons (UHC) emission rates.

Stoichiometric fuel-air ratio and combustion in excess air

Considering that air contains 1 mole of O_2 and 3.76 moles of N_2, and ignoring other components whose content is much lower than oxygen and nitrogen, the following combustion reaction of hydrogen in are can be derived:

$$H_2 + ms \cdot (O_2 + 3.76 \cdot N_2) = H_2O + ms \cdot 3.76 \cdot N_2$$

For complete combustion, the number of moles of air per mole of fuel is $ms = 0.5$. Considering that air enters the combustor, where only 21% is oxygen, the amount of air required for complete combustion is:

$$m_a = 2 \cdot ms \cdot 100/21 \cdot MW_{\text{Air}}$$

Therefore,

$$FAR = \frac{m_f}{m_a} = \frac{2 \cdot 1.008}{0.5 \cdot 100/21 \cdot (2 \cdot 15.999 \cdot 0.21 + 2 \cdot 14 \cdot 0.79)} = 0.02936$$

In other words, around 34.1 kg of air is needed for the complete combustion of 1 kg of H_2. This is much higher than 17.2 kg of air for the complete combustion of 1 kg of CH_4.

Gas turbines do not operate in stoichiometric conditions (globally) but, on the contrary, there is always more air than needed. The equivalence ratio is defined as the ratio from the actual to the stoichiometric Fuel-to-Air Ratio (*FAR*),

$$\phi = \frac{FAR}{(FAR)_s} = \frac{m}{ms}$$

where m is now in excess of ms and results in unreacted oxygen being present in the combustion gas stream. For lean mixtures, $\phi < 1$, and for rich mixtures, $\phi > 1$. ϕ is also useful to assess flame temperature since the maximum adiabatic flame temperature occurs for slightly rich fuel-air mixtures (e.g. $\phi = 1.05$). Moreover, combustion is possible in a narrow range of equivalence ratio only, between the upper and lower equivalence ratios (so called flammability limits).

Heat release, pressure loss and efficiency of combustion
The Heat Release Rate (HRR) in the combustor is defined as follows:

$$HRR = m_f \cdot LHV \cdot \eta_{CC} = m_a \cdot \phi \cdot (FAR)_s \cdot LHV \cdot \eta_{CC}$$

where LHV is the lower heating value of the fuel and η_{CC} is the efficiency of the combustor, defined later in this section. There are several phenomena that contribute to pressure losses of the main flow across the combustor. They can be summarized as follows:

- Skin friction of the mainstream with the components and annulus of the combustion chamber.
- High level of turbulence necessary for combustion, which extracts energy from the mainstream. These two effects are called cold loss and are proportional to the dynamic heat at of the flow at combustor inlet ($1/2\rho u^2$).
- The addition of heat in a flow which, to a certain extent, is not subject to friction (Raleygh flow) causes additional (hot) pressure losses.

The non-dimensional pressure loss can be expressed as:

$$\frac{\Delta P_{12}}{P_1} = PLF \cdot \left(\frac{W_1 \cdot \sqrt{R \cdot T_1/\gamma_1}}{P_1} \right)^2 \cdot \gamma \tag{4.30}$$

where:

- ΔP_{12} is the total pressure loss across the combustor (loss of total pressure).
- P_1 is the total pressure at combustor inlet.
- PLF is the combustor pressure loss factor.
- W_1 is the relative velocity at combustor inlet.
- T_1 is the combustor inlet temperature.
- R is the gas constant.
- γ is the isentropic exponent (c_p/c_v).

The PLF is given by:

$$PLF = K_1 + K_2 \cdot (T_2/T_1 - 1)$$

where K_1 and K_2 take constant values for a given combustor design and T_2 is combustor outlet temperature. Hence, for the cold loss, it is clear that $PLF = K_1$, which represents skin friction and turbulence alone. For an actual combustor, K_1 and K_2 are determined experimentally. Lefebvre states that the cold pressure loss in modern combustors ranges from 2.5 % to 5 % of the combustor inlet pressure [148]. Accordingly, it is common to assume that the combined pressure loss in the combustion chamber is approximately 4 % in total.

Combustor efficiency is defined as the ratio from the thermal energy absorbed by the flow of gases to the total heat released by the complete combustion of the fuel. It can be translated into the ratio from the theoretical FAR for a given temperature rise to the actual FAR for the same temperature rise. Hence, combustion efficiency is given by:

$$\eta_{CC} = \frac{\text{theoretical } FAR \text{ for a given } \Delta T}{\text{actual } FAR \text{ for a given } \Delta T}$$

If h_{t_1} and h_{t_2} are the total specific enthalpies at inlet and outlet of the combustor, the energy equation for this component is expressed as follows:

$$m_a \cdot (h_{t_2} - h_{t_1}) + m_f \cdot h_{t_2} = HHR$$

If the fuel-to-air ratio is introduced:

$$(1 + FAR) \cdot h_{t_2} = h_{t_1} + FAR \cdot LHV \cdot \eta_{CC} \tag{4.31}$$

Therefore, knowing the pressure loss (Eq. 4.30), the temperature rise and the air flow rate entering the combustion chamber, the fuel flow rate can be calculated from Eq. 4.31.

4.6.3 Compressor and turbine

The compressor in a micro gas turbine is a mechanical device used to compress the stream of inlet air before upstream of the combustor. This machine is driven by the turbine, convert the energy of the high-pressure, high-temperature gases generated by the combustion of fuel and compressed air into mechanical work. The surplus mechanical work of the turbine not used

to drive the compressor is then used to produce electricity.

There are several types of compressors and turbines that can be used for microturbines, including axial compressors/turbines, centrifugal compressors/turbines, and mixed-flow compressors/turbines. Centrifugal geometry arrangements are the most common in microturbines due to the low mass flow rates. In addition, centrifugal geometries also benefit from higher reliability, insensitivity to flow disruption as well as high-pressure ratios per stage, amongst other features.

Even though the aim of this section is not to go into the design of compressor and turbine wheels in detail, there are still some principles that are important to understand how these devices are designed. In turbomachinery, power is added to or removed from the fluid by the rotating components, which exert forces on the fluid flow changing both the energy content and angular momentum of the fluid. Euler's equations for turbomachinery relate the change in energy to the change in angular momentum, and it can be expressed as follows [149]:

$$\dot{W} = \dot{m} \cdot \omega(r_1 \cdot c_{1u} - r_2 \cdot c_{2u}) = \dot{m} \cdot (u_1 \cdot c_{1u} - u_2 \cdot c_{2u})$$

where ω is angular velocity, r is mean radius at the inlet/outlet of the blade, c_u is tangential velocity, u is peripheral velocity, $\dot{m}$ is mass flow rate, and $\dot{W}$ is power. 1 and 2 are the inlet and outlet sections of the wheel (rotating element of a compressor/turbine stage).

The performance of the compressor and turbine is of utmost importance for the overall efficiency of the microturbine, not only at the design point but also in off-design conditions. The power range for which the turbomachines are designed is a critical parameter for the isentropic efficiency since scale effects have a direct effect on the aerodynamic losses. Leandro Galanti *et al.* [150] provide detailed information about the isentropic efficiency of both compressors and turbines based on power range. The study shows how efficiency is maintained almost constant in the 50 kW-500 kW range but decreases substantially below 50 kW. In practice, efficiency frops from 86% to 83.5% and from 81% to 75% for turbines and compressors, respectively.

4.6.4 Recuperator

The main function of a recuperator is to preheat the air delivered by the compressor before entering the combustion chamber, making use of the high-grade thermal energy at the exit of the turbine, thereby decreasing fuel consumption and waste heat. This brings about a 10 to 15% efficiency increase.

When designing the recuperator, the main objective is to determine the geometry of this heat exchanger as a compromise between heat transfer effectiveness, pressure drop, small size and low-cost. The main hea exchanger types used for mGTs are primary-surface and plate-fin recuperators. Tubular recuperators have much higher reliability but typically are very large and bulky. Ward and Stephenson [151] reported that for a unit volume of primary-surface recuperator, 2.8 times and 11.8 times unit volume would be needed for plate-fin and tubular recuperators, respectively. The materials used in a recuperator are also very important because this choice determinea the maximum operating temperature of the component due to limitations in corrosion, oxidations, and creep resistance: stainless steel (< 650°C), Inconel (<

800°C), ceramics (> 870°C) [152].

There are mostly two different methods to assess the performance of a heat exchanger: the log mean temperature difference (*LMTD*) method and the effectiveness-*NTU* (ϵ-*NTU*) method. The first method is often used when the inlet and outlet temperatures of both streams are specified. However, if only the inlet temperatures are known, the use of the *LMTD* method requires a cumbersome iterative process. Since the outlet temperatures are not known, the ϵ-*NTU* method is preferred in this case. The objective of this method is to characterise the heat transfer between the hot and cold fluids. To do so, the maximum amount of heat that could be transferred is calculated, q_{max}. this q_{max} can be defined as:

$$q_{\max} = C_{\min}(T_{h,i} - T_{c,i}) \tag{4.32}$$

where $C_{\min}$ is the minimum heat capacity amongst the fluids exchanging heat, $T_{h,i}$ and $T_{c,i}$ are the inlet temperatures of the hot and cold fluids, and ϵ_{HE} is heat exchanger effectiveness, defined as the ratio from the actual heat transfer of the heat exchanger to the maximum hear transfer:

$$\epsilon_{HE} = \frac{q}{q_{\max}} \tag{4.33}$$

If ϵ_{HE}, $T_{h,i}$, and $T_{c,i}$ are known, the actual heat transfer rate can be determined from the expression:

$$q = \epsilon_{HE} C_{\min}(T_{h,i} - T_{c,i}) \tag{4.34}$$

For any heat exchanger, it can be shown that [153]

$$\epsilon_{HE} = f(NTU, \frac{C_{\min}}{C_{\max}})$$

where $C_{\min}/C_{\max}$ would be C_h/C_c or C_c/C_h. *NTU* is defined as the number of the transfer unit, a dimensionless parameter that is widely used for heat exchanger analysis and is defined as

$$NTU = \frac{U \cdot A}{C_{\min}} \tag{4.35}$$

Where *UA* is the product of the overall heat transfer coefficient, and the total area available for heat transfer. Because the geometry of the heat exchanger is unknown during the design process, *NTU* can be obtained from different relations that change according to heat exchanger arrangement. For the case we are dealing with here, primary-surface recuperators, the flow arrangement is counterflow and *NTU* is defined as:

$$NTU = \frac{1}{C_r - 1} \cdot \ln \frac{\epsilon_{HE} - 1}{\epsilon_{HE} C_r - 1} \qquad (C_r < 1) \tag{4.36}$$

$$NTU = \frac{\epsilon_{HE}}{1 - \epsilon_{HE}} \qquad (C_r = 1) \tag{4.37}$$

Therefore, knowing the inlet temperatures of the cold and hot fluids, and imposing target effectiveness for the recuperator, *NTU* can be calculated using Eqs. 4.36 or 4.37. Then, Eq. 4.35 can be used to determine *UA*, from which the heat transfer area can be determined if the

overall heat transfer coefficient is calculated. This is useful if the geometry of the recuperator is to be calculated. However, to solve the thermodynamic cycle, the outlet temperatures of both the hot and cold fluid can be calculated, further developing Eq. 4.33,

$$\epsilon_{HE} = \frac{C_h(T_{h,i} - T_{h,0})}{C_{min}(T_{h,i} - T_{c,i})} \tag{4.38}$$

Imposing a target recuperator effectiveness and applying Eq. 4.38, the thermodynamic conditions at which the recuperator is working can be known without knowing the specific geometry of the heat exchanger at the design point.

Everything discussed so far applies to the calculation of the off-design performance of the recuperator, although a different approach is followed here inasmuch as the geometry of the recuperator is not known yet. The off-design performance of a heat exchanger whose geometry is not known can be estimated with the conductance ratio method, recently discussed by Hoopes *et al.* [154]:

$$hA_{ratio} = \frac{h \cdot A_{hot}}{h \cdot A_{cold}}$$

The application of this method requires that hA_{hot} and hA_{hot} be known in on-design. To calculate these, the heat exchanger is divided into smaller partitions where the properties of both fluids remain constant (i.e., moderate temperature changes across the hear exchanger division. It is assumed that each division contributes with exactly the same duty and that the pressure drop through the heat exchanger as linear; this enables calculating the average properties of the fluid in each division, from which *UA* can then be calculated for each division:

$$Q = U \cdot A \cdot \Delta T \tag{4.39}$$

The values of Q and ΔT calculated previously are used to calculate the term UA for each division. Furthermore, UA can be defined by its constituent hA terms, ignoring conductance across the wall (which is acceptable in steady-state operation). With this, hA_{hot} and hA_{hot} can be calculated as follows [154]:

$$\text{Given: } h \cdot A_{\text{ratio}} \quad \text{and} \quad \frac{1}{U \cdot A} = \frac{1}{h \cdot A_{\text{hot}}} + \frac{1}{h \cdot A_{\text{cold}}}$$

$$\text{Substituting: } \frac{1}{U \cdot A} = \frac{1}{h \cdot A_{\text{hot}}} + \frac{1}{h \cdot A_{\text{hot}} / h \cdot A_{\text{ratio}}}$$

Now that hA_{cold} and hA_{hot} are determined for each division at on-design, the calculation of off-design heat exchanger performance can be carried out knowing the following off-design conditions: mass flow rates (and compositions) on both sides of the heat exchanger and new inlet temperatures and pressures at the inlet section (globally) on both sides.

Considering the same divisions as in the on-design case, Eq. 4.39 can be used to calculate each division's duty:

$$Q_{\text{off-design}} = U \cdot A_{\text{off-design}} \cdot \Delta T_{\text{off-design}}$$

In this case, the division $UA_{\text{off-design}}$ term is estimated by scaling the on-design division hA terms for both the hot and cold sides using the following scaling law:

$$h \cdot A_{\text{off-design}} = h \cdot A_{\text{on-design}} \cdot \left(\frac{\lambda_{\text{off-design}}}{\lambda_{\text{on-design}}}\right) \cdot \left(\frac{Re_{\text{off-design}}}{Re_{\text{on-design}}}\right)^{x} \cdot \left(\frac{Pr_{\text{off-design}}}{Pr_{\text{on-design}}}\right)^{y}$$

Because the off-design flow conditions on the hot and cold sides of the heat exchanger are independent, the hA term for each division is scaled separately on each side of the heat exchanger. To aid in the calculation, Reynolds number is defined in terms of stream mass flow and the lengthscale is assumed to be constant. This allows writting the scaling law as:

$$h \cdot A_{\text{off-design}} = h \cdot A_{\text{on-design}} \cdot \left(\frac{\lambda_{\text{off-design}}}{\lambda_{\text{on-design}}}\right) \cdot \left(\frac{(\dot{m}/\mu)_{\text{off-design}}}{(\dot{m}/\mu)_{\text{on-design}}}\right)^{x} \cdot \left(\frac{Pr_{\text{off-design}}}{Pr_{\text{on-design}}}\right)^{y}$$

where the values for x and y can be defined by the user, separately for the hot and cold sides.

The hot and cold hA for each division can be combined to obtain the value of UA for said division and, therefore, each division's duty in off-design. With this value, the downstream enthalpy oon both sides can be computed. When combined with the downstream pressure, the downstream temperature and all other required properties of the fluid can be calculated from enthalpy.

$$\frac{1}{U \cdot A_{\text{off-design}}} = \frac{1}{h \cdot A^{\text{hot}}_{\text{off-design}}} + \frac{1}{h \cdot A^{\text{cold}}_{\text{off-design}}}$$

The pressure drop on both sides of the heat exchanger can also be scaled for off-design operation as follows:

$$\Delta P_{\text{off-design}} = \Delta P_{\text{on-design}} \cdot \frac{(\dot{m}^2/\rho)_{\text{off-design}}}{(\dot{m}^2/\rho)_{\text{on-design}}}$$

The pressure can be updated for each division, knowing the pressure drop value for each iteration. This is carried out for each division in order to finally determine the outlet temperature of the fluid. This iterative process stops when the error in the outlet temperature for two consecutive iterations is below a certain threshold.

4.6.5 Off-design operation of the micro gas turbine

The current section describes the thermodynamic model adopted to estimate the performance od the mGT in off-design operation. Using in-house software developed at the University of Seville, off-design maps of the compressor and turbine are obtained. A minimum turndown capability of 20% is assumed, from which the running line of the mGT is found by merely matching the off-design performance maps of turbomachines assembled on the same shafts. In this regard, the methodology explained below corresponds to a single-shaft, recuperative gas turbine [155] whose off-design performance comes determined by the interaction of the engine's components: compressor, turbine, combustor, and recuperator. This is the most common arrangement in the mGT industry, applying to almost all engines in the market.

Off-design performance of the compressor and turbine in a micro gas turbine is usually represented by non-dimensional characteristics for the variation of temperature, pressure,

mass flow rate, and speed, whilst isentropic efficiency is the metric for process reversibility. The definitions of these non-dimensional parameters are as follows, assuming the gas behaves ideally:

$$\text{Non-dimensional flow} = \frac{\dot{m}_{in} \cdot \sqrt{R_{in} \cdot T_{in}/\gamma_{in}}}{D^2 \cdot P_1} \tag{4.40}$$

$$\text{Non-dimensional speed} = \frac{N}{\sqrt{\gamma_{in} \cdot R_{in} \cdot T_{in}}} \tag{4.41}$$

$$\text{Pressure ratio} = P_{out}/P_{in} \quad \text{(for a compressor or } P_{in}/P_{out} \text{ if a turbine)} \tag{4.42}$$

$$\tag{4.43}$$

where $\dot{m}_{in}$, T_{in}, P_{in} and D are the inlet mass flow rate, temperature, pressure, and wheel (rotor) diameter of the compressor or turbine, respectively, and N is the rotational speed of the machine (all properties evaluated at the inlet to the machine). P_{out} is the discharge pressure of the compressor or turbine and R_{in} and γ_{in} are the gas constant and isentropic exponent. Figures 4.14 and 4.15 show typical off-design performance maps of radial compressor and turbine in terms of corrected mass flow rate and pressure ratio (compression ratio for the compressor and expansion ratio for the turbine); efficiency islands are also shown.

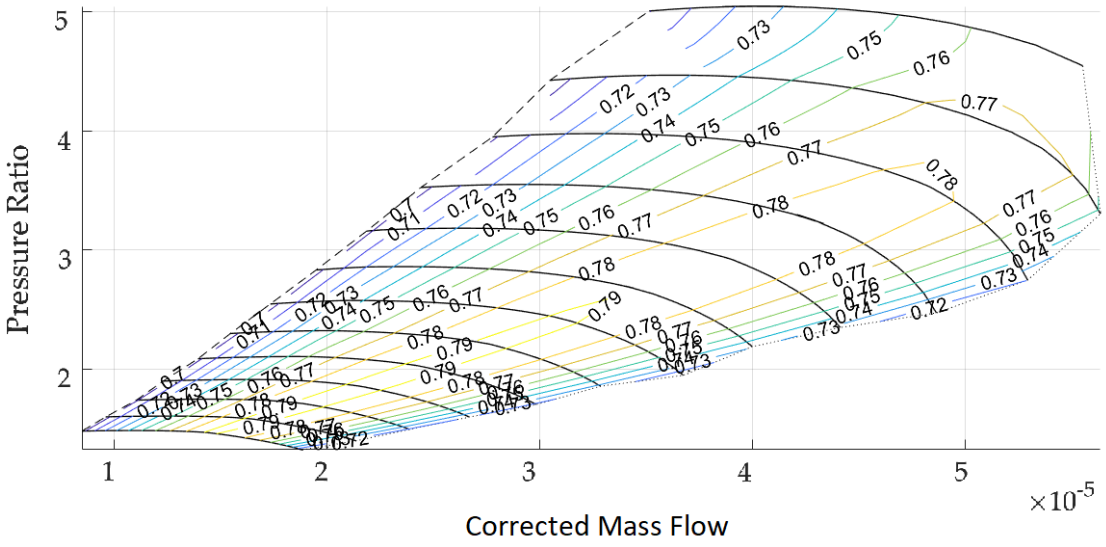

Figure 4.14: Corrected compressor map for a 30 kW mGT. [156]

The matching process between compressor and turbine considers that the pressure losses at the inlet (to the compressor) and outlet (from the expander) are negligible and that the absolute mass flow rate through the compressor and turbine are equal (i.e., hydrogen mass flow rate is much lower than that of air), this latter assumption is justified based on the very high heating value of hydrogen and low turbine inlet temperature of most micro gas turbines (≃1000ºC). The process to find the new operating conditions in off-design is as follows:

Note that 1, 2, 5, and 6 subscripts refer to inlet/outlet of compressor/turbine, respectively.

- Step 1: Specify turbine inlet temperature (T_5), shaft speed (N_1), compressor inlet pressure (P_1) and temperature (T_1).

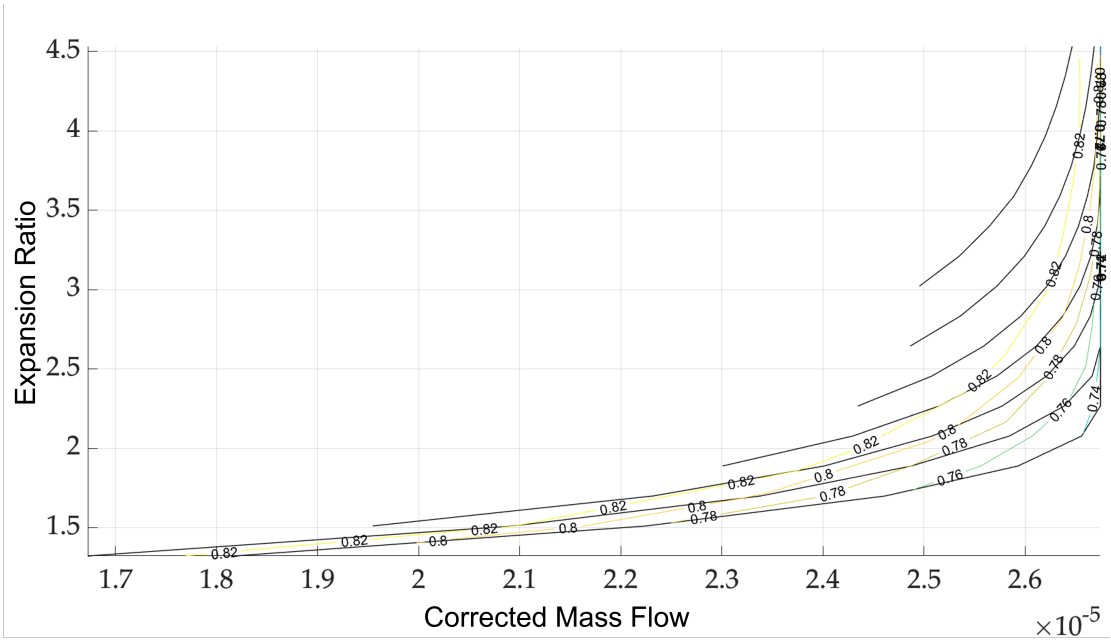

Figure 4.15: Corrected turbine map for a 30 kW mGT. [156]

- Step 2: Estimate compressor inlet flow ($\dot{m}_1$) and pressure ratio (P_2/P_1).
- Step 3: Compressor:
  - Step 3.1: Calculate corrected mass flow rate, Eq.(4.41).
  - Step 3.2: Determine corrected speed and isentropic efficiency (η_{12}) from the corrected performance map of the compressor, Fig. 4.14, using the corrected mass flow rate and pressure ratio (P_2/P_1) of the compressor estimated in previous steps.
  - Step 3.3: Calculate compressor outlet temperature (T_2) and power consumption (W_{comp}):

$$T_2 = T_1 \cdot \left(1 + \frac{(P_2/P_1)^{\frac{\gamma-1}{\gamma}}}{\eta_{12}}\right) \tag{4.44}$$

$$\dot{W}_{comp} = \dot{m}_1 \cdot (h_2 - h_1) \tag{4.45}$$

    where h_1 and h_2 are the specific enthalpies at compressor inlet and outlet.

- Step 4: Turbine:
  - Step 4.1: Calculate corrected mass flow rate (Eq. 4.41).
  - Step 4.2: Determine corrected speed and isentropic efficiency (η_{56}) from the corrected performance map of the turbine, Fig. 4.15, using the corrected flow rate and pressure ratio (P_5/P_6) of the turbine.

  - Step 4.3: Calculate turbine outlet temperature (T_6) and power ($\dot{W}_{tur}$):

$$T_6 = T_5 \cdot \left(1 - \left(\frac{P_6}{P_5}\right)^{\frac{\gamma-1}{\gamma}}\right) \cdot \eta_{56} \tag{4.46}$$

$$\dot{W}_{tur} = \dot{m}_1 \cdot (h_5 - h_6) \tag{4.47}$$

    where h_5 and h_6 are the specific enthalpies at turbine inlet and outlet.

- Step 5: Combustor and recuperator:
  - Step 5.1: Calculate air temperature at the inlet to the combustor or outlet from the recuperative heat-exchanger (T_4).
  - Step 5.2: Calculate combustor outlet temperature (T_5):

$$T_5 = T_4 \cdot \frac{1 + \frac{FAR \cdot \eta_{CC} \cdot LHV_{H_2}}{\overline{c_P} \cdot T_4}}{1 + FAR} \tag{4.48}$$

    where FAR is the fuel-to-air ratio already discussed in a previous section, and $\overline{c_P}$ is the average specific heat between T_4 and T_5, respectively.

- Step 6: Check 1:
  - Step 6.1: Compare the calculated rotational speeds of compressor and turbine. If they are not the same, update $\dot{m}_1$. This loop involves steps 3 and 4.

- Step 7: Check 2:
  - Step 7.1: Compare the calculated turbine inlet temperature and the target *TIT*. If they are not the same, update PR. This involves steps 3, 4, and 5.

After completing the matching process with Figs. 4.14 and 4.15, the performance map of the mGT can be obtained. Figure 4.16 shows this result for a certain engine, making use of a specific set of turbomachinery performance maps. The curves in Fig. 4.16 represent the performance of the engine when running at reduced mass flow rate, with the rated turbine inlet temperature and an ambient temperature of 20 °C. Steps 1 to 7 above must be repeated to find a new set of curves for a different ambient temperature.

4.7 Conclusions

A power-to-hydrogen-to-power system for energy storage is comprised of a number of subsystems, such as power generator running on renewable energy to drive hydrogen production in an electrolyser, followed by a hydrogen storage system. This storage capacity is key to enable decoupling renewable energy generation and coverage of the electricity demand, in spite of the non-dispatchable nature of most renewable energy sources.

The integration of the different systems comprising a power-to-power energy storage system is complex and.sometimes, tedious. Hence, having mathematical models and a tool that facilitates the integration and visualisation of the different key parameters of such a system is instrumental to enable optimisation of both component and system integration. The author of this work has dived in the modelling details of each system, with a special contribution to

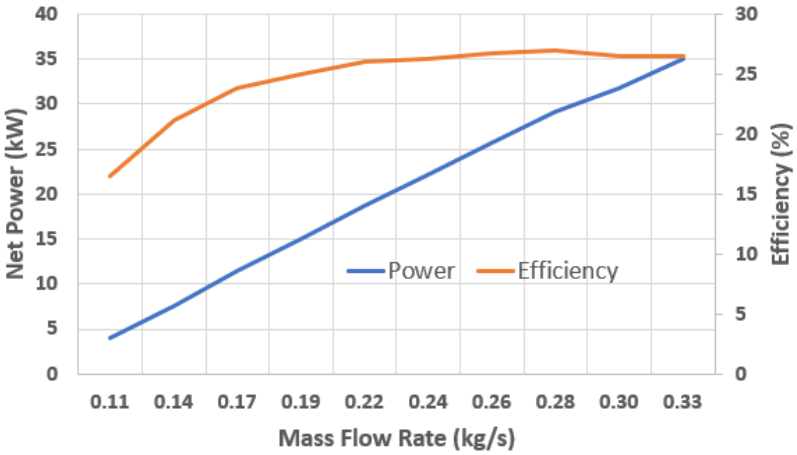

Figure 4.16: Off-design performance of an exemplary 30 kW_e mGT engine. [156]

the modelling of the electrolyser and compression systems. Regarding the latter, the existing literature consistently portrays a simplistic model of the system that assumes a constant volume flow rate and service pressure, regardless of the charging state of the storage system. In addition, various operational strategies have been identified and integrated into the software developed, marking a significant achievement for assessing the P2P-ESS under different scenarios for diverse applications. Moreover, the software has already been utilised to conduct a comprehensive examination of a hydrogen production and storage facility located at the industrial port of Seville, during a training secondment carried out at Alener, and there are plans to make use of it in follow-on collaborations scheduled for the near future.

Equations	PEMEC	SOEC
Voltage	$V = V_{ocv} + V_{act,an} + V_{act,cat} + V_{diff} + V_{ohm}$	
Open Circuit Voltage	$\Delta G = \Delta G^* + R \cdot T_{cell} \cdot ln\frac{a_{H_2} \cdot a_{O_2}^{0.5}}{a_{H_2O}}$ $\Delta G^* = \Delta H^* - T_{cell} \cdot \Delta S^*$	
Activation Overpotential	$V_{act,an} = \frac{R \cdot T_{an}}{\alpha_{an} \cdot F} \sinh^{-1}(\frac{j}{2 \cdot j_{0,an}})$ $V_{act,cat} = \frac{R \cdot T_{cat}}{\alpha_{cat} \cdot F} \sinh^{-1}(\frac{j}{2 \cdot j_{0,cat}})$	
	Table 4.3	$J_{0,i} = \gamma_i \cdot \exp\left(-\frac{E_{act,i}}{R \cdot T}\right)$
Ohmic Overpotential	$\Delta V_{ohm} = (R_{\text{electrolytes}} + R_{\text{mem}}) \cdot i_{\text{useful}} \cdot A$ $R_{\text{electrodes}} = R_{ano} + R_{cat} = \frac{t_{ano} \cdot \rho_{ano}}{A} + \frac{t_{cat} \cdot \rho_{cat}}{A}$ $R_{mem} = \frac{t_{mem}}{\sigma_{mem} \cdot A}$ $\sigma_{mem} = (0.005139 \cdot \lambda - 0.00326) \exp\left[1268 \cdot \left(\frac{1}{303} - \frac{1}{T}\right)\right]$	$R_{eq,ohm} = \frac{r_{cat} \cdot t_{cat} + r_{el} \cdot t_{el} + r_{an} \cdot t_{an}}{A}$ Table 4.5
Difussion Overpotential	$\Delta V_{con} = V_{con_{H_2}} + V_{con_{O_2}} \approx 0$	$\Delta V_{con} = V_{con_{H_2}} + V_{con_{O_2}}$ $V_{con,H_2} = \frac{R \cdot T}{2 \cdot F} \cdot ln\left(\frac{1 + (J \cdot R \cdot T \cdot d_{H_2} / 2 \cdot F \cdot D_{H_2O}^{eff} \cdot P_{H_2}^0)}{1 - (J \cdot R \cdot T \cdot d_{H_2} / 2 \cdot F \cdot D_{H_2O}^{eff} \cdot P_{H_2O}^0)}\right)$ $V_{con,O_2} = \frac{R \cdot T}{4 \cdot F} ln\left(\frac{\sqrt{(P_{O_2}^0)^2 + (J \cdot R \cdot T \cdot \mu \cdot t_{O_2} / 2 \cdot F \cdot B_g)}}{P_{O_2}^0}\right)$

Table 4.10: Summary of equations for the semi-empirical modeling of electrolysers

Tank refilling	Tank dimensions	Compression system
$\frac{T-\gamma \cdot T_e}{T_i-\gamma \cdot T_e} = \frac{1}{1+(K \cdot t/N_i)}$	**Cylindrical Shell:** $t = \frac{P \cdot R}{2 \cdot S \cdot E - 0.2 \cdot P}$	$W_{comp} = n_{st} \cdot \frac{\frac{n}{n-1} \cdot R \cdot T_1 \cdot Z_{avg} \cdot PR^{\frac{n-1}{n}-1}}{\eta_{comp}}$
$\frac{P}{P_i} = 1 + \left(\frac{\gamma \cdot T_e}{T_i}\right)(K \cdot t/N_i)$	**Spherical Shell:** $t = \frac{P \cdot R}{2 \cdot S \cdot E - 0.2 \cdot P}$	$n_{st} = \frac{\log \frac{P_2}{P_1}}{\log PR_{stage}}$
	Ellipsoidal Head: $t = \frac{P \cdot D}{2 \cdot S \cdot E - 0.2 \cdot P}$	$W_{pump} = n_{stages} \cdot \frac{g \cdot H \cdot \frac{\dot{m}_{H_2O}}{\dot{m}_{H_2}}}{\eta_{pump}}$
	Torispherical Head: $t = \frac{0.885PL}{S \cdot E - 0.1 \cdot P}$	$\frac{\dot{m}_{H_2O}}{\dot{m}_{H_2}} = \frac{h_{1_{H_2}} - h_{2_{H_2}}}{h_{2_{H_2O}} - h_{1_{H_2O}}}$
	Hemispherical Head: $t = \frac{P \cdot L}{2 \cdot S \cdot E - 0.2 \cdot P}$	

Table 4.11: Summary of equations for the storage system modeling

5 Power-to-Power Economics

After reviewing the power-to-power concept in Chapter 3 and the modelling of each system in Chapter 4, the current chapter introduces a detailed analysis of the economics of each system by carrying out an extensive literature review and extracting the information for each of the systems, paying special attention to the capital and operational expenditures of the renewable energy technologies, electrolysers, compression system, storage technologies, and micro-gas turbine. Furthermore, metrics are reported to evaluate the impact of economics, such as the levelized cost of hydrogen and energy, as well as the payback period and internal rate of return.

The contents of this chapter are partially available in:

A. Escamilla, D. Sánchez, L. García-Rodríguez, 2023, *Techno-economic study of Power-to-Power renewable energy storage based on the smart integration of battery, hydrogen, and micro gas turbine technologies*, Energy Conversion and Management: X, Vol. 18, pp. 100368.

5.1 Capital and Operating Expenditures for each subsystem

Detailed information of the CapEx and OpEx for each subsystems in the power-to-power energy storage system is of utmost importance to determine the economic viability of the concept proposed. These values are be used to assess the levelised cost of hydrogen and energy, explained in detail in Section 5.3.

This section introduces a literature review of both CapEx and OpEx for: photovoltaic panels, wind turbines, electrolyser (Alkaline, Proton-Exchange Membrane and Solid-Oxide), compression system (diaphragm and reciprocating compressors), high-pressure storage vessels, and micro-gas turbine. However, due to the fast learning curve of these technologies, the index year of the available CapEx and OpEx data must be carefully taken into account, in order for it to still be meaningful. Therefore, along with the literature review, Section 5.2 proposes a methodology to estimate the CapEx for future years based on reference data and learning rate of the technology. To this end, all costs have been updated to 2021 according to the Harmonised Index of Consumer Prices (HICP) for the Eeuro area. The costs in $ are left in that currency, and whenever used in a study, these are converted to the currency used in the study.

5.1.1 Renewable energy: solar PV and wind turbine

Solar and wind power technologies have already achieved high maturity and are consolidated worldwide. The installation costs of these technologies have dropped considerably over the

last 10 years, from 4808 $/kW and 2042 $/kW in 2010 to 883 $/kW and 1325 $/kW in 2020 for solar PV and onshore wind power [157], respectively. Due to the fast learning curve of these technologies, CapEx data from previous publications might get outdated soon. Therefore, the aim of this section is to provide an updated database of CapEx and OpEx for photovoltaic and wind power systems, shown in Table 5.1. Table 5.1 shows the weighted-average costs taken from a recent report published by IRENA on the topic [157], where information about regional variations of costs is also available; this is interesting when different countries are compared and for scenarion analysis. Another report by the National Renewable Energy Laboratory of United States (NREL) provides CapEx and OpEx forwind turbines in specific scenarios [158].

RE Type	Index year[1]	CapEx (2021 $/kW)	OpEx (2021 $/kW)	Source
Onshore wind (land-based[2])	2019	1501	40	[158]
Onshore wind (residential[3])	2019	5675	35	[158]
Onshore wind (commercial[4])	2019	4300	35	[158]
Onshore wind	2020	1325	33-56	[157]
Offshore wind (fixed-bottom[5])	2019	3871	111	[158]
Offshore wind (floating[6])	2019	5557	118	[158]
Offshore wind	2020	2,858	70-129	[157]
PV (commercial)	2020	883	14	[157]
PV (rooftop)	2020	1397[7]	-	[157]

1. Index year refers to the year when the information is published.
2. Based on a 2.6-MW land-based wind turbine.
3. Based on a 20-kW residential distributed reference project.
4. Based on a 100-kW commercial distributed reference project.
5. Based on a 6.1-MW fixed-bottom off-shore reference project.
6. Based on a 6.1-MW floating off-shore reference project.
7. Based on rooftop costs in Spain. Look at reference [157] for other regions.

Table 5.1: Reference CapEx and OpEx of selected renewable energy technologies.

The operation and maintenance (O&M) costs of utility-scale solar PV plants have also decreased in recent years, driven by module efficiency enhancements along with improvements in the reliability of the technology. The aforecited report by IRENA, published in 2020 [157], estimates USD 14/kW per year. These costs include 'all-in' O&M costs, such as insurance and asset management, which are sometimes not reported in other O&M surveys. In the case of onshore wind turbines, O&M changes from region to region and from the year of establishment of the wind farm. Hence, between 2016 and 2018, O&M costs for onshore wind have ranged from USD 33/kW per year (in Denmark) to USD 56/kW per year (in Germany) [157]. In the case of offshore wind farms, the availability of O&M data is limited due to the recent deployment of the technology, as compared to other mature technologies. Additionally, O&M costs of offshore wind farms are higher than those for onshore facilities mostly due to difficulties accessing offshore sites as well as transport of qualified personnel to the site. For 2018, representative ranges for O&M of offshore windfarms ranged from USD 70/kW per year to USD 129/kW per year [157]. The lowest cost has been found for wind farms in Europe and China. However, this wide range is very sensitive to distance to shore and to whether or not the wind farm is placed in an offshore wind hub.

5.1.2 Electrolyser

The main costs of an electrolyser are the ones related to the stack and balance of plant, representing 45% and 55% of the total cost [116], respectively. The cost breakdown of these different components is shown in Fig. 5.1. The stack is the element experiencing highest degradation, having a lifetime of around 100,000 hours (Table 2.6) in the best case scenario. Thus, increasing the lifetime of the stack is of utmost importance to reduce the levelised cost of hydrogen, since it accounts for almost half of the total system cost.

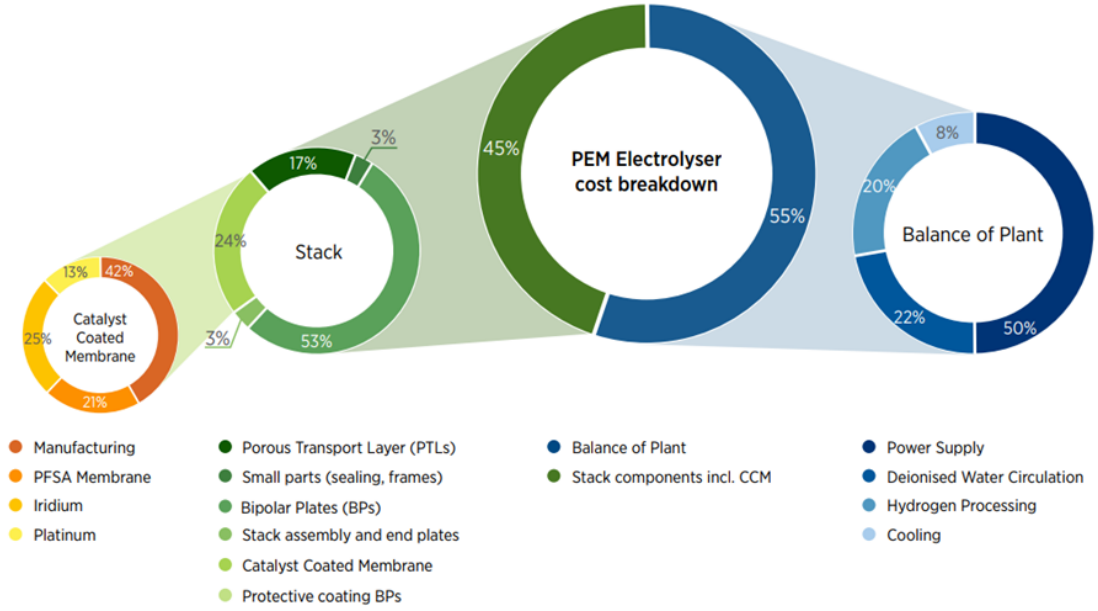

Figure 5.1: Cost breakdown for a 1 MW PEM electrolyser, moving from full system, to stack, to CCM. Courtesy of IRENA [116].

Glenk *et al.* [159] carried out a study to determine the cost of a hybrid power-to-gas plant. They gathered cost estimates of different electrolyser technologies (AEC, PEMEC & SOEC) from manufacturers, operators of power-to-gas plants, scientific articles in peer-reviewed journals and frequently cited grey literature including reports by agencies, consultancies and industry analysts. This study came with the target to harmonise the costs of electrolysers found in different sources and for different applications. All the information from this source [159] has been gathered in Table 5.2, where the original source of information is also reported. Additional data from 2017 onwards has been collected by the author of this thesis.

Due to the diversity of the information collected in this literature review with respect to the fiscal year used as an index to provide costs, a regression model has been applied to compensate for inflation. Figures 5.2, 5.3, and 5.4 show the regression function and the R-square value, showing a clear trend towards lower CapEx, regardless of the electrolyte technology considered.

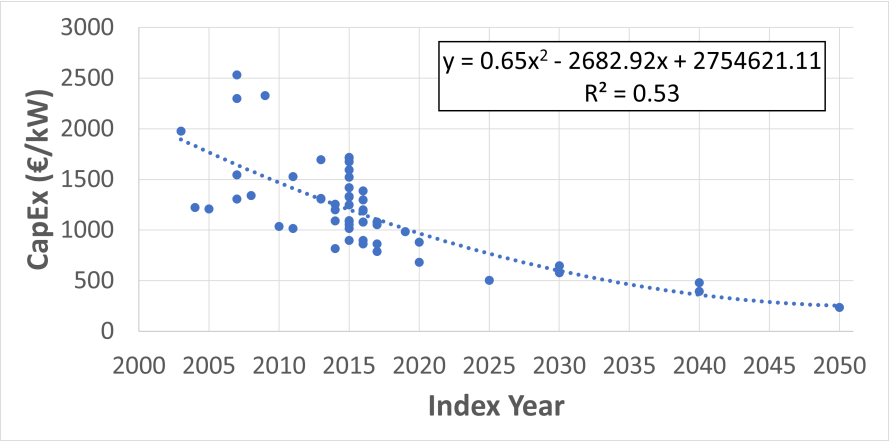

Figure 5.2: Alkaline Electrolyser.

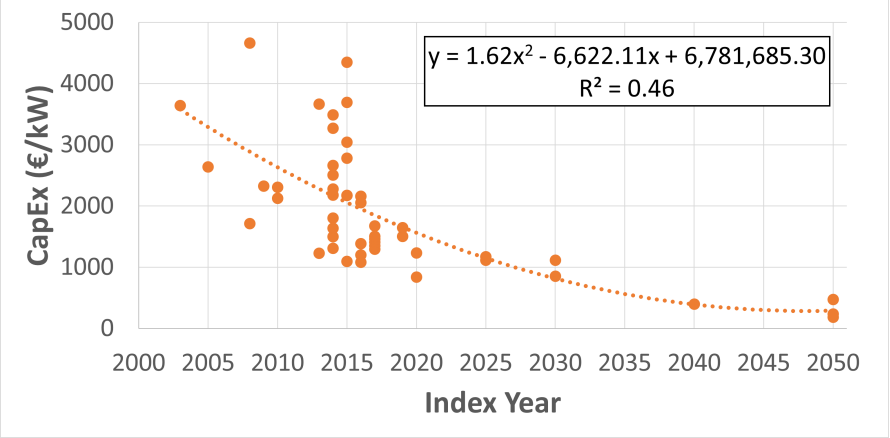

Figure 5.3: Proton-Exchange Membrane Electrolyser.

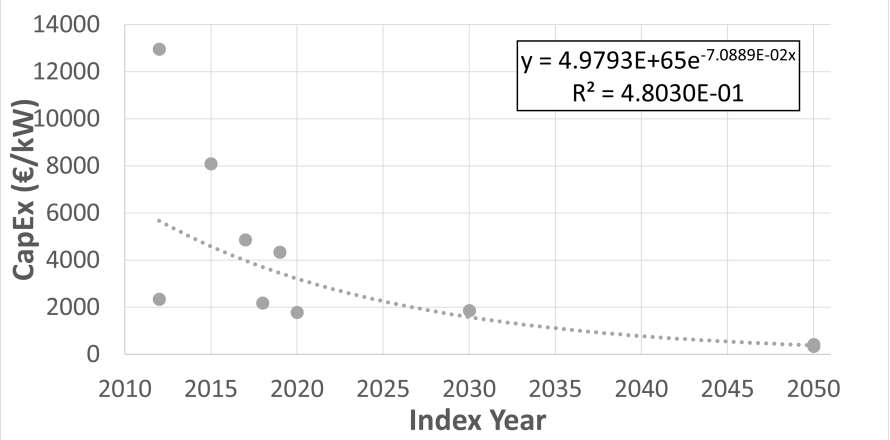

Figure 5.4: Solid Oxide Electrolyser.

Figure 5.5: CapEx vs Index Year for different electrolyser types. In the legend, '*y*' is CapEx and '*x*' is Index Year. R^2 stands for R-squared. The dotted line corresponds to the regression function (quadratic).

Electrolyser Type	Index Year	CapEx (2021 €/kW)	Original Source
AEC	2003	1976	[160]
AEC	2004	1222	Report - N/A (see [159])
AEC	2004	1222	Report - N/A (see [159])
AEC	2005	1210	[161]
AEC	2007	2300	[162]
AEC	2007	1546	[163]
AEC	2007	2553	[164]
AEC	2007	1307	[165]
AEC	2008	1341	[166]
AEC	2009	2327	[167]
AEC	2010	1037	[168]
AEC	2011	1016	[169]
AEC	2011	1531	Report - N/A (see [159])
AEC	2013	1312	[170]
AEC	2013	1313	[171]
AEC	2013	1307	[172]
AEC	2013	1695	[173]
AEC	2014	818	[174]
AEC	2014	1253	[175]
AEC	2014	1253	[176]
AEC	2014	1199	[177]
AEC	2014	1090	[178]
AEC	2015	1717	Interview (see [159])
AEC	2015	1054	Interview (see [159])
AEC	2015	1675	Interview (see [159])
AEC	2015	1593	Interview (see [159])
AEC	2015	1331	Interview (see [159])
AEC	2015	1711	Interview (see [159])
AEC	2015	1418	Interview (see [159])
AEC	2015	1328	Interview (see [159])
AEC	2015	1015	Interview (see [159])
AEC	2015	898	Interview (see [159])
AEC	2015	1087	Report - N/A (see [159])
AEC	2015	1087	Report - N/A (see [159])
AEC	2015	1093	[179]
AEC	2015	1521	[180]
AEC	2015	1250	Report - N/A (see [159])
AEC	2016	1080	[181]
AEC	2016	1201	[182]
AEC	2016	898	Interview (see [159])
AEC	2016	864	Report - N/A (see [159])
AEC	2016	1080	Report - N/A (see [159])
AEC	2016	1386	Presentation (see [159])
AEC	2016	1296	[183]
AEC	2016	1188	[184]
AEC	2017	864	Report - N/A (see [159])
AEC	2017	1080	Report - N/A (see [159])
AEC	2017	1080	Report - N/A (see [159])
AEC	2017	1053	Report - N/A (see [159])
AEC	2017	788	[64])
AEC	2019	984	[185]

Table 5.2: Reference electrolyser CapEx from Glenk *et al.*. [159].

Electrolyser Type	Index Year	CapEx (2021 €/kW)	Original Source
AEC	2020	683	[186]
AEC	2020	881	[116]
AEC	2025	504	[64])
AEC	2030	647	[185]
AEC	2030	579	[186]
AEC	2040	482	[186]
AEC	2050	394	[186]
AEC	2050	235	[116]
PEMEC	2003	3639	[160]
PEMEC	2005	2636	Report - N/A (see [159])
PEMEC	2008	1714	[187]
PEMEC	2008	4661	[166]
PEMEC	2009	2327	[167]
PEMEC	2010	2304	[188]
PEMEC	2010	2124	[168]
PEMEC	2013	3663	Report - N/A (see [159]
PEMEC	2013	1226	Report - N/A (see [159])
PEMEC	2014	2506	[175]
PEMEC	2014	2661	[189]
PEMEC	2014	2179	[176]
PEMEC	2014	1804	Interview (see [159])
PEMEC	2014	1498	Report - N/A (see [159]
PEMEC	2014	3486	[190]
PEMEC	2014	2277	[177]
PEMEC	2014	1307	[191]
PEMEC	2014	1634	Report - N/A (see [159])
PEMEC	2014	3269	[178]
PEMEC	2015	3694	[192]
PEMEC	2015	2173	[193]
PEMEC	2015	1093	[179]
PEMEC	2015	4347	[194]*
PEMEC	2015	2782	[195]
PEMEC	2015	2173	Report - N/A (see [159])
PEMEC	2015	3042	[196]
PEMEC	2016	2160	[181]
PEMEC	2016	1201	[182]
PEMEC	2016	2160	[197]
PEMEC	2016	1386	Report - N/A (see [159])
PEMEC	2016	1080	[183]
PEMEC	2016	2052	[184]
PEMEC	2017	1296	Interview (see [159])
PEMEC	2017	1674	Interview (see [159])
PEMEC	2017	1350	Interview (see [159])
PEMEC	2017	1409	Report - N/A (see [159])
PEMEC	2017	1458	[198]
PEMEC	2017	1503	[64]
PEMEC	2019	1645	[199]
PEMEC	2019	1503	[185]
PEMEC	2020	1234	[116]
PEMEC	2020	840	[186]
PEMEC	2025	1173	[199]
PEMEC	2025	1114	[64]

Continuation of Table 5.2

Electrolyser Type	Year of Estimate	CapEx (2021 €/kW)	Original Source
PEMEC	2030	851	[199]
PEMEC	2030	1114	[185]
PEMEC	2040	395	[199]
PEMEC	2050	184	[199]
PEMEC	2050	235	[116]
PEMEC	2050	473	[186]
SOEC	2012	2346	[200]
SOEC	2012	12963	Report - N/A (see [159])
SOEC	2015	8102	Report - N/A (see [159])
SOEC	2017	4861	Report - N/A (see [159])
SOEC	2018	2179	[201]
SOEC	2019	4351	[185]
SOEC	2020	1786	[186]
SOEC	2030	1865	[185]
SOEC	2050	352	[116]
SOEC	2050	426	[186]

Continuation of Table 5.2

5.1.3 Reciprocating compressor

There are not many options in the market when comes to reciprocating compressors to work with hydrogen. Thus, the limited information about capital and operating costs of these machines might differ largely from one source to another. The aim of this section is to review the data from the main available sources in the open domain.

The requirements of the compression station depend on delivery pressure and, therefore, on the application. Within the aim of the current project, two main scenarios are of interest: hydrogen to be stored in high-pressure vessels at relatively high pressure (from 150 to 500 bar) or hydrogen to be injected in a transmission line, for which the delivery pressure would be lower (between 30 and 100 bar). In addition to this, the most demanding application is for refuelling stations, for which hydrogen needs to be compressed up to circa 1000 bar. This application is not relevant in this study but, given its likely importance in the future, data for it have alo been gathered in the literature review.

A report on hydrogen compression stations issued by NREL [202] reports CapEx and OpEx for different compression stations, using a diaphragm compressor for the first stages and a dry piston compressor for the final stage. The information about these systems was obtained from reciprocating compressor vendors for two different scenarios, central production pipeline scenario and distributed generation, yielding $1500/kW and $1428/kW ($ 2011) are , respectively. Annual maintenance cost was set 4% of the installed compressor cost.

Mohd Adnan Khan *et al.* also analysed the techno-economics of hydrogen compression [203]. They considered CApEx and OpEx correlations provided by the Hydrogen Delivery Scenario Analysis Model (HDSAM) [204], yielding the data reported in Table 5.3.

A study prepared for the Fuel Cell and Hydrogen - Joint Undertaking (FCH-JU) by Tractebel and Hinicio gives detailed correlations for compressor skids and filling centres [198]. The cost model is divided into 2 parts: site cost (first part of Eq. 5.4) and compression system

Compressor Type	Uninstalled Cost (UC)	Indirect Costs (IC)	Fixed O&M
High flow rate - Moderate compression ratio	Pipeline compressor: $2312.48 * kW^{0.8335}$ (5.1)	40 %	6.1 % of TIC
Small flow rate - High compression ratio	350 bar refuelling: $47763.45 * kW^{0.4603}$ (5.2) 700 bar refuelling: $47182.43 * kW^{0.6038}$ (5.3)	28 %	

Table 5.3: Cost correlations for hydrogen compression systems, as reported in reference [203]. 2019 US$. kW represents compressor power

cost (second part of Eq. 5.4). The site cost depends on site volumetric flow capacity (Q). The compression system cost depends on site capacity, compression ratio (PR), and pressure output (P_{out}). Table 5.4 contains the coefficients for Eq. 5.4.

$$\text{CapEx} = A \cdot (Q/Q_{\text{ref}})^{a} + B \cdot (Q/Q_{\text{ref}})^{b} \cdot (PR/PR_{\text{ref}})^{c} \cdot (P_{\text{out}}/P_{\text{ref}})^{d} \tag{5.4}$$

Coefficient	A	B	a	b	c	d	Q_{ref}	PR_{ref}	P_{out}
Filling centre	550 k€	300 k€	0.66	0.66	0.25	0.25	50 kg/h	30	200 barg
Compressor Skid	100 k€	300 k€							

Table 5.4: Coefficients to be used in Eq. 5.4

C. Yang and J. Ogden worked on determining the lowest-cost hydrogen delivery mode [205]. In their study, they used a cost function based on a reference 10 kW compressor to determine the cost of the compressor (Eq. 5.5). They also reported that OpEx of the compressor is 4% of the equipment CapEx (kW represents compressor power).

$$\text{CapEx} = 15000 \cdot \left(\frac{kW}{10}\right)^{0.9} \tag{5.5}$$

Nexant reported the total uninstalled cost of a 2-stage lubricated compressor (Eq. 5.6) based on electric motor rating, which is usually taken as 110 per cent of the actual power consumption of the compressor [206]. If a 3-stage compressor is used in lieu of a 2-stage unit, the compressor cost is estimated to increase to 120 per cent of the total installed cost of a 2-stage compressor

with the same motor rating. Equation 5.6 is valid for a lubricated compressor; in the case non-lubricated compressors are used, the motor rating is estimated to be 110% of the motor rating of a lubricated compressor with the same duty. This compressor cost estimation was developed to be included in the H2A Delivery Models [207].

$$\text{CapEx} = 19207(kW_e)^{0.6089} \tag{5.6}$$

André *et al.* used an adapted linear relationship (Eq. 5.7) from the National Research Council to calculate the investment costs of a compression station to be used at the connection points of a pipeline or for the truck transportation chain [208]. They also estimated an annual maintenance cost fee of 3% of CapEx (Eq. 5.7).

$$\text{CapEx} = 2545 \cdot kW \qquad [\$] \tag{5.7}$$

5.1.4 High-Pressure storage vessels

As was presented in Chapter 3, there are different ways to store and transport hydrogen. This section presents a literature review of the CapeEx and OpEx of high-pressure vessels or tube trailers transported by trucks. Note that Table 3.3 in Chapter 3 provides information about the material and pressure limits of different types of high-pressure vessels.

The aforecited report issued by Tractebel and Hinicio [198] makes a distinction between steel and composite vessels. The former is more suitable for stationary applications, whereas the latter is preferred when the available footprint is limited and/or if high pressure is needed (over 400 bar), such as mobile storage systems. Two designs can be considered for stationary applications: (i) large welded tanks having a water capacity of 50 m^3 and a service pressure of 50 bar, and (ii) assemblies (bundles) of steel cylinders allowing storage at up to 350 bar. In both cases and for pressures up to 350 bar, a CapEx of 470 €/kg_{H_2} is declared (cost per kg of H_2 stored). Stationary pressure vessels made of steel have a lifetime of 30-40 years but require maintenance and inspection every 10 to 15 years. This represents an annual OpEx of 2% of the initial capital investment of the storage system. In regards to the light industry market, hydrogen distribution is done by large bundles and tube-trailers. The capacity of large bundles ranges from 12.5 to 100 kg H_2 and that of tube-trailers varies from 200 to 1135 kg H_2 [209]. Table 5.5 reports CapEx and OpEx of high-pressure vessels in 2017. It also forecasts their costs for 2025. Stationary pressure vessels in steel have a lifetime of 20-30 years but require maintenance and inspection every 10 to 15 years. This represents an annual OpEx of 4% of the initial storage investment.

CapEx [€/kg_{H_2}]	Large Bundles	Tube-Trailers
	2017 - 2025	2017 - 2025
200 bar (steel)	470 - 470	500 - 500
500 bar (composite)	815 - 590	830 - 605

Table 5.5: Large bundle and tube-trailer storage cost projection [198]. Values reported as in the source.

Within the Hydrogen and Fuel Cells Program of the US Department of Energy, the Hydrogen Storage Cost Analysis Report (ST100) [210] reports that the cost of Type IV 220 kg H_2 pressure

vessel is 76851$. This is 350$/kg H_2, approximately. However, not only are pressure vessels needed, but also the steel containment structure, the balance of the plant, and assembly. Taking into account the cost of these complementary systems, a complete tube-trailer containing 4 x Type IV pressure vessels would have a cost of 422688$, which is 480$/kg H_2. It is important to note that any of these costs do not include company markup, which is usually in the range of 10% to 20%. Furthermore, the cost estimation is done considering the production of 100 tube-trailers per year.

5.1.5 Micro gas turbine

Micro gas turbine technology has been developed for a long time, but among the many challenges to better fit in the current energy scenario, it has failed to reduce the initial capital investment to less than 500 €/kW[1]. This section aims at performing a literature review to extract both the total investment and maintenance cost for micro-gas turbines of different sizes.

Matthew A. Cuomo *et al.* carried out an economic and environmental analysis of multi-generation renewable energy systems for dairy farms [211]. In their study, equipment and installation costs as well as maintenance costs are reported for several configurations of mGTs, accounting also for economies of scale; the information is reported in Table 5.6 where it must be highlighted that the study does not reflect the reference year or the original source of the information. Therefore, the reference year is assumed to be the publication year of the article (2020).

Model	Power (kW)	Index Year	CapEx (2021 $/kW)	OpEx (2021 $/kW/year)
T100CHP	100	2020	3601	175.2
2 x C65	130	2020	3079	153.8
3 x C65	195	2020	2946	153.8
C200	200	2020	2902	151.9
4 x C65	260	2020	2750	153.8
C400	400	2020	2583	148.9
C600	600	2020	2265	151.9
C800	800	2020	1980	148.9
C1000	1000	2020	1802	151.9

Table 5.6: CapEx and OpEx of micro gas turbines [211]

In the Master Thesis "Micro Gas Turbines on Mega Yachts - A Feasibility study" [212], the author reported the initial investment costs for 2 x C400 mGTs as well as the associated maintenance costs. The information was supported by a quotation received from Microturbine Marine Energy (MME), where the cost of equipment and installation amounted to 1.12 M€, VAT excluded. The inlet air ducts and the exhaust system added 44.4 k€to this. This translates into a specific installed cost of 1456 €/kW. For maintenance costs, the mGT is expected to run about 4000 hours a year at a cost of 8.87 €/h (for one C200 mGT). Hence, the specific

[1]Within the NextMGT consortium, Giuseppe Tilocca has investigated the reasons why micro gas turbine technology has not enjoyed a wider market deployment so far [109].

maintenance cost would be 177.4 €/kW per year.

A report on CHP technologies issued by the US Environmental Protection Agency[213] describes different CHP scenarios for mGTs of different size. Equipment-only and installed costs are estimated for each representative microturbine system, as seen in Table 5.7. The equipment cost of all units, except for the 30 kW engine, includes an integral waste heat recovery water heater. All units also include a fuel gas booster compressor. Installation costs are based on a CHP system producing hot water from exhaust heat recovery in a basic installation connected to the grid.

Power (kW)	Equipment Cost (2021 $/kW)	Total Installed Cost (2021 $/kW)	OpEx (2021 $/kW/year)
30	2767	4424	-
65	2181	3313	80
200	2181	3241	99
250	1893	2799	68
333	1821	2655	56
1000	1759	2572	74

Table 5.7: mGT CapEx and OpEx for different case scenarios [213]

The OMES Project ran from September 2001 through April 2004 [214]. It tested and demonstrated that a Turbec T100 (100 kW) mGT could be used in a variety of applications (this engine is currently commercialised by Ansaldo). The project reported costs of the T100 unit (FOB) of about 800-860 €/kW ($€_{2004}$), even though this figure varied from one site to another and depending on auxiliary equipment needed for certain applications. Accordingly, the study stated that a cost level of 1000 €/kW including hardware and installation was within reach just a few years after project completion (2004). Regarding maintenance costs, the OMES Project indicated OpEx below 10 €/MWh, even though these were observed to vary between 13 and 15 €/MWh, respectively.

Finally, Capehart wrote a magazine article stating the CapEx and OpEx range of mGTs in the market, obtaining the information from the California Distributed Energy Resources Guide [215]. He stated that the CapEx of mGTs range from 700-1100 $/kW, including all hardware, associated manuals, software, and initial training. If heat recovery is added, the cost increases by 75-350 $/kW. Regarding installation costs, it was highlighted that these are very site-specific but they generally add 30-50% to the total installed cost. Regarding OpEx, these were reported to be in a range from 0.005 to 0.016 $/kWh per year.

5.2 Future cost projection

As for any emerging technology, future cost projections are important in order to evaluate techno-economic performance in future scenarios. Hence, a methodology is presented here to update the cost of the technology cost from a reference year to a future year [216]. A linear curve is often used when the cost reduction of a product or technology is expressed as a

function of cumulative capacity (*CUC*) -i.e., market volume- and experience (*b*) (Eq. 5.8-5.9).

$$\mathrm{CapEx}_f = \mathrm{CapEx}_0 \cdot (\mathrm{CUC}_f / \mathrm{CUC}_0)^b \tag{5.8}$$

$$b = \log(1 - \mathrm{LR}) / \log(2) \tag{5.9}$$

where *0* and *f* stand for the initial and final years considered. Additionally, the experience index (*b*) can be expressed as a function of the learning rate (*LR*) (Eq. 5.10), which assumes that CapEx decrease by 20% everytime the cumulative market capacity (i.e., capacity already installed in the market) is doubled [217].

$$b = \log(1 - \mathrm{LR}) / \log(2) \tag{5.10}$$

Hence, inserting Eq. 5.10 in Eq. 5.8:

$$\mathrm{CapEx}_f = \mathrm{CapEx}_0 \cdot (\mathrm{CUC}_f / \mathrm{CUC}_0)^{\log(1-\mathrm{LR})/\log(2)} \tag{5.11}$$

Many reports and studies in literature report the learning rate of the technologies involved in power-to-power energy storage (P2P-ESS)). However, considering one single (global) learning rate of the system as a whole is misleading and likely to incur large uncertainty. In that case, and whenever possible, considering different learning rates for each component in the system leads to a more accurate CapEx projection. For instance, rather than considering a learning rate for the whole solar PV power plant, it would be more reliable to consider the learning rate of solar panels, inverters, racks, etc. such that Eq. 5.12 can be used to estimate the final CapEx of the system.

$$\mathrm{CapEx}_{f,\mathrm{total}} = \sum_{i=1}^{n} \mathrm{CapEx}_{f_i} \tag{5.12}$$

5.3 Economic Indexes

Levelised Cost of Energy (LCOE) and Levelised Cost of Hydrogen (LCOH) are the two main economic metrics of interest in the application under analysis. LCOE determines the levelised cost of renewable electricity consumed by the electrolyser, whereas LCOH determines the levelised cost of hydrogen consumed by the mGT, throughout the system lifetime in both cases. Finally, LCOE can again be calculated to obtain the cost of electricity of the mGT.

LCOH is strongly dependent on LCOE, since the cost of electricity is the main component setting LCOH. Therefore, the power consumption of the electrolyser plays a key role in LCOH, as it is the component that consumes the largest share of power in the plant (Fig. 3.11).

In addition to LCOE and LCOH, durther figures of merit governing the economic viability of the system are needed. To this end, payback time/period and internal rate of return concepts are introduced.

5.3.1 calculation of LCOE and LCOH

The Fixed Charge Rate (FCR) method is used to calculate LCOE/LCOH in the project [119]. LCOE is the average cost of electrical energy produced by a system over its lifetime. Capital

Recovery Factor (CRF) is the ratio from a constant annuity to the present value of receiving that annuity for a given period of time. To calculated *CRF*, the discount rate, *i*, and accounting lifetime, *N* are used:

$$CRF = \frac{i}{1 - \frac{1}{(1+i)^N}} \tag{5.13}$$

LCOE is then defined as:

$$LCOE = \frac{CRF \cdot TCC + FOC}{AEP} + VOC \tag{5.14}$$

where:

- TCC is the total capital cost, €, or installed capital cost,
- FOC is the fixed annual operating cost, €, or operation & maintenance costs,
- AEP is the annual production of electricity (usually termed 'yield'), kWh, and,
- VOC is the variable operating cost, €/kWh, or operation & maintenance costs per unit of annual yield.

Akin to LCOE, LCOH is defined as the minimum value at which hydrogen must be sold for an energy project to break even. Equation (5.14) can also be applied to LCOH.

The components in Eq. 5.14 are calculated as follows:

$$TCC = TCC_{ec} + TCC_{comp} + TCC_{st} \tag{5.15}$$

$$FOC = TOC_{ec} + TOC_{comp} + TOC_{rep,a} \tag{5.16}$$

$$VOC = VOC_e + VOC_w \tag{5.17}$$

$$\tag{5.18}$$

where:

$$TOC_{rep,a} = CRF \cdot \frac{TOC_{rep}}{(1+i)^t} \tag{5.19}$$

where subscript ec stands for electrolyser, $comp$ stands for compressor, st stands for storage, rep,a stands for electrolyser stack replacement, e stands for electricity, and w stands for water. Table 5.8 shows a summary of the equivalent equations and terms needed to calculate LCOH.

5.3.2 Payback Period

The payback period is a financial metric used to determine the time that it takes for an investor to recover the initial investment (thanks to the positive net cashflow generated by the project). The payback period is often used as an indicator of the investment's risk, as shorter payback periods are generally considered less risky than longer ones. It is also an important consideration for businesses or individuals looking for investments, as it helps determine whether an investment is financially viable or not.

To calculate the payback period, the initial investment is divided by the expected annual cash inflows. The result is the number of years it takes for the investment to generate enough cash flow to cover its initial cost. The following simplified equation provides a mathematical

$LCOH = \frac{CRF \cdot TCC + FOC}{AHP} + VOC$
$CRF = \frac{i(1+i)^N}{(1+i)^N - 1}$
$TCC = CC_{ec} + CC_{comp} + CC_{st}$
$FOC = OC_{ec} + OC_{comp} + OC_{rep,a}$
$OC_{rep,a} = FCR \cdot \frac{OC_{rep}}{(1+i)^t}$
$VOC = OC_e + OC_w$

Table 5.8: Summary of equations for the LCOH

expression of payback; for the sake of simplicity, it is assumed that all fiscal years yield the same cash inflow (denominator).

$$\text{Payback Period} = \frac{\text{Initial Investment - Opening Cumulative Cash Flow}}{\text{Closing Cumulative Cash Flow - Opening Cumulative Cash Flow}} \tag{5.20}$$

The payback period has its limitations, though, as it does not take into account the time value of money, which means that it does not account for the fact that money today is worth more than the same amount of money in the future due to inflation and other factors. Additionally, it does not account for the long-term profitability of investment beyond the payback period.

As an alternative to looking at how quickly an investment is paid back, and given the drawback outlined above, it may be better for firms to look at the internal rate of return (IRR) when comparing projects.

5.3.3 Internal Rate of Return

The internal rate of return (IRR) is a financial metric used to measure the profitability of an investment. It is defined as the discount rate at which the net present value (NPV) of the investment's cash flows equals zero. In other words, the IRR is the rate at which the investment's cash inflows and outflows over the project lifetime cancel each other out, eventually resulting in a zero net present value. Accordingly, IRR is calculated as the discount rate at which the sum of the present values of the expected cash inflows equals the initial investment,

$$0 = NPV = \sum_{n=0}^{N} \frac{CF_n}{(1+IRR)^n} \tag{5.21}$$

where:

- CF_0 = initial investment,
- CF_1, CF_2, CF_3 ... CF_n = annual cash inflows,
- n = time period (typically, year),
- N = Holding period (typically, project lifetime),
- NPV = Net Present Value,
- IRR = Internal Rate of Return,

IRR is often used to compare the profitability of different investment opportunities, as it provides a way to measure the returns on investment in percentage terms. A higher IRR indicates a more profitable investment opportunity, while a lower IRR suggests a less attractive investment. IRR is a useful metric for evaluating investment opportunities because it takes into account the time value of money. It also considers timing and expected cash flows, which is an important consideration for investors who seek to maximise their return. For these reasons, and in spite of certain limitations, IRR remains a popular metric for evaluating the profitability of investment opportunities and is commonly used in financial analysis and decision-making.

5.4 Conclusions

This chapter has provided a detailed analysis of the operating (OpEx) and capital expenditures (CapEx) of several key components of power-to-power energy storage systems. Specifically, wind power, PV power, compression system, storage vessels, and micro gas turbines have been evaluated in terms of OpEx and CapEx. The author has made a major review of the information available in the public domain as well as additional information provided by major stakeholders.

Through this analysis, it has become clear that there are significant differences in the OpEx and CapEx associated with each component in the system, which can have a major impact on the overall cost-effectiveness and profitability of the P2P-ESS. Additionally, it is to note that the OpEx and CapEx of each system can vary significantly depending on a wide range of factors, including the size and scale of the project, location, environmental restrictions, and the specific components and technologies used.

Ultimately, this chapter underlines the importance of carefully evaluating the OpEx and CapEx associated with each component of a P2P-ESS in order to make informed investment decisions and maximise the long-term profitability and sustainability of these critical systems. By doing so, it is possible to make significant progress towards a cleaner, more sustainable future for generations to come.

6 Power-to-Power Practical Case

After reviewing the thermodynamics of the processes and systems involved in a Power-to-Power energy storage system, Chapter 3, and the associated performance models, Chapter 4, the current chapter put the insights gained in practice, explore the design space of the application. The case study presented looks into off-grid applications with a constant demand of 30 kWe, in three European cities: Palermo, Frankfurt, and Newcastle. In the initial phase of the analysis, the results reveal that the latitude of each location plays a crucial role in determining the system's size (hence footprint) and the seasonal storage capacity required. Comparatively, in Frankfurt and Newcastle, the peak power of the PV plant and electrolyser is 37%/41% and 58%/64% higher, respectively, when compared to the original design for Palermo. Furthermore, the seasonal storage capacity substantially increases from 3125 kg H_2 in Palermo to 5023 kg H_2 in Frankfurt and 5920 kg H2 in Newcastle. Consequently, LCOE varies across the cities, with values of 0.86 €/kWh, 1.26 €/kWh, and 1.5 €/kWh for Palermo, Frankfurt, and Newcastle, respectively. Additionally, the round-trip efficiency remains approximately 16.0% across all three designs in the respective cities.

To enhance the base case scenario, the first step involves integrating a battery energy storage system, which reduces the size and capacity requirements of the existing systems. The outcomes of this integration show significant improvements, including a 20% LCOE decrease, a 10% increase in round-trip efficiency, an 18% reduction in seasonal storage capacity, and a 33% decrease in the footprint of the PV solar field.

The study is performed with a Python-based software tool developed by the author of this thesis. As such, the tool has already been employed by the author to make significant contributions to the literature on P2P-ESS based on micro gas turbines, as well as for practical applications in actual hydrogen plants through collaborations with private companies.

The contents of this chapter are partially available in:

A. Escamilla, D. Sánchez, L. García-Rodríguez, 2023, *Techno-economic study of Power-to-Power renewable energy storage based on the smart integration of battery, hydrogen, and micro gas turbine technologies*, Energy Conversion and Management: X, Vol. 18, pp. 100368.

6.1 Introduction to the problem

Mitigating the effects of climate change goes through reducing the emission of greenhouse gases at all levels, from industry to transportation and power generation. There are several technologies that can help this endeavour, such as nuclear power, carbon-neutral technologies such as bio-fuels or biomass, and renewable energy. The first of this selection has the drawback of having radioactive waste and carbon-neutral does not mean carbon-free. Thus, the option that fits the criteria best is utilising renewable energy sources.

Amongst the different technologies in the renewable energy spectrum, both wind and solar technologies are the ones that can usually be installed closer to the consumption node. Furthermore, solar panels are easily installed on any house or building roof, making renewable energy very accessible to consumers. However, this is an intermittent technology that produces energy during sunny hours of the day only, reducing its capacity factor to around 10% to 21% on average [218] (fraction of hours in a year when the installation is running at full capacity). Therefore, those applications whose demand patterns do not match the solar panel power production curve over time need to obtain energy from other sources able to deliver power on demand.

Currently, applications with a share of their energy supply coming from solar panels are usually connected to the grid to both retrieve and deliver energy from and to the grid depending on their energy demand and solar power production. This configuration is highly popular for dwellings but it is a solution more and more frequently adopted by commercial and office buildings, which usually have large roof areas where solar panels can be installed. As the module cost of solar panel solutions is decreasing over time, from 2200 USD/kW in 2010 to 200 USD/kW in 2020 [219], more consumers become interested in using the technology.

In the following sections, a practical scenario is depicted where an off-grid application requires a constant power supply throughout the day. To meet this demand, a PV solar system generates power during sun hours. Part of this power is delivered to the user whilst part of it is stored to fulfil the demand for electricity during dark hours. To this end, a P2P-ESS is utilised.

The reference system is presented in Fig. 6.1. It is an off-grid application comprised of a solar PV installation, electrolyser cells, high-pressure hydrogen storage vessels and microturbines, providing electric power to a small community (demand is 30 kW_e throughout the year, which can be provided by either PV directly or the storage system). After a first analysis of this reference facility, the system is upgraded to incorporate electric batteries (BESS), as shown in Fig. 6.2, with the aim to look for options that would decrease the demand for hydrogen, thereby decreasing the need for seasonal storage and, accordingly, the footprint of the PV solar field and electrolyser systems. Optimisation based on the NSGA-II solver [220] has been carried out to determine the battery bank capacity, the number of PV panels and the number of electrolyser cells that minimise LCOE and surplus energy. All calculations are done with the software tool presented in Chapters 4 and 5.

A large number of studies dealing with Power-to-X ESS must be also acknowledged. Heyman *et al.* [221] use figures of merit for plant size, energy conversion technology, configuration, and cost structure to compare the performance of power-to-gas sites. Also Loisel *et al.* [222] present

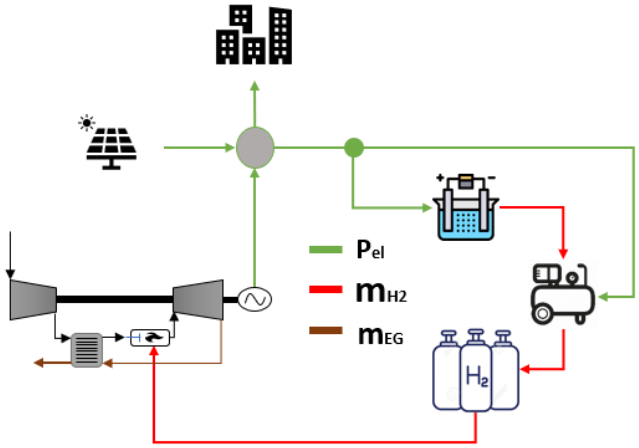

Figure 6.1: Layout of the reference Power-to-Power energy storage system. P_{el} stands for exchange of electric power and $\dot{m}_{H_2}$ and $\dot{m}_{EG}$ stand for streams of hydrogen, and exhaust gases, respectively.

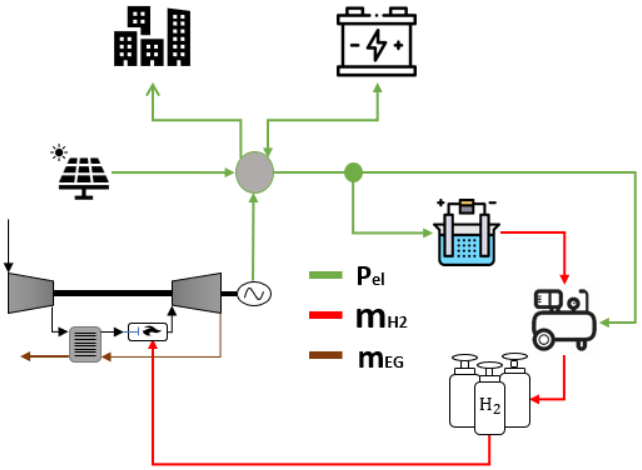

Figure 6.2: Layout of the upgraded Power-to-Power energy storage system incorporating electric batteries. P_{el} stands for exchange of electric power and $\dot{m}_{H_2}$, and $\dot{m}_{EG}$ stand for streams of hydrogen, and exhaust gases, respectively.

an economic evaluation to estimate LCOH for different scenarios in France but without any thermodynamic analysis. Escamilla *et al.* [223] present a thermodynamic analysis of different options for the different systems in a P2P-ESS using mGTs to evaluate the round-trip efficiency (RTE) but without economic analysis. Skordoulias *et al.* [224] present a techno-economic evaluation of mid-scale power-to-hydrogen-to-CHP, focusing on the values of LCOH and capacity factor (*CF*) that would eventually yield an appealing business case for the ESS replacing CH_4. Other authors have looked into P2P-ESS integrated with BESS. Crespi *et al.* [225] compare the use of hydrogen-based P2P systems, battery systems and hybrid hydrogen-battery systems to supply a constant 1 MW_e with electricity generated locally by a photovoltaic plant. Zhang *et al.* [226] perform a comparative study of hydrogen storage and BESS in grid-connected PV systems, focusing on the operational strategy of the system in different operating modes and

scenarios. Shahid *et al.* [227] carry out a techno-economic feasibility analysis of P2P-ESS for small French islands, considering fuel cells as prime movers: the authors report an average LCOE of 0.42 €/kWh when combining hydrogen and BESS. Parra *et al.* [228] perform a simulation of battery and hydrogen technologies for renewable energy management in a single grid-connected house in the UK. The work shows an increase in the local use of PV energy generated on-site: 171% and 159% for the battery and hydrogen systems, respectively.

The aforecited works share common features with the work presented in this chapter. Nevertheless, there are also major differences. Firstly, as far as the authors know, this is the first time mGTs are considered in P2P-ESS (fuel cells are the usual technology of choice). Secondly, the current study is focused not only on thermodynamic and economic features but also on the feasibility to install such a system under certain boundary conditions, bearing in mind the footprint of the different systems and other specific characteristics that may apply in certain locations. Thirdly, the consequences of seasonal storage, which has been found to increase LCOH substantially, are not considered in any of the studies found by the authors. Table 6.1 summarises the main differences between the articles.

Subject	PhD	[223]	[221]	[222]	[224]	[225]	[226]	[227]	[228]
Market research		X		X					
Round-trip efficiency analysis	X	X	X		X	X		X	X
Power-to-power system	X	X		X	X	X	X	X	X
Site-specificity	X		X					X	
Detailed mathematical modelling	X			X			X		
Hourly energy balance	X			X		X	X		X
Battery storage	X					X	X	X	X
Micro gas turbine	X	X							
Optimisation	X					X	X	X	
LCOE & LOCH	X			X	X	X	X	X	X
Seasonal storage	X								

Table 6.1: Comparison between the features considered in this work (PhD) and other works available in the literature. "X" indicates that a reference incorporates/covers the feature in the corresponding row of the first column.

6.2 System description and design parameters

The model described in Chapter 4 is used to determine the size and energy balance of each system in the P2P-ESS unit. To this end, the interconnection between systems is described first, followed by the input parameters of the model. The following assumptions apply to the design of the P2P-ESS:

- The systems are designed to meet the electrical demand (rated output).
- Power demand is given priority over hydrogen production.
- Heat demand is null.
- The power rating of the electric demand is set to 30 kW_e continuously.
- The application is off-grid.
- The computational time step is set to 1 hour.

- Hydrogen is stored at a pressure of 400 bar.
- The pressure ratio of the H_2 compressor is constant.
- Vessel H_2 leakage is considered null.

Figure 6.1 showed the process diagram of the reference P2P-ESS. Power produced from RES is first used to meet the end-user demand for electricity. In the case of surplus energy, this is used to operate a Proton-Exchange Membrane Electrolyser (PEMEC) which produces H_2 that is then stored in high-pressure vessels using a set of reciprocating compressors. In periods when RES is not sufficient to cover the electric demand of the end-user, this stored hydrogen is used to run an mGT in order to make up for the lack of electricity coming from the PV field. This describes the base-case scenario, whose layout is later upgraded through the addition of batteries with the final aim of lowering the LCOE and footprint of the system. Figure 6.2 shows the layout of this second case.

In order to assess the effect of boundary conditions on the techno-economic performance of the system, the P2P-ESS system described is evaluated at geographical locations that satisfy the following GHI criteria,

- City 1: GHI > 4.5 kWh/m^2/day.
- City 2: 3 < GHI ≤ 4.5 kWh/m^2/day.
- City 3: GHI ≤ 3 kWh/m^2/day.

The cities selected are Palermo (IT), Frankfurt (GE), and Newcastle upon Tyne (UK) where GHI is 4.73, 3.26, and 2.75 kWh/m^2/day, respectively.

6.2.1 Solar photovoltaic plant

Table 4.1 summarised the main input parameters of the performance model of the photovoltaic system, created in nrel-pysam 2.2.4 [120] (Aug 20, 2021). A single solar panel and configuration are chosen, with the specifications shown in Table 6.2 and this is then applied to all locations reported in the foregoing section. For each of these, irradiation data are extracted from the European Commission JRC's Photovoltaic Geographical Information System (PVGIS) [229].

Parameter	**Unit**	**Value**
Manufacturer of modules	-	SunPower
Module model	-	SPR-a410-COM
Module peak rated output	W_{DC}	448.4
Module rated efficiency	%	22.09
Tilt	deg	30
Azimuth	deg	180
Total DC loss	%	4.44
Total AC loss	%	1
Soiling loss	%	5

Table 6.2: Specifications of the solar PV module.

6.2.2 Battery energy storage system

The Battery Energy Storage System considered in this study is installed *behind-the-meter* and DC-connected, as shown in Fig. 6.3. The battery of choice is of the Lithium-ion type and the

corresponding performance is modelled as in DiOrio *et. al* [230]. This latter model is actually simplified to account for charging and discharging losses only.

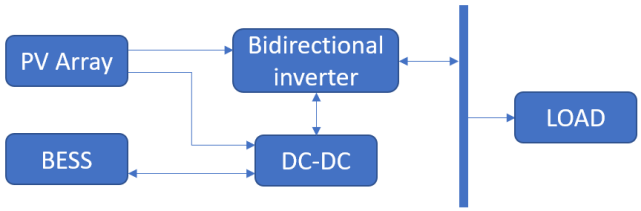

Figure 6.3: BESS Layout (Behind-the-meter and DC-connected).

In order to design the BESS, the nominal bank capacity and power output and the charge/discharge depth are specified, with round-trip efficiency of the BESS being defined by the charging/discharging efficiency. The following equations apply:

$C-rate_{disch}$ = Maximum Discharge Power / Bank Capacity

$C-rate_{char}$ = Maximum Charge Power / Bank Capacity

$t_{max.power}$ = Bank Capacity / Maximum Bank Power Output

Table 6.3 shows the design specifications adopted for the BESS. In this case, the charging/discharging efficiencies have been set to 90%, slightly lower than the current state-of-the-art, in order to compensate for minor losses that are not considered by the model. Rated output is set to 30 kW so that the BESS can cover the demand of the end-user self-sufficiently, without needing the support of the mGT system. Therefore, once the BESS runs out of energy, the mGT starts up to satisfy the energy demand until the PV solar field starts producing energy again. The minimum and maximum States-of-Charge (SoC) are set to 20% and 90% respectively, to prevent a high degradation rate of the battery. Finally, the energy capacity of the battery bank is left to take values within a certain range, in order to carry out optimisation in Section 6.5 later. The range considers a minimum duration of 4 hours and a maximum duration of 13 hours, with the system running at full capacity.

Parameter	**Unit**	**Value**
Bank power output	kW	30
Bank capacity	kWh	(120, 400)
Minimum state-of-charge	%	20
Maximum state-of-charge	%	90
Charge/discharge efficiency	%	90

Table 6.3: BESS design specifications.

6.2.3 Proton-exchange membrane electrolyser

As discussed in a previous chapter, the performance of an electrolyser can be illustrated using a polarisation curve. This curve provides information about the actual voltage needed to run the stack, which is higher than the voltage needed to run an equivalent, ideal (reversible). The voltage difference (loss, also overpotential) between the actual cell and the reference, ideal

cell can be broken down into three contributions/sections: (1) activation loss, (2) ohmic loss, and (3) mass transport loss. All these voltage losses are added to the reversible voltage, or the theoretical minimum voltage for the electrochemical reaction to develop in the absence of energy losses. This can be assessed in Eq. 2.12 where V_{ocv} is the open circuit potential (theoretical minimum voltage to operate the ideal cell), V_{act} is the overpotential due to the activation energy of the electrochemical reaction, V_{diff} is the diffusion overpotential brought about by limited mass transport in the electrolysers, and V_{ohm} is the ohmic overpotential caused by the resistance of the electrolyser cell to the flow of ions/electrons. The polarisation curve of the electrolyser is calculated using Eq. (2.12), whose associated details are discussed in Section 4.3 and in other works published by the author of this thesis [31].

The afore-described model is used to determine the polarisation curve of a specific PEMEC, which is essentially not affected by the number of cells and stacks (array of cells) in the system. Out of the modelling of the electrolyser, the polarisation curve for the design parameters summarised in Table 6.4 is shown in Fig. 6.4. This input data remains constant for all scenarios and cases.

Parameter	Unit	Value
Current Density Range	A/cm^2	0.2-2.0
Auxiliary Power	% of rated	10
Cell Area	cm^2	160
Cathode temperature	°C	50
Cathode pressure	bar	30

Table 6.4: PEMEC design specifications.

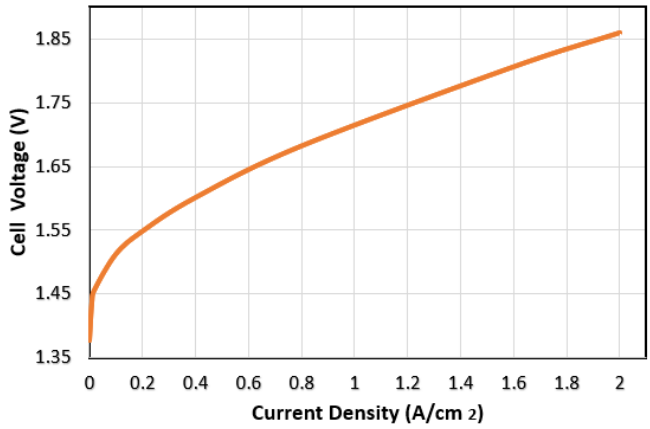

Figure 6.4: PEMEC polarisation curve. Validated against experimental data in [231].

6.2.4 High-pressure hydrogen storage

The compression process is initially assumed to be comprised of an isentropic compression with intercooling, in order to resemble a quasi-isothermal process with minimum compression work. It is also assumed that the pressure delivered by the compressor is always the target

storage pressure, regardless of the amount of hydrogen stored in each tank. This is not true for two reasons: i) the pressure of the storage tank actually depends on the amount of hydrogen stored, ii) in practice, since the pressure delivered by the compressor must be slightly higher than that of the tank, there must be a certain overpressure Δp delivered by the compressor at each time step. Overall, this assumption for pressure-balance is conservative and allows to decouple the filling process from the number of vessels and their filling status. The model of the reciprocating compressor was presented in Section 4.4.

The storage vessel is designed according to ASME Section VIII, Division 1, 2, or 3 [121], as discussed in Section 4.4. The equations of interest belong to the "under internal pressure" category. The minimum wall thickness (t) depends mostly on the design internal pressure (P) and internal radius (R) of the vessel, and on the allowable stress (S) and joint efficiency (E) of the material. In the case of the vessel's head, the radius is not a valid measure anymore and the inside diameter of the head skirt (D) or the inside crown radius (L) is used. The data used for the design of the high-pressure vessel and compression system are listed in Table 6.5. It is assumed that the outlet temperature from each compressor stage cannot be higher than 420 K [73] and that the pressure ratio between the hot and cold sides of the intercooler is 10. The latter facilitates the calculation of the work done by the water pump and determines the maximum pressure ratio that the heat exchanger must endure. This criterion is set to determine the number of stages that the reciprocating compressor must have to deliver a pressure ratio of 13.33.

Parameter	**Unit**	**Value**
Inside radius	m	0.4
Shell length	m	1.87
Joint efficiency factor	-	1
Allowable material stress	MPa	55
Material density	kg/m^3	2000
Final storage pressure	MPa	40
Compressor isentropic efficiency	%	75
Maximum compressor outlet temperature	K	420
Pump isentropic efficiency	%	90
Coolant	-	Water
Coolant inlet/maximum outlet temperature	K	293/363

Table 6.5: Design specifications of the hydrogen storage system.

6.2.5 Micro gas turbine

The micro gas turbine's design and performance assessment processes have been presented in Section 4.6.5 in detail. They are therefore not repeated here. Figures 4.14 and 4.15 presented in Section 4.6.5 belonged to the design used in this practical case. These off-design performance maps of the compressor and turbine were obtained with in-house software developed at the University of Seville. Considering a minimum turndown capability of 20%, the running line of the mGT results from merely matching the off-design performance of turbomachines on the

same shafts.

The performance map of the entire 30 kW_e mGT is shown in Fig. 6.5. This set of curves is then used to obtain the operating conditions of the mGT at different settings depending on the power demand of the end user. It is worthwhile to mention that the curve has been obtained for an atmospheric temperature of 20 °C. In the case of different atmospheric temperature, step 1 to 7 must be repeated to find the new working mGT curve.

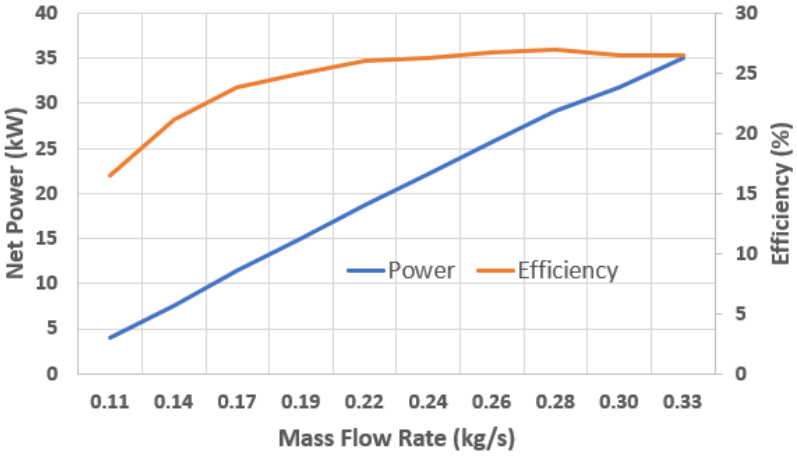

Figure 6.5: Off-design curve of the 30 kW_e mGT used in this work.

6.3 Economic analysis of the storage systems

An extensive literature review has been conducted to obtain the necessary economic information about the systems involved in the P2P-ESS installation: PV, BESS, PEMEC, H_2-compressor, H_2-tanks, and mGT. From the economic data gathered, the values presented in Table 6.6 have been chosen for the different systems at each location. It is assumed that the costs associated with each technology remain unchanged from one location to another except for the case of the PV plant, for which information about regional costs (CapEx and OpEx) of utility-scale PV plants is taken from the report on renewable energy costs issued by IRENA and already cited in this work [232].

6.4 Base-case scenario: power-to-power P2P with mGT

This section presents the design of the base-case P2P-ESS layout shown in Fig. 6.1 in the aforecited locations (Palermo, Frankfurt, and Newcastle). The assumptions and integration layouts of each model presented in Chapter 4 are incorporated into the in-house software for techno-economic system assessment, and a detailed analysis of the energy balance for each system is performed at 1-hour time-steps over a year. The actual sizing of the ESS is carried out for the city of Palermo and the resulting specifications are then placed in Frankfurt and Newcastle to understand how the location would affect the energy balance and economic parameters of a standardised design. Then, the ESS is specifically designed for Frankfurt and Newcastle and the resulting techno-economic performance is compared against the information obtained for the standardised solution previously.

System	Parameter	Unit	Value [€$_{2021}$]	Reference
PV Solar	CapEx	€/kW	664/587/717	[232]
	Fixed OpEx	€/kW per year	15.4 (OECD)	[232]
	Variable OpEx	€/kWh	0.0	
	Lifetime	year	25	
BESS	CapEx	€/kWh	402.5[1]	[233]
	Fixed OpEx	% of CapEx	2.5	[234]
	Stack Replacement	% of CapEx	40	[233]
	Stack Lifetime	year	15	[234]
PEMEC	CapEx	€/kW	1100[2]	[116, 186]
	Fixed OpEx	% of CapEx	1.5	
	Stack replacement	% of CapEx	45	[116]
	Stack lifetime	year	10	
	Water cost	€/m^3	4.9	
Compressor	CapEx	€/kW	4500	[203] [207]
	OpEx	% of CapEx	4	[207]
Vessel	CapEx	€/kg H_2	470	[198]
	OpEx	% of CapEx	2	[198]
mGT	CapEx	€/kW	2689	[213]
	Fixed OpEx	€/kW	150	[211]
General	Interest Rate	%	4	
	Project Lifetime	year	25	

1. Based on a rated output of 1 MW$_e$ and a total storage capacity of 4 hr Lithium-Ion BESS.
2. Based on a 500 kW PEMEC.

Table 6.6: Input economic data of the components of the plant. These data are used to calculate the LCOH and LCOE of the P2P-ESS. €refers to 2021.

Weather files for each location have been obtained from the Photovoltaic Geographical Information System (PVGIS) [229] for a Typical Meteorological Year (TMY). A TMY is a meteorological dataset with yearly values for a given geographical location, resulting from averaged sets of data collected in that particular location over a longer period of time (usually 10 years or more)[1]. These files are directly used in SAM for the modelling of the PV field. The information needed to design the system is found in Tables 6.2, 6.4, 6.5, and 6.7, which apply to the reference system in Fig. 6.1.

Table 6.8 shows the annual energy balance of the reference P2P-ESS along with the economic data for LCOH and LCOE. In addition, Fig. 6.6 shows the hourly energy balance of the power-to-power system over the entire year, information that is completed by Figs. 6.7 and 6.8 for a better understanding. Figure 6.7 shows the energy balance of the power-to-hydrogen process: energy yield of the PV panels (red line), power consumed by the electrolyser (blue line), and the production of hydrogen for each time step (black dots). The significant oversizing of the PV array and the electrolyser becomes evident. This is mostly due to the low round-trip efficiency of the ESS as well as to the need for a very large production of hydrogen during sun hours in order to compensate for the lack of production during the night. As opposed to this, Fig. 6.8 shows the hydrogen-to-power process, represented by the load of the mGT, which is operated when renewable energy is not available. It is confirmed that the mGT works at partial load

[1] PVGIS generates the TMY following the procedure described in ISO 15927-4

System	Parameter	Unit	Value
PV Solar	Modules per String	-	8
	Strings in parallel	-	175
	Peak power output	kW_{DC}	627.8
	Energy yield	kWh_{DC}/kW	1731
	Total module area	m^2	2842
PEMEC	No Stacks	-	6
	No cells/stacks	-	112
	Peak power consumption	kW	463
	Rated H_2 production	Nm^3/h	89.3
Storage	Vessel Volume	m^3	1.208
	Tank weight	kg	7081
	Shell/head thickness	mm	428/157
	Compressor min/max flow rate	Nm^3/h	9.1/88.6
	Compressor pressure ratio	-	13.33
	Compressor power rating	kW	12.8
mGT	Rated output	kW	30
	No units	-	1
	Rated electric efficiency	%	26.9

Table 6.7: Design specifications for Palermo.

only rarely, which has a strong, positive impact on round-trip efficiency.

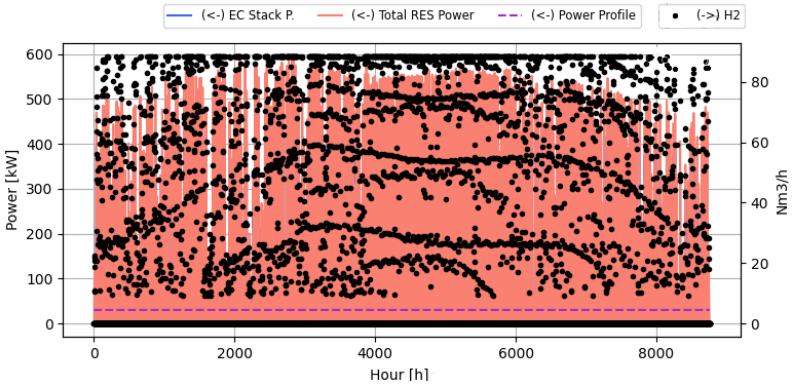

Figure 6.6: Energy Balance of a P2P-ESS system designed and operated in Palermo over a complete year (8760 hours). Close-ups in periods of interest are shown in Figs. 6.7 and 6.8.

Table 6.8 shows similar information for a system designed in Palermo but operated in Frankfurt and Newcastle. These two locations are at a much more Northern latitude than Palermo and, therefore, receive less radiation (W/m^2·year), meaning that the system is not able to fulfil the energy demand of the end-user without grid support. This simple exercise is meant to quantify how much the location of a P2P-ESS does not only affect the footprint of the system but also LCOH and LCOE. For the system designed in Palermo, the net-H_2[2] produced by the end of the year is about 141 kg, whereas hydrogen production decreases considerably due to the lower capacity factor of the solar panels when the same system is installed in either of the other two

[2] H_2 production minus consumption at the end of the year

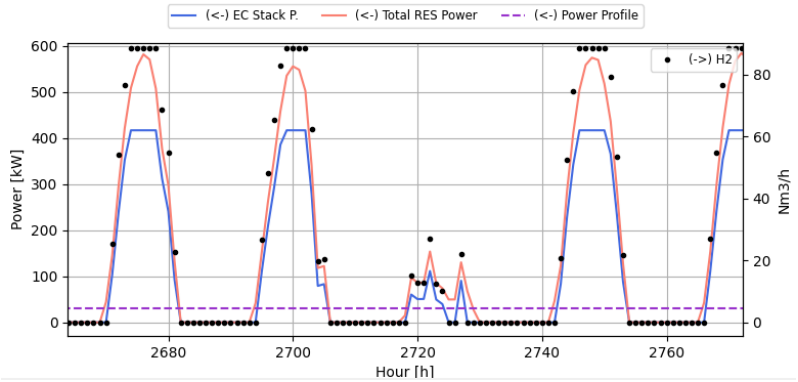

Figure 6.7: Close-up of the Power-to-H_2 energy balance for selected days in Fig. 6.6.

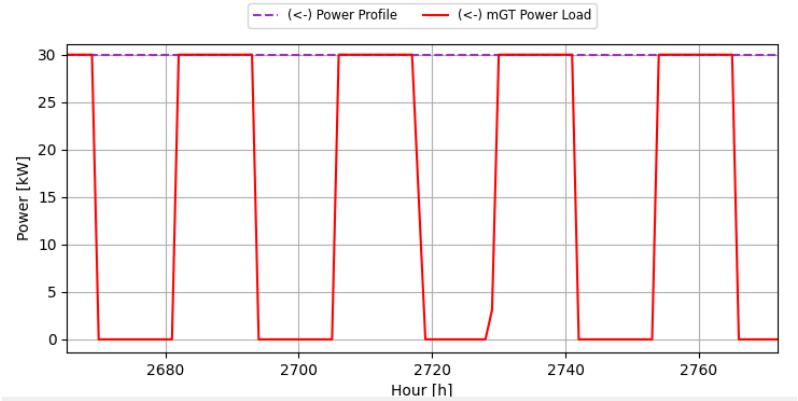

Figure 6.8: Close-up of the H_2-to-Power energy balance for selected days in Fig. 6.6.

locations. In particular, for the locations of Frankfurt and Newcastle, the net-H_2 balance at the end of the year in order to satisfy the 30 kW_e is (5247) kg and (7302) kg, approximately, where "()" means a negative value (i.e., the hydrogen deficit implies that there is a hydrogen shortage at some points and the 30 kW_e demand cannot be covered). Figure 6.9 shows the hourly evolution of the net hydrogen balance for each location; as noted, it is clear that not enough hydrogen is produced during the sunny season to cope with a long winter. Hence, for the sake of the economic comparison between the different locations, the same amount of seasonal storage as for the case of Palermo is considered, 3125 kg H_2. This parameter affects the number of vessels that must be in place to enable storing this amount of H_2.

Figures 6.10 and 6.11 show the resulting LCOH and $LCOE_{mGT}$ for the cities of Palermo, Frankfurt, and Newcastle. Even if it must be acknowledged that the system is designed for Palermo, regardless of the actual installation site, it becomes apparent that the much higher costs of producing hydrogen and power in Northern Europe are not due to this reason; actually, the upsurge in energy and hydrogen costs is influenced mainly by the increasing $LCOE_{PV}$ due to the lower radiation and lower capacity factors (lower yield for the same CapEx). In addition, the breakdown of costs associated with LCOH suggests that seasonal storage is the cost that contributes the most to the final price of hydrogen, about 50%. This is followed by the installation cost of the electrolyser (CapEx) and the power consumed by the EC. When

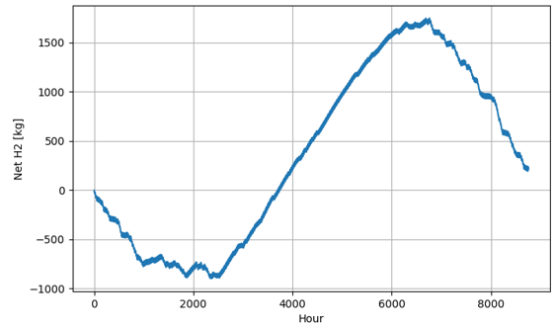

Palermo.

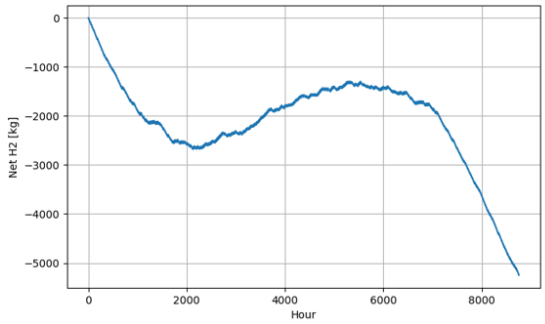

Frankfurt.

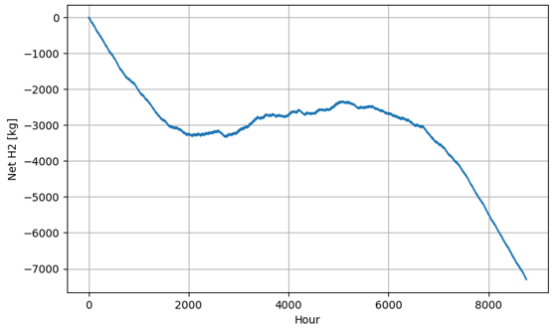

Newcastle upon Tyne.

Figure 6.9: Net hourly hydrogen balance of the P2P-ESS for the reference locations. Design parameters are listed in Table 6.7.

Parameter	Unit	Palermo	Frankfurt	Newcastle upon Tyne
RES Energy	MWh	1086.7	783.4	679.8
mGT Energy	MWh	148.4	151.6	155.0
PEMEC Energy	MWh	(939.5)	(648.9)	(551.7)
Compression Work	MWh	(27.0)	(19.0)	(16.3)
Application Energy	MWh	(262.8)	(262.8)	(262.8)
Surplus Energy	MWh	(32.8)	(23.4)	(20.3)
$[\text{Net } H_2]_{\text{at end year}}$	kg H_2	141	(5247)	(7302)
Seasonal Storage	kg H_2	3125	3125	3125
PV Solar CF	%	18.2	13.2	11.5
LCOH	€/kg H_2	12.72	17.74	21.03
LCOE_{PV}	€/kWh	0.0335	0.0425	0.0566
LCOE_{mGT}	€/kWh	1.49	2.05	2.42
LCOE	€/kWh	0.86	1.20	1.44
RTE	%	16.0	-	-

Table 6.8: Energy balance at different locations when using the system sized for Palermo.

the costs associated with compression and storage of H_2 are not considered, the LCOH and LCOE_{mGT} are reduced to 5.19 €/kg H_2 and 0.65 €/kWh, 6.74 €/kg H_2 and 0.82 €/kWh, and 8.22 €/kg H_2 and 0.99 €/kWh, for the cities of Palermo, Frankfurt, and Newcastle respectively. Therefore, it is of utmost importance to include the cost of storing H_2 in the calculation of the LCOE of a P2P-ESS.

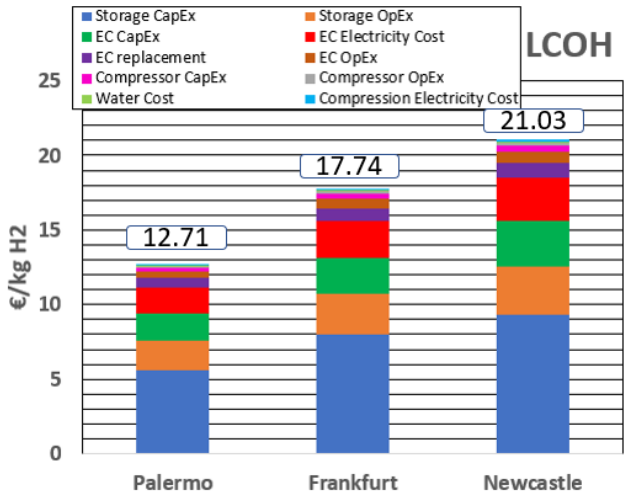

Figure 6.10: Breakdown of the Levelised Cost of Hydrogen LCOH of a P2P-ESS installed in Palermo, Frankfurt, and Newcastle upon Tyne. Design parameters and detailed energy balance are listed in Tables 6.7 and 6.8.

Tailoring of the P2P-ESS to every installation site is against the standardisation of the product, which then contributes to higher capital costs of the technology. Nevertheless, in order to assess the potential to enhance the performance of the system by producing specific designs adapted to the installation site, a new section is now presented where the ESS is resized for the

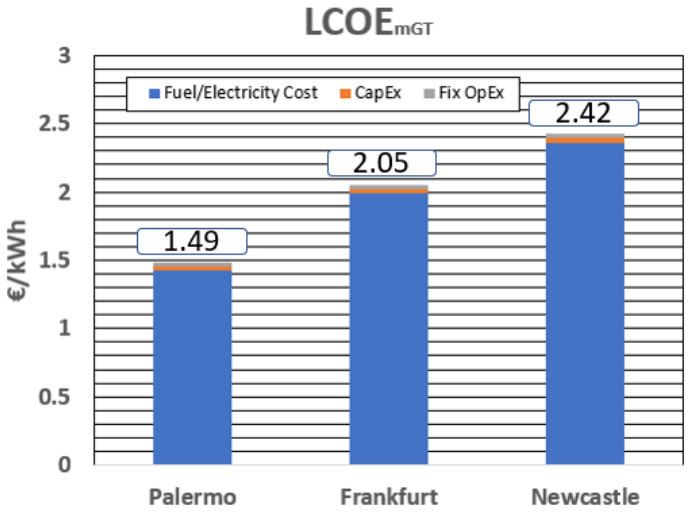

Figure 6.11: Breakdown of the Levelised Cost of Energy of the micro gas turbine LCOE$_{mGT}$ of a P2P-ESS installed in Palermo, Frankfurt, and Newcastle upon Tyne. Design parameters and detailed energy balance are listed in Tables 6.7 and 6.8.

particular boundary conditions of the locations in Germany and the United Kingdom. The condition to meet the energy demand of the end user will nevertheless remain in the new analysis. The next section will shed light on how the standardised solution must change from a high GHI site to a lower GHI site.

6.4.1 Performance enhancement gained from tailored P2P-ESS designs

The previous section examined the possibility to produce a standardised design which could then be used in locations with largely different boundary conditions from those of the reference location. As opposed to this, this section explores the performance enhancement that could be attained if the ESS were tailored to the site in order to obtain a positive net-H_2 at the end of the year, as well as the minimum surplus energy such that these quantities were comparable for the three cities considered. The aim of this section is therefore to compare the footprints of each system, LCOH and LCOE.

Table 6.9 shows the design specifications that are needed in the cities of Palermo, Frankfurt, and Newcastle in order to have a positive net-H_2 balance at the end of the year as well as to minimise the solar energy that is curtailed (i.e., not used by either the end-user directly or the electrolyser); this curtailed power is termed *Surplus Energy* in the tables. It is worth noting that, as expected, the systems involved in the Power-to-H_2 process are oversized in the Northern locations, with the Peak Power of the solar field/electrolyser increasing by 37%/41% and 58%/64% for Frankfurt and Newcastle, with respect to Palermo respectively. Regarding footprint, the total module area increases from 2845 m^2 to 3898 m^2 and 4499 m^2, respectively. Overall, this means that the footprint of the P2P-ESS increases significantly as latitude increases (in the Northern hemisphere) in order to ensure that the annual yield remains high.

In addition to the oversizing of the solar field and electrolyser, Table 6.10 shows that seasonal storage becomes more challenging as the amount of hydrogen that needs to be produced

System	Parameter	Unit	Palermo	Frankfurt	Newcastle
PV Solar	Modules per string	-	8	8	8
	Strings in parallel	-	175	240	277
	Peak power	kW_{DC}	628	861	994
	Energy yield	kWh_{DC}/kW	1731	1248	1082
	Total module Area	m^2	2842	3898	4499
PEMEC	No Stacks	-	6	10	11
	No cells/stack	-	112	95	100
	Peak power	kW	463	655	758
	Rated H_2 production	Nm^3/h	89.3	126.3	146.2
Storage	Vessel volume	L	1208	1208	1208
	Tank weight	kg	7081	7081	7081
	Shell/head thickness	mm	428/157	428/157	428/157
	Compressor min/max flow rate	Nm^3/h	9.1/88.6	12.9/125.3	14.9/145.1
	Compressor pressure ratio	-	13.33	13.33	13.33
	Compressor power rating	kW	12.8	18.2	21.0
mGT	Rated output	kW	30	30	30
	No Units	-	1	1	1
	Rated electric efficiency	%	26.9	26.9	26.9

Table 6.9: Tailored design parameters for the locations considered

during summer and stored for winter incraeases: 5023 kg and 5920 kg of H_2 for Frankfurt and Newcastle, as compared to 3125 kg H_2 for Palermo in the former design case; interestingly, the annual yield of the mGT is almost the same for the 3 cases. This indicates that the mGT is in operation during dark hours most of the time and that the application is powered by the PV panels during sunny hours only; this can also be seen in Figs. 6.7 and 6.8. Moreover, the electricity produced by the solar field and consumed by the electrolyser is almost the same for the three cases, but the rated output increases when located further up North because the capacity factor of the PV panels and the electrolysers decrease considerably, affecting LCOH and LCOE (Table 6.10).

The levelised costs LCOH/$LCOE_{mGT}$ also increase when changing the reference design conditions: by 49%/47% from Palermo to Frankfurt and by 76%/73% from Palermo to Newcastle, respectively. For $LCOE_{mGT}$, this is mostly driven by fuel cost (H_2 in this case), as seen in Fig. 6.11, whereas the higher LCOH is clearly brought about by the largest storage capacity needed (Fig. 6.12). If the storage capacity is not considered in the calculation of LCOH/$LCOE_{mGT}$, the costs are 5.0 €/kg H_2 / 0.62 €/kWh, 6.69 €/kg H_2 / 0.81 €/kWh, and 8.07 €/kg H_2 / 0.97 €/kWh for Palermo, Frankfurt and Newcastle, respectively. LCOH can also be converted into €/MWh, in which case it yields 166.7, 223, and 269 €/MWh($H_{2,LHV}$), respectively. If these costs are compared with the peak price of the *Dutch TTF Gas Futures* [235] in August 2022 -349.9 €/MWh-, the price of H_2 resulting from the analysis is not far from being competitive already.

The discussion presented in this section confirms that, as expected, latitude plays a very strong role in the sizing (footprint) and costs of the subsystems that form the P2P-ESS, as well as the amount of seasonal storage. As expected, departing north- or south-wise from the Ecuadorian line has a negative impact on these metrics. If seasonal storage is considered, the hydrogen storage system also becomes larger due to the fewer sun hours during winter, impacting LCOH negatively and, consequently, $LCOE_{mGT}$.

Parameter	Unit	Palermo	Frankfurt	Newcastle
RES energy	MWh	1086.7	1074.4	1076.0
mGT energy	MWh	148.4	149.5	151.2
PEMEC energy	MWh	(939.5)	(927.9)	(929.3)
Compression work	MWh	(27.0)	(27.1)	(27.5)
Application energy	MWh	(262.8)	(262.8)	(262.8)
Surplus energy	MWh	(32.8)	(33.3)	(35.1)
$[\text{Net } H_2]_{\text{at end year}}$	kg H_2	141	106	106
Seasonal storage	kg H_2	3125	5023	5920
PV solar CF	%	18.2	13.1	11.3
Capacity factor electrolyser	%	23.8	16.9	14.8
LCOH	€/kg H_2	12.72	18.96	22.36
LCOE_{PV}	€/kWh	0.0335	0.0425	0.0566
LCOE_{mGT}	€/kWh	1.49	2.19	2.57
$\overline{\text{LCOE}}$	€/kWh	0.856	1.265	1.497
RTE	%	16.0	16.3	16.5

Table 6.10: Techno-economic data for the cities of Palermo, Frankfurt, and Newcastle upon Tyne, when tailored designs are considered.

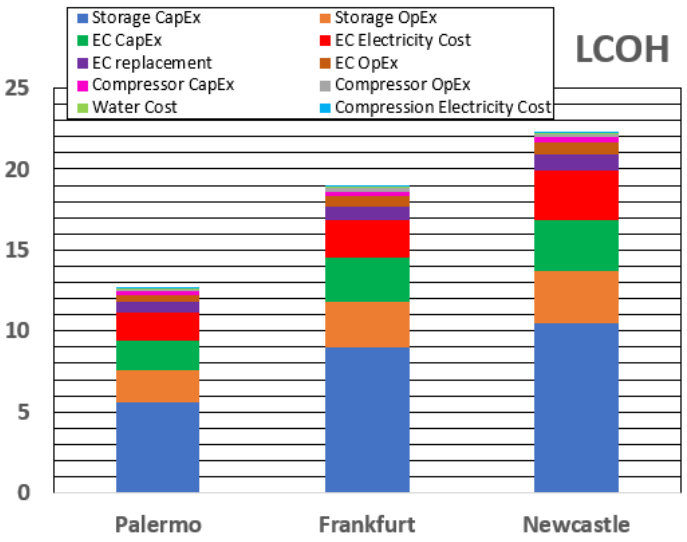

Figure 6.12: LCOH breakdown for a P2P-ESS in Palermo, Frankfurt, and Newcastle upon Tyne. Design parameters for each location can be found in Table 6.9.

In addition to this, the analysis of energy balance and footprint shows that using a P2P-ESS coupled to a mGT is not practical in an application without grid support, due to the large oversizing of the subsystems and the not-competitive values of LCOE. To overcome this hurdle, the P2P-ESS can be hybridised with other ESSs, if grid support is still not available, or it can be resized if the system can rely on importing energy from the grid. This latter option is, however, not under discussion in this work since the focus is on systems that are off-grid. Therefore, the next section will explore the room for optimisation of the system designed for Palermo through hybridisation of a P2P-ESS with electric batteries (BESS).

6.5 Performance enhancement through hybridisation with battery storage

Installing a P2P-ESS to power an application without grid support leads to high LCOE as well as a large footprint of the solar field and electrolyser system. Adopting the P2P layout described in Fig. 6.1 seems therefore impractical. Based on this conclusion, this section explores the adoption of a new layout to expectedly make the system more competitive in terms of lower LCOE and space occupation.

The layout that is now adopted is presented in Fig. 6.2. This system is applied to the city of Palermo only, since the relative performance enhancement for this location would still be applicable to other cities. The new P2P layout incorporates a battery bank that is charged by the PV module during sun hours and discharged when the solar field cannot meet the power demand of the end-user. Hence, charging of the BESS is prioritised over the operation of the electrolyser, due to the higher round-trip efficiency and lower cost of the former storage system. The model of the BESS is described in Section 6.2.2.

An optimisation solver is used to solve the techno-economic problem and to account for the many trade-offs existing between the different sizing parameters of the systems involved. Thus, multi-objective optimisation using the NSGA-II solver [220] is used to calculate a Pareto front based on the following optimisation problem:

- f(1) = min (LCOE)
- f(2) = min (surplus energy)
- subject to:
  - 50 > net H_2 (kg) < 400

Minimisation of surplus energy is selected because this is an application without grid support and, therefore, surplus energy would be directly dumped off the system; in addition, minimising this parameter also ensures the lowest footprint of the system. Table 6.11 shows both the settings of the optimiser and the design space for each input parameter.

	Parameter	**Unit**	**Range**
Settings	Population Size	-	100
	No Generations	-	50
	No Offsprings	-	50
	Crossover Rate	-	0.9
	Mutation Rate	-	0.1
Input	No Modules	-	(100, 175)
	Bank Capacity	kWh_{DC}	(120, 400)
	No Stack	-	(3, 6)
	No Cell	-	(80, 120)

Table 6.11: Settings of the optimisation problem. P2P-ESS with BESS in Palermo.

Figure 6.13 shows the Pareto Front produced by the optimiser with the settings and inputs displayed in Table 6.11. The main trend shown is that accepting higher surplus energy seems to yield lower LCOE. This is because the capacity factor of the electrolyser increases as the

rated output of the PV module increases and the peak power of the electrolyser decreases, as shown in Fig. 6.14.

The first consequence of considering the integration of a BESS is therefore a lower LCOE. Nevertheless, the introduction of the BESS has a negative, direct effect on the capacity factor of the electrolyser and mGT since the BESS is prioritised over the mGT due to its higher round-trip efficiency. Thus, even if the overall trend is a reduction of the $\overline{\text{LCOE}}$, both LCOH and LCOE_{mGT} still increase.

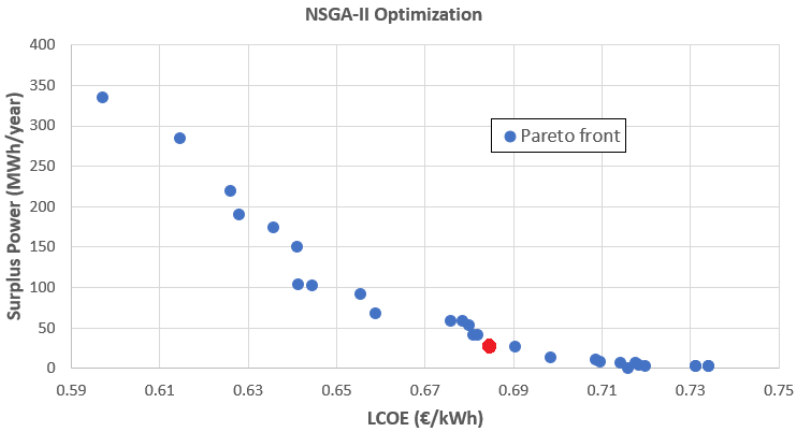

Figure 6.13: Pareto front of the global optimisation problem. Settings displayed on Table 6.11.

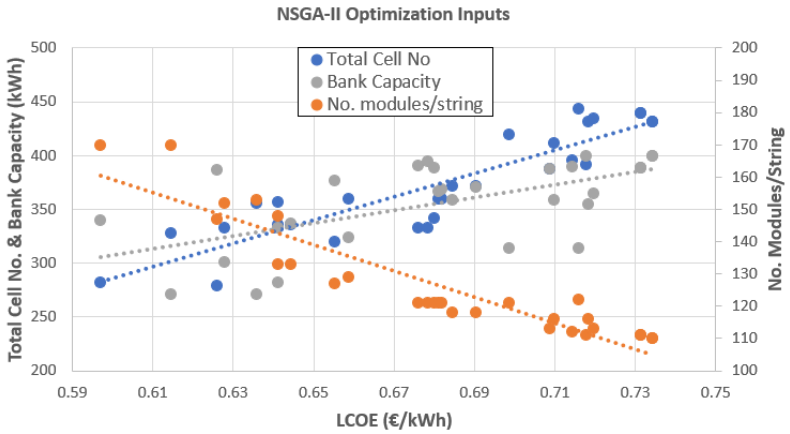

Figure 6.14: Input parameters for the Pareto front displayed on Fig. 6.13, and associated linear trends.

Amongst the possible system designs shown in Figure 6.13, the design marked in red is selected based on the condition that the maximum surplus energy shall not exceed 30 MWh and that LCOE is lowest amongst the possible designs compliant with this requirement (i.e., the design is on the front). For this design, Table 6.12 shows the input parameters and Table 6.13 shows the energy balance and economic metrics. In these two tables, an additional column has been added for the design for the city of Palermo, using the configuration displayed in Fig. 6.1 and

discussed in Section 6.4.

System	Parameter	Unit	Palermo	
			Optimized	Reference (w/o BESS)
PV Solar	Modules per string	-	8	8
	Strings in parallel	-	118	175
	Peak power	kW_{DC}	423	628
	Energy yield	kWh_{DC}/kW	1731	1731
	Total module area	m^2	1916	2842
BESS	Bank capacity	kWh	359	-
	Bank power	kW	30	-
	Charge/discharg efficiency	%	90/90	-
PEMEC	Number of stacks	-	4	6
	Number of cells/stack	-	93	112
	Peak power	kW	256	463
	Rated H_2 production	Nm^3/h	49	89.3
Storage	Vessel volume	L	1208	1208
	Tank weight	kg	7081	7081
	Shell/head thickness	mm	428/157	428/157
	Compressor min/max flow rate	Nm^3/h	5/49	9.1/88.6
	Compressor pressure ratio	-	13.33	13.33
	Rated compressor power	kW	7.1	12.8
mGT	Nominal capacity	kW	30	30
	Number of units	-	1	1
	Rated electric efficiency	%	26.9	26.9

Table 6.12: Design parameters of the optimised design in the city of Palermo

Parameter	Unit	Palermo	
		Optimized	Reference (w/o BESS)
RES energy	MWh	732.7	1086.7
mGT energy	MWh	76.5	148.4
BESS discharged energy	MWh	73.5	-
BESS charged energy	MWh	(97.2)	-
PEMEC energy	MWh	(497.0)	(939.5)
Compression work	MWh	(14.2)	(27.0)
Application energy	MWh	(262.8)	(262.8)
Surplus energy	MWh	(26.7)	(32.8)
$[\text{Net } H_2]_{\text{at end year}}$	kg H_2	94	141
Seasonal storage	kg H_2	2558	3125
PV solar CF	%	18.2	18.2
EC CF	%	22.7	23.8
mGT CF	%	29.5	56.5
LCOH	€/kg H_2	17.0	12.72
$LCOE_{PV}$	€/kWh	0.0335	0.0335
$LCOE_{BESS}$	€/kWh	0.25	-
$LCOE_{mGT}$	€/kWh	2.04	1.49
$\overline{LCOE}$	€/kWh	0.69	0.86
RTE	%	26.2	16.0

Table 6.13: Techno-economic figures of merit for the optimised design in the city of Palermo.

The reduction in footprint and peak power of the PV module and electrolyser with respect to

the solution without BESS is remarkable. Both the footprint and rated output of the PV system are reduced by 32.5% compared to the base case scenario, which adds up to a 45% reduction of the peak power of the electrolyser. This reduction is a consequence of the introduction of a BESS with a capacity of 359 kWh, equivalent to operating at the rated output for 12 hours (it must be noted though that, considering the depth of charge/discharge, the actual duration is approximately 8 hours). On the other hand, the RTE of the ESS is increased from 16.0% to 26.2% due to the higher RTE of the BESS. In addition, the CF of the mGT is almost halved, from 56.5% to 29.5% (Table 6.13). Interestingly, even though the $\overline{\text{LCOE}}$ is largely reduced for the optimised solution, 0.69 €/kWh *vs.* 0.86 €/kWh, LCOH increases from 12.72 €/kg H_2 to 17 €/kg H_2. The reason for this is found in Fig. 6.15 which shows the breakdown of LCOH for the two ESS layouts considered (for the city of Palermo). It is observed that the CapEx of storage is much higher now (11.45 €/kg H_2 *vs.* 7.55 €/kg H_2).

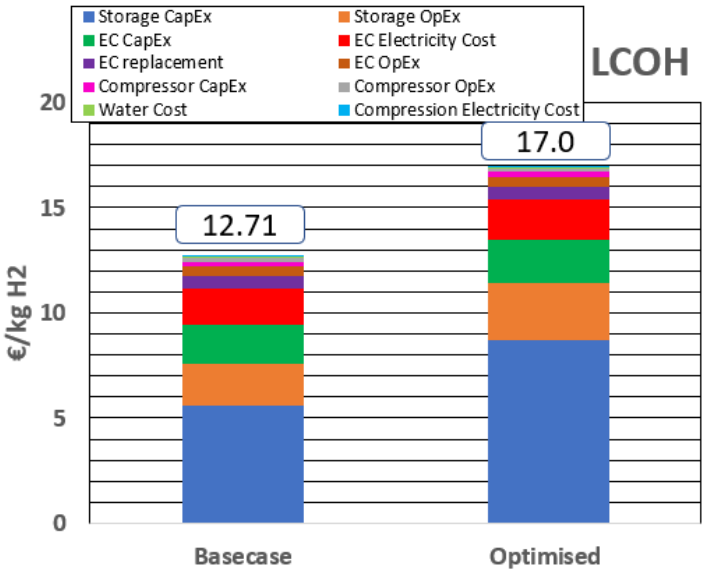

Figure 6.15: LCOH for the base-case (Tables 6.7 and 6.8) and the optimised scenario (Tables 6.12 and 6.13). Results correspond to the city of Palermo.

As observed in the Pareto fron in Fig. 6.13, other designs can achieve lower LCOEs. Figure 6.14 shows the linear trends for the different inputs considered to minimise the LCOE. These trends show that a higher number of modules/strings and a lower capacity of the battery and electrolyser yield lower LCOE. This comes about because the CF of the electrolyser increases with decreasing electrolyser capacity and increasing rated output of the PV system, whilst LCOE_{PV} remains constant due to the moderate effect of economies of scale in the range considered. As a consequence, LCOH is reduced. However, when things proceed in this direction, the amount of surplus energy increases and, since this is an off-grid application, so does the amount of energy dumped off the system. Unexpectedly, even though LCOE_{BESS} is much lower than LCOE_{mGT}, $\overline{\text{LCOE}}$ decreases for decreasing capacities of the battery bank. This is so because when the battery bank capacity increases, the *CF* of the electrolyser decreases. At the same time, the consumption of H_2 decreases as more energy is supplied by the battery, while the production of H_2 also decreases but at a much lower rate. This leads to the requirement

set on net H_2 at the end of the year (net $H_2 < 400$ kg) not being met; this implies that either the rated output of the solar field or that of the electrolyser must be reduced. When this is done, the *CF* of the electrolyser increases (yielding lower LCOH) and the same applies to the need for seasonal storage (which yields higher LCOHs). The latter effect is stronger and therefore, the final result is a higher $\overline{\text{LCOE}}$.

It can therefore be concluded that hybridising the P2P-ESS with a BESS brings down the LCOE of the application. Additionally, it is important to remark that this is an off-grid application, so energy must be produced onsite and surplus electricity cannot be sold. Furthermore, heat production is not considered in the reference system; i.e., the techno-economics of the case considered here could be highly improved if it included an application with both heat and power demand. These two features, demand for heat and grid integration, will be considered by the author of the thesis in further work, possibly with larger-scale systems where economies of scale could also be applied.

6.6 Conclusions

This chapter applies the models presented in previous sections of the thesis to a particular case where an off-grid end-user demands a constant supply of electricity from renewable energy systems. The conclusions can be drafted as follows:

1. The storage capacity of an off-grid power-to-power energy storage system (P2P-ESS) cannot be disregarded in the techno-economic assessment since H_2 seasonal storage has a very strong impact on the economic figures of merit.
2. The location of the off-grid P2P-ESS has a very strong impact on the amount of H_2 produced for seasonal storage and on the footprint of the PV plant and storage system.
3. The main parameters affecting the cost of hydrogen (LCOH) for an off-grid power-to-power energy storage system are the CapEx and OpEx of the storage system, followed by the capital cost of the electrolyser and by the cost of electricity.
4. The incorporation of a battery energy storage system (BESS) into a P2P-ESS helps to considerably reduce the footprint of the systems as well as the cost of electricity (LCOE).

As a final remark, it becomes clear that the option to use P2P-ESS based on micro gas turbines in off-grid applications has non-negligible disadvantages, in particular, because of the low round-trip efficiency of the system and, accordingly, the large oversizing that is needed in order to produce hydrogen for seasonal storage. There could be other applications, not off-grid, where economies of scale or energy trading with the grid could yield a cost-effective solution. In addition, the option to use hydrogen-fired micro gas turbine might be of interest in combined heat and power applications, helping decarbonise sectors demanding high-grade heat supply.

In the light of the results, the subsequent phase of this research involves presenting strategies to enhance the power-to-heat ratio of the micro-gas turbine. The objective is to raise the overall round-trip efficiency of the P2P-ESS, resulting in a lower footprint of the renewable energy and electrolyser plants.

7 High-efficiency micro gas turbines

The analysis in Chapter 6 highlighted that the round-trip efficiency of the P2P-mGT energy storage system currently lacks competitiveness compared to other options, even if, as the only system capable of storing a large amount of energy, it must also be recognised that the concept proposed enables larger shares of non-dispatchable renewable sources. Previously, Section 3.3 had also identified the mGT and electrolyser systems as key areas for potential efficiency improvements. From this background, this chapter focuses on enhancing the round-trip efficiency of the P2P system by improving the electric efficiency of micro gas turbines and incorporating waste heat to power technology. The study aims to exceed the 45% electric efficiency threshold necessary, a value that is set as a first estimate to ensuer competitiveness of P2P-ESS based on gas turbines against alternatives using internal combustion engines and fuel cells. Achieving higher electric efficiency in the mGT would lead to reduced hydrogen consumption, system footprint, and overall capital expenditure. To accomplish this, the study proposes an integration of the recuperative Brayton cycle with bottoming organic Rankine cycle system, enabling electric efficiencies exceeding 45%.

A thorough comparison of different integration organic Rankine cycle systems with recuperative Brayton cycles reveals the potential to achieve 46% electrical efficiency by combining an intercooled-recuperative Brayton cycle with a simple recuperated ORC. The study validates the efficiency improvements, considering realistic turbomachinery specifications for this small-scale application (taken from Balje's diagrams) built upon a 30 kW mGT utilising the intercooled and recuperative Brayton cycle along with the added ORC system. This upgraded configuration enhances the efficiency of the power generation system from 26.1% to 42.1%. Reevaluating the case from Chapter 6 with the upgraded mGT-ORC unit provides valuable insights into the very strong positive impact on the economics of the energy storage system.

The contents of this chapter are partially available in:

A. Escamilla, D. Sánchez, L. García-Rodríguez, 2023, *Achieving 45% micro gas turbine efficiency through hybridisation with organic Rankine cycles*, in: 7^{th} International Seminar on O.R.C. Power Systems. September 4-6, 2023. 86. Accepted.

7.1 Introduction to the problem

Previous chapters of this thesis have shown that the cost-effectiveness of P2P-ESS is compromised by the low efficiency of the prime mover (mGT). In particular, making use of the

most efficient micro gas turbines in the market today for the power range considered (26.9% LHV efficiency for 30 kWe rated output) yields a very low round-trip efficiency of 15.5% only, which is not high enough to compensate for the high capital cost required to implement this solution [156]. This highlights that the incorporation of much more efficient power generation devices into these P2P-EES systems is the most critical route towards the development of cost-effective, small-scale P2P-EES solutions based on green hydrogen.

Micro gas turbines have power outputs below 500 kW_e, typically, a range where the main competing technologies are Internal Combustion Engines (ICE) and Fuel Cells (FC), technologies featuring higher efficiency than mGTs and, for ICEs, also lower capital cost (CapEx). Therefore, despite the visible advantages of mGTs (low NOx, high-grade heat, flexibility, fast-response capability), these do not suffice to emerge as the most interesting prime mover option. It is therefore mandatory for mGTs to increase their electric efficiency in order to gain market share in a future energy system transitioning towards decentralised energy solutions [109]. In this regard, the Aurelia A400 engine features the highest electric efficiency of all mGTs in the market, 40.2% (LHV) [113], [209], an efficiency that is comparable to ICEs and FCs of similar power output but which cannot be attained at smaller scales because of the need to adopt simpler cycles or due to the impact of scale effects on component efficiency.

In the foregoing context, the current study aims to increase the efficiency of mGTs for a wider output range in order to accomplish the cost-effectiveness of P2P-mGT ESS. To this end, past work by the authors concluded that the efficiency of the power conversion unit must be, at least, ≈45% since this boosts the round-trip efficiency of the resulting solution to ≈26% (in lieu of 15.5% for an mGT with 26.9% efficiency). The consequence of this is an almost 45% reduction in hydrogen consumption of the mGT, which translates into a footprint reduction of all systems involved in a P2P-mGT ESS, largely reducing the CapEx of the overall system. Two options to enable such efficiency increase are considered: higher efficiency mGTs and combined mGT + waste heat to power bottoming system. In the latter case, the exhaust gas from the mGT is used to drive a thermomechanical energy conversion system to produce additional electric power from the mGT waste heat. Two options are typically considered for WHP: Steam Rankine Cycle (SRC) and Organic Rankine Cycle (ORC). Amongst the two, steam is not cost-effective on a small scale, given the very low performance and high cost of steam turbines of a few hundred kilowatts [236]. Therefore, this research investigates the thermodynamic feasibility of integrating ORC systems into different recuperative Brayton cycle layouts, used by microturbines, to boost electric efficiency. A short literature review on the topic is presented below.

Bao *et al.* presented a review of organic working fluid and expander options for ORC systems, screening the most prominent Key Performance Indicators for the selection of these two elements [237]. Bonolo de Campos *et al.* reviewed the combination of micro gas turbines and ORC systems, concluding that the efficiency of a 100 kWe mGT could increase from 30% to 35% when combined with an ORC system, even if at the expense of 48% higher capital cost; it is to note that the work cited is a review and does not rely on calculations by the authors [238]. Mago *et al.* examined the potential of using the exhaust gas from microturbines in ORC systems, considering microturbines with different power outputs and different fluids in the ORC system, and basing the analysis on electric and exergy efficiencies [239]. For this,

the authors considered a set isentropic efficiency for both the ORC turbine and pump, and also a fixed electric efficiency for the mGT (ranging from 25% to 31%, depending on power output). The work gives a good understanding of which fluids might perform better whereas the present paper goes into more detail about the assessment of potential configurations of Brayton cycles and ORC systems that could help raise global efficiency, and therefore, the round-trip efficiency of the P2P-mGT ESS that the authors have previously investigated. This is of course not a new concept, as the forecited works have studied it already, but the integration of the mGT within a P2P ESS with the objective to break the 45% efficiency barrier and the improvements that are needed is innovative, as deduced from the literature review carried out by the authors. For that, systems forming both cycles will need to be dealt with in detail in the forthcoming sections.

Furthermore, it is recognised that the input data and specifications of the cycle and components, especially for the turbomachinery parts, are strongly influenced by scale even though this is mostly not considered in the literature reviewed. Thus, to assess the relevance of this common assumption, the first part of this paper provides an analysis of the impact of scale effects on the performance of compressors and turbines, which is then used to set the appropriate input data to run simulations. This is aimed at ensuring the credibility of the results. Moreover, the study incorporates diverse configurations of the Brayton cycle and varying power outputs to encompass the entire design range of micro-gas turbines, spanning from 1 kW to 500 kW that could be integrated into the P2P ESS. It is worth noting that the primary fuel utilised in this study is natural gas (for the sake of generality).

The authors acknowledge that increasing the system's complexity will inevitably lead to higher CapEx and OpEx for the mGT. However, if the overall context is considered -integration of an mGT within a P2P ESS- the increase in CapEx and OpEx of the mGT will be hardly noted as the main source of CapEx and OpEx are the PV arrangement, electrolyser and H_2 storage system.

The study in this chapter is organised as follows: 1) introduction to the concepts of P2P-mGT ESSs and waste-heat-to-power applications and literature review of hybrid micro gas turbines and ORC systems; 2) description of the integration layouts considered; 3) discussion of the design parameters used for each mGT layout and ORC system, as well as of the list of organic fluids used in the simulations; 4) discussion of the results, in particular sensitivity analysis of the impact of varying the maximum pressure of the ORC system, 5) presentation of the main conclusions and next steps.

7.2 Introduction to the integration of the Brayton cycle with a bottoming organic Rankine cycle

Gas turbines operate according to a Brayton cycle, comprised of gas compression, heating, expansion and (virtual) cooling; in a practical engine, this latter process involved direct heat and mass transfer between the engine and the environment. Organic Rankine cycles are Rankine cycles where the working fluid is organic, typically with high molar mass and molecular complexity, whose evaporation temperature is lower than that of steam at the usual operating pressures. Heavy-duty combined cycle power plants make use of use of a topping Brayton cycle and a bottoming steam Rankine cycle harvesting the available heat at the exhaust from

the former. Gas turbines in these systems feature very high turbine inlet temperatures and pressure ratios of around 25:1. When micro gas turbines are used, the turbine inlet temperature is low (limited by the material melting point since blade cooling cannot be used) and so is the associated pressure ratio accomplished by radial turbomachinery. Therefore, these engines rely on recuperative Brayton cycles to increase gas turbine performance, which implies lower exhaust gas temperatures, typically not higher than 250ºC. For this temperature, ORC systems are better suited than steam Rankine cycles.

Brayton cycles can adopt multiple configurations to increase either thermal efficiency, specific power, or both. Nevertheless, as thermal efficiency increases, the number of components and the complexity of system integration also increases. In the next sections, two possible Brayton cycle layouts are discussed: a recuperative Brayton cycle and an intercooled-recuperative Brayton cycle, the latter in a twin-spool arrangement. Though the added number of components and the complexity of the cycle becomes very visible, adopting the latter layout boosts thermal efficiency by 10 percentage points compared to the single spool recuperative Brayton cycle. Therefore, both configurations will be used in the current research.

The implementation of Brayton cycles in gas turbines renders an open-cycle engine (except on very rare occasions) whilst ORC power systems are closed-cycle systems incorporating a condenser for heat rejection. Figure 7.1 shows the configuration of the reference mGT-ORC system used in this research. The mGT module can adopt different configurations, introduced in the following section, but the exhaust gases in all of them are directed to the heat recovery vapour generator where the organic fluid discharged from the pump undergoes heating and phase change. The resulting (typically saturated) vapour is then expanded across the turbine and then cooled down and condensed; these processes are carried out cyclically. It is to note that, even though recuperative heat exchangers are typically used in other applications of ORC systems to use the available sensible heat at turbine exhaust to preheat the liquid working fluid upstream of the vapour generator, this is not typically the case for waste heat recovery applications as this has a negative impact on the amount of waste heat from the gas turbine that can be recovered.

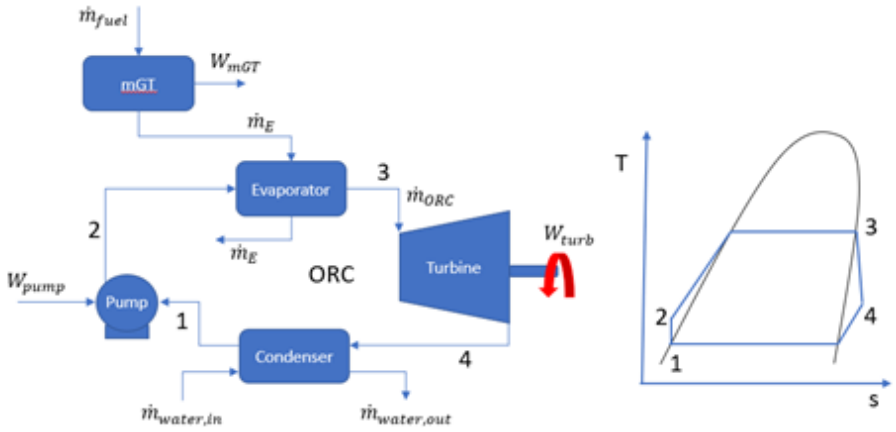

Figure 7.1: Combined mGT-ORC system layout and T-s diagram of the bottoming cycle.

7.3 Simulation of base case scenario

7.3.1 Selection of thermodynamic cycle parameters and simulation

Three micro gas turbine layouts are considered, as shown in Figs. 7.2, 7.3, and 7.4, all of which are coupled to the bottoming ORC system shown in Fig. 7.1, and a complete simulation model is then implemented in Thermoflex [240].

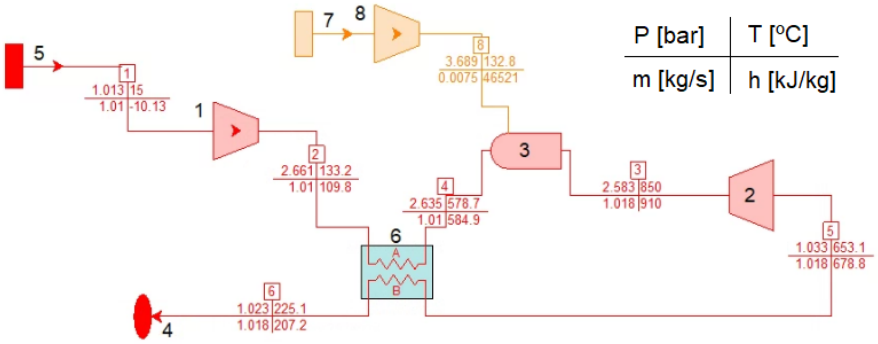

Figure 7.2: Heat and mass balance of R-MGT-1.

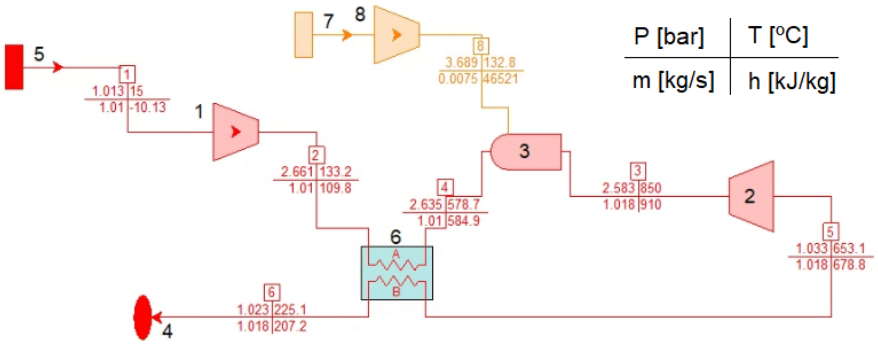

Figure 7.3: Heat and mass balance of R-MGT-2.

Out of all the equipment involved, the systems which are affected by scale effects the most are the compressor and turbine in the micro gas turbine, due to the aerodynamic and secondary loss effects; therefore, while carrying out the simulation, it is important to consider the power output (i.e, size) of the system under consideration. In this regard, the micro gas turbine options presented in Figs. 7.2 to 7.4 have the following output: 5 and 100 kW_e for the R-MGT configuration and 400 kW_e for ICR-MGT. The polytropic efficiencies given in Table 7.1 have been selected for each case, based on the considerations given in the work by Galanti *et al.* [150].

The global performance parameters of the systems shown are presented in Table 7.2. Electric efficiency for each base-case scenario is 26.5%, 29.2% and 40.2%. The electric efficiency increase comes from three different sources: upscaling of turbomachinery, turbine inlet temperature, and thermodynamic cycle layout enhancement. Interestingly, each of these cases is

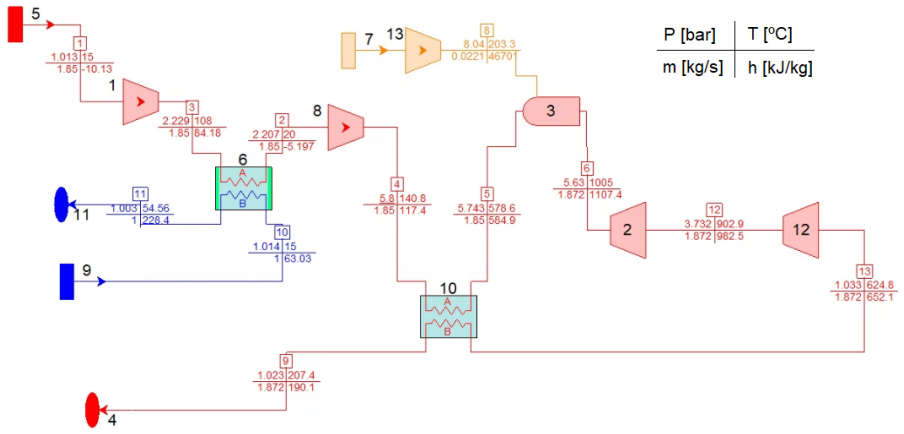

Figure 7.4: Heat and mass balance of ICR-MGT.

Parameter	Unit	Value		
		R-MGT-1	R-MGT-2	ICR-MGT
Ambient temperature and pressure	°C / bar	15 / 1.03	15 / 1.03	15 / 1.03
Working fluid	-	Air	Air	Air
Fuel	-	NG	NG	NG
Exhaust gas flow	kg/s	0.0569	1.018	1.872
Gross electric power	kW	5.08	101.5	401.0
Turbine inlet temperature	°C	850	850	1005
Total pressure ratio	-	2.5	2.5	5.8
HP compressor polytropic efficiency	%	-	-	80.2
HP turbine polytropic efficiency	%	-	-	85.2
LP compressor polytropic efficiency	%	76.5	80.5	81.0
LP turbine polytropic efficiency	%	83.8	85.2	85.8
HE thermal effectiveness	%	85.0	85.0	90.5
Combustor efficiency	%	96.0	96.0	98.0
Compressor inlet pressure loss	%	1.0	1.0	1.0
HE pressure loss	%	1.0	1.0	1.0
Combustor pressure loss	%	2.0	2.0	2.0
Mechanical efficiency	%	98.5	98.5	98.5
Generator efficiency	%	96.0	96.0	96.0

Table 7.1: Input data for the simulation of the Brayton cycle for different layouts.

intended to replicate existing commercial micro-gas turbines – MTT-EnerTwin [114], Ansaldo-AE-T100 [112], and Aurelia-A400 [113] -, even if the specifications reported in Table 7.1 deviate from the commercial specs announced by the Original Equipment Manufacturers (they are intended to be representative of the technologies used in the engines cited, but not to replicate their exact performance).

Parameter		Unit	R-MGT-1	R-MGT-2	ICR-MGT
Thermal efficiency (LHV)		%	29.4	32.2	43.4
Electric efficiency (LHV)		%	26.5	29.2	40.3
Net electric output		kW	5.08	101.5	401.0
Exhaust gas temperature		°C	231.5	225.1	204.5
Fuel Input (LHV)		kW	19.2	347.4	995.7
Exhaust gas flow		kg/s	0.0569	1.018	1.872
Exhaust gas composition	O_2	% mole	18.08	18.046	16.555
	CO_2	% mole	1.261	1.276	1.967
	H_2O	% mole	3.352	3.382	4.697
	AR	% mole	0.919	0.919	0.913
	N_2	% mole	76.387	76.376	75.868

Table 7.2: Main output parameters of the simulated micro gas turbines. Input data are displayed in Table 7.1.

7.3.2 Selection of organic working fluid and parameters of the ORC system

There is a wide range of organic fluids whose utilisation in ORC systems has been assessed. This selection of the working fluid is not only critical from a thermodynamic standpoint but also in terms of health and safety requirements and capital cost. Furthermore, the working fluid of choice must be tailored to the type and quality of heat available to drive the cycle, which adds another degree of freedom to the optimisation problem. Guoquan Qiu proposed a methodology, based on check-steps, to decide which organic fluids could be suitable for certain applications [241]. The methodology is applied in this work, narrowing down the portfolio of organic fluids to be studied, and it is also complemented with information from similar works looking for the most suitable organic fluids for the application considered in this study: waste heat from small gas turbines [237, 239, 242].

Table 7.3 shows the fluids and associated thermodynamic properties considered in the analysis whilst Table 7.4 lists other parameters needed for the simulation of the organic Rankine cycle whose layout was presented in Fig. 7.1. It is worth noting that condenser pressure is different for each fluid as this comes determined by the saturation temperature at the condenser, and this depends on ambient temperature (same for all cases). In practice, this translates into condenser pressures equal to 0.91 bar, 1.48, and 4.99 bar for R123, R245fa, and R1234ze, respectively. One of the noteworthy features of using organic fluids in the Rankine cycle is the avoidance of vacuum conditions in the condenser. This has several advantages, the most salient of which being that deaeration is no longer needed given that the entire system operates under pressure. This reduces the cost of the system and increases the useful life of components, thanks to the corrosion triggered by oxygen leaking into the system. Additional benefits relate to the mechanical design of components. Based on this, and to avoid vacuum conditions in the condenser, it is decided to set the following condenser pressures for the three fluids considered: 1.25 bar, 1.5 bar, and 5 bar, respectively.

Ultimately, it is of utmost importance to mention that there have been global efforts to phase down the use of hydrofluorocarbons (HFCs) due to their high GWP. The phasedown is being implemented under the Kigali Amendment to the Montreal Protocol, which is an international

Parameter	Unit	Fluid		
		R123	R245fa	R1234ze
Critical pressure	MPa	3.66	3.64	3.64
Critical temperature	°C	183.7	157.5	109.4
Boiling temperature[*1]	°C	27.8	15.3	-18.95
Molar mass	g/mol	153	134	114
GWP (AR5)	-	79.0	858.0	1.00
1. at 1 bar.				

Table 7.3: Thermodynamic properties of fluids (Coolprop [76]).

Parameter	Unit	Value		
		R-MGT-1	R-MGT-2	ICR-MGT
Condenser temperature	°C	25	25	25
Pump isentropic efficiency	%	85.0	85.0	85.0
Pump motor efficiency	%	88.0	88.0	88.0
Turbine isentropic efficiency	%	83.8	85.2	85.8
Evaporator pinch point	°C	5	5	5
Mechanical efficiency	%	98.5	98.5	98.5
Generator efficiency	%	96.0	96.0	96.0

Table 7.4: Input parameters for the ORC layouts considered.

agreement aimed at reducing the production and consumption of substances that deplete the ozone layer. Under this Kigali Amendment [243], different schedules and targets have been established for the phasedown of HFCs, depending on the GWP of the fluid and its intended application. The amendment sets out a gradual reduction in the production and consumption of HFCs, with different phase-down schedules for developed and developing countries.

It is important to note though that the phasedown of HFCs does not necessarily mean an outright ban on all HFC fluids. Rather, it aims to limit their production, import, and use in order to reduce their impact on climate change. Accordingly, the specific regulations and restrictions on HFCs can vary by country and region.

R123 has undergone is now banned for new HVAC equipment starting from January 1^{st}, 2020. However, its production will continue specifically for servicing equipment until 2030. On the other hand, R1234ze is facing a potential ban as part of a joint restriction proposal under the European REACH regulations [244]. The proposal aims to include R1234ze in a broader restriction proposal that intends to ban PFAS (per- and polyfluoroalkyl substances). If approved, these proposals would come into effect in 2025, providing an 18-month transition period for the adoption of alternative substances. As for R245fa, while it does have certain restrictions for specific applications, there are no current restrictions in place for its use in ORC systems, to the best knowledge of the author.

7.4 Integration of mGT and ORC systems

Once the base case scenarios have been set, this section explores the benefits of using the exhaust gases from the different mGT layouts to drive an ORC system, considering several organic fluids. The analysis aims to understand how the global (gross) electric efficiency of the power generation system is impacted by the integration proposed, calculated as follows:

$$\eta_{e,gross}(LHV) = \frac{\text{Useful power output}}{\text{Energy input}} = \frac{P_{e,GEN1} - P_{e,fuel} + P_{e,GEN2} - P_{e,pump}}{\text{Fuel Input (LHV)}} \tag{7.1}$$

Where P_e stands for electric power. Generator 1 (GEN1) refers to the generator of the mGT (electric output at generator terminals) whilst Generator 2 is driven by the expander of the ORC system. FUEL and PUMP refer to the electric motors driving the fuel compressor of the Brayton cycle and pump in the ORC unit. There is only one fuel input source: the fuel added in the combustor of the mGT.

The bottoming ORC system is coupled with the stream of exhaust gases from each mGT considered (Table 7.2) as shown in Fig. 7.5, where stream '2' is the hot gas coming from the turbine. For each mGT layout, three different organic fluids used in the ORC are considered, yielding nine cases in total. In the first part of the study, the bottoming system is designed considering a minimum evaporator's pinch point of 5° and a maximum pressure of 20 bar. Next, a sensitivity analysis of the maximum pressure of the ORC system is carried out to understand the maximum potential of the ORC system to boost the total electric efficiency of the system. The upper limit of the maximum cycle pressure is set by the critical pressure of each organic fluid, Table 7.3.

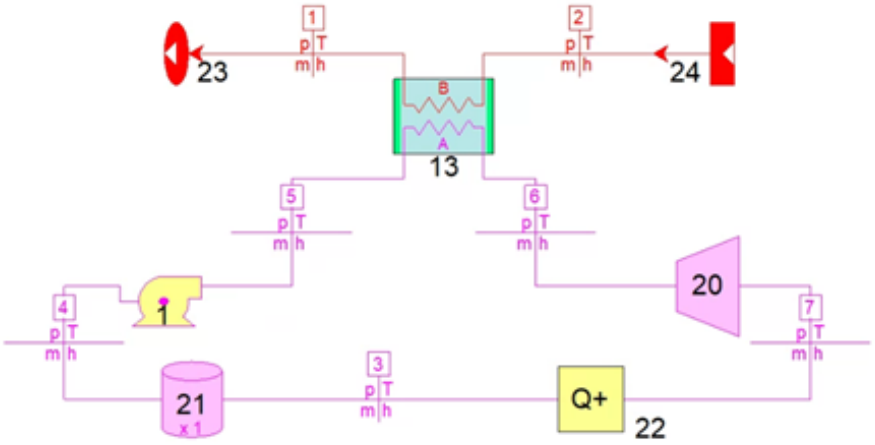

Figure 7.5: Layout of the ORC (3-4-5-6-7-3) coupled with the exhaust gas stream of the mGT (1 – 2).

Table 7.5 shows the results of the first analysis, considering a 5°C minimum pinch point in the Heat Recovery Vapour Generator and a maximum pressure of the ORC system of 20 bar. The results are highly influenced by the condensation temperature of 25°C, since this directly affects the pressure ratio through modifications of condenser pressure from one case to another. This is reflected in the electric efficiency of the ORC unit, revealing that achieving 45%

global efficiency is only possible if the ICR-MGT gas turbine layout is combined with an ORC system running on R245fa. Additionally, there is a clear trend in the contribution of the ORC unit to total power output. This is measured through the ORC Power ratio, (ORC System Power Output)/(Total Power Output), which decreases as the electric efficiency of the mGT increases, given the lower energy content of the exhaust gases from the turbine; i.e., the lower turbine exhaust temperature reduces the efficiency of the Heat Recovery Vapour Generator, meaning that a lower amount of heat is recovered from the turbine exhaust.

Parameter	**Unit**	**Value (R-MGT-1/R-MGT-2/ICR-MGT)**								
		R123			**R245fa**			**R1234ze**		
ORC pressure ratio	-	16			13.3			4		
Total electric efficiency	%	35.8	37.9	44.3	35.7	38.2	45.5	32.9	35.5	43.9
ORC system efficiency	%	16.0	16.2	16.3	15.0	15.3	15.4	10.5	10.7	10.7
Total gross electric power	kW	6.88	131.6	441.3	6.85	132.8	453.1	6.32	123.3	437.4
ORC/Total power ratio	-	0.26	0.23	0.09	0.26	0.24	0.12	0.20	0.18	0.08

Table 7.5: Results of the combined (Brayton + ORC) system considering a maximum pressure of 20 bar. Input parameters are found in Table 7.4.

The effect of maximum cycle pressure is studied next, assuming a pinch point of 5°C in the vapour generator and a condensation temperature of 25°C. Figure 7.6 shows how total electric efficiency is affected by pressure ratio. ICR-MGT is the only configuration that achieves the 45% total electric efficiency target when in combination with the bottoming system running on R245fa. In general, for the upper limit of the pressure ratio, it becomes clear that R245fa outperforms R123. For the lower limit of pressure ratio, on the contrary, R1234ze outperforms the other two fluids considered, regardless of the mGT configuration considered. It is worth noting that, due to the constraints set for condensation temperature, the maximum efficiency attainable by R1234ze is limited to 43.5%, corresponding to the ICR-MGT configuration.

The results reveal that the utilisation of a bottoming ORC unit running on R245fa enables achieving the target total electric efficiency of 45%, for a pressure ratio of 10. However, this comes at an environmental cost since, out of the three organic fluids, R245fa has the highest GWP (Table 7.3), whereas R1234ze presents the lowest value of this index.

Based on these latter results, the authors have conducted a sensitivity analysis in order to identify the conditions that would enable using an ICR-MGT engine bottomed by an ORC unit running on the lowest GWP working fluid (R1234ze), still attaining 45% global electric efficiency. The assessment is based on calculating the break-even condensation temperature that would yield 45% total electric efficiency for maximum bottoming cycle pressure of 20 bar and 35 bar. The results obtained suggest that the break-even pressure ratio is 5.8 for the former case (20 bar), for a condensation temperature of 13.3°C; these figures increase pressure ratio to 7.7 and decreases condensation temperature to 22°C (given that turbine inlet temperature set to that achievable for the turbine exhaust temperature available). Therefore, the adoption of R1234ze instead of R245fa in the bottoming system would enable 45% total electric efficiency if the condensation temperature could be reduced.

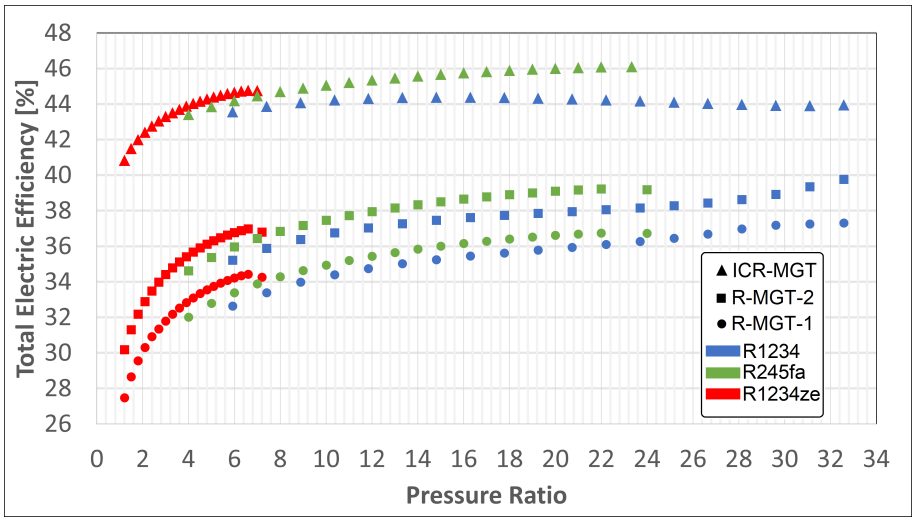

Figure 7.6: Total electric efficiency as a function of pressure ratio of the ORC system, for the three mGT configurations and three organic fluids considered.

The upcoming sections will concentrate on the utilisation of R1234ze as the operational substance for the ORC system because it possesses the lowest GWP. However, it should be noted that there is presently a proposal under consideration to prohibit the use of this organic fluid after 2025. In such a scenario, R245fa can be employed as an alternative, despite having a considerably higher GWP. Interestingly, the performance achieved with R245fa surpasses that of R1234ze, primarily due to a superior expansion ratio when the condensation temperature is restricted to 25°C.

7.5 Turbomachinery efficiency using specific speed *vs.* specific diameter diagrams

This section aims to identify the type and foreseen performance of the turbomachines that would be needed to realise the ICR-MGT layout of the gas turbine and also the expander in the ORC system. Additionally, it is also of interest to determine whether the ICR-MGT layout can be downscaled to 30 kW_e instead of 400 kW_e. This will allow us to assess the performance of the system presented in that was used in Chapter 6 when incorporating the ICR-MGT layout rather than the standard recuperative cycle.

The fact efficiency of a compressor or turbine is a function of a limited number of similarity parameters determined by features of the flow, geometry of the machine and boundary conditions. Several parameters can be selected for this aim, the most common of which are specific speed (n_s) and specific diameter (d_s), on the assumption that Reynolds number is high enough so as to neglect its effect on efficiency [245]. Specific speed and diameter are defined as:

$$n_s = \frac{\omega \cdot \dot{q}^{1/2}}{(\Delta h)^{3/4}} \tag{7.2}$$

$$d_s = \frac{D \cdot (\Delta h)^{1/4}}{\dot{q}^{1/2}} \tag{7.3}$$

$$\tag{7.4}$$

where ω is the rotational speed (rad/s), $\dot{q}$ is volume flow rate (m^3/s), Δh is enthalpy change (J/kg), and D is rotor diameter (m). $\dot{q}$ is defined at the inlet to the compressor and outlet from the turbine.

Figures 7.7 and 7.8 present the impact of these two parameters on the performance of the machine, provided by the iso-efficiency contours. Interestingly, for each $n_s - d_s$ pair, the efficiency comes also associated with a particular machine layout: volumetric, dynamic and specific subcategories within these two groups. These charts can be used to select the most suitable machine type (specific diameter) for a given specific speed (mostly duty of the machine) and, after this, to have a first estimate of machine efficiency. Accordingly, radial machines are seen to be more suitable for low specific speed applications (low flow, high head) whereas the opposite holds true for axial machinery. Lastly, it must be remarked that these are theoretical charts, developed from a number of assumptions that must be checked for each particular application.

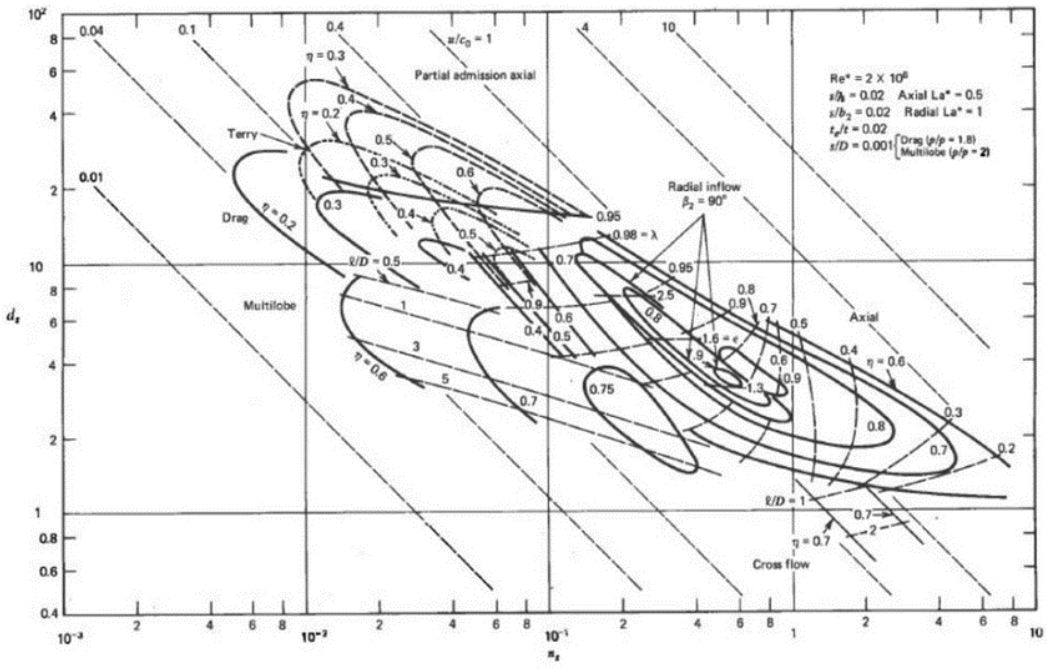

Figure 7.7: Specific speed (n_s) vs. specific diameter (d_s) diagram for single stage turbines [246].

Specific speed for the machines to be used in the application considered in this chapter can be estimated from the information in Fig. 7.4 and Tables 7.1, 7.2, 7.4, and 7.5, by merely applying

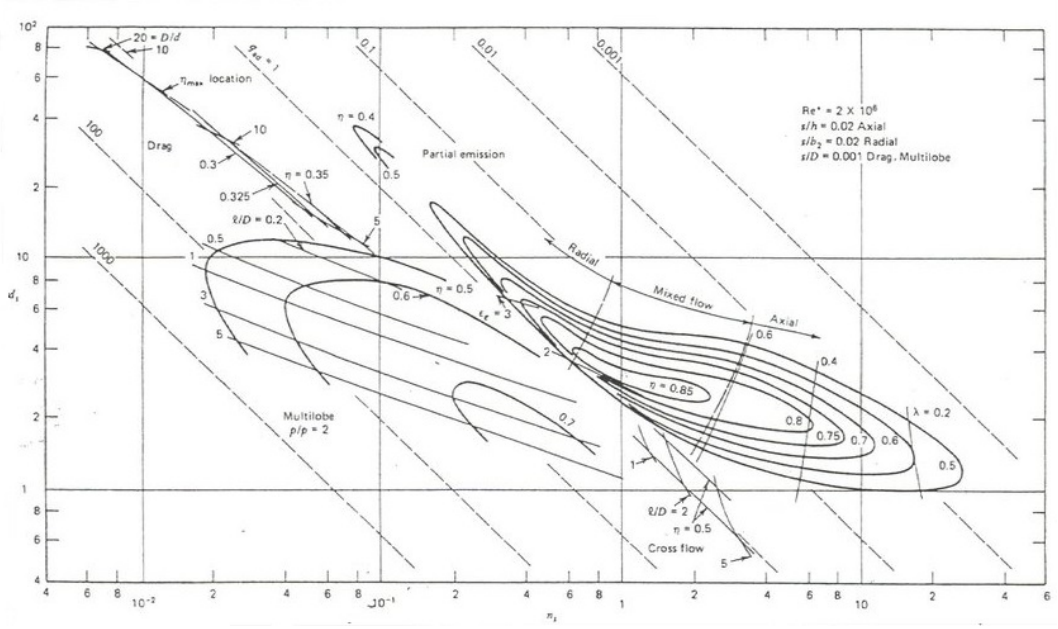

Figure 7.8: Specific speed (n_s) vs. specific diameter (d_s) diagram for single stage compressors [246].

the charts presented previously in this section (summarised in Table 7.6). In particular, the rotating speed and diameter of the machines are set by merely selecting (n_s, d_s) values yielding peak efficiency: (0.4, 1) and (0.6, 3) for radial turbine and compressor stages. The results are shown in Table 7.7.

Parameter	**Unit**	**Value**									
		Inlet					**Outlet**				
		LP C.	HP C.	HP T.	LP T.	ORC T.	LP C.	HP C.	HP T.	LP T.	ORC T.
Pressure	Pa	101.3	220.7	563	373.2	2000	222.9	580	373.2	103.3	500
Temperature	K	288	293	1278	1175.9	352.8	381	413.8	1175.9	897.8	302.9
Enthalpy	kJ/kg	288.23	292.98	1370.9	1250.4	251.6	381.88	414.82	1250.4	931.1	229.31
Mass flow rate	kg/s	1.85	1.85	1.872	1.872	1.768	1.85	1.85	1.872	1.872	1.768
Density	kg/m^3	1.226	2.626	1.532	1.104	119.62	2.037	4.875	1.104	0.401	25.784

Table 7.6: Inlet and outlet conditions of turbomachines in the ICR-MGT + ORC system using R1234ze, as reported in Table 7.5.

The ICR-MGT layout is representative of the Aurelia A400 engine, even though the parameters differ slightly from the specifications of the OEM. Matti *et al.* disclose some of the parameters for the early conceptual stage of the Aurelia A400 engine [247], amongst which a rotational speed of 32,300 rpm for the low and high-pressure shafts. Nevertheless, the overall pressure ratio of that design was lower than 5, whereas it is 5.8 for the solution presented in Chapter 6. This implies a rotational speed of around 60,000 rpm in order to reach peak efficiency according to the n_s *vs.* d_s charts.

n_s	Shaft Speed N (rpm)				
	LP C.	HP C.	HP T.	LP T.	ORC T.
0.6	32,186	60,655	-	-	-
3.0	160,929	303,275	-	-	-
0.4	-	-	22,348	39,401	26,610
1.0	-	-	55,871	98,504	66,525

Table 7.7: Rotational speed for the low and high-pressure compressors and turbines of the ICR-MGT layout and turbine of the ORC system. Obtained from the specific speed and diameter diagrams.

The same process is repeated for the ORC turbine. Out of the three fluids that were evaluated, the R1234ze is eventually adopted due to the lowest GWP, even if the efficiency is not as high as for the R245fa. The input parameters and results are also shown in Tables 7.6 and 7.7.

After calculating specific speed, or the rotational speed for each turbomachine, n_s *vs.* d_s charts can be used to calculate the optimum specific diameter for maximum efficiency at the given specific speed. Based on Figs. 7.7 and 7.8, and on the n_s ranges reported in Table 7.7, Table 7.8 shows the d_s range for each turbomachine.

System	n_s	iso-efficiency	d_s
LP C.	0.6 to 3.0	0.8 to 0.85	1.9 to 5.9
HP C.	0.6 to 3.0	0.8 to 0.85	1.9 to 5.9
HP T.	0.4 to 1.0	0.8 to 0.9	2.7 to 7.8
LP T.	0.4 to 1.0	0.8 to 0.9	2.7 to 7.8
ORC T.	0.4 to 1.0	0.8 to 0.9	2.7 to 7.8

Table 7.8: Rotational speed for the low and high-pressure compressors and turbines of the ICR-MGT layout and for the turbine of the ORC system, as obtained from the n_s *vs.* d_s charts.

Using Eq. 7.4 and the data provided in Table 7.8, Table 7.9 shows the range of diameters for the specified range of n_s and d_s.

d_s	D(cm)				
	LP C.	HP C.	HP T.	LP T.	ORC T.
1.9	10.3	6.3	-	-	-
5.9	32.1	19.5	-	-	-
2.7	-	-	16.0	14.8	5.8
7.8	-	-	46.3	42.7	16.7

Table 7.9: Diameter for the low and high-pressure compressors and turbines of the ICR-MGT layout and for the turbine of the ORC system, as obtained from the n_s *vs.* d_s charts.

Tables 7.7 and 7.9 confirm that the turbomachinery components required for the Brayton cycle and ORC system fall within the acceptable range of rotational speed and dimensions. This ensures that fabricating high-efficiency turbomachinery is feasible. However, it should

be noted that other factors such as loss effects and mechanical safety need to be taken into account in later stages of the design process, which are beyond the scope of this study. Another important fact to highlight is that the efficiencies that were chosen in the preliminary assessment of the technology -between 80% and 86% for each turbomachine- are in good agreement with the results obtained from the specific speed and diameter charts.

After conducting the techno-economic study outlined in Chapter 6, focused on a recuperated 30 kWe mGT, the next step is to investigate whether the more efficient Brayton cycle with intercooling and recuperation can be applied to the same 30 kWe mGT system. By employing the same analytical approach as previously used, the feasibility of implementing centrifugal, high-efficiency machines can be determined. Consequently, the resulting rotational speed and diameter will serve as indicators to validate the hypothesis of integrating an intercooling and recuperative Brayton cycle into a 30 kWe mGT engine.

7.5.1 Applying intercooling and internal heat recovery in a 30 kWe mGT

This section downgrades the 400 kWe mGT discussed before to 30 kWe mGT while keeping the same Brayton cycle layout -intercooling and internal heat recovery- presented in Fig. 7.4. In the same process, turbomachinery efficiency is also upgraded to account for scale effects. Table 7.10 shows the input parameters for this 30 kWe mGT engine with updated polytropic efficiency of the turbomachines, based on the informatino reported by Galanti [150].

Parameter	**Unit**	**Value**
Ambient temperature and pressure	°C / bar	15 / 1.03
Working fluid	-	Air
Fuel	-	NG
Exhaust gas flow	kg/s	0.1467
Gross Electric power	kW	30.6
Turbine inlet temperature	°C	1005
Total pressure ratio	-	5.8
HP compressor polytropic efficiency	%	79.5
HP turbine polytropic efficiency	%	84.0
LP compressor polytropic efficiency	%	79.5
LP turbine polytropic efficiency	%	84.0
HE thermal effectiveness	%	90.5
Combustor efficiency	%	98.0
Compressor inlet pressure loss	%	1.0
Recuperator pressure loss	%	1.0
Combustor pressure loss	%	2.0
Mechanical efficiency	%	98.5
Generator efficiency	%	96.0

Table 7.10: Input data for the simulation of the upgraded 30 kWe micro gas turbine.

Figure 7.9 shows the heat and mass balance of the upgraded engine and Table 7.11 shows the key performance indicators of engine performance. The net electric efficiency of the plant is reduced from 40.2% to 39% when power output is reduced from 400 kWe to 30 kWe, mostly due

to the impact of downscaling on the efficiency of turbomachinery; recuperator effectiveness and turbine inlet temperature were assumedto remain the same as in the reference case with 400 kWe (Table 7.1).

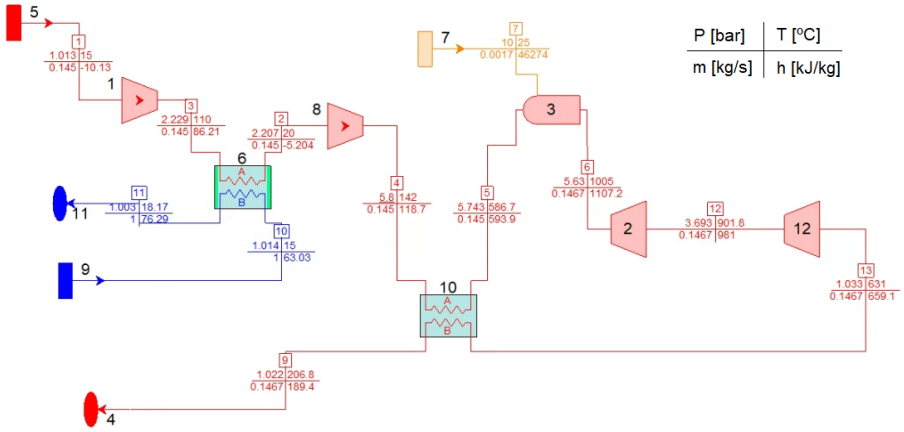

Figure 7.9: Heat and mass balance of the upgraded 30 kWe mGT incorporating intercooling and internal heat recovery.

Based on the output parameters, the ORC system is simulated considering the same input parameters as in the previous study running on R1234ze (Table 7.4). Table 7.12 and Fig. 7.10 show the updated results for a topping 30 kWe with an upgraded layout incorporating intercooling and internal heat recovery, and a bottoming ORC cycle running on R1234ze.

Parameter		**Unit**	**Values**
Thermal efficiency (LHV)		%	42.5
Electric efficiency (LHV)		%	39.0
Net electric output		kW	30.6
Exhaust gas temperature		°C	206.8
Fuel input (LHV)		kW	79.52
Exhaust gas flow		kg/s	0.1467
Exhaust gas composition	O_2	% mole	16.477
	CO_2	% mole	2.003
	H_2O	% mole	4.766
	AR	% mole	0.913
	N_2	% mole	75.842

Table 7.11: Main performance parameters of the upgraded micro gas turbine. Input data are displayed on Table 7.10

The results of the new simulations of the combined upgraded mGT and ORC power system is now used to calculate both the rotational speed and diameter of turbomachines to achieve highest efficiency based on the specific speed and diameter diagrams, Figs. 7.7 and 7.8. Referring to Table 7.8 and employing the same methodology as described in the previous section to compute rotational speed and diameter of the machine within the specified ranges of n_s

Parameter	Unit	Value
ORC pressure ratio	-	4
Total electric efficiency	%	42.1
ORC system efficiency	%	10.7
Total gross electric power	kW	33.5
ORC power ratio	-	0.08

Table 7.12: Results of the combined Brayton + ORC system. The ORC system has a peak pressure of 20 bar and runs on R1234ze. Input data shown in Table 7.4.

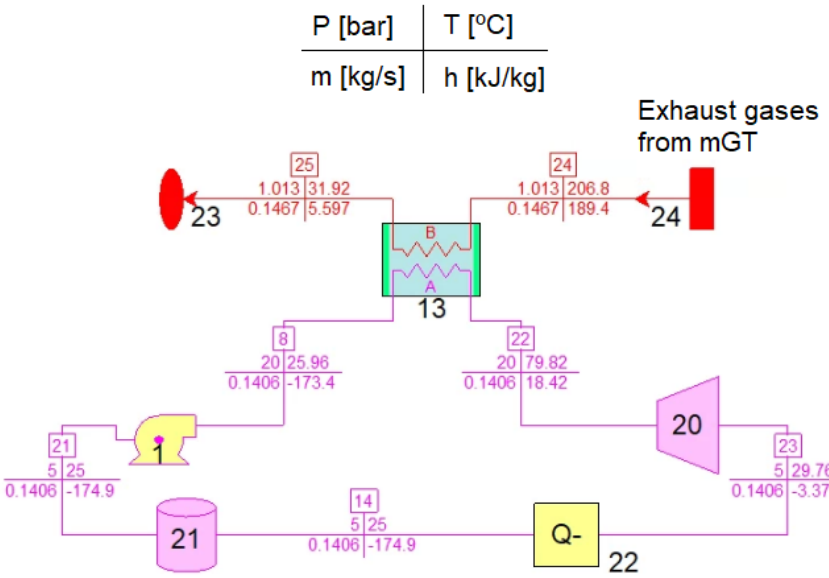

Figure 7.10: Heat and mass balance of an ORC system running on R1234ze. Exhaust gas corresponds to mGT exhaust.

and d_s, the outcomes are presented in Tables 7.13 and 7.14. The findings indicate that, as expected, the rotational speed must increase as the volume flow rate decreases in order to keep efficiency as constant as possible.

n_s	N (rpm)				
	LP C.	HP C.	HP T.	LP T.	ORC T.
0.6	113,492	212,473	-	-	-
3.0	567,461	1,062,363	-	-	-
0.4	-	-	66,103	82,870	94,839
1.0	-	-	165,258	207,176	237,098

Table 7.13: Shaft speed of the low and high-pressure compressors and turbines of the intercooled, recuperated 30 kWe engine and of the turbine in the bottoming ORC system, as obtained from the n_s *vs.* d_s charts.

Rotational speed can be increased to some extent but there are two main factors to be taken

$\mathbf{d_s}$	D(cm)				
	LP C.	HP C.	HP T.	LP T.	ORC T.
1.9	2.95	1.78	-	-	-
5.9	9.15	5.54	-	-	-
2.7	-	-	5.41	7.01	1.63
7.8	-	-	15.62	20.25	4.71

Table 7.14: Diameter of the low and high-pressure compressors and turbines of the intercooled, recuperated 30 kWe engine and of the turbine in the bottoming ORC system, as obtained from the n_s *vs.* d_s charts.

into consideration: 1) maximum centrifugal force, and 2) maximum rotational speed of the generator. The latter is typically addressed by utilising power electronics whilst, when examining the range of rotational speeds and diameters for the turbines and compressors, they appear to align with the physical limitations. However, the high and low-pressure shafts would need to operate at different rotational speeds in order to achieve the specific speed that optimises efficiency as much as possible. Once again, the polytropic efficiency chosen for each turbomachine agrees well with the specific speed and diameter diagrams.

If centrifugal machines are not viable, an alternative approach would involve replacing the compressor with a volumetric compressor, resulting in a significant drop in efficiency and pulsatory flow. Another option to consider is to restrict the minimum power output for which the upgraded cycle layout is allowed. However, based on the earlier analysis, it appears that approximately 30 kW would be the minimu, output threshold for adopting this particular configuration.

7.6 Incorporation of the upgraded combined mGT-ORC system into the power-to-power energy storage system

The closure of this chapter comes from applying the last layout studied to the practical case that was discussed in Chapter 6, with the aimed to reduce both the footprint and final LCOE of the P2P ESS of an off-grid installation.

Chapter 6 concluded that the very low electric efficiency of the mGT (26.9%) made the footprint of the off-grid energy system extremely large, with a direct effect on LCOH, and therefore, LCOE. The reason for that comes from the high storage capacity needed to support seasonal storage of H_2 from summer to winter. The first iteration carried out in the thesis was the introduction of battery storage, which drastically reduced the footprint of the systems, the seasonal storage and, therefore, the average LCOE.

The next step towards validating this solution is to introduce mGT-ORC systems into the overall P2P ESS to verify the foreseen benefits. The concept will be introduced for the solution adopted in Chapter 6, both with and without BESS. The incorporation of the combined mGT-ORC solution would incur higher costs, for obvious reasons, and, therefore, the CapEx and OpEx reported in Chapter 6 for the gas turbine (Table 6.6) are increased from 2689 €/kW and 150 €/kW to 4033 €/kW and 200 €/kW. Given the high uncertainty on the final CapEx and

OpEx, the author has decided to take a conservative approach and increase these costs by 50% and 33.3% respectively[238]. However, given that fuel cost is the primary driver of LCOE, the higher CapEx and OpEx are anticipated to have minimal impact on $LCOE_{mGT}$.

The off-design curve of the mGT that is used to determine the working parameters and has a weak impact on the final result inasmuch as the mGT works at full load most of the time in the application considered (> 98%). For this reason, the off-design performance curve of the upgraded mGT+ORC system is not upgraded but, rather, the same off-design performance curve is adopted. In other words, the efficiency curve of the micro gas turbine presented in Chapter 6, Fig. 6.5, is shifted upwards to match the rated efficiency of the upgraded mGT in the combined mGT-ORC system considered in this Chapter, yielding a conservative assessment of the technology (Fig. 7.11). This simplification allows for a quick verification of the benefits of the proposed upgraded system, with a peak efficiency, 42.1%, extrapolating the results obtained in the previous section (Table 7.12).

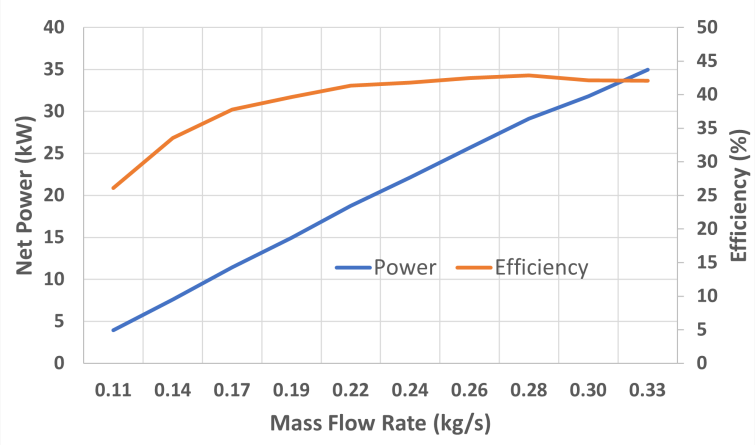

Figure 7.11: Scaling of the off-design performance curve of the upgraded 30 kWe mGT used in Chapter 6 to a rated efficiency of 42.1%.

The case will only be run for the case of Palermo, as similar results would be obtained for the cases of Frankfurt and Newcastle. Furthermore, it is expected that the increase in mGT efficiency has stronger effects in the latter two cases given that their footprint and LCOE are higher. Tables 7.15 and 7.16 show the comparison of design parameters and energy balance between the base-case scenarios from Chapter 6 and the same cases when the mGT is upgraded to a nominal efficiency of 42.1%.

From this last analysis, the benefits obtained from increasing electric efficiency of the mGT are validated. In particular, the reduction in footprint and LCOE are noteworthy. If the first approach, without BESS and with 26.9% mGT efficiency, is compared to the final solution, with the introduction of BESS and higher mGT electric efficiency (42.1%), the rated capacity and footprint of the PV solar system is reduced by almost 50%, the rated capacity of the electrolyser is reduced by 60% and the need for seasonal storage capacity is reduced by 40%. These changes lead to a reduction in the final $LCOE_{aver}$ from 0.86 €/kWh to 0.52 €/kWh, making this seasonal energy storage solution much more competitive.

System	Parameter	Unit	Palermo			
			w/o BESS		w/ BESS	
			Base	mGT-ORC	Base	mGT-ORC
PV Solar	Modules per string	-	8	8	8	8
	Strings in parallel	-	175	120	118	94
	Rated capacity	kW_{DC}	628	431	423	337
	Energy yield	kWh_{DC}/kW	1731	1731	1731	1731
	Total module area	m^2	2842	1949	1916	1527
BESS	Bank capacity	kWh	-	-	359	353
	Bank power	kW	-	-	30	30
	Charge/discharge efficiency	%	-	-	90/90	90/90
PEMEC	No Stacks	-	4	3	4	3
	No cells/stack	-	112	135	108	86
	Rated capacity	kW	463	298	256	178
	Rated H_2 production	Nm^3/h	89.3	56.9	49	34
Storage	Vessel volume	L	1208	1208	1208	1208
	Tank weight	kg	7081	7081	7081	7081
	Shell/head thickness	mm	428/157	428/157	428/157	428/157
	Compressor min/max flow rate	Nm^3/h	9.1/88.6	6.0/57.0	5/49	3.5/34.0
	Compressor pressure ratio	-	13.33	13.33	13.33	13.33
	Rated compressor power	kW	12.8	8.3	7.1	4.9
mGT	Nominal capacity	kW	30	30	30	30
	No Units	-	1	1	1	1
	Nominal electric efficiency	%	26.9	42.1	26.9	42.1

Table 7.15: Comparison of the rated specifications of the P2P-ESS designed for the city of Palermo, based on an upgraded intercooled, recuperated mGT (rated efficiency of 42.1%).

Parameter	Unit	Palermo			
		w/o BESS		w/ BESS	
		Base	mGT-ORC	Base	mGT-ORC
RES energy	MWh	1086.7	745.2	732.7	583.7
mGT energy	MWh	148.4	150.8	76.5	82.2
BESS discharged energy	MWh	-	-	73.5	70.8
BESS charged energy	MWh	-	-	(97.2)	(93.6)
PEMEC energy	MWh	(939.5)	(605.0)	(497.0)	(347.4)
Compression work	MWh	(27.0)	(17.3)	(14.2)	(9.9)
Application energy	MWh	(262.8)	(262.8)	(262.8)	(262.8)
Surplus energy	MWh	(32.8)	(28.1)	(26.7)	(32.8)
$[\text{Net } H_2]_{\text{at end year}}$	kg H_2	141	111	94	304
Seasonal storage	kg H_2	3125	2004	2558	1843
PV solar CF	%	18.2	18.2	18.2	18.2
EC CF	%	23.8	23.8	22.7	22.7
mGT CF	%	56.5	57.4	29.5	31.3
LCOH	€/kg H_2	12.72	12.71	17.0	17.4
$LCOE_{PV}$	€/kWh	0.0335	0.0335	0.0335	0.0335
$LCOE_{BESS}$	€/kWh	-	-	0.25	0.25
$LCOE_{mGT}$	€/kWh	1.49	0.99	2.04	1.4
$\overline{\text{LCOE}}$	€/kWh	0.86	0.58	0.69	0.52
RTE	%	16.0	25.6	26.2	38.2

Table 7.16: Techno-economic performance of a P2P-ESS designed for the city of Palermo, based on an upgraded intercooled, recuperated mGT (rated efficiency of 42.1%).

7.7 Conclusions

The rationale behind this study is to develop integrated mGT-ORC systems that help increase the round-trip efficiency of hydrogen-based power-to-power energy storage systems. The author estimates that breaking the 45% electric efficiency barrier would make mGTs much more competitive and a more solid candidate against internal combustion engines and fuel cells [209, 156, 109]. To this end, the study focused on three mGT layouts, including a recuperative Brayton cycle (R-MGT), an intercooled and recuperated Brayton cycle (ICR-MGT), and a combinde mGT and bottoming ORC system with the simplest layout possible (evaporator, turbine, condenser, pump).

The results of the paper show that the 45% electric efficiency target can be achieved if the ICR-MGT layout is adopted in the topping cycle. In particular, the total efficiency of a moderate size system could theoretically be as high as 46.1%, with the bottoming ORC system adding 58 kWe to the 400 kWe produced by the mGT. The latter would be achieved with an ORC system running on R245fa, a pressure ratio of 10 and a condensation temperature of 25°C. The 45% electric efficiency barrier could also be exceeded if the ORC sytem ran on R1234ze, which has lowest GWP value, but reducing condensation tempeature to 22°C and pressure ratio to 7.7.

Following the diagrams of specific speed *vs.* specific diameter, the feasibility of the guessed polytropic efficiencies for each turbomachine is confirmed. This verification involves determining the appropriate rotational speed and diameter that ensure that the selected polytropic efficiencies are attainable in practice. This is particularly important for the ICR-MGT Brayton cycle which exhibits larges thermodynamic potential but also lowest size of turbomachines for given power output. Consequently, the author proceeded to verify the technical viability of this cycle for a 30 kW mGT. The findings indicate that the application of this Brayton layout is feasible for a power output starting from the range of 30 to 50 kW. Once this verification is complete, the rated efficiency of the 30 kW mGT-ORC hybridised system increases to 42.1% which, when applied to the case study discussed in Chapter 6) and considering hybridisation with batteries, yield a 50% reduction in the footprint of the PV system, 60% decrease in the rated capacity of the electrolyser, and 40% reduction in the levelised cost of electricity (LCOE).

The next steps of this research would need to look deeper into the correction factors (<1) introduced by scaling effects into turbomachinery performance and into the economics of the system, in particular as a function of maximum ORC pressure. However, it is to highlight that the additional cost of adopting such a solution would not render any major concern, as the solution would be integrated into a hydrogen-based power-to-power energy storage system that would dilute the additional cost (i.e., it would be a small share of the total cost of the system).

8 Conclusions

Energy is the lifeblood of modern society, powering our homes, businesses, and industries. It is the driving force behind technological advancements and economic growth. However, as global energy demand continues to rise and concerns about climate change intensify, the need for sustainable and efficient energy sources becomes increasingly urgent. The objective of this study has been to introduce the notion of power-to-power and explore the integration of a micro-gas turbine as a renewable gas-based thermo-mechanical power conversion unit. Additionally, the research has sought to enhance our understanding of how this solution fits into the paradigm of off-grid applications tackling the energy trilemma.

Each chapter provided specific conclusions. Now, this chapter presents specific conclusions initially and then introduces the main, high-level conclusions. The chapter concludes with recommendations for the next steps of this research regarding the enhancement and integration of power-to-power energy storage systems based on micro gas turbines into the energy mix.

The following specific conclusions are presented first:

- Photovoltaic plants are identified as the primary source of renewable energy that has the potential to feed electrolysers due to the ubiquitous availability of solar energy (as opposed to wind). However, its typical power curve is certainly not beneficial for the working condition of the electrolyser nor for the low capacity factor at which the electrolyser would be working, compromising the cost-effectiveness of the reference business case. The main drivers for future development are higher-density solar cells and higher peak efficiency.
- Proton-exchange electrolysers are thought to be the best fit for intermittent renewable energy but at a higher cost than alkaline electrolysers (30% to 50% higher). Yet, alkaline technology holds some advantages, thermodynamically and economically, that could make it ideal when connected to the grid and working at full load. Solid oxide electrolysers are still to be developed at an industrial scale, but they are deemed as a game-changer due to their ability to work reversibly (electrolyser and fuel cell modes) and with high utilisation of the electricity provided. The main drivers for future electrolyser development are higher electric efficiency and lower capital cost.
- Storage and transportation are identified as the most challenging processes for the widespread use of hydrogen, due to its low density at atmospheric conditions. Therefore, decentralisation and close-to-the-end-user production facilities are instrumental

in the massive deployment of hydrogen. In the case of high-volume, long-distance transportation (>200 km) of hydrogen, not only are capital and operational expenditure challenging, but there still are many technical and energy difficulties to overcome. Pushing for close-to-the-end-user hydrogen production plants would be a priority, reducing infrastructure inefficiencies and wide-spreading the associated social benefits in sparsely populated areas. The main drivers for future development are lower capital costs of storage vessels and higher storage capacity per single unit.

- Micro gas turbines are deemed essential for the decentralisation of the power grid. They are highly efficient when used in combined heat and power configurations. However, a higher power-to-heat ratio is often required and, then, micro gas turbines are not technically and economically competitive against other alternatives. Increasing the power-to-heat ratio by utilising waste-to-power solutions is a high priority for the further development of the technology in the coming years. The main drivers for future development are a higher power-to-heat ratio, higher electric efficiency, and lower capital cost. When upgrading the Brayton layout from recuperative to intercooled, recuperative and considering the integration of the micro-gas turbine with bottoming organic Rankine cycles, the electric efficiency of a 30 kWe micro gas turbine can be upgraded from around 25% to over 40%

Improvements in each constituent component contribute to enhancing the overall techno-economic performance of the power-to-power energy storage system. However, upgraded integration layouts can also help to enhance global performance, as proved throughout the development of this research. With this in mind, the following general conclusions about power-to-power energy storage systems can be drawn:

- With contemporary commercial solutions and considering the best-case scenario, the highest round-trip efficiency (energy out/energy in) of power-to-power energy storage using micro gas turbine technology is close to 29% (considering a solid oxide electrolyser and metal hydride hydrogen storage). However, with mature and industrial scale technologies, this number is reduced to ≈21% (considering an alkaline or proton-exchange membrane electrolyser and high-pressure storage). The main conclusion from these figures is that there is still a large margin for performance enhancement of the technology.
- Taking into account precise mathematical models developed to evaluate the performance characteristics of the power-to-power system, and applying them to an off-grid case study with a constant demand for electric power of 30 kWe, round-trip efficiency falls rapidly to slightly higher than 15%, which is a very modest key performance indicator.
- The analysis of various locations in Europe revealed that location has a very weak impact on round-trip efficiency, but a very strong effect on the costs of hydrogen and energy, as well as on the footprint of the photovoltaic and electrolyser systems.
- Standardisation of power-to-power system is in contradiction to cost-effectiveness, as it is crucial to maximise the capacity factor of the electrolyser and minimise the storage capacity in order to fulfil the necessary requirements for a viable business case, and this relies on tailoring the system to a particular location.
- Breaking down the levelised cost of hydrogen reveals that 50% of the costs can be attributed to capital and operational expenses of the storage system. This is closely

followed by the capital cost of the electrolyser and the cost of electricity required to sustain hydrogen production. Accordingly, the incorporation of seasonal storage becomes incredibly important, particularly for off-grid applications that heavily rely on this feature.
- The levelised cost of electricity for the micro gas turbine depends mostly on the cost of hydrogen, since this accounts for over 95% of the total cost; accordingly, the capital cost of the micro gas turbine takes a secondary role. Contrary to common belief, the capital cost of the micro gas turbine is not a decisive factor in these types of applications.
- Optimising the power-to-power system layout through hybridisation with battery storage and through micro-gas turbine upgrades (from 26.9% efficiency to ≈42%) renders much higher round-trip efficiency: circa 40% as opposed to 16.0% for the reference case. This translates into 50% reduction of the PV solar system footprint, 60% reduction in the rated capacity of the electrolyser system, and 40% reduction in the levelised cost of electricity.

It is the candidate's opinion that this thesis convincingly showcases the initial progress made in implementing power-to-power energy storage systems incorporating micro gas turbines for off-grid applications. Furthermore, by constructing design models for each component of the system and integrating them with a tool for economic evaluation, the thesis effectively identifies key factors to be taken into account during the design phase. Significantly, it draws attention to areas of vulnerability in need of further research and development to enable the successful deployment of this technology. The ultimate goal of this development is to attain a minimum environmental footprint and levelised cost of electricity, while also contributing to the widespread adoption of renewable energy sources and to the global efforts to mitigate climate change. Hence, given the need to build upon a cost-effective business case for the electrolyser module and the power conversion unit, it is essential to direct efforts towards exploring the potential of reversible operation of high-temperature electrolysers for hydrogen production, and towards investigating waste heat recovery options to further enhance the power-to-heat ratio of the micro gas turbine.

Annexes

Annexe I: tank refilling

Yang presents a thermodynamic assessment of the gaseous hydrogen filling of a fuel tank [142]. The cited author considers both ideal and non-ideal gas behaviour for gaseous hydrogen. The refuelling procedure is analysed under different conditions: adiabatic, isothermal, or diathermal conditions of the tank. This Annex focuses on the ideal gas model with adiabatic and diathermal treatment.

Adiabatic process (ideal gas)

Equation 4.17 describes the refilling process of any ideal or non-ideal gas. If both ideal-gas and adiabatic process assumptions are considered, Eq. 4.17 can be transformed into Eq. 8.1.

$$\frac{u-(u_e+R\cdot T_e)}{u_i-(u_e+R\cdot T_e)}=\frac{1}{1+\widehat{t}} \tag{8.1}$$

where u_i is the initial molar internal energy of the system. u_e, T_e and R (= 8.314 J/mol·K) are the molar internal energy, temperature of the entering stream, and universal gas constant respectively. $\widehat{t}\equiv K\cdot t/N_i$ is a dimensionless time.

Internal energy can be expressed as a function of temperature as follows:

$$u=u_0+c_v\cdot(T-T_0);\qquad u_i=u_0+c_v\cdot(T_i-T_0);\qquad u_e=u_0+c_v\cdot(T_e-T_0)$$

where u_0 is the molar internal energy at the reference temperature T_0 and c_v is the molar specific heat at constant volume, and c_v does not change with temperature. Hence, Eq. 8.1 can be simplified to:

$$\frac{T-\gamma\cdot T_e}{T_i-\gamma\cdot T_e}=\frac{1}{1+\widehat{t}} \tag{8.2}$$

where $\gamma=(c_v+R)/c_v$. Hence, the tank temperature can be expressed as a function of time, depending on inlet stream temperature and molar flow rate, and initial tank temperature. At the same time, the pressure of the tank can be also calculated at any time t during refilling, using Eq. 8.1 and the ideal equation of state.

$$\frac{P\cdot V}{R\cdot T}=N_i+K\cdot t \tag{8.3}$$

Where V is the volume of the tank. Substituting Eq. 8.3 for Eq. 8.2 and simplifying,

$$\frac{P}{P_i}=1+\left(\frac{\gamma\cdot T_e}{T_i}\right)\widehat{t} \tag{8.4}$$

Equation 8.4 can be used either to determine the time (t_f) needed to refill the tank to a desired pressure (P_f) for any given T_e, T_i, K and P_i, or to determine the molar flow rate (K) to fill up the tank in a specific time (t) for any given T_e, T_i, P_i, P_f and t_f.

Diathermal process (ideal gas)
When there is a transfer of heat between the system and its surroundings and the system is not isothermal (which is a specific type of diathermal process), the Q term in Eq. 4.17 can be conveniently expressed by utilising an overall heat transfer coefficient ($U_H T$), the heat transfer area of the tank (A_t), and the temperature difference between the surrounding temperature (T_∞) and the temperature pf the tank (T). By using a constant overall heat transfer coefficient, the detailed analysis of heat transfer from the interior of the tank to the interior surface of the tank, through the tank wall, and from the exterior surface of the tank to the surroundings can be simplified.

$$(N_i + K \cdot t)\frac{du}{dt} + u \cdot K = U_{HT} \cdot A_t \cdot (T_\infty - T) + (u_e + P_e v v_e) \cdot K \tag{8.5}$$

Following the same process as the adiabatic process above, Eq. 8.5 becomes

$$(N_i + K \cdot t)\frac{dT}{dt} = K \cdot \left(\frac{U_{HT} \cdot A_t}{K \cdot c_v}(T_\infty - T) + (T_e - T) + \frac{R}{c_v}T_e\right)$$

Integrating the equation with the initial condition at $t = 0$, $T = T_i$ yields

$$\left(\frac{(1+St) \cdot T - \gamma \cdot T_e - St \cdot T_\infty)}{(1+St) \cdot T_i - \gamma \cdot T_e - St \cdot T_\infty)}\right) = \left(\frac{1}{1+\widehat{t}}\right)^{(1+St)} \tag{8.6}$$

where $St = U_{HT} A_t / K c_v$, which can be considered as a form of dimensionless heat transfer Stanton number [248]. Equation 8.6 represents the temperature of the tank at time t during a diathermal refilling process. Furthermore, the pressure of the tank at any time during refilling can be derived from $N = N_i + K \cdot t$, Eq. 8.6 and the ideal-gas law.

$$\frac{P}{P_i} = \left(\frac{1}{1+\widehat{t}}\right)^{St} + \frac{\gamma \cdot T_e + St \cdot T_\infty}{(1+St) \cdot T_i}\left((1+\widehat{t}) - \left(\frac{1}{1+\widehat{t}}\right)^{S} t\right) \tag{8.7}$$

Equation 8.7 reduces to Eq. 8.4 when $St = 0$ (adiabatic condition).

Bibliography

[1] UNFCCC, What is the kyoto protocol?, accessed: 2023-06-20 (Dec 1997).
URL https://unfccc.int/kyoto_protocol

[2] E. Comission, Paris agreement, accessed: 2021-03-18.
URL https://ec.europa.eu/clima/policies/international/negotiations/paris_en#tab-0-0

[3] UNFCCC, Katowice climate package, accessed: 2023-06-20 (2018).
URL https://unfccc.int/process-and-meetings/the-paris-agreement/the-katowice-climate-package/katowice-climate-package

[4] UNFCCC, Marrakech partnership for global climate action, accessed: 2023-06-20.
URL https://unfccc.int/sites/default/files/marrakech_partnership_for_global_climate_action.pdf

[5] M. . Company, Global energy perspectives 2022 (2022).
URL https://www.mckinsey.com/industries/oil-and-gas/our-insights/global-energy-perspective-2022

[6] I. E. A. (IEA), Global energy review 2021 (2021).
URL https://www.iea.org/reports/global-energy-review-2021

[7] IEA, World energy outlook (weo) (2022).
URL https://www.iea.org/reports/world-energy-outlook-2022

[8] IEA, IRENA, UNSD, W. Bank, WHO, Tracking sdg7: The energy progress report (2023).
URL https://www.irena.org/Publications/2023/Jun/Tracking-SDG7-2023

[9] E. ToolBox, Fossil and alternative fuels energy content, 2020-10-15 (2008).
URL https://www.engineeringtoolbox.com/fossil-fuels-energy-content-d_1298.html

[10] W. E. C. (WEC), Innovation insights brief: New hydrogen economy - hope or hype? (2019).
URL https://www.worldenergy.org/publications/entry/innovation-insights-brief-new-hydrogen-econor

[11] P. Nikolaidis, A. Poullikkas, A comparative overview of hydrogen production processes, Renewable and Sustainable Energy Reviews 67 (2017) 597–611. doi:https://doi.org/10.1016/j.rser.2016.09.044.

[12] A. Godula-Jopek, Introduction, John Wiley & Sons, Ltd, 2015. doi:https://doi.org/10.1002/9783527676507.ch1.

[13] J. Silveira, Sustainable Hydrogen Prodution Processes, 2017. doi:https://doi.org/10.1007/978-3-319-41616-8.

[14] M. Kayfeci, A. Keçebaş, M. Bayat, Chapter 3 - hydrogen production, in: F. Calise, M. D. D'Accadia, M. Santarelli, A. Lanzini, D. Ferrero (Eds.), Solar Hydrogen Production, Academic Press, 2019, pp. 45–83. doi:https://doi.org/10.1016/B978-0-12-814853-2.00003-5.

[15] A. Bakhtyari, M. A. Makarem, M. R. Rahimpour, Hydrogen Production Through Pyrolysis, Springer New York, New York, NY, 2017, pp. 1–28. doi:https://doi.org/10.1007/978-1-4939-2493-6_956-1.

[16] D. Das, T. Veziroğlu, Hydrogen production by biological processes: a survey of literature, International Journal of Hydrogen Energy 26 (1) (2001) 13–28. doi:https://doi.org/10.1016/S0360-3199(00)00058-6.

[17] P. Mishra, S. Krishnan, S. Rana, L. Singh, M. Sakinah, Z. Ab Wahid, Outlook of fermentative hydrogen production techniques: An overview of dark, photo and integrated dark-photo fermentative approach to biomass, Energy Strategy Reviews 24 (2019) 27–37. doi:https://doi.org/10.1016/j.esr.2019.01.001.

[18] G. Duman, K. Akarsu, A. Yilmazer, T. Keskin Gundogdu, N. Azbar, J. Yanik, Sustainable hydrogen production options from food wastes, International Journal of Hydrogen Energy 43 (23) (2018) 10595–10604, the 2nd International Hydrogen Technologies Congress (IHTEC-2017). doi:https://doi.org/10.1016/j.ijhydene.2017.12.146.

[19] F. Dawood, M. Anda, G. Shafiullah, Hydrogen production for energy: An overview, International Journal of Hydrogen Energy 45 (7) (2020) 3847–3869. doi:https://doi.org/10.1016/j.ijhydene.2019.12.059.

[20] M. Goedkoop, M. Demmers, M. Collignon, The eco-indicator 95. manual for designers; de eco-indicator 95. handleiding voor ontwerpers (Jul 1995).

[21] A. Ozbilen, I. Dincer, M. A. Rosen, A comparative life cycle analysis of hydrogen production via thermochemical water splitting using a cu–cl cycle, International Journal of Hydrogen Energy 36 (17) (2011) 11321–11327, international Conference on Hydrogen Production (ICH2P)-2010. doi:https://doi.org/10.1016/j.ijhydene.2010.12.035.

[22] M. N. . G. C. I. P. PLC, Green hydrogen: water use implications and opportunities, accessed: 2023-05-18 (dec 2021).
URL https://itm-power-assets.s3.eu-west-2.amazonaws.com/Green_Hydrogen_Water_Use_56b96f577d.pdf

[23] A. Mehmeti, A. Angelis-Dimakis, G. Arampatzis, S. J. McPhail, S. Ulgiati, Life cycle assessment and water footprint of hydrogen production methods: From conventional to emerging technologies, Environments 5 (2) (2018). doi:https://doi.org/10.3390/environments5020024.

[24] C. Acar, I. Dincer, Comparative assessment of hydrogen production methods from renewable and non-renewable sources, International Journal of Hydrogen Energy 39 (1) (2014) 1–12. doi:https://doi.org/10.1016/j.ijhydene.2013.10.060.

[25] A. Christensen, Assessment of hydrogen production costs from electrolysis: United states and europe (June 2020).

[26] U. D. o. E. Energy Information Administration, The impact of increased use of hydrogen on petroleum consumption and carbon dioxide emissions (Sept 2008).

[27] U. D. o. E. Office of Fossil Energy, Hydrogen strategy: Enabling a low-carbon economy (2020).

[28] C. Meyer, A. S. of Mechanical Engineers, A. R. C. on Properties of Steam, ASME Steam Tables: Thermodynamic and Transport Properties of Steam Comprising Tables and Charts for Steam and Water, Calculated Using the 1967 IFC Formulation for Industrial Use in Conformity with the the 1963 International Skeleton Tables, as Adopted by the Sixth International Conference on the Properties of Steam, American Society of Mechanical Engineers, 1993.

[29] X. Li, L. Zhao, J. Yu, X. Liu, X. Zhang, H. Liu, W. Zhou, Water splitting: From electrode to green energy system, Nano-Micro Letters 12 (2020) 131. doi:https://doi.org/10.1007/s40820-020-00469-3.

[30] C. Lamy, P. Millet, A critical review on the definitions used to calculate the energy efficiency coefficients of water electrolysis cells working under near ambient temperature conditions, Journal of Power Sources 447 (2020) 227350. doi:https://doi.org/10.1016/j.jpowsour.2019.227350.

[31] Exergy Analysis of Green Power-to-Hydrogen Chemical Energy Storage, Vol. Volume 4: Cycle Innovations; Cycle Innovations: Energy Storage of Turbo Expo: Power for Land, Sea, and Air. doi:10.1115/GT2022-82107.

[32] W. Kreuter, H. Hofmann, Electrolysis: The important energy transformer in a world of sustainable energy, International Journal of Hydrogen Energy 23 (8) (1998) 661–666. doi:https://doi.org/10.1016/S0360-3199(97)00109-2.

[33] M. Laguna-Bercero, Recent advances in high temperature electrolysis using solid oxide fuel cells: A review, Journal of Power Sources 203 (2012) 4–16. doi:https://doi.org/10.1016/j.jpowsour.2011.12.019.

[34] M. Riedel, M. Heddrich, K. Friedrich, Analysis of pressurized operation of 10 layer solid oxide electrolysis stacks, International Journal of Hydrogen Energy 44 (10) (2019) 4570–4581. doi:https://doi.org/10.1016/j.ijhydene.2018.12.168.

[35] J. Proost, State-of-the art capex data for water electrolysers, and their impact on renewable hydrogen price settings, International Journal of Hydrogen Energy 44 (9) (2019) 4406–4413, european Fuel Cell Conference & Exhibition 2017. doi:https://doi.org/10.1016/j.ijhydene.2018.07.164.

[36] S. Grigoriev, V. Fateev, D. Bessarabov, P. Millet, Current status, research trends, and challenges in water electrolysis science and technology, International Journal of Hydrogen Energy 45 (49) (2020) 26036–26058, progress in Hydrogen Production and Utilization. doi:https://doi.org/10.1016/j.ijhydene.2020.03.109.

[37] A. Ursua, L. M. Gandia, P. Sanchis, Hydrogen production from water electrolysis: Current status and future trends, Proceedings of the IEEE 100 (2) (2012) 410–426. doi:https://doi.org/10.1109/JPROC.2011.2156750.

[38] W. Ju, L. Pusterla, M. Heinz, D. Burnat, C. Battaglia, U. Vogt, Developments for alkaline electrolysis: From materials to laboratory electrolysis, 2017.

[39] M. of International Trade, I. (MITI), The strategic road map for hydrogen and fuel cells (2019).

[40] I. E. A. (IEA), The future of hydrogen (2019).
URL https://www.iea.org/reports/the-future-of-hydrogen

[41] I. R. E. A. (IRENA), Renewable power-to-hydrogen (2019).
URL https://www.irena.org/-/media/Files/IRENA/Agency/Publication/2019/Sep/IRENA_Power-to-Hydrogen_Innovation_2019.pdf

[42] S. Siracusano, V. Baglio, S. Grigoriev, L. Merlo, V. Fateev, A. Aricò, The influence of iridium chemical oxidation state on the performance and durability of oxygen evolution catalysts in pem electrolysis, Journal of Power Sources 366 (2017) 105–114. doi:https://doi.org/10.1016/j.jpowsour.2017.09.020.

[43] A. Fedotov, S. Grigoriev, E. Lyutikova, P. Millet, V. Fateev, Characterization of carbon-supported platinum nano-particles synthesized using magnetron sputtering for application in pem electrochemical systems, International Journal of Hydrogen Energy 38 (1) (2013) 426–430, european Fuel Cell 2011. doi:https://doi.org/10.1016/j.ijhydene.2012.09.121.

[44] F. Andolfatto, R. Durand, A. Michas, P. Millet, P. Stevens, Solid polymer electrolyte water electrolysis: electrocatalysis and long-term stability, International Journal of Hydrogen Energy 19 (5) (1994) 421–427. doi:https://doi.org/10.1016/0360-3199(94)90018-3.

[45] A. Ganesan, M. Narayanasamy, Ultra-low loading of platinum in proton exchange membrane-based fuel cells: a brief review, Materials for Renewable and Sustainable Energy 8 (12 2019). doi:https://doi.org/10.1007/s40243-019-0156-x.

[46] H. Zhang, P. Shen, Recent development of polymer electrolyte membranes for fuel cells, Chemical reviews 112 (2012) 2780–832. doi:https://doi.org/10.1021/cr200035s.

[47] A. Pandiyan, A. Uthayakumar, R. Subrayan, S. W. Cha, S. B. Krishna Moorthy, Review of solid oxide electrolysis cells: a clean energy strategy for hydrogen generation, Nanomaterials and Energy 8 (1) (2019) 2–22. doi:https://doi.org/10.1680/jnaen.18.00009.

[48] K. Chen, S.-S. Liu, N. Ai, M. Koyama, S. P. Jiang, Why solid oxide cells can be reversibly operated in solid oxide electrolysis cell and fuel cell modes?, Phys. Chem. Chem. Phys. 17 (2015) 31308–31315. doi:https://doi.org/10.1039/C5CP05065K.

[49] C. Yang, C. Shu, H. Miao, Z. Wang, Y. Wu, J. Wang, J. Zhao, W. Ye, J. Yuan, Dynamic modelling and performance analysis of reversible solid oxide fuel cell with syngas, International Journal of Hydrogen Energy 44 (02 2019). doi:https://doi.org/10.1016/j.ijhydene.2019.01.068.

[50] J. R. Morante, T. Andreu, G. García, J. Guilera, A. Tarancón, M. Torrell, Hidrógeno: Vector energético de una economía descarbonizada, Fundación Naturgy, 2020.
URL https://www.fundacionnaturgy.org/publicacion/hidrogeno-vector-energetico-de-una-economia-d

[51] F. Cells, H. . J. Undertaking, Hydrogen roadmap europe: A sustainable pathway for the european energy transition (Jan. 2019).
URL https://www.fch.europa.eu/publications/hydrogen-roadmap-europe-sustainable-pathway-europe

[52] M. para la trasición ecológica y el reto demográfico, Hoja de ruta del hidrógeno: una apuesta por el hidrógeno renovable (oct 2020).
URL https://www.miteco.gob.es/es/ministerio/planes-estrategias/hidrogeno/default.aspx

[53] Gasnam, mapa de hidrogeneras en españa., accessed: 2023-05-18.
URL https://gasnam.es/terrestre/mapa-de-hidrogeneras/

[54] Energy stock, accessed: 2020-10-26.
URL https://www.energystock.com/about-energystock/the-hydrogen-project-hystock

[55] International energy agency (iea), accessed: 2020-10-26.
URL https://www.iea.org/reports/hydrogen-projects-database

[56] IRENA(2020), Renewable energy statistics 2020, accessed: 2021-03-25.
URL www.irena.org/publications/2020/Jul/Renewable-energy-statistics-2020

[57] H. Council, Path to hydrogen competitiveness: A cost perspective (2020).
URL https://hydrogencouncil.com/en/path-to-hydrogen-competitiveness-a-cost-perspective/

[58] M. Thema, F. Bauer, M. Sterner, Power-to-gas: Electrolysis and methanation status review, Renewable and Sustainable Energy Reviews 112 (2019) 775–787. doi:https://doi.org/10.1016/j.rser.2019.06.030.

[59] C. Wulf, J. Linßen, P. Zapp, Review of power-to-gas projects in europe, Energy Procedia 155 (2018) 367–378, 12th International Renewable Energy Storage Conference, IRES 2018, 13-15 March 2018, Düsseldorf, Germany. doi:https://doi.org/10.1016/j.egypro.2018.11.041.

[60] F. Cell, H. E. A. (FCHEA), Road map to a us hydrogen economy (Dec. 2020).

[61] Hydrogen, F. C. S. Council, The strategic road map for hydrogen and fuel cells (Mar. 2019).

[62] G. o. C. Ministry of Energy, National green hydrogen strategy (Nov. 2020).
URL https://energia.gob.cl/sites/default/files/national_green_hydrogen_strategy_-_chile.pdf

[63] I. R. E. A. (IRENA), Global renewables outlook: Energy transformation 2050 (2020).
URL https://www.irena.org/publications/2020/Apr/Global-Renewables-Outlook-2020

[64] I. R. E. A. (IRENA), Hydrogen from renewable power: technology outlook for the energy transition, Tech. rep. (09 2018).

[65] I. E. A. (IEA), Energy technology perspectives 2020 (2020). doi:10.1787/ab43a9a5-en.
URL https://www.iea.org/reports/energy-technology-perspectives-2020

[66] Sunfire, Sunfire hydrogen electrolyzer, (accessed: 19.03.2021).
URL https://www.sunfire.de/en/hydrogen

[67] Enapter, Enapter hydrogen electrolyzer, (accessed: 19.03.2021).
URL https://www.enapter.com/electrolyser

[68] G. Hydrogen, Green hydrogen hydrogen electrolyzer, (accessed: 19.03.2021).
URL https://greenhydrogen.dk/#electrolyzers

[69] McPhy, Mcphy hydrogen electrolyzer, (accessed: 19.03.2021).
URL https://mcphy.com/en/equipment-services/electrolyzers/

[70] N. Hydrogen, Nel hydrogen hydrogen electrolyzer, (accessed: 19.03.2021).
URL https://nelhydrogen.com/water-electrolysers-hydrogen-generators/?gclid=Cj0KCQjwl9GCBhDvARIsAFunhsnLZjZNkEVldj2L1FS6_UFlviwP3GVpA9S9m3t5rSa5GMjwYfptfroaAsrjEALw_wcB

[71] I. Power, Itm power hydrogen electrolyzer, (accessed: 19.03.2021).
URL https://www.itm-power.com/products

[72] N. . E. Group, Hydrogen compressors, accessed: 2021-03-19.
URL https://www.neuman-esser.de//en/compressors/hydrogen-compressors/

[73] S. Mokhatab, W. A. Poe, Chapter 11 - natural gas compression, in: S. Mokhatab, W. A. Poe (Eds.), Handbook of Natural Gas Transmission and Processing (Second Edition), second edition Edition, Gulf Professional Publishing, Boston, 2012, pp. 393–423. doi:https://doi.org/10.1016/B978-0-12-386914-2.00011-X.
URL https://www.sciencedirect.com/science/article/pii/B978012386914200011X

[74] I. López-Paniagua, J. Rodríguez-Martín, S. Sánchez-Orgaz, J. J. Roncal-Casano, Step by step derivation of the optimum multistage compression ratio and an application case, Entropy 22 (6) (2020). doi:10.3390/e22060678.
URL https://www.mdpi.com/1099-4300/22/6/678

[75] C. W. Magazine, Pressure vessel tank types, accessed: 2021-04-08.
URL https://www.compositesworld.com/articles/pressure-vessel-tank-types

[76] I. H. Bell, J. Wronski, S. Quoilin, V. Lemort, Pure and pseudo-pure fluid thermophysical property evaluation and the open-source thermophysical property library coolprop, Industrial & Engineering Chemistry Research 53 (6) (2014) 2498–2508. arXiv:http://pubs.acs.org/doi/pdf/10.1021/ie4033999, doi:10.1021/ie4033999.
URL http://pubs.acs.org/doi/abs/10.1021/ie4033999

[77] H. Walnum, D. Berstad, M. Drescher, P. Nekså, H. Quack, C. Haberstroh, J. Essler, Principles for the liquefaction of hydrogen with emphasis on precooling processes, Refrigeration Science and Technology 2012 (2012) 273–280.

[78] G. Petitpas, Simulation of boil-off losses during transfer at a lh2 based hydrogen refueling station, International Journal of Hydrogen Energy 43 (46) (2018) 21451–21463. doi:https://doi.org/10.1016/j.ijhydene.2018.09.132.
URL https://www.sciencedirect.com/science/article/pii/S0360319918330234

[79] IDEALHY, H2020 idealhy (grant agreement no. 278177, accessed: 2021-03-22.
URL https://www.idealhy.eu/

[80] L. Decker, M. Bracha, Grosstechnische wasserstoffverflussigung in leuna, tagung; 35, deutscher kalte- und klimatechnischer verein; dkv-tagungsbericht 2008, in: Deutscher Kalte- und Klimatechnischer Verein; DKV-Tagungsbericht 2008, DKV TAGUNGSBERICHT, Tagung; 35, Deutscher Kalte- und Klimatechnischer Verein; DKV-Tagungsbericht 2008, Vol. 35, DKV;, Hannover, 2008, pp. 455–460.
URL https://www.tib.eu/de/suchen/id/BLCP%3ACN072767821

[81] U. Cardella, L. Decker, H. Klein, Roadmap to economically viable hydrogen liquefaction, International Journal of Hydrogen Energy 42 (19) (2017) 13329–13338, special Issue on The 21st World Hydrogen Energy Conference (WHEC 2016), 13-16 June 2016, Zaragoza, Spain. doi:https://doi.org/10.1016/j.ijhydene.2017.01.068.
URL https://www.sciencedirect.com/science/article/pii/S0360319917302355

[82] U. Cardella, L. Decker, H. Klein, Economically viable large-scale hydrogen liquefaction, IOP Conference Series: Materials Science and Engineering 171 (2017) 012013. doi:10.1088/1757-899x/171/1/012013.
URL https://doi.org/10.1088/1757-899x/171/1/012013

[83] C. Baker, R. Shaner, A study of the efficiency of hydrogen liquefaction, International Journal of Hydrogen Energy 3 (3) (1978) 321–334. doi:https://doi.org/10.1016/0360-3199(78)90037-X.
URL https://www.sciencedirect.com/science/article/pii/036031997890037X

[84] T. FUKANO, N. YAMASHITA, K. OHIRA, A study of the large hydrogen liquefaction process, Journal of High Pressure Institute of Japan 38 (5) (2000) 298–305. doi:10.11181/hpi1972.38.298.

[85] Q. Hans, Conceptual design of a high efficiency large capacity hydrogen liquefier, AIP Conf. Proc. 613 (05 2002). doi:10.1063/1.1472029.

[86] O. K., A summary of liquid hydrogen and cryogenic technologies in japan's we-net project, AIP Conference Proceedings 710 (1) (2004) 27–34. arXiv:https://aip.scitation.org/doi/pdf/10.1063/1.1774663, doi:10.1063/1.1774663.
URL https://aip.scitation.org/doi/abs/10.1063/1.1774663

[87] M. A. Shimko, Iii.7 innovative hydrogen liquefaction cycle, FY 2008 Annual Progress Report, DOE Hydrogen Program (2008).

[88] E. Macchi, G. Valenti, Liquid hydrogen: from clean coal to filling station. part a: proposal on an innovative, highly-efficient, large-scale liquifier (2007).

[89] D. O. Berstad, J. H. Stang, P. Nekså, Large-scale hydrogen liquefier utilising mixed-refrigerant pre-cooling, International Journal of Hydrogen Energy 35 (10) (2010) 4512–4523, novel Hydrogen Production Technologies and Applications. doi:https://doi.org/10.1016/j.ijhydene.2010.02.001.
URL https://www.sciencedirect.com/science/article/pii/S0360319910002363

[90] G. R., O. W., P. A., W. M., Liquid hydrogen for europe - the linde plant at ingolstadt. fluessigwasserstoff fuer europa - die linde-anlage in ingolstadt (Jan 1994).

[91] h2planet, Metal hydride for hydrogen storage products, accessed: 2021-04-05.
URL https://www.h2planet.eu/en/products/professional/Hydrogenstorage

[92] A. Godula-Jopek, W. Jehle, J. Wellnitz, Hydrogen Storage Technologies, John Wiley & Sons, Incorporated, 2012.

[93] HBank, Metal hydride for hydrogen storage products, (accessed: 05.04.2021).
URL http://www.hbank.com.tw/fuelcell.html

[94] P. Industries, Metal hydride for hydrogen storage products, (accessed: 05.04.2021).
URL https://www.pragma-industries.com/hydrogen-storage/

[95] hydrexia, Ground storage products, (accessed: 23.03.2021).
URL http://hydrexia.com/hydrexia-hydrogen-storage-technology

[96] HyLAW, Hydrogen law and removal of legal barriers to the deployment of fuel cells and hydrogen applications, (accessed: 12.04.2021).
URL https://www.hylaw.eu/database

[97] IEA, Current limits on hydrogen blending in natural gas networks and gas demand per capita in selected locations, access: 15/07/2023 (2023).
URL https://www.iea.org/data-and-statistics/charts/current-limits-on-hydrogen-blending-in-natural-gas-net

[98] marcogaz, Overview of available test results and regulatory limits for hydrogen admission into existing natural gas infrastructure and end use (Oct 2019).

[99] D. Deparment of Energy, Hydrogen pipeline, (accessed: 13.04.2021).
URL https://www.energy.gov/eere/fuelcells/hydrogen-pipelines#:~:text=Approximately%201%2C600%20miles%20of%20hydrogen,as%20the%20Gulf%20Coast%20region.

[100] U. D. of Energy (DOE), Fuel cell technologies - fact sheet, (accessed: 11.05.2021).
URL https://www.energy.gov/sites/prod/files/2015/11/f27/fcto_fuel_cells_fact_sheet.pdf

[101] I. E. A. (IEA), Natural gas-fired power (June 2020).
URL https://www.iea.org/reports/natural-gas-fired-power

[102] HYFLEXPOWER-H2020, Hydrogen as a flexible energy storage for a fully renewable european power system, (accessed: 25.03.2021).
URL https://cordis.europa.eu/project/id/884229

[103] ROBINSON-H2020, Smart integration of local energy sources and innovative storage for flexible, secure and cost-efficient energy supply on industrialized islands, (accessed: 25.03.2021).
URL https://flexnconfu.eu/

[104] FLEXnCONFU-H2020, Flexibilize combined cycle power plant through power-to-x solutions using non-conventional fuels, (accessed: 25.03.2021).
URL https://flexnconfu.eu/

[105] A. Perna, M. Minutillo, E. Jannelli, V. Cigolotti, . W. Nam, K. J. Yoon, Performance assessment of a hybrid sofc/mgt cogeneration power plant fed by syngas from a biomass downdraft gasifier, Applied Energy 227 (2018) 80–91, transformative Innovations for a Sustainable Future – Part III. doi:https://doi.org/10.1016/j.apenergy.2017.08.077.

[106] X. Cai, R. Lin, J. Xu, Y. Lu, Construction and analysis of photovoltaic directly coupled conditions in pem electrolyzer, International Journal of Hydrogen Energy 47 (10) (2022) 6494–6507. doi:https://doi.org/10.1016/j.ijhydene.2021.12.017.

[107] OMSOP, Microturbines for solar power, (accessed: 13.07.2023).
URL https://cordis.europa.eu/project/id/308952

[108] U. Damo, M. Ferrari, A. Turan, A. Massardo, Solid oxide fuel cell hybrid system: A detailed review of an environmentally clean and efficient source of energy, Energy 168 (11 2018). doi:10.1016/j.energy.2018.11.091.

[109] G. Tilocca, D. Sánchez, M. Torres-García, Application of the theory of constraints to unveil the root causes of the limited market penetration of micro gas turbine systems, Energy 278 (2023) 127717. doi:https://doi.org/10.1016/j.energy.2023.127717.

[110] C. T. Corporation, Capstone products, (accessed: 24.03.2021).
URL https://www.capstoneturbine.com/products

[111] F. E. Solutions, Flex energy turbines, (accessed: 24.03.2021).
URL https://www.flexenergy.com/turbine-innovations/

[112] A. Energia, Ansaldo energia microturbine ae-100, (accessed: 24.03.2021).
URL https://www.ansaldoenergia.com/business-lines/new-units/microturbines

[113] A. Turbines, Aurelia microturbine a400, (accessed: 24.03.2021).
URL https://aureliaturbines.com/company/business

[114] M. T. T. B.V., Mtt enertwin, (accessed: 24.03.2021).
URL https://enertwin.com/enertwin/

[115] E. blog (ESS), Round-trip efficiency for ess, (accessed: 25.03.2021).
URL https://energymag.net/round-trip-efficiency/

[116] I. R. E. A. (IRENA), Green hydrogen cost reduction (2020).
URL https://irena.org/publications/2020/Dec/Green-hydrogen-cost-reduction

[117] W. De Paepe, M. Montero Carrero, S. Bram, A. Parente, F. Contino, Towards higher micro gas turbine efficiency and flexibility — humidified mgts: A review., Journal of Engineering for Gas Turbines and Power 140 (11 2017). doi:10.1115/1.4038365.

[118] M. Sterner, I. Stadler, Handbook of Energy Storage Demand, Technologies, Integration: Demand, Technologies, Integration, 2019. doi:10.1007/978-3-662-55504-0.

[119] C. National Renewable Energy Laboratory. Golden, System advisor model version 2020.11.29 (sam 2020.11.29), (accessed: 10.01.2021).
URL https://sam.nrel.gov

[120] C. National Renewable Energy Laboratory. Golden, Pysam version 2.2.0., (accessed: 10.01.2021).
URL https://github.com/nrel/pysam

[121] ASME, Online Companion Guide to the ASME Boiler and Pressure Vessel Codes: Criteria and Commentary on Select Aspects of the Boiler; Pressure Vessel Codes, ASME Press, 2020. doi:10.1115/1.861981.
URL https://doi.org/10.1115/1.861981

[122] F. Marangio, M. Santarelli, M. Calì, Theoretical model and experimental analysis of a high pressure pem water electrolyser for hydrogen production, International Journal of Hydrogen Energy 34 (3) (2009) 1143–1158. doi:https://doi.org/10.1016/j.ijhydene.2008.11.083.
URL https://www.sciencedirect.com/science/article/pii/S0360319908016571

[123] I. H. Bell, J. Wronski, S. Quoilin, V. Lemort, Pure and pseudo-pure fluid thermophysical property evaluation and the open-source thermophysical property library coolprop, Industrial & Engineering Chemistry Research 53 (6) (2014) 2498–2508. arXiv:http://pubs.acs.org/doi/pdf/10.1021/ie4033999, doi:10.1021/ie4033999.
URL http://pubs.acs.org/doi/abs/10.1021/ie4033999

[124] M. Carmo, D. L. Fritz, J. Mergel, D. Stolten, A comprehensive review on pem water electrolysis, International Journal of Hydrogen Energy 38 (12) (2013) 4901–4934. doi:https://doi.org/10.1016/j.ijhydene.2013.01.151.
URL https://www.sciencedirect.com/science/article/pii/S0360319913002607

[125] P. Choi, D. G. Bessarabov, R. Datta, A simple model for solid polymer electrolyte (spe) water electrolysis, Solid State Ionics 175 (1) (2004) 535–539, fourteenth International Conference on Solid State Ionics. doi:https://doi.org/10.1016/j.ssi.2004.01.076.
URL https://www.sciencedirect.com/science/article/pii/S0167273804006423

[126] K. W. Harrison, E. Hernández-Pacheco, M. Mann, H. Salehfar, Semiempirical Model for Determining PEM Electrolyzer Stack Characteristics, Journal of Fuel Cell Science and Technology 3 (2) (2005) 220–223. arXiv:https://asmedigitalcollection.asme.org/electrochemical/article-pdf/3/2/220/5896281/220_1.pdf, doi:10.1115/1.2174072.
URL https://doi.org/10.1115/1.2174072

[127] R. Kopitzke, C. Linkous, H. Anderson, G. Nelson, Conductivity and water uptake of aromatic-based proton exchange membrane electrolytes, Journal of The Electrochemical Society 147 (2000) 1677–1681. doi:10.1149/1.1393417.

[128] T. Springer, T. Zawodzinski, S. Gottesfeld, Polymer electrolyte fuel cell model, Journal of The Electrochemical Society 138 (1991) 2334–2342.

[129] D. M. Bernardi, M. W. Verbrugge, Mathematical model of a gas diffusion electrode bonded to a polymer electrolyte, AIChE Journal 37 (8) (1991) 1151–1163. doi:https://doi.org/10.1002/aic.690370805.

[130] P. Colbertaldo, S. L. Gómez Aláez, S. Campanari, Zero-dimensional dynamic modeling of pem electrolyzers, Energy Procedia 142 (2017) 1468–1473, proceedings of the 9th International Conference on Applied Energy. doi:https://doi.org/10.1016/j.egypro.2017.12.594.
URL https://www.sciencedirect.com/science/article/pii/S1876610217363506

[131] Z. Kang, J. Mo, G. Yang, Y. Li, D. A. Talley, B. Han, F.-Y. Zhang, Performance modeling and current mapping of proton exchange membrane electrolyzer cells with novel thin/tunable liquid/gas diffusion layers, Electrochimica Acta 255 (2017) 405–416. doi:https://doi.org/10.1016/j.electacta.2017.09.170.

[132] P. Kazempoor, R. Braun, Model validation and performance analysis of regenerative solid oxide cells: Electrolytic operation, International Journal of Hydrogen Energy 39 (6) (2014) 2669–2684. doi:https://doi.org/10.1016/j.ijhydene.2013.12.010.

[133] M. Ni, M. K. Leung, D. Y. Leung, A modeling study on concentration overpotentials of a reversible solid oxide fuel cell, Journal of Power Sources 163 (1) (2006) 460–466, special issue including selected papers presented at the Second International Conference on Polymer Batteries and Fuel Cells together with regular papers. doi:https://doi.org/10.1016/j.jpowsour.2006.09.024.

[134] E. Hernandez-Pacheco, M. Mann, Sofc performance under various gasifier compositions using an electro-thermal model, Proceedings - Electrochemical Society 2005-07 (2005) 895–902. doi:https://doi.org/10.1149/200507.0895PV.

[135] J. Veldsink, R. van Damme, G. Versteeg, W. van Swaaij, The use of the dusty-gas model for the description of mass transport with chemical reaction in porous media, The Chemical Engineering Journal and the Biochemical Engineering Journal 57 (2) (1995) 115–125. doi:https://doi.org/10.1016/0923-0467(94)02929-6.

[136] R. C. Reid, J. M. Prausnitz, B. E. Poling, The properties of gases and liquids (1 1987).
URL https://www.osti.gov/biblio/6504847

[137] E. Hernández-Pacheco, D. Singh, P. N. Hutton, N. Patel, M. D. Mann, A macro-level model for determining the performance characteristics of solid oxide fuel cells, Journal of Power Sources 138 (1) (2004) 174–186. doi:https://doi.org/10.1016/j.jpowsour.2004.06.051.

[138] B. Todd, J. Young, Thermodynamic and transport properties of gases for use in solid oxide fuel cell modelling, Journal of Power Sources 110 (1) (2002) 186–200. doi:https://doi.org/10.1016/S0378-7753(02)00277-X.

[139] H. Zhu, R. Kee, V. M. Janardhanan, O. Deutschmann, D. Goodwin, Modeling elementary heterogeneous chemistry and electrochemistry in solid-oxide fuel cells, Journal of The Electrochemical Society 152 (2005).

[140] J. H. Nam, D. H. Jeon, A comprehensive micro-scale model for transport and reaction in intermediate temperature solid oxide fuel cells, Electrochimica Acta 51 (17) (2006) 3446–3460. doi:https://doi.org/10.1016/j.electacta.2005.09.041.

[141] O. Ulleberg, Stand-alone power systems for the future: Optimal design, operation and control of solar-hydrogen energy systems (Dec 1998).

[142] J. C. Yang, A thermodynamic analysis of refueling of a hydrogen tank, International Journal of Hydrogen Energy 34 (16) (2009) 6712–6721, 4th Dubrovnik Conference. doi:https://doi.org/10.1016/j.ijhydene.2009.06.015.

[143] A. The American Sociaty of Mechanical Engineer.

[144] G. Sdanghi, G. Maranzana, A. Celzard, V. Fierro, Review of the current technologies and performances of hydrogen compression for stationary and automotive applications, Renewable and Sustainable Energy Reviews 102 (2019) 150–170. doi:https://doi.org/10.1016/j.rser.2018.11.028.

[145] InIPED, Expert know-how with hydrogen compressors, accessed: 2022-02-07.
URL https://youtu.be/UvcQXFGm6lE

[146] M. Wilcox, R. Baldwin, A. Garcia-Hernandez, , K. Brun, Guideline for gas turbine inlet air filtration systems, Proceedings of the Gas Machinery Research Council (2010).

[147] M. Wilcox, R. Kurz, K. Brun, Technology review of modern gas turbine inlet filtration systems, International Journal of Rotating Machinery 2012 (03 2012). doi:10.1155/2012/128134.

[148] A. Lefebvre, D. Ballal, Gas Turbine Combustion: Alternative Fuels and Emissions, 2010, third Edition (3rd ed.). doi:https://doi.org/10.1201/9781420086058.

[149] T. Lencero, V. Staff, A. Blanco, F. Aguilar, Turbomaquinas Termicas, Síntesis Editorial, 2004.

[150] L. Galanti, A. F. Massardo, Micro gas turbine thermodynamic and economic analysis up to 500kwe size, Applied Energy 88 (12) (2011) 4795–4802. doi:https://doi.org/10.1016/j.apenergy.2011.06.022.

[151] M. Ward, M. Stephenson, Primary surface recuperator durability and applications, Report No. TTS006/395, Solar Turbines, Inc., San Diego, CA (1995).

[152] T. Rosfjord, W. Tredway, A. Chen, J. Mulugeta, T. Bhatia, Advanced microturbine systems, Tech. rep., United Technologies Corporation, Farmington, CT (United States) (2008).

[153] K. M, L. L, Compact Heat Exchangers (3rd Edition), Scientific International, 2018.
URL https://books.google.es/books?id=gq_PxgEACAAJ

[154] K. Hoopes, D. Sánchez, F. Crespi, A new method for modelling off-design performance of sco2 heat exchangers without specifying detailed geometry, The 5th International Symposium - Supercritical CO2 Power Cycles, 2016.

[155] A. Razak, Industrial Gas Turbines: Performance and Operability, Industrial Gas Turbines: Performance and Operability, Woodhead Pub, 2007.
URL https://books.google.es/books?id=W_jXzgEACAAJ

[156] A. Escamilla, D. Sánchez, L. García-Rodríguez, Techno-economic study of power-to-power renewable energy storage based on the smart integration of battery, hydrogen, and micro gas turbine technologies, Energy Conversion and Management: X 18 (2023) 100368. doi:https://doi.org/10.1016/j.ecmx.2023.100368.

[157] I. R. E. A. (IRENA), Renewable power generation costs in 2020, Tech. rep. (06 2021).

[158] T. Stehly, P. Beiter, P. Duffy, 2019 cost of wind energy review, Tech. rep., nREL/TP-5000-78471 (06 2020).

[159] G. Glenk, S. Reichelstein, Economics of converting renewable power to hydrogen, Nature Energy 4 (2019) 216–222.

[160] N Lymberopoulos, Hydrogen production from renewables, in: Center for Renewable Energy Sources (CRES), Pikermi Attiki, Project Technical Assistant Framework Contract EESD Contract No: NNE5-PTA-2002-003/1 (2005).

[161] J. I. Levene, Economic analysis of hydrogen production from wind: Preprint (5 2005).
URL https://www.osti.gov/biblio/884985

[162] C. Brunetto, G. Tina, Optimal hydrogen storage sizing for wind power plants in day ahead electricity market, Renewable Power Generation, IET 1 (2008) 220 – 226. doi:10.1049/iet-rpg:20070040.

[163] C. Greiner, M. Korpås, A. Holen, A norwegian case study on the production of hydrogen from wind power, International Journal of Hydrogen Energy 32 (2007) 1500–1507. doi:10.1016/j.ijhydene.2006.10.030.

[164] J. Linnemann, R. Steinberger-Wilckens, Realistic costs of wind-hydrogen vehicle fuel production, International Journal of Hydrogen Energy 32 (10) (2007) 1492–1499, eHEC2005. doi:https://doi.org/10.1016/j.ijhydene.2006.10.029.

[165] F. Mueller-Langer, E. Tzimas, M. Kaltschmitt, S. D. Peteves, Techno-economic assessment of hydrogen production processes for the hydrogen economy for the short and medium term, International Journal of Hydrogen Energy 32 (2007) 3797–3810.

[166] Michael Wenske, Wasserstoff – Herstellung per Elektrolyse, in: 17th energie symposium, Citeseer (2008).

[167] M. Sterner, Bioenergy and renewable power methane in integrated 100% renewable energy systems. limiting global warming by transforming energy systems, Fraunhofer IWES (01 2010).

[168] T. Smolinka, M. Günther, J. Garche, Stand und entwicklungspotenzial der wasserelektrolyse zur herstellung von wasserstoff aus regenerativen energien. now-studie: Kurzfassung des abschlussberichts, Tech. rep. (07 2011).

[169] C. Mansilla, S. Dautremont, B. Shoai Tehrani, G. Cotin, S. Avril, E. Burkhalter, Reducing the hydrogen production cost by operating alkaline electrolysis as a discontinuous process in the french market context, International Journal of Hydrogen Energy 36 (11) (2011) 6407–6413. doi:https://doi.org/10.1016/j.ijhydene.2011.03.004.

[170] C. Mansilla, J. Louyrette, S. Albou, C. Bourasseau, S. Dautremont, Economic competitiveness of off-peak hydrogen production today – a european comparison, Energy 55 (2013) 996–1001. doi:https://doi.org/10.1016/j.energy.2013.03.022.

[171] U. Albrecht, M. Altmann, J. Michalski, T. Raksha, W. Weindorf, Analyse der Kosten Erneuerbarer Gase, 2013.

[172] F. Graf, M. Götz, M. Henel, T. Schaaf, R. Tichler, Abschlussbericht „techno-ökonomische studie von power-to-gas-konzepten“ (01 2014).

[173] G. M.-S. et al., Entwicklung von modularen konzepten zur erzeugung, speicherung und einspeisung von wasserstoff und methan ins erdgasnetz, Tech. rep. (02 2013).

[174] M. Jentsch, T. Trost, M. Sterner, Optimal use of power-to-gas energy storage systems in an 85% renewable energy scenario, Energy Procedia 46 (2014) 254–261, 8th International Renewable Energy Storage Conference and Exhibition (IRES 2013). doi:https://doi.org/10.1016/j.egypro.2014.01.180.

[175] R. Tichler, M. Lehner, H. Steinmüller, M. Koppe, Power-to-Gas: Technology and Business Models, 2014. doi:10.1007/978-3-319-03995-4.

[176] M. Sterner, I. Stadler, Energiespeicher - Bedarf, Technologien, Integration, Springer Vieweg, Berlin, Heidelberg, 2014. doi:https://doi.org/10.1007/978-3-642-37380-0.

[177] L. B. et al., Study on development of water electrolysis in the eu, Tech. rep. (02 2014).

[178] H. Steinmüller, R. Tichler, G. Reiter, M. Koppe, M. Harasek, M. Haider, W. Gawlik, R. Haas, Power to gas – eine systemanalyse. markt- und technologiescouting und -analyse, Tech. rep. (01 2014).

[179] R. Winkler-Goldstein, A. Rastetter, Power to gas: The final breakthrough for the hydrogen economy?, Green 3 (01 2013). doi:10.1515/green-2013-0001.

[180] B. Zakeri, S. Syri, Electrical energy storage systems: A comparative life cycle cost analysis, Renewable and Sustainable Energy Reviews 42 (2015) 569–596. doi:https://doi.org/10.1016/j.rser.2014.10.011.

[181] M. G. et al., Renewable power-to-gas: A technological and economic review, Renewable Energy 85 (2016) 1371–1390. doi:https://doi.org/10.1016/j.renene.2015.07.066.

[182] S. B. Walker, U. Mukherjee, M. Fowler, A. Elkamel, Benchmarking and selection of power-to-gas utilizing electrolytic hydrogen as an energy storage alternative, International Journal of Hydrogen Energy 41 (19) (2016) 7717–7731, special Issue on Progress in Hydrogen Production and Applications (ICH2P-2015), 3-6 May 2015, Oshawa, Ontario, Canada. doi:https://doi.org/10.1016/j.ijhydene.2015.09.008.

[183] J. D. Bucy, O. Lacroix, L. Jammes, The potential of power-to-gas, Tech. rep. (01 2016).

[184] W. V. et al., Power-to-gas: Short term and long term opportunities to leverage synergies between the electricity and transport sectors through power-to-hydrogen, Tech. rep., in: Hinicio SA and LBST-Ludwig-Bölkow-Systemtechnik GmbH (02 2016).

[185] I. E. Agency, The Future of Hydrogen, 2019. doi:https://doi.org/https://doi.org/10.1787/1e0514c4-en.

[186] T. B. et al., dena-leitstudie integrierte energiewende: Impulse für die gestaltung des energiesystems bis 2050, Tech. rep. (07 2018).

[187] S. Hočevar, W. Summers, Hydrogen Technology: Hydrogen production, Springer, 2008. doi:https://doi.org/10.1007/978-3-540-69925-5.

[188] P. Menanteau, M.-M. Quéméré, A. alain.le duigou@cea.fr, S. Bastard, Une analyse économique de la production d'hydrogène à partir d'électricité éolienne pour des usages transport, Revue de l'Energie (09 2010).

[189] T. E. Lipman, J. L. Edwards, D. M. Kammen, Fuel cell system economics: comparing the costs of generating power with stationary and motor vehicle pem fuel cell systems, Energy Policy 32 (1) (2004) 101–125. doi:https://doi.org/10.1016/S0301-4215(02)00286-0.

[190] C. Ainscough, D. Peterson, E. Miller, Hydrogen production cost from pem electrolysis, Tech. rep. (07 2014).

[191] Fichtner, Erstellung eines entwicklungskonzeptes energiespeicher in niedersachsen, Tech. rep. (07 2014).

[192] B. Guinot, F. Montignac, B. Champel, D. Vannucci, Profitability of an electrolysis based hydrogen production plant providing grid balancing services, International Journal of Hydrogen Energy 40 (29) (2015) 8778–8787. doi:https://doi.org/10.1016/j.ijhydene.2015.05.033.

[193] S. Schiebahn, T. Grube, M. Robinius, V. Tietze, B. Kumar, D. Stolten, Power to gas: Technological overview, systems analysis and economic assessment for a case study in germany, International Journal of Hydrogen Energy 40 (04 2015). doi:10.1016/j.ijhydene.2015.01.123.

[194] G. E. A. DENA, Power to gas system solution, Tech. rep. (2015).

[195] T. Smolinka, Cost break down and analysis of pem electrolysis systems for different industrial and power to gas applications (2015).
URL https://publica-stage.fraunhofer.de/handle/publica/391109

[196] M. e. a. Wei, A total cost of ownership model for low temperature pem fuel cells in combined heat and power and backup power applications (6 2014). doi:10.2172/1163271.

[197] D. G. E. Agency, Potenzialatlas power to gas: Klimaschutz umsetzen, erneuerbare energien integrieren, regionale wertschöpfung ermöglichen, Tech. rep. (06 2016).

[198] Tractebel, Engie, Hinicio, Study on early business cases for h2 in energy storage and more broadly power to h2 applications, Tech. rep. (07 2017).

[199] M. Tengler, Green hydrogen: Time to scale up, Tech. rep. (10 2020).

[200] B. Annabelle, J. Schefold, High temperature electrolysis at eifer, main achievements at cell and stack level, Energy Procedia 29 (2012) 53–63. doi:10.1016/j.egypro.2012.09.008.

[201] L. B. et al., Development of water electrolysis in the european union. final report., Tech. rep. (02 2014).

[202] G. Parks, R. Boyd, J. Cornish, R. Remich, Hydrogen station compression, storage, and dispensing technical status and costs independent review, Tech. rep. (05 2014). doi:10.13140/RG.2.2.23768.34562.

[203] M. Khan, C. Young, C. MacKinnon, D. Layzell, Technical brief: The techno-economics of hydrogen compression, Tech. Rep. 1 (10 2021).

[204] Hydrogen delivery scenario analysis model (hdsam), argonne national laboratory, accessed: 2022-04-19.
URL https://hdsam.es.anl.gov/index.php?content=hdsam

[205] C. Yang, J. Ogden, Determining the lowest-cost hydrogen delivery mode, International Journal of Hydrogen Energy 32 (2) (2007) 268–286. doi:https://doi.org/10.1016/j.ijhydene.2006.05.009.

[206] I. Nexant, H2a hydrogen delivery infrastructure analysis models and conventional pathway options analysis results, Tech. rep. (2008).

[207] H2a: Hydrogen analysis production models, accessed: 2022-04-21.
URL https://www.nrel.gov/hydrogen/h2a-production-models.html

[208] J. André, S. Auray, D. De Wolf, M.-M. Memmah, A. Simonnet, Time development of new hydrogen transmission pipeline networks for france, International Journal of Hydrogen Energy 39 (20) (2014) 10323–10337. doi:https://doi.org/10.1016/j.ijhydene.2014.04.190.

[209] A. Escamilla, D. Sánchez, L. García-Rodríguez, Assessment of power-to-power renewable energy storage based on the smart integration of hydrogen and micro gas turbine technologies, International Journal of Hydrogen Energy (2022). doi:https://doi.org/10.1016/j.ijhydene.2022.03.238.

[210] C. Houchins, B. D. James, Hydrogen storage cost analysis (st100), Tech. rep., accessed: 2022-04-22 (05 2020).
URL https://www.hydrogen.energy.gov/pdfs/review20/st100_houchins_2020_o.pdf

[211] M. A. Cuomo, E. D. Kool, B. V. Reddy, M. A. Rosen, Economic and environmental analyses of multi-generation renewable energy system for dairy farms, European Journal of Sustainable Development Research 6 (2022). doi:https://doi.org/10.21601/ejosdr/11397.

[212] Álvaro F. Benet Pérez, Micro gas turbines on mega yachts - a feasibility study, Master's thesis, University of Liege and Ecole Centrale de Nantes, The address of the publisher, developed at Rostock University in the framework of the "EMSHIP" (1 2016).

[213] K. Darrow, R. Tidball, J. Wang, A. Hampson, Catalog of chp technologies, Tech. rep., funded by the U.S. Environmental Protection Agency and the U.S. Department of Energy (09 2017).

[214] A. H. Pedersen, Microturbine energy systems. the omes project, Tech. rep., eU Project No.: NNE5-1999-20128 (06 2004).

[215] B. L. Capehart, Microturbines, 2022-05-10 (12 2016).
URL https://www.wbdg.org/resources/microturbines

[216] L. Sens, U. Neuling, M. Kaltschmitt, Capital expenditure and levelized cost of electricity of photovoltaic plants and wind turbines – development by 2050, Renewable Energy 185 (2022) 525–537. doi:https://doi.org/10.1016/j.renene.2021.12.042.

[217] H. Junginger, Learning in renewable energy technology development (01 2005).

[218] IEA, Average annual capacity factors by technology (2018).
URL https://www.iea.org/data-and-statistics/charts/average-annual-capacity-factors-by-technology-20

[219] IEA, Evolution of solar pv module cost by data source, 1970-2020 (2018).
URL https://www.iea.org/data-and-statistics/charts/evolution-of-solar-pv-module-cost-by-data-source

[220] K. Deb, A. Pratap, S. Agarwal, T. Meyarivan, A fast and elitist multiobjective genetic algorithm: Nsga-ii, IEEE Transactions on Evolutionary Computation 6 (2) (2002) 182–197. doi:10.1109/4235.996017.

[221] F. Heymann, M. Rüdisüli, F. vom Scheidt, A. S. Camanho, Performance benchmarking of power-to-gas plants using composite indicators, International Journal of Hydrogen Energy 47 (58) (2022) 24465–24480. doi:https://doi.org/10.1016/j.ijhydene.2021.10.189.

[222] R. Loisel, L. Baranger, N. Chemouri, S. Spinu, S. Pardo, Economic evaluation of hybrid off-shore wind power and hydrogen storage system, International Journal of Hydrogen Energy 40 (21) (2015) 6727–6739. doi:https://doi.org/10.1016/j.ijhydene.2015.03.117.

[223] A. Escamilla, D. Sánchez, L. García-Rodríguez, Assessment of power-to-power renewable energy storage based on the smart integration of hydrogen and micro gas turbine technologies, International Journal of Hydrogen Energy 47 (40) (2022) 17505–17525. doi:https://doi.org/10.1016/j.ijhydene.2022.03.238.

[224] N. Skordoulias, E. I. Koytsoumpa, S. Karellas, Techno-economic evaluation of medium scale power to hydrogen to combined heat and power generation systems, International Journal of Hydrogen Energy 47 (63) (2022) 26871–26890. doi:https://doi.org/10.1016/j.ijhydene.2022.06.057.

[225] E. Crespi, P. Colbertaldo, G. Guandalini, S. Campanari, Design of hybrid power-to-power systems for continuous clean pv-based energy supply, International Journal of Hydrogen Energy 46 (26) (2021) 13691–13708, european Fuel Cell Conference & Exhibition 2019. doi:https://doi.org/10.1016/j.ijhydene.2020.09.152.

[226] Y. Zhang, P. E. Campana, A. Lundblad, J. Yan, Comparative study of hydrogen storage and battery storage in grid connected photovoltaic system: Storage sizing and rule-based operation, Applied Energy 201 (2017) 397–411. doi:https://doi.org/10.1016/j.apenergy.2017.03.123.

[227] Z. Shahid, M. Santarelli, P. Marocco, D. Ferrero, U. Zahid, Techno-economic feasibility analysis of renewable-fed power-to-power (p2p) systems for small french islands, Energy Conversion and Management 255 (2022) 115368. doi:https://doi.org/10.1016/j.enconman.2022.115368.

[228] D. Parra, G. S. Walker, M. Gillott, Modeling of pv generation, battery and hydrogen storage to investigate the benefits of energy storage for single dwelling, Sustainable Cities and Society 10 (2014) 1–10. doi:https://doi.org/10.1016/j.scs.2013.04.006.

[229] H. T, P. P. I, G. A. A, PVGIS 5: Internet tools for the assessment of solar resource and photovoltaic solar systems (2017).

[230] N. DiOrio, A. Dobos, S. Janzou, A. Nelson, B. Lundstrom, Technoeconomic modeling of battery energy storage in sam (9 2015). doi:10.2172/1225314.
URL https://www.osti.gov/biblio/1225314

[231] V. Liso, G. Savoia, S. S. Araya, G. Cinti, S. K. Kaer, Modelling and experimental analysis of a polymer electrolyte membrane water electrolysis cell at different operating temperatures, Energies 11 (12) (2018). doi:10.3390/en11123273.

[232] I. R. E. A. (IRENA), Renewable power generation costs in 2021, Tech. rep. (07 2022).

[233] P. N. N. L. (PNNL), 2020 grid energy storage technology cost and performance assessment, Tech. rep. (12 2020).

[234] W. Cole, A. W. Frazier, C. Augustine, Cost projections for utility-scale battery storage: 2021 update, Tech. rep. (6 2021).

[235] Ice endex: Dutch ttf gas futures, accessed: 2022-09-15.
URL https://www.theice.com/products/27996665/Dutch-TTF-Gas-Futures/data

[236] B. Vanslambrouck, I. Vankeirsbilck, M. Van den Broek, S. Gusev, M. De Paepe, Efficiency comparison between the steam cycle and the organic rankine cycle for small scale power generation, 2012, p. 13.

[237] J. Bao, L. Zhao, A review of working fluid and expander selections for organic rankine cycle, Renewable and Sustainable Energy Reviews 24 (2013) 325–342. doi:https://doi.org/10.1016/j.rser.2013.03.040.

[238] Bonolo de Campos, Gustavo, Bringhenti, Cleverson, Traverso, Alberto, Takachi Tomita, Jesuino, A review on combining micro gas turbines with organic rankine cycles, E3S Web Conf. 113 (2019) 03007. doi:10.1051/e3sconf/201911303007.
URL https://doi.org/10.1051/e3sconf/201911303007

[239] P. J. Mago, R. Luck, Energetic and exergetic analysis of waste heat recovery from a microturbine using organic rankine cycles, International Journal of Energy Research 37 (8) (2013) 888–898. doi:https://doi.org/10.1002/er.2891.

[240] Thermoflow, Thermoflex, version 30 (2022).

[241] G. Qiu, Selection of working fluids for micro-chp systems with orc, Renewable Energy 48 (2012) 565–570. doi:https://doi.org/10.1016/j.renene.2012.06.006.

[242] S. Clemente, D. Micheli, M. Reini, R. Taccani, Bottoming organic rankine cycle for a small scale gas turbine: A comparison of different solutions, Applied Energy 106 (2013) 355–364. doi:https://doi.org/10.1016/j.apenergy.2013.02.004.

[243] U. N. E. P. (UNEP), Phase down of hfcs – the kigali amendment, access: 18/07/2023.
URL https://www.unep.org/ozonaction/who-we-are/about-montreal-protocol

[244] E. C. A. (ECHA), Echa publishes pfas restriction proposal, access: 18/07/2023.
URL https://echa.europa.eu/-/echa-publishes-pfas-restriction-proposal

[245] H. Krain, Review of Centrifugal Compressor's Application and Development, Journal of Turbomachinery 127 (1) (2005) 25–34. doi:https://doi.org/10.1115/1.1791280.

[246] O. E. Balje, D. Japikse, Turbomachines—A Guide to Design Selection and Theory, Journal of Fluids Engineering 103 (4) (1981) 644–644. doi:10.1115/1.3241788.

[247] Design of a 400 kW Gas Turbine Prototype, Vol. Volume 8: Microturbines, Turbochargers and Small Turbomachines; Steam Turbines of Turbo Expo: Power for Land, Sea, and Air. doi:10.1115/GT2016-56444.

[248] R. B. Bird, W. E. Stewart, , E. N. Lightfoot, Transport phenomena, AIChE Journal 7 (2) (1961). doi:https://doi.org/10.1002/aic.690070245.